The Influence of Dendritic Properties on the Dynamics of Oscillatory Neurons

By

MICHAEL ARTHUR SCHWEMMER
B.A. (Queens College, CUNY) 2005
DISSERTATION

Submitted in partial satisfaction of the requirements for the degree of

DOCTOR OF PHILOSOPHY

in

APPLIED MATHEMATICS

in the

OFFICE OF GRADUATE STUDIES

of the

UNIVERSITY OF CALIFORNIA

DAVIS

Approved:

Timothy J. Lewis

_____

Timothy J. Lewis (Chair)

Joseph Biello

_____

Joseph Biello

Brian Mulloney

_____

Brian Mulloney

Committee in Charge
2010

i

To My Family

Contents

iv

5 Effects of Dendritic Load on the Firing Frequency of Oscillating Neurons 78

6 Bistability in a Leaky Integrate-and-Fire Neuron with a Passive Dendrite 118

Michael A. Schwemmer
August 2010
Applied Mathematics

The Influence of Dendritic Properties on the Dynamics of Oscillatory Neurons

Abstract

Synchronization of oscillatory activity in neuronal networks arises in many areas of neuroscience. In the mammalian cortex, oscillatory behavior arises as a result of the synchronized electrical activity of large populations of cortical neurons. Much effort has been put into tying this observed cortical oscillatory activity to different behavioral functions. However, directly linking these cortical oscillations to precise functional roles is a difficult task and more work must be done before this can occur. Rather than directly addressing the issue of the functional role of these oscillations, one can first address the question of what are the biophysical mechanisms that underlie the observed synchronous electrical activity? A deep understanding of these mechanisms can allow one to extract the functional role of the aforementioned synchronous oscillatory behavior. It is known that networks of inhibitory interneurons play a fundamental role in generating the oscillatory electrical behavior seen in the cortex. Furthermore, it has been shown experimentally that the inhibitory neurons in these networks are highly interconnected by electrical synapses on their dendrites, and that the dendrites of these inhibitory neurons appear to display effectively passive electrical behavior. Concurrently, theoretical studies have shown that passive dendritic filtering can change the phase-locking behavior in networks of neuronal oscillators. Therefore, even passive dendritic properties can be important in the flow of electrical activity between inhibitory neurons in the cortex, and, consequently, in the generation of the synchronous electrical activity seen there. Here, we examine the role that passive dendritic properties play in shaping the oscillatory electrical activity of neuronal networks.

Acknowledgments and Thanks

This is my opportunity to thank the incredible people who have made the completion of my graduate career possible.

First and foremost I would like to thank my advisor Prof. Tim Lewis for advising me in many things besides the research contained in this dissertation. Tim always made time for me and has been a great mentor and friend. None of this would have been possible without his guidance and support.

I would also like to thank my committee members Prof. Joseph Biello and Prof. Brian Mulloney for reading my dissertation and for their invaluable comments on the various drafts.

I would like to thank Prof. Alex Mogilner because every time I speak with him I feel I learn something.

Thank you Prof. Bob Guy for your incredible help with my various computing issues and for the always amusing conversations.

Thank you Prof. Mark Goldman for your organization of the many enlightening computational neuroscience reading groups.

To everyone involved in the CLIMB program, Carole Hom, Rick Grosberg, Sebastian Schreiber, and of course the wonderful students, thank you so very much for letting me be a part of this program. It was a truly invaluable experience that I will never forget.

I have to thank the staff of the mathematics department including Perry Gee, Celia Davis, and Tina Denena (to name a few) for their incredible helpfulness and support through my graduate school journey.

To my family who has kept me grounded and supported me throughout my count-

less endeavors, I owe you so very much. My parents John and Susan who have always been a source of encouragement. My brother Eric who has and will continue being a constant source of inspiration. The rest of my family who have always been interested in what I have been doing with my life. Thank you all.

To my friends in Davis I would like to thank every single one of you, so I will try my best: Blake for being the first good friend I made in Davis, Chris and Dave for all the times in the dork shed, Deanna for always listening, Eli for being a substitute academic older brother, Emi for being Emi, Gabe for our countless conversations about everything except research, Eddie for being the most personable person I've ever met, Hillel for being there when I needed someone to talk to, Matt Rathbun for your humorously antagonistic nature, Perry for introducing me to wonderful places to eat, Roberto, Rob for being a great wingman, Rohit for being a great friend, Tami and Dave, and Tyler for being my most distracting officemate. And to all those I may have left out, thank you for making grad school a truly wonderful experience.

To my friend Lianne for listening to me from $3,000$ miles away.

To Bailey, for coming into my life at just the right moment.

Chapter 1

Introduction

Synchronization of oscillatory activity in neuronal networks arises in many areas of neuroscience and has been linked to various behavioral functions. There is little doubt that the oscillatory behavior of these networks plays a major role in generating motor patterns of repetitive activity such as locomotion, feeding, and breathing [86, 92, 105]. In the mammalian cortex, oscillatory behavior arises as a result of the synchronized electrical activity of large populations of cortical neurons. This oscillatory behavior is apparent in electroencephalogram (EEG) recordings and can occur in different frequency bands and in different areas of the cortex [14]. Oscillations within these different frequency bands have been hypothesized to correspond with different behavioral functions. For example, synchronized gamma-frequency (30-80Hz) oscillations in the mammalian sensory cortex have been hypothesized to be important in sensory information processing, e.g. in the olfactory system [57] and the visual system [42], in motor programming [68], and associative learning [66]. However, linking these cortical oscillations directly to precise functional roles is a difficult task and more work has to be done before this can occur. Therefore, rather than directly addressing the issue of the functional role of these oscillations, one can first address the question of

what are the biophysical mechanisms that underlie the observed synchronous electrical activity? A deep understanding of these mechanisms can allow one to extract the functional role of the aforementioned synchronous oscillatory behavior.

Oscillatory network behavior can be generated from individual neurons that are non-oscillatory (e.g. [8, 103, 111]), or from individual neurons that fire periodically in the absence of coupling (e.g. [33, 46, 59]). Here, we will be concerned with behavior that arises in networks of oscillatory neurons that are coupled together. In this case, the network behavior is shaped by the properties of the coupling (such as the time course and strength of the synapse, e.g. [53, 110]) and the dynamics of the individual neurons (such as the types of intrinsic currents that the neurons contain, e.g. [17, 74]). Therefore, an understanding of the activity in individual neurons that make up a neuronal network is of vital importance in understanding the overall behavior of networks like these.

In the classic view, neurons typically consist of a dendritic tree where the majority of inputs to the cell are received, a soma (cell body) in which these inputs are integrated, and an axon. Signal transmission in neurons usually occurs as follows. A presynaptic neuron releases neurotransmitter onto the dendritic tree of a postsynaptic neuron. The neurotransmitter causes a change in the membrane potential of the dendritic tree of the postsynaptic neuron. This change in potential, or signal, then propagates along the dendritic tree down to the soma, usually with some attenuation. The amount of attenuation depends on the types of ion channels that exist in the membrane of the dendritic tree. The signal is then integrated in the soma of the postsynaptic neuron. If the resulting integrated input to the neuron is large enough, an action potential, a large and transient depolarization of the membrane potential, will be initiated in the axon hillock of the neuron. The action potential

then propagates down the axon and causes the release of neurotransmitter onto a different postsynaptic cell, and the process starts over. As such, neurons are spatially extensive, heterogeneous objects. They are often modeled as single-compartment objects that ignore the spatial anatomy of the cell. This simplification is made for mathematical tractability and computational efficiency. However, many neurons are not electrotonically compact, and single-compartment models cannot be expected to fully capture their behavior. Dendrites can have substantial effects on the dynamics of individual neurons. For example, the architecture and ionic channel density of a dendritic tree can alter the firing pattern and encoding properties of a neuronal oscillator [52, 56, 61].

Networks of inhibitory interneurons play a fundamental role in generating the oscillatory electrical behavior seen in the cortex [4, 15, 93, 98]. As a result, synchronization in inhibitory networks is a topic of much theoretical and experimental research [64, 65]. It has been shown experimentally that (i) the inhibitory neurons in these networks are highly interconnected by electrical synapses on their dendrites [2, 36], and (ii) the dendrites of these inhibitory neurons appear to display effectively passive electrical behavior [48]. Concurrently, theoretical studies have shown that passive dendritic filtering can change the phase-locking behavior in networks of neuronal oscillators [12, 20, 59]. Therefore, even passive dendritic properties can be important in the flow of electrical activity between inhibitory neurons in the cortex, and, consequently, in the generation of the synchronous electrical activity seen there.

The purpose of this dissertation is to examine how dendritic properties affect the dynamics of single oscillatory neurons and the phase-locking behavior of networks of these neuronal oscillators coupled by electrical synapses.

The outline of this dissertation is as follows: this first chapter serves as an intro-

duction to the physiological and theoretical background that motivated this study. The second chapter reviews basic neuronal electrophysiology, single-compartment Hodgkin-Huxley-type neuron models, and the Leaky-Integrate-and-Fire neuron model, which is a reduced model. The third chapter introduces the cable equation, the concept of equivalent cylinders, and two spatially extended neuron models that will be used extensively in this thesis. The fourth chapter presents the theory of weakly coupled oscillators, which is the main analytical tool that we use to probe how weak dendritic influences affect the dynamics of single and electrically coupled neuronal oscillators. The fifth and sixth chapters examine how influences from the dendrite modulate the dynamics of individual neuronal oscillators. The seventh chapter examines how weak dendritic influences can affect the phase-locking behavior of networks of electrically coupled neurons.

A slightly modified form of Chapter 4 will appear in the book *Phase Response Curves in Neuroscience* (N. Schultheiss and A. Prinz, eds.). Slightly modified forms of Chapters 5 and 6 have been submitted to Physical Review E and SIAM Journal of Applied Math, respectively. The work in Chapter 7 will give rise to two manuscripts that will be submitted to appropriate scholarly journals.

1.1   Summary

In this chapter, we have reviewed the biological and theoretical motivation for studying how dendritic properties affect the dynamics and oscillatory behavior of single neurons, and the phase-locking behavior of networks of electrically coupled neuronal oscillators, which will be the focus of this dissertation.

Chapter 2

Basic Neuronal Electrophysiology and Single-Compartment Neuron Models

We review basic neuronal electrophysiology and introduce two types of single-compartment neuron models: the Hodgkin-Huxley model, and the leaky-integrate-and-fire model. We also discuss the typical ways that these single-compartment neuron models can begin to display oscillatory electrical behavior.

2.1 Introduction

Neurons receive and integrate synaptic inputs and actively transmit the signal resulting from these integrated inputs along their cell length via action potentials, which are large and transient depolarizations of their membrane potentials (see Chapter 1). The action potential is the main carrier of information within neurons in the brain. Therefore, an understanding of the biophysical mechanisms of action poten-

tial dynamics is necessary before one can even begin to understand the mechanisms underlying the electrical activity of neuronal networks. In this chapter, we discuss the basic electrophysiology of the neuron, and explain the generation of the action potential with the use of the Hodgkin-Huxley model of the squid giant axon [44]. Furthermore, we describe the different ways that single neurons can begin displaying oscillatory electrical behavior. Lastly, we present a reduction of the Hodgkin-Huxley-type models known as the leaky-integrate-and-fire (LIF) neuron [1, 99] which is more amenable to mathematical analysis and will be utilized in Chapter 6. Note that in this chapter, we assume that the neuron is represented as a single-compartment, with no spatial dependence. Spatially extended neuron models will be discussed in Chapter 3.

2.2 Neuronal Membrane Physiology

The cellular membrane of a neuron is composed of a phospholipid bilayer in which are embedded various proteins. Some of these proteins act as channels that allow ions (such as sodium Na^+ and potassium K^+) to pass through the membrane down their electrochemical gradient. Other proteins behave as pumps and use energy in the form of ATP in to move ions across the membrane against their electrochemical gradient. For example, the Na^+-K^+ pump exchanges 3 intracellular Na^+ for 2 extracellular K^+. The existence of the neuronal membrane along with the work of the ion pumps permits internal potential of the neuron to be different from the potential of the medium surrounding the neuron. More specifically, the membrane separates the internal and external medium of the neuron while the action of the Na^+-K^+ pump causes the internal (external) concentration of K^+ (Na^+) to be greater than the external (internal) concentration. It is the difference between the internal and external

potential that is commonly referred to as the *membrane potential* of the neuron, i.e. $V = V_I - V_E$ where V_I is the internal potential (or voltage) and V_E is the potential of the external medium. The *resting potential* is the membrane potential of the neuron in the absence of any external influences and is typically around $-65\ mV$.

The *action potential* is a large and transient rise (depolarization) of membrane potential above rest usually in response to some external stimulation, e.g. from another neuron via an excitatory synapse. This rapid change in membrane potential is the way that neurons transmit information to one another. To begin understanding how a neuron can generate an action potential, we will first look at the underlying electrical components of the membrane. First off, due to the properties of the phospholipid molecules, ions typically cannot pass directly through the membrane except through the specific protein channels. Thus, the membrane acts as an insulator separating two conducting solutions, and behaves like a capacitor. When the voltage across the membrane changes, a current will be generated. This capacitive current is given by

$$I_C = C_m \frac{dV(t)}{dt}, \tag{2.2.1}$$

where C_m is the specific capacitance of the membrane in units of $\mu F/cm^2$ and $V(t)$ is the membrane potential, in units of mV, at time t.

Since ions can flow through the membrane by way of the embedded protein channels, there will also be transmembrane currents associated with the movement of these ions through the channels. These protein channels act as linear Ohmic resistors with variable resistance R. The reason the resistance is variable is due to the fact that the channels can be "voltage-gated", meaning that the channels can contain multiple "gates" whose opening and closing is a function of the membrane potential. Thus, the current through the channels will be given by Ohm's Law and Kirchhoff's

conservation of current law

$$I_{ion} = \frac{1}{R_{ion}(V)}(V(t) - V_{ion}) = g_{ion}(V)(V(t) - V_{ion}), \qquad (2.2.2)$$

where $R_{ion}(V)$ is the specific ion channel resistivity in units of $k\Omega \cdot cm^2$ that could be a function of the membrane potential, $g_{ion}(V)$ is the specific ionic conductance ($\frac{1}{R_{ion}(V)}$) in units of mS/cm^2, and V_{ion} is the reversal potential of the ion channel in units of mV. The reversal potential (also known as the Nernst potential) is given by

$$V_{ion} = \frac{RT}{zF} \ln \frac{[ion]_o}{[ion]_i}, \qquad (2.2.3)$$

where $R = 8.314472(15) \frac{J}{Kmol}$ is the universal gas constant, T is the absolute temperature, z is the valence of the ion, $F = 9.64853399(24) \times 10^4 \frac{C}{mol}$ is Faraday's constant, and $[ion]_o$ ($[ion]_i$) is the external (internal) concentration of the ion. The reversal potential of the channel is the potential at which there is no net current flow through the channel for that specific ion. It determines whether a particular ionic current will be and inward or outward current relative to the resting potential. For example, suppose the internal concentration of K^+ is about 20 times greater than the external concentration. At room temperature, $V_K \approx -77 \ mV$. Since the resting potential is around $-65 \ mV$, this means that the opening of K^+ channels will cause current to flow out of the neuron. Thus, K^+ would be an outward current.

In the next section, we will present the Hodgkin-Huxley model [44], which provided the first quantitative biophysical explanation for the generation of the action potential in the squid giant axon.

2.3   The Hodgkin-Huxley Model

The Hodgkin-Huxley model assumes that the electrical activity of the squid giant axon is mainly due to the movement of Na^+ and K^+ ions across the membrane. Thus, in the model, the neuronal membrane contains Na^+ channels, K^+ channels, and a leakage channel through which various other ionic species, such as chloride Cl^-, can pass. The equivalent circuit diagram corresponding to the Hodgkin-Huxley model is shown in Figure 2.3.1.
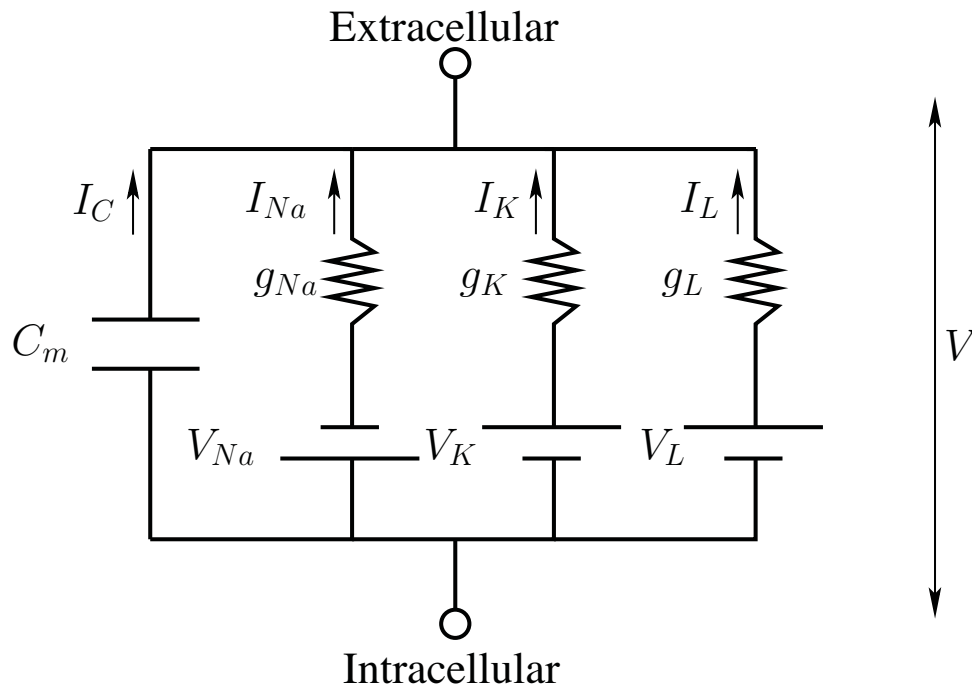
Figure 2.3.1: **Circuit Diagram for the Hodgkin-Huxley Model of the Squid Giant Axon**. The membrane itself acts as a capacitor since it separates two conducting solutions. The embedded protein channels behave like resistors with a driving force given by the reversal potential of the channel. In this model, the membrane is assumed to consist of only Na^+ channels, K^+ channels, and leakage channels where Cl^- and other ions flow through.

The conductances of the Na^+ and K^+ channels are functions of time and the membrane potential, while the conductance of the leakage channel is a constant and

unaffected by changes in the membrane potential. Furthermore, the Na^+ channel consists of three activation gates that are independent of each other and open when the membrane potential is depolarized above rest, and an inactivation gate that closes the channel when the neuron has been depolarized above rest for a certain amount of time. Thus, the Na^+ current has the form

$$I_{Na} = \bar{g}_{Na} m(t)^3 h(t)(V(t) - V_{Na}), \tag{2.3.1}$$

where $\bar{g}_{Na}$ is the maximum conductance of the channel, $m(t)$ is the fraction of open activation gates at time t, and $h(t)$ is the fraction of open inactivation gates at time t. Since the membrane is assumed to have many ion channels embedded in it, the variables m and h represent the fraction of all activation and inactivation gates, respectively, of the Na^+ channels in the open state.

Similarly, the K^+ channel has four independent activation gates that open when the neuron is depolarized. Thus, the current flowing through the K^+ channel has the form

$$I_K = \bar{g}_K n(t)^4 (V(t) - V_K), \tag{2.3.2}$$

where $\bar{g}_K$ is the maximum conductance of the channel and $n(t)$ is the fraction of open activation gates at time t.

Each of the gating variables m, h, and n also obey a differential equation of the form

$$\frac{dy}{dt} = \alpha_y(V)(1 - y) - \beta_y(V)y = \frac{y_\infty(V) - y}{\tau_y(V)}, \tag{2.3.3}$$

where $y = m, h, n$, $\beta_y(V)$ is the rate that the gate switches from the open state to

the closed state, $\alpha_y(V(t))$ is the rate that the gate switches from the closed state to the open state, $y_\infty(V) = \frac{\alpha_y(V)}{\alpha_y(V)+\beta_y(V)}$ is the steady-state fraction of open gates, and $\tau_y(V) = \frac{1}{\alpha_y(V)+\beta_y(V)}$ is the time constant associated with the change in the fraction of open gates. The functional forms of $y_\infty(V)$ and $\tau_y(V)$ were actually found experimentally by Hodgkin and Huxley by fitting voltage clamp data [44]. Figure 2.3.2 plots the values of the steady-state gating variables for the Hodgkin-Huxley model along with their associated time constants.

(a)   **(b)**
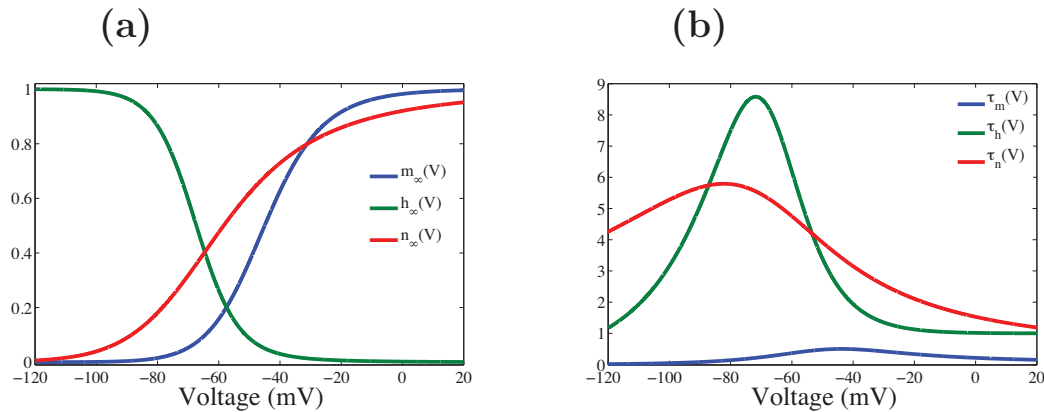
Figure 2.3.2: **Steady-State Gating Variables and Associated Time Constants for the Hodgkin-Huxley Model**. (a) Steady-state gating variables plotted as a function of the membrane potential. Note that $h_\infty(V)$ decreases as V increases, which corresponds to the Na^+ channel inactivating as the membrane potential increases. (b) Time constants for the gating variables as a function of the membrane potential. Note that $\tau_m(V)$ is much smaller than the time constants for h and n. This indicates that changes in Na^+ activation occur much faster than Na^+ inactivation or K^+ activation.

Invoking Kirchhoff's conservation of current law and using Figure 2.3.1, the Hodgkin-Huxley model can be written compactly as

$$I_C + I_{Na} + I_K + I_L = I_{appl}, \tag{2.3.4}$$

where I_{appl} is an external current applied to the neuron. The above equation can be

rewritten to obtain the complete Hodgkin-Huxley model

$$
\begin{cases}
C_m \dfrac{dV}{dt} = -\bar{g}_{Na} m^3 h (V - V_{Na}) - \bar{g}_K n^4 (V - V_K) - g_L (V - V_L) + I_{appl} \\
\dfrac{dy}{dt} = \alpha_y(V)(1 - y) - \beta_y(V)y = \dfrac{y_\infty(V) - y}{\tau_y(V)}, \quad y = m, h, n.
\end{cases}
\tag{2.3.5}
$$

The introduction of the Hodgkin-Huxley model in 1956 [44] provided quantitative explanations and predictions about the nature of action potential generation in the squid giant axon. Furthermore, it introduced a modeling formalism for neurons that is still used today. Thus, when we refer to Hodgkin-Huxley-type models throughout this dissertation, we will be referring to models of the form

$$
C_m \frac{dV}{dt} = - \sum_i I_i + I_{appl},
\tag{2.3.6}
$$

where I_i denotes the individual ionic currents of the model which all have the form

$$
I_i(t) = \bar{g}_i x^p y^q (V(t) - V_i),
\tag{2.3.7}
$$

where x and y satisfy equation (2.3.3), and the subscript i refers to the ion that flows through the channel.

2.3.1 Generation of the Action Potential

The Hodgkin-Huxley model provides a quantitative explanation of the mechanisms involved in the generation of action potentials in the squid giant axon. Furthermore, this explanation can be qualitatively applied to action potential generation in many different neurons. That is, when the membrane potential of the neuron is depolarized

above rest, a number of Na^+ channels open quickly due to the small time constant associated with the m variable (see Figure 2.3.2 (b)). This allows more Na^+ to flow into the neuron due to the electrochemical gradient, i.e. the inside of the membrane is more negative than the outside and it has a lower concentration of Na^+. The influx of extracellular Na^+ causes the cell to become more depolarized opening more and more Na^+ channels and leading to the large abrupt depolarization seen at the beginning of an action potential (Figure 2.3.3 I). At this point, enough time has passed (roughly 2 $msec$) so that the the Na^+ inactivation gates begin to close and the K^+ activation gates begin to open, which slows the influx of extracellular Na^+ and allows K^+ to flow down its electrochemical gradient out of the cell, thus causing the membrane potential to begin repolarizing (Figure 2.3.3 II). The membrane potential then hyperpolarizes due to the fact that the Na^+ gates are now inactivated and the K^+ gates are still open causing the membrane potential of the neuron to approach the K^+ reversal potential, which is lower than the resting potential (Figure 2.3.3 III). Finally, the potassium gates begin to close as the leakage current brings the cell back to its resting potential, and all of the variables approach their resting values (Figure 2.3.3 IV).

2.3.2   Refractory Period

The Hodgkin-Huxley model can also be used to explain another commonly observed phenomenon known as the *refractory period* of a neuron. More specifically, the *absolute refractory period* refers to the time during which a neuron cannot fire an action potential, and the *relative refractory period* refers to the time following the absolute period during which the neuron requires a larger current stimulus than it would need at rest to fire an action potential. Both of these periods can be explained by exam-
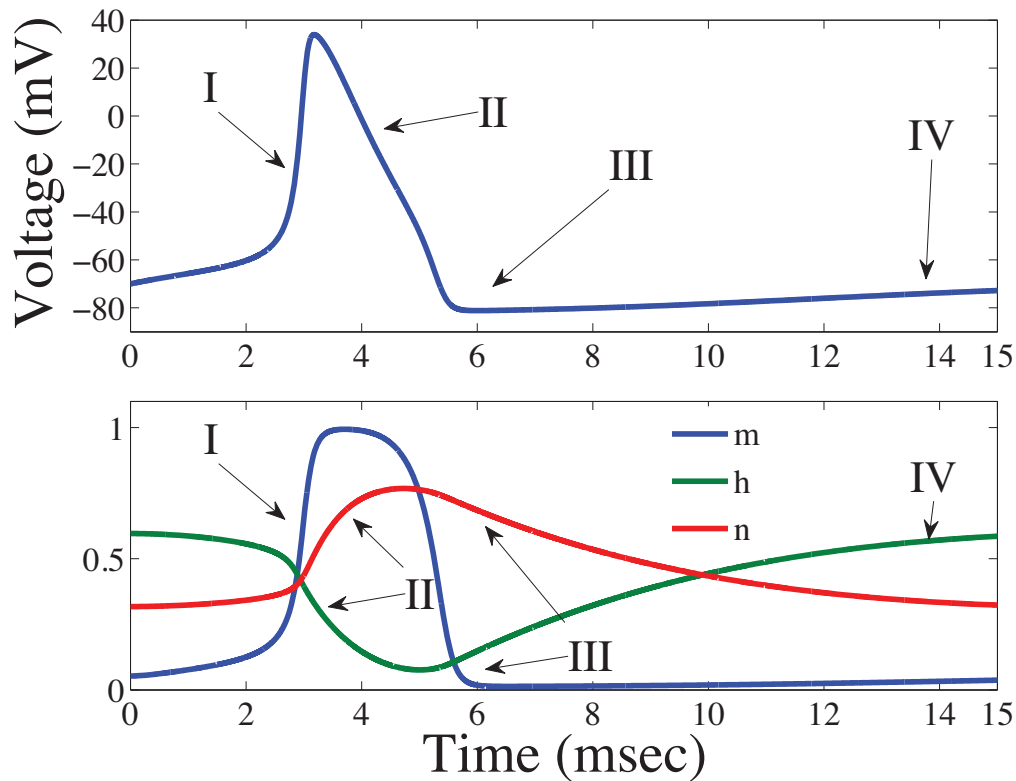
Figure 2.3.3: **Generation of the Action Potential in the Hodgkin-Huxley Model of the Squid Giant Axon**. The upper plot shows the voltage of the neuron during an action potential, while the lower plot shows how the gating variable m, h, and n change during the action potential. The Roman numerals refer to different stages of the action potential (refer to text for explanation).

ining the lower half of Figure 2.3.3. When the membrane potential is depolarized during the action potential, h decreases, causing the Na^+ channels to inactivate. Once inactivated, these channels cannot be reopened until the membrane potential repolarizes for a sufficient amount of time. Thus, the large amount of inactivated Na^+ channels that is seen when the membrane potential hyperpolarizes (Figure 2.3.3 III) effectively prohibits the generation of a second action potential. As the membrane potential begins to repolarize, h increases and the Na^+ gates start to be released from inactivation. At the same time, n is large relative to its resting value corresponding

to a large amount of K^+ channels to be open. This causes the membrane potential to hyperpolarize towards the K^+ channel reversal potential. The combination of the neuron having more inactivated Na^+ channels and more open K^+ channels than it would have at rest causes it to require a larger current stimulus to generate an action potential. As the neuron approaches its resting membrane potential, the current required to generate a second action potential decreases to its resting value. The return of the membrane potential to rest marks the end of the refractory period.

2.4   Neuronal Oscillations

When stimulated with a constant external applied current of sufficient amplitude, many neurons exhibit the periodic firing of action potentials seen in Figure 2.4.1. Moreover, it is also important to note that a wide class of neurons are intrinsically active, firing regularly and responding to inputs through perturbations to otherwise regular spike times [5, 6, 7, 113]. This behavior is reproduced in Hodgkin-Huxley-type models when the parameter I_{appl} is sufficiently large, or when other parameters, e.g. E_L, are large.

The first person to classify neuronal excitability was Alan Hodgkin in 1948 [45]. By injecting steps of currents of various amplitudes into neuronal membranes and looking at the resulting behavior, Hodgkin found that most neurons fall into two major classes oscillatory behavior:

- Class I neural excitability refers to neurons that can fire action potentials at arbitrarily low frequencies.

- Class II neural excitability refers to neurons where the onset of periodic behavior occurs at a non-zero frequency, and the firing frequency of the neuron is
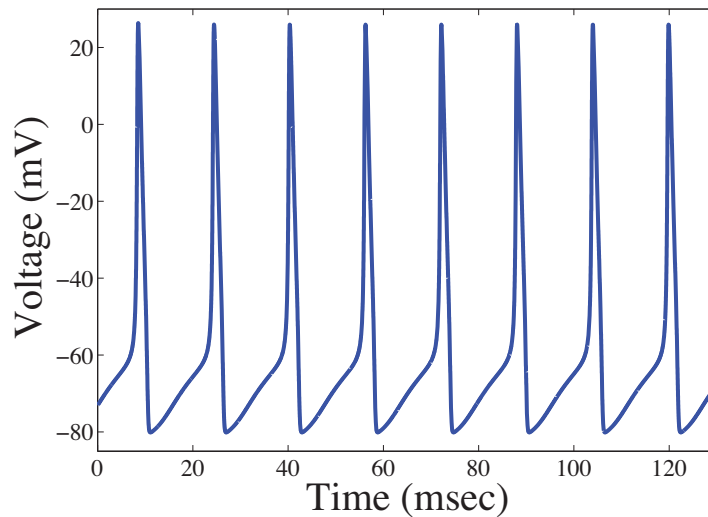
Figure 2.4.1: **Periodic Firing of Action Potentials**. When the parameter I_{appl} is large enough in the Hodgkin-Huxley model, the membrane potential begins displaying periodic firing of action potentials. This behavior is also seen in real neurons [45].

relatively insensitive to changes in the applied current.

Figure 2.4.2 illustrates the two different classes of neural excitability in (b) the standard Hodgkin-Huxley neuron and (b) a modified Hodgkin-Huxley neuron [47].

Class I, or Type I neurons, fire with a frequency that can vary smoothly from 0 Hz to 180 Hz, as shown in Figure 2.4.2. On the other hand, Class II neurons fire in a narrower frequency band that varies from about 55 Hz to 80 Hz, as shown in Figure 2.4.2.

In the language of dynamical systems, if I_{appl} is treated as a bifurcation parameter, then Hodgkin's classes of neural excitability can be reinterpreted as [49, 89]:

- Class I neural excitability refers to neuronal models where the onset of periodic oscillations arises from either a saddle-node on invariant cycle (SNIC) bifurcation or a homoclinic bifurcation.

(a)

(b)
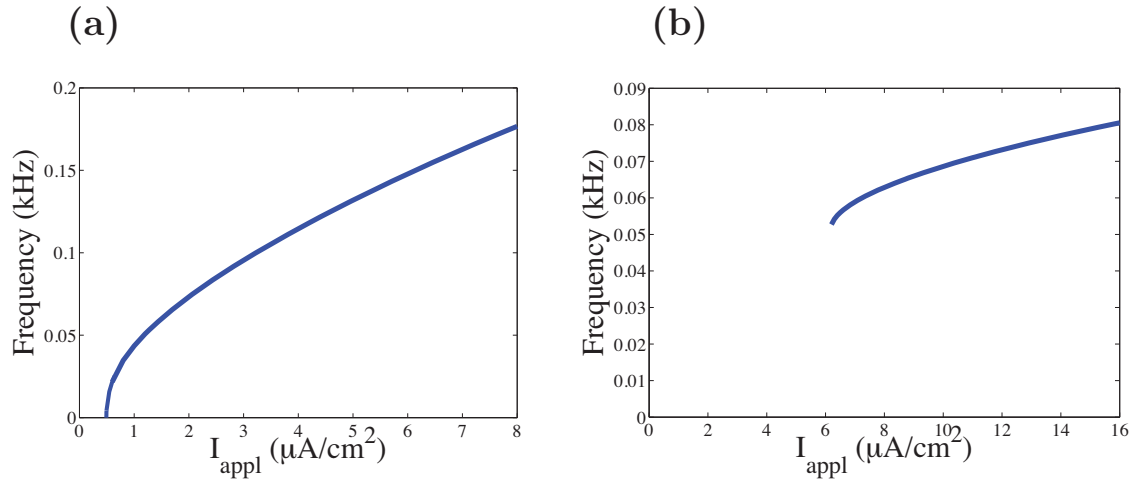
Figure 2.4.2: **Frequency-Applied Current Curves for Two Neuron Models Displaying Class I and Class II Excitability**. (a) For this model, action potentials can be generated with arbitrarily low frequency, corresponding to Hodgkin's Class I neural excitability. (b) Periodic firing of action potentials in this model turn on at a non-zero frequency corresponding to Hodgkin's Class II neural excitability.

- Class II neural excitability refers to neuronal models where the onset of periodic oscillations arises from either a supercritical or subcritical Hopf bifurcation.

These are the most common bifurcations that lead to periodic firing in neuronal models.

2.5 The Leaky-Integrate-and-Fire Model

Although Hodgkin-Huxley-type models provide quantitative descriptions of neuronal electrophysiology, they are mathematically difficult to analyze due to their highly non-linear nature. However, there exist various reduced models that capture the essential features of the Hodgkin-Huxley-type models, while at same time being conducive to mathematical analysis. One such model, which we use in this thesis, is known as the

Leaky-Integrate-and-Fire Neuron [1, 99].

The idea behind the leaky-integrate-and-fire model comes from the fact that the action potential of a neuron can be characterized as having 2 phases: (i) a slow depolarization of the membrane potential until it reaches a "threshold" value, and (ii) a rapid depolarization followed by a repolarization back to rest. This second phase often has an invariant shape that is determined by the interaction of the nonlinear Na^+ and K^+ currents and is typically not affected by changes in the applied current. Thus, to simplify phase (ii) we assume that the nonlinear currents can be replaced by a nonlinear threshold with a reset condition. Lastly, we make the assumption that the subthreshold dynamics (phase (i)) are dominated by the leakage current. Thus, by removing I_{Na} and I_K and their gating variables from equation (2.3.5), we can write the leaky-integrate-and-fire model as

$$C_m \frac{dV}{dt} = -g_L(V - V_L) + I_{appl}, \tag{2.5.1}$$

with the condition that when $V(t)$ reaches a threshold voltage V_{th}, it is immediately reset to a potential V_R. Thus, the subthreshold dynamics of the LIF neuron is modeled as an RC-circuit. However, when I_{appl} is large enough, the LIF model will display periodic firing. Note that since phase (ii) is assumed to be invariant, one could add a spike shape to the LIF model without changing its dynamics [17, 50, 58]. In Figure 2.5.1 (a), we plot an example of periodic firing in the LIF model with a simple spike function that jumps the voltage up to a value β once the neuron reached threshold, and then immediately resets the potential to V_R.

A major reason why the leaky-integrate-and-fire model is popular among theorists is because of the fact that it contains only a threshold nonlinearity. Thus, one can often write down the analytic solution. Below threshold

(a)   **(b)**
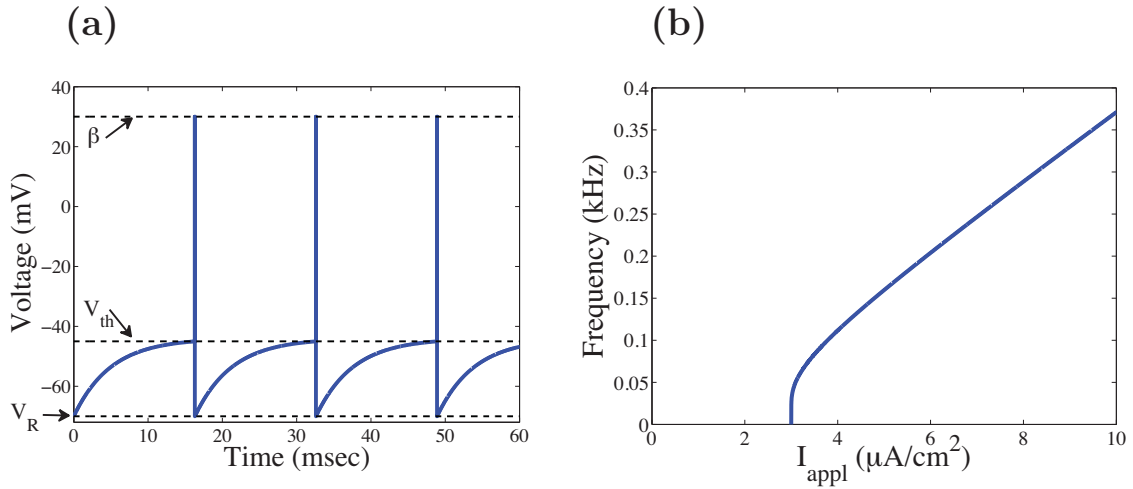
Figure 2.5.1: **the Leaky-Integrate-and-Fire Model Displays Action Poten-tial and Oscillatory Dynamics Similar to that of Hodgkin-Huxley-Type Models**. (a) Example voltage trace of the leaky-integrate-and-fire neuron with a spike added on. When the voltage reaches a threshold $V_{th} = -30$ its is jumped up to $\beta = 30$ and then immediately reset to $V_R = -70$. (b) Frequency-applied current curve for the leaky-integrate-and-fire neuron given by equation (2.5.3). The leaky-integrate-and-fire neuron can fire at arbitrarily low frequencies. Thus, it falls into Hodgkin's Class I of neuronal excitability.

$$V(t) = V(t_0)e^{g_L/C_m(t_0-t)} + \left[V_L + \frac{I_{appl}}{g_L}\right]\left(1 - e^{g_L/C_m(t_0-t)}\right), \qquad (2.5.2)$$

where t_0 is the start time. The LIF model can also display oscillatory behavior seen in Hodgkin-Huxley-type models, e.g. Figure 2.5.1 (b). Because we have the analytic solution (2.5.2), it is possible to write down an equation for the frequency of the oscillations, f, as a function of the system parameters

$$f = \begin{cases} \left[\dfrac{C_m}{g_L} \ln \left(\dfrac{V_R - \left[V_L + \frac{I_{appl}}{g_L}\right]}{V_{th} - \left[E_L + \frac{I_{appl}}{g_L}\right]} \right) + T_s \right]^{-1} & \text{if } I_{appl} > g_L(V_{th} - E_L) \\ \\ 0 & \text{else ,} \end{cases} \qquad (2.5.3)$$

where T_s is the duration of the spike which is 0 in Figure 2.5.1 (b). Thus, one can analytically examine how changes in different parameters affect the dynamics of the leaky-integrate-and-fire neuron.

The leaky-integrate-and-fire model captures some of the essential features of the electrical activity of neurons, such as threshold behavior and periodic firing of actions potentials, while at the same time being amenable to mathematical analysis. As such, many theorists have utilized this simplified model in order to probe the mechanisms of various phenomena such as phase-locking in neuronal networks, e.g. [12, 58, 108]. However, It is important to note that the leaky-integrate-and-fire model does not capture every feature of the Hodgkin-Huxley-type models. For example, the leaky-integrate-and-fire model has oversimplified threshold dynamics and unrealistic refractory properties [3, 16].

2.6   Summary

In this chapter, we have reviewed basic concepts from neuronal electrophysiology and explained the mechanisms underlying the generation of action potentials in neurons with the use of the Hodgkin-Huxley model. We have also described the different ways that neurons can begin to exhibit oscillatory electrical behavior. Lastly, we presented a simplified neuronal model known as the leaky-integrate-fire neuron that

will be used in Chapter 6.

Chapter 3

The Cable Equation, Equivalent Cylinders, and the Rall Lumped-Soma and Ball-and-Stick Model Neurons

The cable equation, originally derived by Lord Kelvin in 1855 to study the transatlantic telegraph cable, has become one of the standard models for studying the voltage profiles of spatially extended neurons. Here, we present the derivation of the cable equation, and introduce the concept of an *equivalent cylinder* which, under certain circumstances, allows one to reduce a branched dendritic structure into a single cylinder. For our purposes, the equivalent cylinder method provides an analytically tractable approach to studying the effects of dendritic properties on the dynamics of neuronal oscillators by collapsing the often complicated branching dendritic structure of a neuron into a single cylinder. Lastly, we close this chapter by introducing the

Rall Lumped-Soma and Ball-and-Stick model neurons. Both models consist of an isopotential soma attached to a single passive dendritic cable (which can be thought of as arising from the equivalent cylinder of a branched dendritic structure). The only difference between the two models is that the Rall lumped-soma model assumes that the somatic membrane consists of ion channels that behave like linear Ohmic resistors (generally referred to as a *passive* membrane), while the ball-and-stick model allows for nonlinear voltage-gated Hodgkin-Huxley-like ion channels (see Chapter 2) in the somatic membrane (generally referred to as an *active* membrane). The ball-and-stick neuron model will be used in Chapters 5 and 7, while a slight variation of the Rall lumped-soma model will be used in Chapter 6.

3.1   Introduction

Neurons are spatially extensive heterogeneous objects (see Chapter 1). As such, it is unlikely that the membrane potential of the neuron will be same at every point. It is often the case that the membrane potential undergoes significant attenuation and delay as it travels down the cable-like structure of axons or dendrites. One of the first people to investigate how a neurons structure affects its electrical activity was Wilfrid Rall [78, 79, 80, 83, 84]. At the time, not much attention was being paid to dendrites, as the prevailing opinion was that dendrites were so electrotonically long that any inputs on the dendrite could not affect the electrical activity of the soma (cell body) in any significant way [26]. However, using a combination of mathematical theory and the little physiological data that was available to him, Rall [78] was able to convincingly show that this "standard motoneurone" model [26] underestimated the dendritic contribution by a significant amount. Although Rall's ideas were met with resistance early on, his results have now become standard in the field of computational

neuroscience [95]. Furthermore, his application of the theory of electrical flow through leaky cables to studying dendrites has also become a core part of the computational neuroscience curriculum.

3.2 Assumptions

We begin by assuming that the dendrite is a cylindrical piece of a phospholipid bilayer membrane surrounding an interior of cytoplasm (top of Figure 3.2.1). There are two main types of current that can arise in this cylinder: the first is due to the movement of ions through protein channels embedded in the neuronal membrane (the trans-membrane current); and the second is due to the movement of ions through the cytoplasm (the axial current). Since the resistance that the ions encounter when flowing through the membrane is typically much greater than the resistance flowing through the cytoplasm, and since the diameters of dendrites are typically much smaller than their lengths, the dominant fraction of current inside the cylinder flows parallel to its longitudinal axis, with only a small fraction flowing perpendicularly through the membrane. Furthermore, by comparing the membrane potential obtained from the solution of Laplace's equation in cylindrical coordinates in three dimensions with the solution of the one-dimensional cable equation, Rall [82] showed that the membrane potential typically decays 10^{4th} times faster in the radial and angular directions, than in the direction parallel to its longitudinal axis. Therefore, we can safely assume that the axial current and the transmembrane current are the only two types of current in the cylinder. This implies that we only have to solve for the voltage in one spatial dimension [1]. Thus, the dendrite can be modeled as a one-dimensional cable.

The cytoplasm inside the cylinder as well as the extracellular medium are ap-

---

[1]This assumption is also known as the *core conductor assumption* [84]

proximated by linear ohmic resistances, as the ions encounter resistance as they flow through either medium. To further simplify the situation, we assume that the intracellular resistance of the cytoplasm and the extracellular resistance of the external medium are constant along the length of the cable. Furthermore, we assume that the radius of the cylinder is constant along its length. However, this assumption can be easily removed to incorporate a spatially varying dendritic radius.
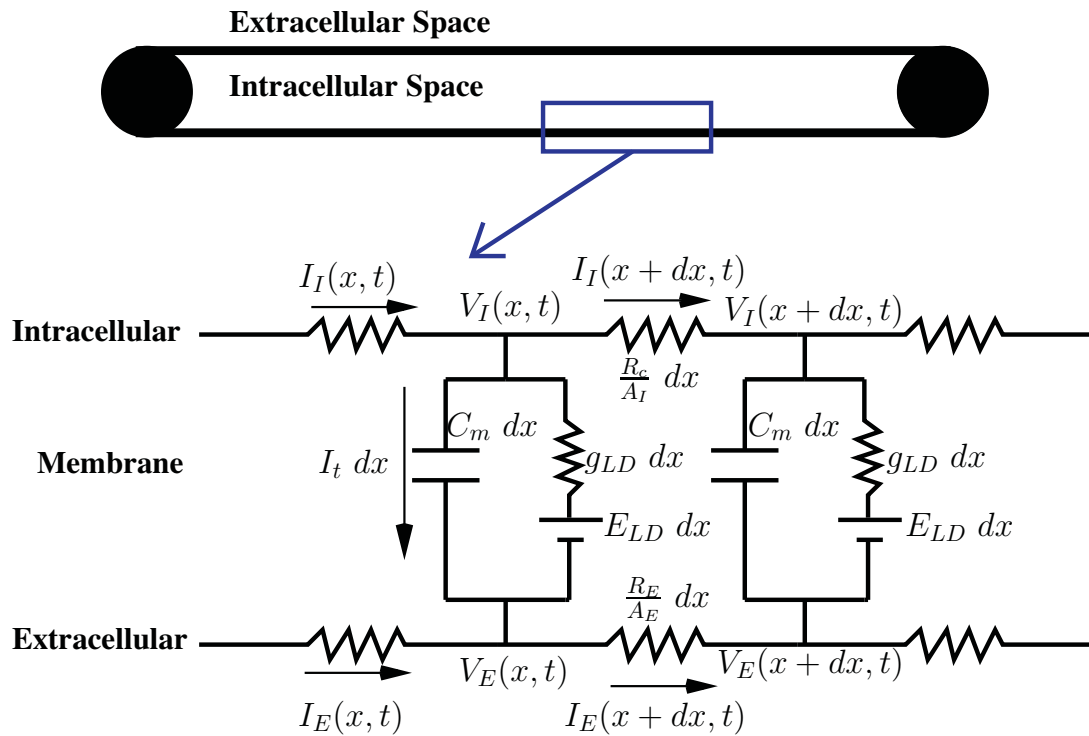
Figure 3.2.1: **Circuit Diagram for the Cable Equation** The dendrite is modeled as a cylindrical phospholipid bilayer membrane surrounding cytoplasm. The voltage inside the cylinder is referred to as $V_I(x, t)$, while the voltage outside the cylinder is referred to as $V_E(x, t)$. This cylinder is then broken up into small segments of length dx. R_c is the cytoplasmic resistivity, A_I is the cross-sectional area of the cylinder, R_E is the external medium resistivity, A_E is the external cross-sectional area, C_m is the capacitance, g_{LD} is the leakage conductance, and E_{LD} is the reversal potential of the leakage channel. Note that all of these parameters are assumed to be constant along the length of the dendrite.

3.3 Derivation

Next, we divide the cable up into small isopotential segments of length dx. In each segment, we have the transmembrane current and the axial current on the inside and outside of the cell. The transmembrane current is made up of a capacitive current and an ionic current coming from the movement of ions through protein channels embedded in the membrane (Figure 3.2.1). Since we are concerned with passive membrane properties, we assume that the ion channels are not voltage-gated and can be approximated by linear ohmic resistances, i.e. the resistance of each channel is constant. Thus, the transmembrane current density for a segment is given by[2]

$$I_t = 2\pi a \left(C_m \frac{\partial V}{dt} + g_{LD}(V - E_{LD}) \right), \qquad (3.3.1)$$

where $V(x,t) = V_I(x,t) - V_E(x,t)$ is the membrane potential at position x and time t in units of mV, $V_I(x,t)$ $(V_E(x,t))$ is the voltage inside (outside) the cylinder, $p = 2\pi a$ is the perimeter of the cylinder in units of cm, a is the radius of the cylinder in units of cm, C_m is the capacitance of the membrane in units of $\mu F/cm^2$, g_{LD} is the conductance of the ion channel in units of mS/cm^2, and E_{LD} is the reversal potential of the channel in units of mV.

Since the internal and external medium are both assumed to behave like ohmic resistors, we have

$$I_I(x,t)\frac{R_c}{A_I}dx = V_I(x - dx, t) - V_I(x,t) \qquad (3.3.2)$$

$$I_E(x,t)\frac{R_E}{A_E}dx = V_E(x - dx, t) - V_E(x,t) \qquad (3.3.3)$$

---

[2]see Chapter 2

where $\frac{R_c}{A_I}dx$ is the resistance of the internal medium, R_c is the cytoplasmic resistivity in units of $k\Omega{\cdot}cm$, $A_I = \pi a^2$ is the cross-sectional area of the cylindrical cable in units of cm^2, and $\frac{R_E}{A_E}dx$ is the resistance of the external medium with external resistivity R_E and external cross-sectional area A_E. Note that for large external volumes, the effective external resistance is essentially 0. In this case, $V_E(x,t)$ would be equal to a constant that is usually set to zero.

Kirchhoff's conservation of current law requires that the current entering one point must balance the current leaving that point. According to Figure 3.2.1, this implies that

$$- I_t dx = I_I(x + dx, t) - I_I(x, t),\tag{3.3.4}$$

and

$$I_t dx = I_E(x + dx, t) - I_E(x, t).\tag{3.3.5}$$

Since there are no additional current sources, the total axial current is given by $I_{Ta} = I_I + I_E$. Furthermore, I_{Ta} is constant along the cable since summing equations (3.3.4) and (3.3.5) yields

$$0 = \frac{I_I(x + dx, t) - I_I(x, t)}{dx} + \frac{I_E(x + dx, t) - I_E(x, t)}{dx},\tag{3.3.6}$$

which, as $dx \to 0$, limits to

$$0 = \frac{\partial I_I}{\partial x} + \frac{\partial I_E}{\partial x},\tag{3.3.7}$$

which implies that $I_I + I_E$ is constant along the length of the cylinder. Using this

fact along with equations (3.3.2) and (3.3.3), and that $V = V_I - V_E$, one finds

$$I_{Ta} = \frac{A_I}{R_c}\left[\frac{V(x - dx, t) - V(x, t)}{dx}\right] + \left(\frac{R_c + \frac{A_I}{A_E}R_E}{R_c}\right)I_E(x, t), \qquad (3.3.8)$$

which implies that

$$I_E(x, t) = \left(\frac{R_c}{R_c + \frac{A_I}{A_E}R_E}\right)I_{Ta} - \frac{1}{\frac{R_c}{A_I} + \frac{R_E}{A_E}}\left[\frac{V(x - dx, t) - V(x, t)}{dx}\right]. \qquad (3.3.9)$$

Plugging the above expression into equation (3.3.5) and dividing both sides by dx yields

$$I_t = \frac{1}{\frac{R_c}{A_I} + \frac{R_E}{A_E}}\left[\frac{V(x - dx, t) - 2V(x, t) + V(x + dx, t)}{dx^2}\right], \qquad (3.3.10)$$

where we have used the fact that I_{Ta} is constant along the cable. As $dx \to 0$, the above expression limits to

$$2\pi a\left(C_m\frac{\partial V}{\partial t} + g_{LD}(V - E_{LD})\right) = \frac{1}{\frac{R_c}{A_I} + \frac{R_E}{A_E}}\frac{\partial^2 V}{\partial x^2}. \qquad (3.3.11)$$

Note that we have also assumed that the leakage conductance of the membrane, g_{LD}, and the reversal potential of the leak channel are constant along the length of the dendrite. If the extracellular resistance is ignored we can rearrange equation (3.3.11) to arrive at the standard form for the passive cable equation

$$\tau_m\frac{\partial V}{\partial t} = \lambda^2\frac{\partial^2 V}{\partial x^2} - (V - E_{LD}), \qquad (3.3.12)$$

where $\tau_m = R_m C_m$ is the membrane time constant, $R_m = 1/g_{LD}$ is the membrane resistivity in units of $k\Omega \cdot cm^2$, and $\lambda = \sqrt{\frac{R_m a}{2R_c}}$ is the length constant of the cylin-

der. Similarly to the membrane time constant, the length constant of the cylinder is the distance at which the membrane potential of the cylinder has decayed by a factor of e^{-1}. Thus, cables with large (small) length constants experience less (more) attenuation of the voltage along the length of the cylinder.

3.4   Equivalent Cylinder

Dendritic trees of real neurons are generally more complicated than a single cylinder. However, under certain assumptions, one can show that the branching structure of a dendritic tree can be collapsed in a so-called *equivalent cylinder* [79, 81].

First, we nondimensionalize time and space using $\bar{t} = t/\tau_m$, $\bar{x} = x/\lambda$, and shift V using $\bar{V}(\bar{x}, \bar{t}) = V(x/\lambda, t/\tau_m) - E_{LD}$. Plugging these new variables into equation (3.3.12) yields

$$\frac{\partial \bar{V}}{\partial \bar{t}} = \frac{\partial^2 \bar{V}}{\partial \bar{x}^2} - \bar{V}. \tag{3.4.1}$$

The steady-state of equation (3.4.1) obeys

$$\frac{d^2 \bar{V}}{d\bar{x}^2} = \bar{V}. \tag{3.4.2}$$

3.4.1   A Note on Boundary Conditions

In order to solve (3.4.2), we must first specify the domain and the boundary conditions. Since we are going to be considering cables of finite length, we will consider our domain to be the interval $[0, L]$ where L is the electrotonic (nondimensional) length of the cable. More specifically, the electrotonic length, L, is equal to the physical length, ℓ, of the cable divided by the length constant, λ. Dendrites with small (large)

electrotonic lengths experience less (more) voltage attenuation along their physical lengths.

Next, if we want to know the steady state voltage profile of a cable when we inject a constant current at one end and hold the voltage fixed at the other end (i.e. voltage clamp), then the appropriate boundary conditions for (3.4.2) would then be

$$\frac{\pi a^2}{R_c \lambda} \frac{d\bar{V}}{d\bar{x}}(0) = -I_0 \tag{3.4.3}$$

$$\bar{V}(L) = V_f. \tag{3.4.4}$$

Equation (3.4.3) is obtained by assuming that no current leaks through the neuronal membrane at $\bar{x} = 0$ (see next paragraph), and by using conservation of current. I_0 is the constant current injection in units of $\mu A/cm^2$, and V_f is the voltage clamp potential at the distal $(x = L)$ end of the cable. By integrating equation (3.4.2) twice and applying the above boundary conditions, one finds

$$\bar{V}(\bar{x}) = \frac{V_f}{e^L + e^{-L}} \left(e^{\bar{x}} + e^{-\bar{x}}\right) + I_0 \left(\frac{\frac{\sqrt{2R_c R_m}}{\pi a^{3/2}}}{e^L + e^{-L}}\right) \left(e^{L-\bar{x}} - e^{-L+\bar{x}}\right). \tag{3.4.5}$$

Figure 3.4.1 (a) shows an example of the steady-state voltage profile of the cable when current is injected at one end and voltage clamped to $V_f = 0$ at the other end.

Lastly, suppose that we wanted to model a cable with a constant current injection at one end as before, but, rather than clamping the voltage at the other end, we want to consider the natural condition where the end of the cable is covered with the neuronal membrane with resistivity R_m. In this case, the resistance at the terminal end of the cable will be $R_m/\pi a^2$. For realistic values of R_m and a, this terminal

(a)   **(b)**
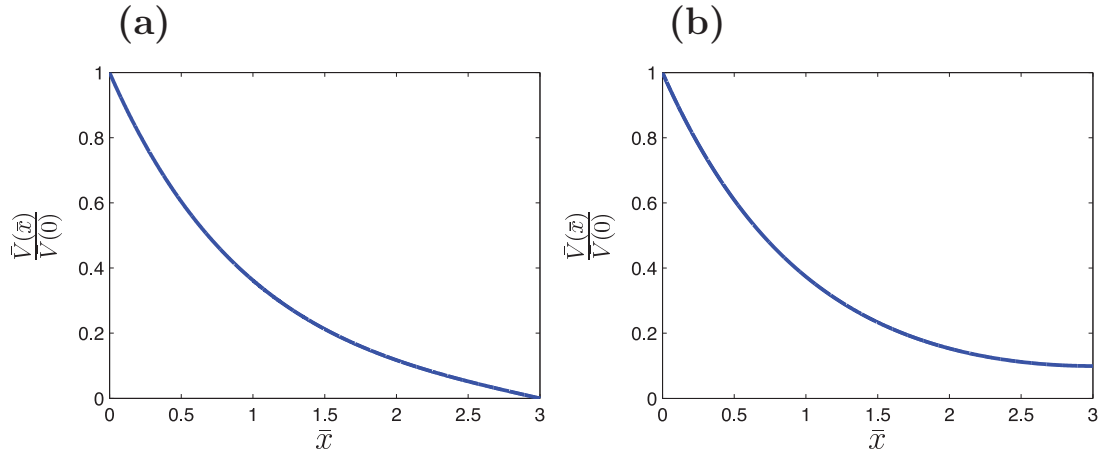
Figure 3.4.1: **Solutions of equation (3.4.2) with Different Boundary Conditions.** $R_m = 7 \ k\Omega \cdot cm^2$, $R_c = .09 \ k\Omega \cdot cm$, $I_0 = 2 \ \mu A/cm^2$, $L = 3$, and $a = 3 \times 10^{-3}$ cm. (a) Steady-state voltage profile of the cable with constant current injection at $x = 0$ and voltage clamped to $V_f = 0$ at $x = L$. (b) Voltage profile with constant current injection at $x = 0$ and sealed-end (no-flux) boundary condition at $x = L$.

resistance is quite large [79]. Therefore, we make the assumption that the terminal resistance is infinite, which then implies that no current flows through the distal end of the cable. The boundary conditions for this situation are then

$$\frac{\pi a^2}{R_c \lambda} \frac{d\bar{V}}{d\bar{x}}(0) = -I_0 \tag{3.4.6}$$

$$\frac{d\bar{V}}{d\bar{x}}(L) = 0 \tag{3.4.7}$$

where (3.4.7) represents the "sealed-end" boundary condition for the cable. Note that equations (3.4.3) and (3.4.6) are a specific case of the sealed-end boundary condition where a constant current is being injected at the end of the cylinder. The corresponding solution to (3.4.2) would then be

$$\bar{V}(\bar{x}) = I_0 \frac{\sqrt{2R_c R_m}}{\pi a^{3/2}} \frac{\cosh(x-L)}{\sinh(L)}. \tag{3.4.8}$$

Figure 3.4.1 (b) shows an example of the steady-state voltage profile of the cable when current is injected at one end and sealed end boundary condition at the other end. Note that the only difference between the two plots in Figure 3.4.1 is the boundary condition at $\bar{x} = L$. Figure 3.4.1 (a) has the voltage at $\bar{x} = L$ clamped to zero, while Figure 3.4.1 (b) has zero current at $\bar{x} = L$.

3.4.2 A Simple Branching Structure

In this section, we illustrate how the cable equation can be used to examine the potential of a simple branching structure consisting of a parent branch and two daughter branches (Figure 3.4.2).
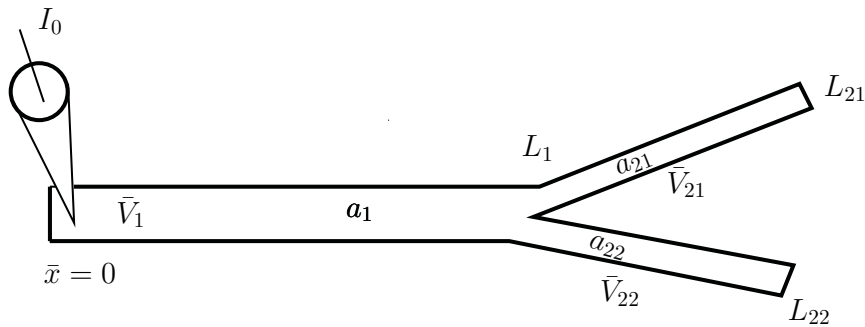
Figure 3.4.2: **A Simple Branching Structure**. A parent branch of length L_1 and radius a_1 splits off into two daughter branches with lengths L_{21} and L_{22} and radii a_{21} and a_{22}.

Suppose that the parent branch has nondimensional length L_1 and radius a_1 and is connected to 2 daughter branches who are nondimensional distances L_{21} and L_{22} from $x = 0$. The steady-state potential of each cable is governed by equation (3.4.2). However, they differ in their boundary conditions. For example, suppose that a

constant current is injected at the beginning ($\bar{x} = 0$) of the parent branch

$$\frac{\pi a_1^{3/2}}{\sqrt{2 R_c R_m}} \frac{d\bar{V}_1}{d\bar{x}}(0) = -I_0. \tag{3.4.9}$$

At the junction connecting the branches, we know that

$$\bar{V}_1(L_1) = \bar{V}_{21}(L_1) = \bar{V}_{22}(L_1). \tag{3.4.10}$$

Furthermore, by conservation of current at the junction

$$\frac{\pi a_1^{3/2}}{\sqrt{2 R_c R_m}} \frac{d\bar{V}_1}{d\bar{x}}(L_1) = \frac{\pi a_{21}^{3/2}}{\sqrt{2 R_c R_m}} \frac{d\bar{V}_{21}}{d\bar{x}}(L_1) + \frac{\pi a_{22}^{3/2}}{\sqrt{2 R_c R_m}} \frac{d\bar{V}_{22}}{d\bar{x}}(L_1), \tag{3.4.11}$$

where we have assumed that the cables have the same values of R_m and R_c, but they differ in the values of their radii. Note that the radii being raised to the $3/2$ power arises naturally from the fact that $\frac{\pi a^2}{R_c \lambda} = \frac{\pi a^{3/2}}{\sqrt{2 R_c R_m}}$. Lastly, if we specify that the daughter branches both have sealed-end boundary conditions

$$\frac{d\bar{V}_{21}}{d\bar{x}}(L_{21}) = \frac{d\bar{V}_{22}}{d\bar{x}}(L_{22}) = 0, \tag{3.4.12}$$

then, using the general solutions for (3.4.2)

$$\bar{V}_1(\bar{x}) = A_1 \sinh(\bar{x}) + B_1 \cosh(\bar{x}) \tag{3.4.13}$$

$$\bar{V}_{21}(\bar{x}) = A_{21} \sinh(\bar{x} - L_{21}) + B_{21} \cosh(\bar{x} - L_{21}) \tag{3.4.14}$$

$$\bar{V}_{22}(\bar{x}) = A_{22} \sinh(\bar{x} - L_{22}) + B_{22} \cosh(\bar{x} - L_{22}), \tag{3.4.15}$$

we have six equations (the boundary conditions) and six unknowns. The coefficients are then found to be

$$A_1 = -\frac{\sqrt{2R_c R_m}}{\pi a_1^{3/2}} I_0 \tag{3.4.16}$$

$$B_1 = A_1 \frac{a_{21}^{3/2} \tanh(L_1 - L_{21}) \tanh(L_1) + a_{22}^{3/2} \tanh(L_1 - L_{22}) \tanh(L_1) - a_1^{3/2}}{a_1^{3/2} \tanh(L_1) - a_{21}^{3/2} \tanh(L_1 - L_{21}) - a_{22}^{3/2} \tanh(L_1 - L_{22})} \tag{3.4.17}$$

$$A_{21} = 0 \tag{3.4.18}$$

$$B_{21} = \frac{A_1 \sinh(L_1) + B_1 \cosh(L_1)}{\cosh(L_1 - L_{21})} \tag{3.4.19}$$

$$A_{22} = 0 \tag{3.4.20}$$

$$B_{22} = \frac{A_1 \sinh(L_1) + B_1 \cosh(L_1)}{\cosh(L_1 - L_{22})} \tag{3.4.21}$$
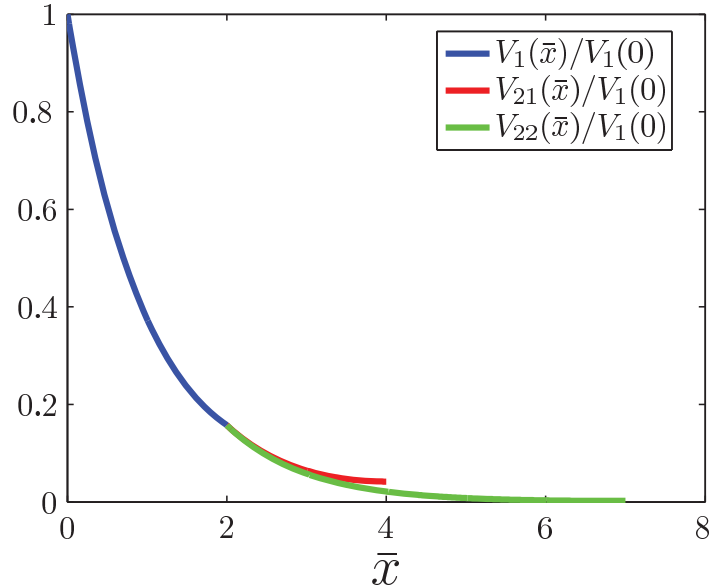
Figure 3.4.3: **Steady-State Voltage Profile for the Simple Branching Structure.** $R_m = 7\ k\Omega \cdot cm^2$, $R_c = .09\ k\Omega \cdot cm$, $I_0 = 2\ \mu A/cm^2$, $L_1 = 2$, $a_1 = 3 \times 10^{-3}$ cm, $L_{21} = 4$, $a_{21} = 5 \times 10^{-6}\ cm$, $L_{22} = 7$, and $a_{22} = 8 \times 10^{-4}\ cm$. Notice that the voltage attenuation is smaller along the shorter and thinner cable.

Figure 3.4.3 plots an example of the solution obtained for the simple branched structure. It is important to note that this technique can also be used for more complicated branching structures that are made up of passive components [79].

3.4.3   Equivalent Cylinder for the Simple Branching Structure

Here, we illustrate the equivalent cylinder technique on the simple branching structure from the previous section.

Continuing with the same example from the previous section, if we further assume that the daughter branches are both the same nondimensional distance from $\bar{x} = 0$, i.e. $L_{21} = L_{22}$, then $\bar{V}_{21}$ and $\bar{V}_{22}$ both obey the same differential equation (3.4.2) on the same domain, and have identical boundary conditions, (3.4.10) and (3.4.12). It follows that $\bar{V}_{21} = \bar{V}_{22}$. Furthermore, from (3.4.11) we now have

$$a_1^{3/2}\frac{d\bar{V}_1}{d\bar{x}}(L_1) = (a_{21}^{3/2} + a_{22}^{3/2})\frac{d\bar{V}_{21}}{d\bar{x}}(L_1). \qquad (3.4.22)$$

At this point, we see that the solution would behave like a single cable with a jump in its radius at $\bar{x} = L_1$. However, if

$$a_1^{3/2} = a_{21}^{3/2} + a_{22}^{3/2}, \qquad (3.4.23)$$

then $\bar{V}_1$ and $\bar{V}_{21}$ have the same derivative and value at L_1, and they obey the same differential equation[3]. It follows that the composite function

---

[3]This is known as the "three halves law" [79, 81]

$$\bar{V} = \begin{cases} \bar{V}_1(\bar{x}) & \text{if } 0 \leq \bar{x} \leq L_1 \\[2mm] \bar{V}_{21}(\bar{x}) & \text{if } L_1 \leq \bar{x} \leq L_{21}, \end{cases} \tag{3.4.24}$$

solves (3.4.2) on the domain $[0, L_{21}]$. Thus, the two daughter branches can be collapsed into an equivalent cylinder of length L_{21} and radius a_1, and there is no jump in the radius of the cable at $\bar{x} = L_1$.

To further illustrate the point, let us compare the solution from the branched structure to that obtained with the equivalent cylinder. The general solutions of the branched structure with the equivalent cylinder are given by

$$\bar{V}_1 = \tilde{A}_1 \sinh(\bar{x}) + \tilde{B}_1 \cosh(\bar{x}) \tag{3.4.25}$$

$$\bar{V}_{21} = \tilde{A}_{21} \sinh(\bar{x} - L_{21}) + \tilde{B}_{21} \cosh(\bar{x} - L_{21}). \tag{3.4.26}$$

Using (3.4.10), (3.4.12), (3.4.22), and (3.4.23), it follows that

$$\tilde{A}_1 = -\frac{\sqrt{2R_c R_m}}{\pi a_1^{3/2}} I_0 \tag{3.4.27}$$

$$\tilde{B}_1 = \tilde{A}_1 \frac{\tanh(L_1 - L_{21})\tanh(L_1) - 1}{\tanh(L_1) - \tanh(L_1 - L_{21})} \tag{3.4.28}$$

$$\tilde{A}_{21} = 0 \tag{3.4.29}$$

$$\tilde{B}_{21} = \frac{\tilde{A}_1 \sinh(L_1) + \tilde{B}_1 \cosh(L_1)}{\cosh(L_1 - L_{21})} \tag{3.4.30}$$

Notice that (3.4.27-3.4.30) are the same as (3.4.16-3.4.19) when $L_{21} = L_{22}$ and (3.4.23) is true. Thus, the solutions for the steady-state membrane potential of the branched structure and the equivalent cylinder are equivalent as illustrated in Figure 3.4.4.
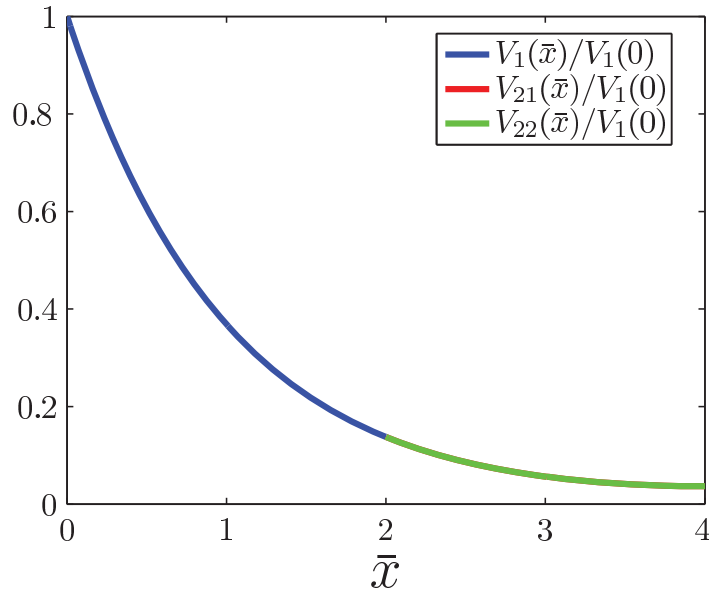
Figure 3.4.4: **Steady-State Voltage Profile for the Simple Branching Structure with the Equivalent Cylinder**. $R_m = 7\ k\Omega \cdot cm^2$, $R_c = .09\ k\Omega \cdot cm$, $I_0 = 2\ \mu A/cm^2$, $L_1 = 2$, $L_{21} = L_{22} = 4$, $a_{21} = 5 \times 10^{-6}\ cm$, $a_{22} = 8 \times 10^{-4}\ cm$, and $a_1 = (a_{21}^{3/2} + a_{22}^{3/2})^{2/3}$. Notice that the voltage traces for the two daughter branches now overlap and are described by the single equation (3.4.26).

It was shown by Rall [79, 81, 84] that if a structure with N daughter branches satisfies: (i) R_m and R_c are the same on every branch; (ii) each branch is the same nondimensional distance from $\bar{x} = 0$; (iii) $a_1^{3/2} = \sum_{j=1}^{N} a_{2j}^{3/2}$ where a_1 is the radius of the parent branch; and (iv) the daughter branches all have the same distal boundary condition; then all of the daughter branches can be collapsed into an equivalent cylinder of radius a_1 and length L_{21}. Note that it is possible to collapse more complex branching structures into one long equivalent cylinder as long as (i)-(iv) are satisfied at each branch point. However, these conditions are generally not satisfied by real dendritic trees. Furthermore, equivalent cylinders really only describe the steady-state membrane potential of the branched structure. Nonetheless, using this simplified view of a dendritic tree, Rall [78] was able to show that inputs to the

dendrite can significantly affect the membrane potential at the soma. Thus, this sim-

plified model can provide insight into how dendritic properties affect the dynamics of

the somatic membrane potential. In the next section, we introduce a standard model

that incorporates the dynamics of the soma into this simplified dendritic framework.

3.5   The Rall Lumped-Soma Model

The Rall Lumped-Soma Model is one of the simplest models that incorporates the

spatial structure of a neuron. It assumes that the entire dendritic tree of a neuron is

modeled as a single cylinder (or equivalent cylinder) of length L

$$C_m \frac{\partial V}{\partial t} = \frac{a}{2R_c} \frac{\partial^2 V}{\partial x^2} + g_{LD}(V - E_{LD}). \tag{3.5.1}$$

Furthermore, it assumes that the soma (located at $x = 0$) is an isopotential sphere

whose membrane only contains a passive leakage channel (i.e. it behaves like an RC

circuit). To obtain the somatic boundary condition, we again make use of Kirchhoff's

conservation of current law and balance the current coming from the dendrite at $x = 0$

with the current coming from the soma

$$\pi d^2 \left(C_m \frac{\partial V}{\partial t}(0, t) + g_L(V(0, t) - E_L) - I_{appl} \right) = \frac{\pi a^2}{R_c} \frac{\partial V}{\partial x}(0, t), \tag{3.5.2}$$

where πd^2 is the surface area of the soma, d is the diameter of the soma in units of

cm, g_L is the leakage conductance of the soma in units of mS/cm^2, E_L is the leakage

reversal potential in units of mV, I_{appl} is a constant current injection to the soma in

units of $\mu A/cm^2$, and we have assumed for convenience that the dendrite and the soma

both have the same capacitance C_m in units of $\mu F/cm^2$. Although any biologically

reasonable boundary condition can be used at the distal end of the dendrite, we will

assume that we have a sealed-end cable. Thus, the Rall Lumped-Soma Model can written compactly as

$$
\begin{cases}
C_m\dfrac{\partial V}{\partial t} = \dfrac{a}{2R_c}\dfrac{\partial^2 V}{\partial x^2} + g_{LD}(V - E_{LD}) \\[2mm]
C_m\dfrac{\partial V}{\partial t}(0,t) = -g_L(V(0,t) - E_L) + I_{appl} + \dfrac{a^2}{d^2 R_c}\dfrac{\partial V}{\partial x}(0,t) \\[2mm]
\dfrac{\partial V}{\partial x}(L,t) = 0.
\end{cases}
\qquad (3.5.3)
$$

We will use this model with a slight modification in a later chapter where we examine how non-weak dendritic influences can alter the dynamics of a somatic oscillator.

In the next section, we present a small generalization of the Rall Lumped-Soma Model called the "Ball-and-Stick" model [20] which we will make extensive use of throughout this dissertation.

3.6 The Ball-and-Stick Model

The Ball-and-Stick model is a slight generalization of the Rall Lumped-Soma model to incorporate active (nonlinear) ionic conductances into the somatic membrane. In essence, the two models have the same assumptions. Namely that the dendritic tree is modeled as a single cable and the soma is modeled as an isopotential sphere (Figure 3.6.1). The only difference is that we allow the soma to contain Hodgkin-Huxley-like [44] active currents

$$
\begin{cases}
C_m \dfrac{\partial V}{\partial t} = \dfrac{a}{2R_c} \dfrac{\partial^2 V}{\partial x^2} + g_{LD}(V - E_{LD}) \\[2mm]
C_m \dfrac{\partial V}{\partial t}(0,t) = -I_{ion}(V(0,t),\vec{w}) + I_{appl} + \dfrac{a^2}{d^2 R_c} \dfrac{\partial V}{\partial x}(0,t) \\[2mm]
\dfrac{\partial V}{\partial x}(L,t) = 0.
\end{cases}
\qquad (3.6.1)
$$

where $I_{ion}(V(0,t),\vec{w})$ represents the sum of the HH-type ionic currents (see Chapter 1) and $\vec{w}$ is a vector containing the gating variables of the ionic conductances. The gating variables in the vector $\vec{w}$ are described by equations of the form $\frac{d\vec{w}}{dt} = \frac{1}{\tau_{\vec{w}}(V)}(\vec{w}_\infty(V) - \vec{w})$.
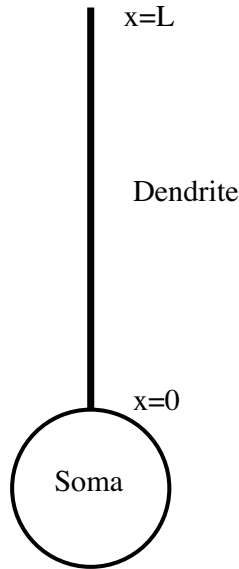
Figure 3.6.1: **Ball-and-Stick Model Neuron**. An isopotential active soma is attached to a single passive dendrite of length L.

3.7   Summary

In this chapter, we have presented the main ideas behind cable theory, which will be used throughout this dissertation as the model for a passive dendrite. We have also introduced our main modeling tools for investigating the spatial dynamics of neurons, namely the Ball-and-Stick model and the Rall Lumped-Soma Model.

Chapter 4

The Theory of Weakly Coupled Oscillators

4.1   Introduction

This chapter focuses on the application of the theory of weakly coupled oscillators [71, 54, 29] to studying the dynamics of networks of neuronal oscillators. The theory can be used to predict phase-locking in neuronal networks with any form of coupling, but as the name suggests, the coupling between cells must be sufficiently "weak" for these predictions to be quantitatively accurate. This implies that the coupling can only have small effects on neuronal dynamics over any given period. However, these small effects can accumulate over time and lead to phase-locking in the neuronal network. The theory of weak coupling allows one to reduce the dynamics of each neuron, which could be of very high dimension, to a single differential equation describing the phase of the neuron. These "phase equations" take the form of a convolution of the input to the neuron via coupling and the neuron's infinitesimal PRC (iPRC).

The iPRC measures the response to a small brief (δ-function-like) perturbation and acts like an impulse response function or Green's function for the oscillating neurons. Through the dimension reduction and exploiting the form of the phase equations, the theory of weakly coupled oscillators provides a way to identify phase-locked states and understand the mechanisms that underlie them.

The main goal of this chapter is to illustrate how a weakly coupled neuronal network is reduced to its phase model description. Three different ways to 'derive' the phase equations are presented, each providing different insight into the underlying dynamics of phase response properties and phase-locking dynamics. The first derivation (the "Seat-of-the-Pants" deviation in section 4.3) is the most accessible. It captures the essence of the theory of weak coupling and only requires knowledge of some basic concepts from dynamical system theory, and a good understanding of what it means for a system to behave linearly. The second derivation (The Geometric Approach in section 4.4) is somewhat more mathematically sophisticated and provides deeper insight into the phase response dynamics of neurons. To make this second derivation more accessible, we tie all concepts back to the explanations in the first derivation. The third derivation (The Single Perturbation Approach in section 4.5) is the most mathematically abstract but it provides the cleanest derivation of the phase equations. It also explicitly shows that the iPRC can be computed as a solution of the "adjoint" equations.

During these three explanations of the theory of weak coupling, the phase model is derived for a pair of coupled neurons to illustrate the reduction technique. The later sections (section 4.6 and 4.7) briefly discuss extensions of the phase model to include heterogeneity, noise, and large networks of neurons.

4.2 Neuronal Models and Reduction to a Phase Model

4.2.1 General Form of Neuronal Network Models

The general form of a single or multi-compartmental Hodgkin-Huxley-type neuronal model [44] is

$$\frac{dX}{dt} = F(X), \tag{4.2.1}$$

where X is a N-dimensional state variable vector of containing the membrane potential(s) and gating variables[1], and $F(X)$ is a vector function describing the rate of change of the variables in time. For the Hodgkin-Huxley (HH) model [44], $X = [V, m, h, n]^T$ and

$$F(X) = \begin{bmatrix} \frac{1}{C}\left(-g_{Na}m^3h(V - E_{Na}) - g_K n^4(V - E_K) - g_L(V - E_L) + I\right) \\ \frac{m_\infty(V) - m}{\tau_m(V)} \\ \frac{h_\infty(V) - h}{\tau_h(V)} \\ \frac{n_\infty(V) - n}{\tau_n(V)}, \end{bmatrix}, \tag{4.2.2}$$

In this chapter, we assume that the isolated model neuron (equation (4.2.1)) exhibits stable T-periodic firing (e.g. top trace of Figure 4.3.1). In the language of dynamical systems, we assume that the model has an asymptotically stable T-periodic *limit cycle*. These oscillations could be either due to intrinsic conductances or induced by

---

[1]The gating variables could be for ionic membrane conductances in the neuron, as well as those describing the output of chemical synapses.

applied current.

A pair of coupled model neurons is described by

$$\frac{dX_1}{dt} = F(X_1) + \varepsilon I(X_1, X_2) \tag{4.2.3}$$

$$\frac{dX_2}{dt} = F(X_2) + \varepsilon I(X_2, X_1), \tag{4.2.4}$$

where $I(X_1, X_2)$ is a vector function describing the coupling between the two neurons, and ε scales the magnitude of the coupling term. Typically, in models of neuronal networks, cells are only coupled through the voltage (V) equation. For example, a pair of electrically coupled HH neurons would have the coupling term

$$I(X_1, X_2) = \begin{bmatrix} \frac{1}{C} \left(g_C(V_2 - V_1) \right) \\ 0 \\ 0 \\ 0 \end{bmatrix}. \tag{4.2.5}$$

where g_C is the coupling conductance of the electrical synapse.

It is important to note that in order to apply the theory of weak coupling, the equations for the neuronal network (4.2.3-4.2.4) should be put in dimensionless form in order to identify the "small" parameter ε relative to the parameters describing the intrinsic dynamics of the neurons.

4.2.2   Phase models, the G-Function and Phase-Locking

The power of the theory of weakly coupled oscillators is that it reduces the dynamics of each neuronal oscillator in a network to a single phase equation that describes the rate of change of its relative phase, ϕ_j. The phase model corresponding to the pair of coupled neurons (4.2.3-4.2.4) is of the form

$$\frac{d\phi_1}{dt} = \varepsilon H(\phi_2 - \phi_1) \tag{4.2.6}$$

$$\frac{d\phi_2}{dt} = \varepsilon H(-(\phi_2 - \phi_1)). \tag{4.2.7}$$

$$\tag{4.2.8}$$

The following sections present three different ways of deriving the function H, which is often called the interaction function.

Subtracting the phase equation for cell 1 from that of cell 2, the dynamics can be further reduced to a single equation that governs the evolution of the phase difference between the cells, $\phi = \phi_2 - \phi_1$

$$\frac{d\phi}{dt} = \varepsilon(H(-\phi) - H(\phi)) = \varepsilon G(\phi). \tag{4.2.9}$$

In the case of a pair of coupled Hodgkin-Huxley neurons (as described above), the number of equations in the system is reduced from the original 8 describing the dynamics of the voltage and gating variables to a single equation. The reduction method can also be readily applied to multicompartment model neurons (e.g. [116, 59]), which can render a significantly larger dimension reduction. In fact, the method has been applied to real neurons as well (e.g. [64]).

Note that the function $G(\phi)$ or "G-function" can easily be used to determine the

phase-locking behavior of the coupled neurons. The zeros of the G-function, ϕ^*, are the steady state phase differences between the two cells. For example, if $G(0) = 0$, this implies that that the synchronous solution is a steady state of the system. To determine the stability of the steady state note that when $G(\phi) > 0$, ϕ will increase and when $G(\phi) < 0$, ϕ will decrease. Therefore, if the derivative of G is positive at a steady state ($G'(\phi^*) > 0$) then the steady state is unstable. Similarly, if if the derivative of G is negative at a steady state ($G'(\phi^*) < 0$) then the steady state is stable. Figure 4.2.1 shows an example G-function for two coupled identical cells. Note that this system has 4 steady states corresponding to $\phi = 0, T$ (synchrony), $\phi = T/2$ (antiphase), and two other asynchronous states. It is also clearly seen that $\phi = 0, T$ and $\phi = T/2$ are stable steady states and the other asynchronous states are unstable. Thus, the two cells in this system exhibit bistability, and they will either synchronize their firing or fire in anti-phase depending upon the initial conditions.

In sections 4.3, 4.4 and 4.5, we present three different ways of derive the interaction function H and therefore the G-function. These derivations make several approximations that require the coupling between neurons to be sufficiently weak. "Sufficiently weak" implies that the neurons' intrinsic dynamics dominate the effects due to coupling at each point in the periodic cycle, i.e. during the periodic oscillations, $|F(X_j(t))|$ should be an order of magnitude greater than $|\varepsilon I(X_1(t), X_2(t))|$. However, it is important to point out that, even though the phase models quantitatively capture the dynamics of the full system for sufficiently small ε, it is often the case that they can also capture the qualitative behavior for moderate coupling strengths [58, 70].
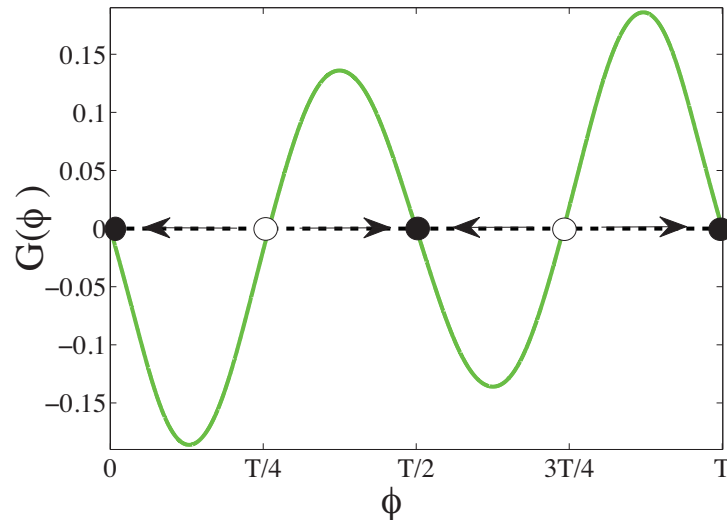
Figure 4.2.1: **Example G function**. The G function for two model FS interneurons coupled with gap junctions on the distal ends of their passive dendrites is plotted. The arrows show the direction of the trajectories for the system. This system has four steady state solutions $\phi_S = 0, T$ (synchrony), $\phi_{AP} = T/2$ (anti-phase), and two asynchronous states. One can see that synchrony and anti-phase are the only stable steady-states for this system (filled in circles). Thus, depending on the initial conditions, the two neurons will fire synchronously or in anti-phase.

4.3   A "Seat-of-the-Pants" Approach

This section will describe perhaps the most intuitive way of deriving the phase model for a pair of coupled neurons [58]. The approach highlights the key aspect of the theory of weakly coupled oscillators, which is that neurons behave linearly in response to small perturbations and therefore obey the principle of superposition.

4.3.1   Defining Phase

T-periodic firing of a model neuronal oscillator (equation (4.2.1)) corresponds to repeated circulation around an asymptotically stable T-periodic limit cycle, i.e. a closed orbit in state space X. We will denote this T-periodic limit cycle solution as

$X_{LC}(t)$. Phase of a neuron is a measure of the time that has elapsed as the neuron's moves around its periodic orbit, starting from an arbitrary reference point in the cycle. We define the phase of the periodically firing neuron j at time t to be

$$\theta_j(t) = (t + \phi_j) \mod T, \qquad (4.3.1)$$

where $\theta_j = 0$ is set to be at the peak of the neurons' spike (Figure 4.3.1).[2] The constant ϕ_j, which is referred to as the *relative phase* of the jth neuron, is determined by the position of the neuron on the limit cycle at time $t = 0$. Note that each phase of the neuron corresponds to a unique position on the cell's T-periodic limit cycle, and any solution of the uncoupled neuron model that is on the limit cycle can be expressed as

$$X_j(t) = X_{LC}(\theta_j(t)) = X_{LC}(t + \phi_j). \qquad (4.3.2)$$

When a neuron is perturbed by coupling current from other neurons or by any other external stimulus, its dynamics no longer exactly adhere to the limit cycle, and the exact correspondence of time to phase (equation (4.3.1)) is no longer valid. However, when perturbations are sufficiently weak, the neuron's intrinsic dynamics are dominant. This ensures that the perturbed system remains close to the limit cycle and the inter-spike intervals are close to the intrinsic period T. Therefore, we can approximate the solution of neuron j by $X_j(t) \simeq X_{LC}(t + \phi_j(t))$, where the realtive phase ϕ_j is now a function of time t. Over each cycle of the oscillations, the weak perturbations to the neurons produce only small changes in ϕ_j. These changes are negligible over a single cycle, but they can slowly accumulate over many cycles and

---

[2]Phase is often normalized by the period T or by $T/2\pi$, so that $0 \le \theta < 1$ or $0 \le \theta < 2\pi$ respectively. Here, we do not normalize phase and take $0 \le \theta < T$.
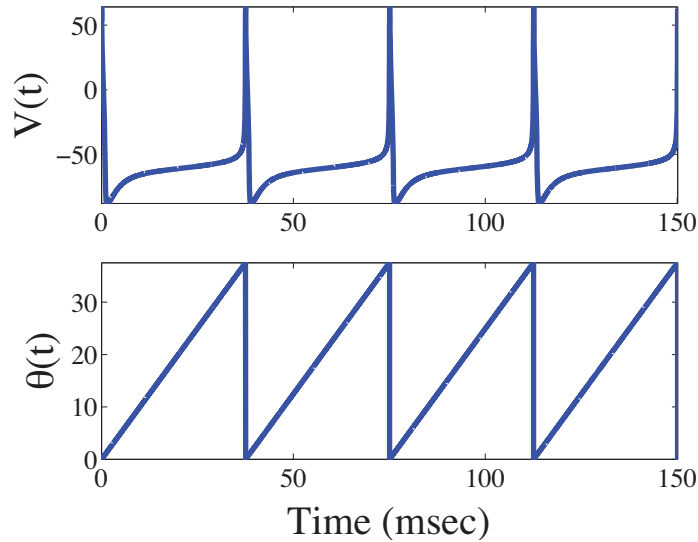
Figure 4.3.1: **Phase**. a) Voltage trace for the Fast-Spiking interneuron model from Erisir et al. [27] with $I_{appl} = 35 \ \mu A/cm^2$ showing T-periodic firing. b) The phase, $\theta(t)$ of these oscillations increases linearly from 0 to T, and we have assumed that zero phase occurs at the peak of the voltage spike.

produce substantial effects on the relative firing times of the neurons.

The goal now is to understand how the relative phase $\phi_j(t)$ of the coupled neurons evolves slowly in time. To do this, we first consider the response of a neuron to small abrupt current pulses.

4.3.2   The Infinitesimal Phase Response Curve

Suppose that a small brief square current pulse of amplitude εI_0 and duration Δt is delivered to a neuron when it is at phase θ^*. This small, brief current pulse causes the membrane potential to increase abruptly by $\delta V \simeq \varepsilon I_0 \Delta t / C$, i.e. the change in voltage will approximately equal the total charge delivered to the cell by the stimulus, $\varepsilon I_0 \Delta t$, divided by the capacitance of the neuron, C. In general, this perturbation can cause the cell to fire sooner (phase advance) or later (phase delay) than it would have

fired without the perturbation. The magnitude and sign of this *phase shift* depends on the amplitude and duration of the stimulus, as well as the phase in the oscillation at which the stimulus was delivered. This relationship is quantified by the Phase Response Curve (PRC), which gives the phase shift $\Delta\phi$ as a function of the phase θ^* for a fixed $\varepsilon I_0 \Delta t$ (Figure 4.3.2).

For sufficiently small and brief stimuli, the neuron will respond in a linear fashion, and the PRC will scale linearly with the magnitude of the current stimulus

$$\Delta\phi(\theta^*) \simeq Z_V(\theta^*) \, \delta V = Z_V(\theta^*) \, \left(\frac{1}{C}\varepsilon I_0\Delta t\right), \quad 0 \le \theta^* < T, \tag{4.3.3}$$

where $Z_V(\theta^*)$ describes the proportional phase shift as a function of the phase of the stimulus. The function $Z_V(\theta)$ is known as the infinitesimal phase response curve (iPRC) or the phase-dependent sensitivity function for voltage perturbations. The iPRC $Z_V(\theta)$ quantifies the normalized phase shift due to an infinitesimally small δ-function-like voltage-perturbation delivered at any given phase on the limit cycle.

4.3.3 The Phase Model for a Pair of Weakly Coupled Cells

Now we can reconsider the pair of weakly coupled neuronal oscillators (equations (4.2.3-4.2.4)). Recall that, because the coupling is weak, the neurons' intrinsic dynamics dominate the dynamics of the coupled-cell system, and $X_j(t) \simeq X_{LC}(\theta_j(t)) = X_{LC}(t+\phi_j(t))$ for $j = 1, 2$. This assumes that the coupling current can only affect the speed at which cells move around their limit cycle and does not affect the amplitude of the oscillations. Thus, the effects of the coupling are entirely captured in the slow time dynamics of the relative phases of the cells $\phi_j(t)$.

The assumption of weak coupling also ensures that the perturbations to the neurons are sufficiently small so that the neurons respond linearly to the coupling current.
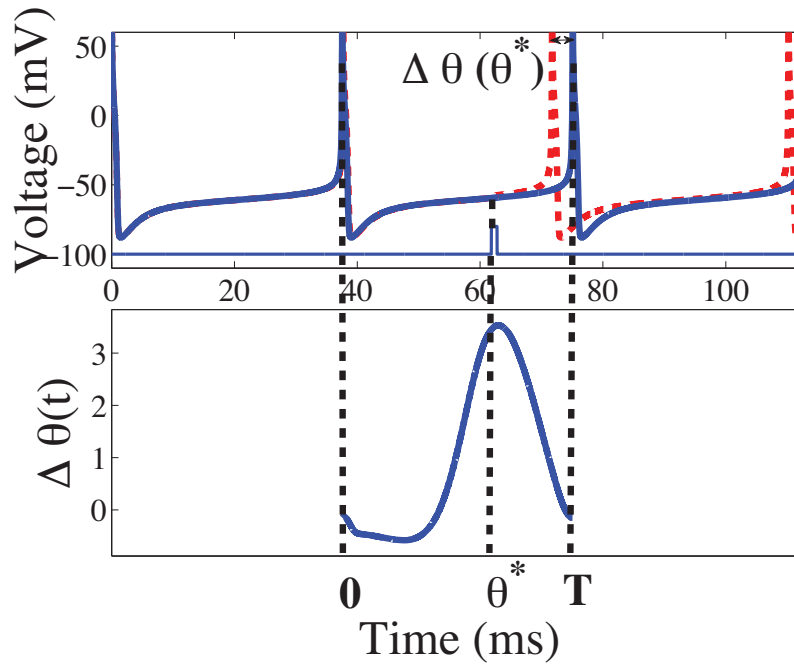
Figure 4.3.2: **Measuring the Phase Response Curve from Neurons**. The voltage trace and corresponding PRC is shown for the same FS model neuron from Figure 4.3.1. The PRC is measured from a periodically firing neuron by delivering small current pulses at every point, θ^*, along its firing period and measuring the subsequent change in period, $\Delta\theta$, caused by the current pulse.

That is, (i) the small phase shifts of the neurons due to the presence of the coupling current for a brief time Δt can be approximated using the iPRC (equation (4.3.3)), and (ii) these small phase shifts in response to the coupling current sum linearly (i.e. the principle of superposition holds). Therefore, by equation (4.3.3), the phase shift due to the coupling current from t to $t + \Delta t$ is

$$\Delta\phi_j(t) \quad = \quad \phi_j(t + \Delta t) - \phi_j(t) \tag{4.3.4}$$

$$= \quad Z_V(\theta_j(t)) \; (\varepsilon I(X_1(t), X_2(t))) \, \Delta t. \tag{4.3.5}$$

$$= \quad Z_V(t + \phi_j(t)) \; (\varepsilon I(X_{LC}(t + \phi_j(t)), X_{LC}(t + \phi_k(t)))) \, \Delta t. \tag{4.3.6}$$

Furthermore, by dividing the above equation by Δt and taking the limit as $\Delta t \to 0$, we obtain a system of differential equations that govern the evolution of the relative phases of the two neurons

$$\frac{d\phi_j}{dt} = \varepsilon \; Z_V(t + \phi_j) \; I(X_{LC}(t + \phi_j), X_{LC}(t + \phi_k)), \quad j, k = 1, 2; /j \neq k. \tag{4.3.7}$$

Note that, by integrating this system of differential equations to find the solution $\phi_j(t)$, we are assuming that phase shifts in response to the coupling current sum linearly.

The explicit time-dependence on the righthand side of equation (4.3.7) can be eliminated by "averaging" over the period T. Note that $Z_V(t)$ and $X_{LC}(t)$ are T-periodic functions, and the scaling of the righthand side of equation (4.3.7) by the small parameter ε indicates that changes in the relative phases ϕ_j occur on a much slower time scale than T. Therefore, we can integrate the righthand side over the full period T holding the values of ϕ_j constant to find the average rate of change of the ϕ_j over a cycle. Thus, we obtain equations that approximate the slow time evolution of the relative phases ϕ_j

$$\frac{d\phi_j}{dt} \quad = \quad \varepsilon \frac{1}{T} \int_0^T Z_V(\tilde{t}) \left(I(X_{LC}(\tilde{t}), X_{LC}(\tilde{t} + \phi_k - \phi_j)) \right) d\tilde{t} \qquad (4.3.8)$$

$$= \quad \varepsilon H(\phi_k - \phi_j), \quad j, k = 1, 2; \ j \neq k, \qquad (4.3.9)$$

i.e. the relative phases ϕ_j are assumed to be constant with respect to the integral over T in $\tilde{t}$, but they vary in t. This averaging process is made rigorous by averaging theory [43, 34].

We have reduced the dynamics of a pair of weakly coupled neuronal oscillators to an autonomous system of two differential equations describing the phases of the neurons and therefore finished the first derivation of the phase equations for a pair of weakly coupled neurons.[3] Note that the above derviation can be easily altered to obtain the phase model of a neuronal oscillator subjected to T-periodic external forcing as well. The crux of the derivation was identifying the iPRC and exploiting the approximately linear behavior of the system in response to weak inputs. In fact, it is useful to note that the interaction function H takes the form of a convolution of the iPRC and the coupling current, i.e. the input to the neuron. Therefore, one can think of the iPRC as an impulse response function or Green's function for the system.

Averaging Theory

Averaging theory [43, 34] states that there is a change of variables that maps solutions of

---

[3]Note that this reduction is not valid when T is of the same order of magnitude as the time scale for the changes due to the weak coupling interactions (e.g. close to a SNIC bifurcation), however an alternative reduction can be performed in this case [32].

$$\frac{d\phi}{d\tilde{t}} = \varepsilon g(\phi, \tilde{t}), \tag{4.3.10}$$

where $g(\phi, \tilde{t})$ is a T-periodic function in ϕ and $\tilde{t}$, to solutions of

$$\frac{d\varphi}{dt} = \varepsilon \bar{g}(\varphi) + \mathcal{O}(\varepsilon^2), \tag{4.3.11}$$

where

$$\bar{g}(\varphi) = \frac{1}{T} \int_0^T g(\varphi, \tilde{t}) d\tilde{t}, \tag{4.3.12}$$

and $\mathcal{O}(\varepsilon^2)$ is Landau's "Big O" notation which represents terms that either have a scaling factor of ε^2 or go to zero at the same rate as ε^2 goes to zero as ε goes to zero.

4.4 A Geometric Approach

In this section, we describe a geometric approach to the theory of weakly coupled oscillators originally introduced by Yoshiki Kuramoto [54]. The main asset of this approach is that it gives a beautiful geometric interpretation of the iPRC and deepens our understanding of the underlying mechanisms of the phase response properties of neurons.

4.4.1 The One-to-One Map Between Points on the Limit Cycle and Phase

Consider again a model neuron (4.2.1) that has a stable T-periodic limit cycle solution, $X_{LC}(t)$ such that the neuron exhibits a T-periodic firing pattern (e.g. top trace of Figure 4.3.1). Recall that the phase of the oscillator along its limit cycle is defined

as $\theta(t) = (t + \phi) \mod T$, where the relative phase ϕ is a constant that is determined by the initial conditions. Note that there is a one-to-one correspondence between phase and each point on the limit cycle. That is, the limit cycle solution takes phase to a unique point on the cycle, $X = X_{LC}(\theta)$, and its inverse maps each point on the limit cycle to a unique phase, $\theta = X_{LC}^{-1}(X) = \Phi(X)$.

Note that it follows immediately from the definition of phase (4.3.1) that the rate of change of phase in time along the limit cycle is equal to 1, i.e. $\frac{d\theta}{dt} = 1$. Therefore, if we differentiate the map $\Phi(X)$ with respect to time using the chain rule for vector functions, we obtain the following useful relationship

$$\frac{d\theta}{dt} = \nabla_X \Phi(X_{LC}(t)) \cdot \frac{dX_{LC}}{dt} = \nabla_X \Phi(X_{LC}(t)) \cdot F(X_{LC}(t))) = 1, \qquad (4.4.1)$$

where $\nabla_X \Phi$ is the gradient of the map $\Phi(X)$ with respect to the vector of the neuron's state variables $X = (x_1, x_2, \cdots, x_N)$

$$\nabla_X \Phi(X) = \left(\frac{\partial \Phi}{\partial x_1}, \frac{\partial \Phi}{\partial x_2}, \dots, \frac{\partial \Phi}{\partial x_N} \right) \Big|_X. \qquad (4.4.2)$$

4.4.2 Asymptotic Phase and the Infinitesimal Phase Response Curve

The map $\theta = \Phi(X)$ is well-defined for all points X on the limit cycle. We can extend the domain of $\Phi(X)$ to points off the limit cycle by defining the concept of *asymptotic phase*. If X_0 is a point on the limit cycle and Y_0 is a point in a neighborhood of the limit cycle[4], then we say that Y_0 has the same asymptotic phase

---

[4]In fact, the point Y_0 can be anywhere in the basin of attraction of the limit cycle.

as X_0 if $||X(t; X_0) - X(t; Y_0)|| \to 0$ as $t \to \infty$. This means that the solution starting at the initial point Y_0 off the limit cycle converges to the solution starting at the point X_0 on the limit cycle as time goes to infinity. Therefore, $\Phi(Y_0) = \Phi(X_0)$. The set of all points off the limit cycle that have the same asymptotic phase as the point X_0 on the limit cycle is known as the *isochron* [114] for phase $\theta = \Phi(X_0)$. Figure 4.4.1 shows some isochrons around the limit cycle for the Morris-Lecar neuron [67]. It is important to note that the figure only plots isochrons for a few phases and that *every* point on the limit cycle has a corresponding isochron.

Equipped with the concept of asymptotic phase, we can now show that the iPRC is in fact the gradient of the phase map $\nabla_X \Phi(X_{LC}(t))$ by considering the following phase resetting "experiment". Suppose that, at time t, the neuron is on the limit cycle in state $X(t) = X_{LC}(\theta^*)$ with corresponding phase $\theta^* = \Phi(X(t))$. At this time, it receives a small aburpt external perturbation εU, where ε is the magnitude of the perturbation and U is the unit vector in the direction of the perturbation in state space. Immediately after the perturbation, the neuron is in the state $X_{LC}(\theta^*) + \varepsilon U$, and its new asymptotic phase is $\tilde{\theta}^* = \Phi(X_{LC}(\theta^*) + \varepsilon U)$. Using Taylor series,

$$\tilde{\theta} = \Phi(X_{LC}(\theta^*) + \varepsilon U) = \Phi(X_{LC}(\theta^*)) + \nabla_X \Phi(X_{LC}(\theta^*)) \cdot (\varepsilon U) + \mathcal{O}(\varepsilon^2). \quad (4.4.3)$$

Keeping only the linear term (i.e. $\mathcal{O}(\varepsilon)$ term), the phase shift of the neuron as a function of the phase θ^* at which it receives the εU perturbation is given by

$$\Delta\phi(\theta^*) = \tilde{\theta} - \theta^* = \nabla_X \Phi(X_{LC}(\theta^*)) \cdot (\varepsilon U). \quad (4.4.4)$$

As was done in section 4.3.2, we normalize the phase shift by the magnitude of the

(a)

(b)   **(c)**
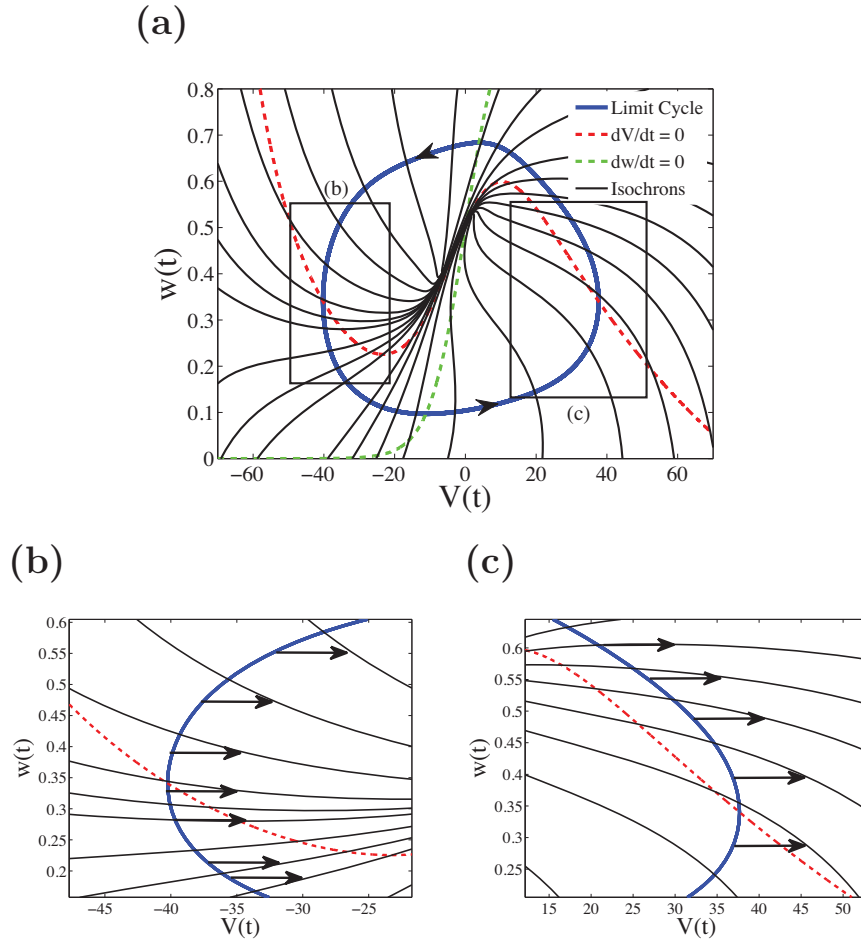
Figure 4.4.1: **Example Isochron Structure**. a) The limit cycle and isochron structure for the Morris-Lecar neuron [67] is plotted along with the nullclines for the system. b) Blow up of a region on the left side of the limit cycle showing how the same strength perturbation in the voltage direction can cause different size phase delays and even a phase advance. c) Blow up of a region on the right side of the limit cycle showing also that the same size voltage perturbation can cause different size phase advances.

stimulus,

$$\frac{\Delta\phi(\theta^*)}{\varepsilon} = \nabla_X \Phi(X_{LC}(\theta^*)) \cdot U = Z(\theta^*) \cdot U. \tag{4.4.5}$$

Note that $Z(\theta) = \nabla_X \Phi(X_{LC}(\theta))$ is the iPRC. It quantifies the normalized phase shift

due to a small delta-function-like perturbation delivered at any given point on the limit cycle. As was the case for the iPRC Z_V derived in the previous section (see equation (4.3.3)), $\nabla_X \Phi(X_{LC}(\theta))$ captures only the linear response of the neuron and is quantitively accurate only for sufficiently small perturbations. However, unlike Z_V, $\nabla_X \Phi(X_{LC}(\theta))$ captures the response to perturbations in any direction in state space and not only in one variable (e.g. the membrane potential). That is, $\nabla_X \Phi(X_{LC}(\theta))$ is the vector iPRC; its components are the iPRCs for every variable in the system (see Figure 4.4.2).
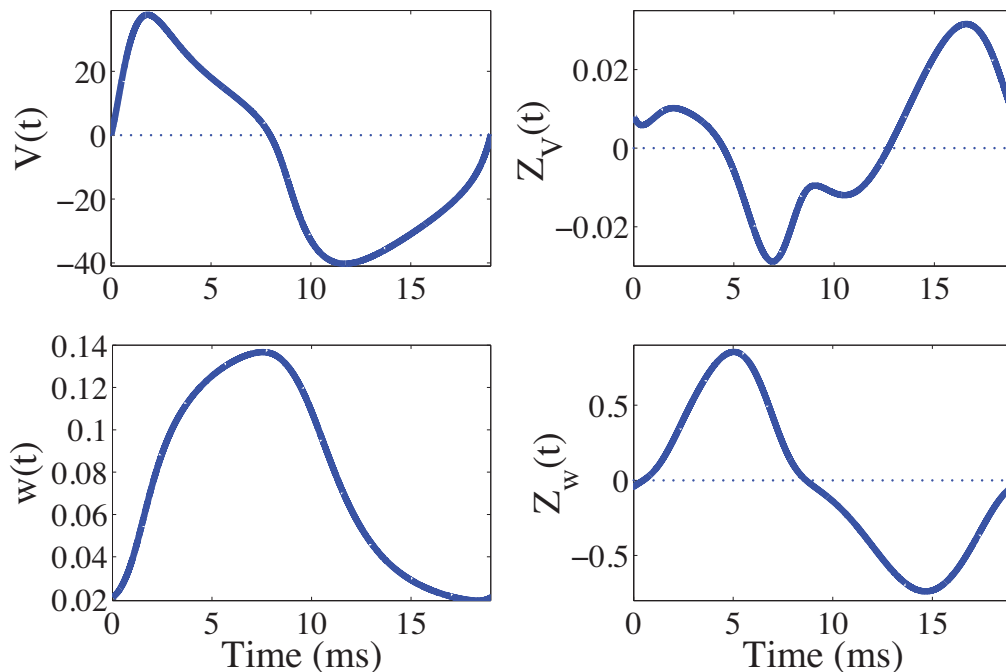
Figure 4.4.2: **iPRCs for the Morris-Lecar Neuron**. The voltage, $V(t)$ and channel, $w(t)$, components of the limit cycle for the same Morris-Lecar neuron as in Figure 4.4.1 are plotted along with their corresponding iPRCs. Note that the shape of voltage iPRC can be inferred from the insets of Figure 4.4.1. For example, the isochronal structure in Figure 4.4.1 (c) revales that perturbations in the voltage component will cause phase advances when the voltage is increasing from roughly 30 to 38 mV.

In the typical case of a single-compartment HH model neuron subject to an applied current pulse (which perturbs only the membrane potential), the perturbation would be of the form $\varepsilon U = (p, 0, 0, \cdots, 0)$ where x_1 is the membrane potential V. By equation (4.4.3), the phase shift is

$$\Delta\phi(\theta) = \frac{\partial\Phi}{\partial V}(X_{LC}(\theta))\, p = Z_V(\theta)\, p, \tag{4.4.6}$$

which is the same as equation (4.3.3) derived in the previous section with $p = \left(\frac{1}{C}\varepsilon I_0 \Delta t\right)$.

With the understanding that $\nabla_X \Phi(X_{LC}(t))$ is the vector of iPRC's for the system, we now derive the phase model for two weakly coupled neurons.

4.4.3   A Pair of Weakly Coupled Oscillators

Now consider the system of weakly coupled neurons (4.2.3-4.2.4). We can use the map Φ to take the variables $X_1(t)$ and $X_2(t)$ to their corresponding asymptotic phase, i.e. $\theta_j(t) = \Phi(X_j(t))$ for $j = 1, 2$. By the chain rule, we obtain the change in phase with respect to time

$$
\begin{aligned}
\frac{d\theta_j}{dt} &= \nabla_X \Phi(X_j(t)) \cdot \frac{dX_j}{dt} \\
&= \nabla_X \Phi(X_j(t)) \cdot [F(X_j(t)) + \varepsilon I(X_j(t), X_k(t))] \\
&= \nabla_X \Phi(X_j(t)) \cdot F(X_j(t)) + \nabla_X \Phi(X_j(t)) \cdot [\varepsilon I(X_j(t), X_k(t))] \\
&= 1 + \varepsilon \nabla_X \Phi(X_j(t)) \cdot I(X_j(t), X_k(t)), \tag{4.4.7}
\end{aligned}
$$

where we have used the "useful" relation (4.4.1). Note that the above equations are exact. However, in order to solve the equations for $\theta_j(t)$, we would already have to

know the full solutions $X_1(t)$ and $X_2(t)$, in which case you wouldn't need to reduce the system to a phase model. Therefore, we exploit that fact that ε is small and make the approximation $X_j(t) \sim X_{LC}(\theta_j(t)) = X_{LC}(t + \phi_j(t))$, i.e. the coupling is assumed to be weak enough so that it does not affect the amplitude of the limit cycle, but it can affect the rate at which the neuron moves around its limit cycle. By making this approximation in equation (4.4.7) and making the change of variables $\theta_j(t) = t + \phi_j(t)$, we obtain the equations for the evolution of the relative phases of the two neurons

$$\frac{d\phi_j}{dt} = \varepsilon \nabla_X \Phi(X_{LC}(t + \phi_j(t))) \cdot I(X_{LC}(t + \phi_j(t)), X_{LC}(t + \phi_k(t))). \qquad (4.4.8)$$

Note that these equations are the vector versions of the equations (4.3.7) with the iPRC written as $\nabla_X \Phi(X_{LC}(t))$. As described in the previous section, we can average these equations over the period T to eliminate the explicit time dependence and obtain the phase model for the pair of coupled neurons

$$\frac{d\phi_j}{dt} = \varepsilon \frac{1}{T} \int_0^T \nabla_X \Phi(X_{LC}(\tilde{t})) \cdot I(X_{LC}(\tilde{t}), X_{LC}(\tilde{t} - (\phi_k - \phi_j))) d\tilde{t} = \varepsilon H(\phi_k - \phi_j). \quad (4.4.9)$$

Note that, while the above approach to deriving the phase equations provides substantial insight into the geometry of the neuronal phase response dynamics, it does not provide a computational method to compute the iPRC for model neurons, i.e. we still must directly measure the iPRC using extensive numerical simulations as described in the previous section.

4.5 A Singular Perturbation Approach

In this section, we describe the singular perturbation approach to derive the theory of weakly coupled oscillators. This systematic approach was developed independently by Malkin [62, 63], Neu [71], and Ermentrout [29]. The major practical asset of this approach is that it provides a simple method to compute iPRCs for model neurons.

Consider again the system of weakly coupled neurons (4.2.3-4.2.4). We assume that the isolated neurons have asymptotically stable T-periodic limit cycle solutions $X_{LC}(t)$ and that coupling is weak (i.e. ε is small). As previously stated, the weak coupling has small effects on the dynamics of the neurons. On the time-scale of a single cycle, these effects are negligible. However, the effects can slowly accumulate on a much slower time-scale and have a substantial influence on the relative firing times of the neurons. We can exploit the differences in these two time-scales and use the method of multiple scales to derive the phase model.

First, we define a "fast time" $t_f = t$, which is on the time-scale of the period of the isolated neuronal oscillator, and a "slow time" $t_s = \varepsilon t$, which is on the time-scale that the coupling affects the dynamics of the neurons. Time, t, is thus a function of both the fast and slow times, i.e. $t = f(t_f, t_s)$. By the chain rule, $\frac{d}{dt} = \frac{\partial}{\partial t_f} + \varepsilon \frac{\partial}{\partial t_s}$. We then assume that solutions $X_1(t)$ and $X_2(t)$ can be expressed as power-series in ε that depend both on t_f and t_s,

$$X_j(t) = X_j^0(t_f, t_s) + \varepsilon X_j^1(t_f, t_s) + \mathcal{O}(\varepsilon^2), \quad j = 1, 2.$$

Substituting these expansions into equations (4.2.3-4.2.4) yields

$$\frac{\partial X_j^0}{\partial t_f} + \varepsilon \frac{\partial X_j^0}{\partial t_s} + \varepsilon \frac{\partial X_j^1}{\partial t_f} + \mathcal{O}(\varepsilon^2) = F(X_j^0 + \varepsilon X_j^1 + \mathcal{O}(\varepsilon^2)) \qquad (4.5.1)$$

$$+ \varepsilon I(X_j^0 + \varepsilon X_j^1 + \mathcal{O}(\varepsilon^2), X_k^0 + \varepsilon X_k^1 + \mathcal{O}(\varepsilon^2)), \quad j, k = 1, 2; j \neq k.$$

Using Taylor series to expand the vector functions F and I in terms of ε, we obtain

$$F(X_j^0 + \varepsilon X_j^1 + \mathcal{O}(\varepsilon^2)) = F(X_j^0) + \varepsilon DF(X_j^0)X_j^1 + \mathcal{O}(\varepsilon^2) \qquad (4.5.2)$$

$$\varepsilon I(X_j^0 + \varepsilon X_j^1 + \mathcal{O}(\varepsilon^2), X_k^0 + \varepsilon X_k^1 + \mathcal{O}(\varepsilon^2)) = \varepsilon I(X_j^0, X_k^0) + \mathcal{O}(\varepsilon^2), \quad (4.5.3)$$

where $DF(X_j^0)$ is the Jacobian, i.e. matrix of partial derivatives, of the vector function $F(X_j)$ evaluated at X_j^0. We then plug these expressions into equations (4.5.1), collect like terms of ε, and equate the coefficients of like terms.[5]

The leading order ($\mathcal{O}(1)$) terms yield

$$\frac{\partial X_j^0}{\partial t_f} = F(X_j^0), \quad j = 1, 2. \qquad (4.5.4)$$

These are the equations that describe the dynamics of the uncoupled cells. Thus, to leading order, each cell exhibits the T-periodic limit cycle solution $X_j^0(t_f, t_s) = X_{LC}(t_f + \phi_j(t_s))$. Note that equation (4.5.4) implies that the relative phase ϕ_j is constant in t_f, but it can still evolve on the slow time-scale t_s.

Substituting the solutions for the leading order equations (and shifting t_f appropriately), the $\mathcal{O}(\varepsilon)$ terms of equations (4.5.1) yield

---

[5]Because the equation should hold for arbitrary ε, coefficients of like terms must be equal.

$$\mathcal{L}X_j^1 = \frac{\partial X_j^1}{\partial t_f} - DF(X_{LC}(t_f))X_j^1$$

$$= I(X_{LC}(t_f), X_{LC}(t_f - (\phi_j(t_s) - \phi_k(t_s)))) - X'_{LC}(t_f)\frac{d\phi_j}{dt_s}. \qquad (4.5.5)$$

To simplify notation, we have defined the linear operator $\mathcal{L}X = \frac{\partial X}{\partial t_f} - DF(X_{LC}(t_f))X$, which acts on a T-periodic domain and is therefore bounded. Note that equation (4.5.5) is a linear differential equation with T-periodic coefficients. In order for our power series solutions for $X_1(t)$ and $X_2(t)$ to exist, a solution to equation (4.5.5) must exist. Therefore, we need to find conditions that guarantee the existence of a solution to equation (4.5.5), i.e. conditions that ensure that the righthand side of equation (4.5.5) is in the range of the operator $\mathcal{L}$. The Fredholm Alternative explicitly provides us with these conditions.

Theorem (Fredholm's Alternative). Consider the following equation

$$(*) \qquad \mathcal{L}x = \frac{dx}{dt} + A(t)x = f(t); \quad x \in \mathbb{R}^N,$$

where $A(t)$ and $f(t)$ are continuous and T-periodic. Then, there is a continuous T-periodic solution $x(t)$ to (*) if and only if

$$(**) \qquad \frac{1}{T}\int_0^T Z(t) \cdot f(t)dt = 0,$$

for each continuous T-periodic solution, $Z(t)$, to the adjoint problem

$$\mathcal{L}^*x = -\frac{dZ}{dt} + \{A(t)\}^T Z = 0.$$

In the language of the above theorem,

$$A(t) = -DF(X_{LC}(t_f)),$$

and

$$f(t) = I(X_{LC}(t_f), X_{LC}(t_f - (\phi_j(t_s) - \phi_k(t_s)))) - X'_{LC}(t_f)\frac{d\phi_j}{dt_s}.$$

Thus, the solvability condition (**) requires that

$$\frac{1}{T}\int_0^T Z(t_f) \cdot \left[I(X_{LC}(t_f), X_{LC}(t_f - (\phi_j(t_s) - \phi_k(t_s)))) - X'_{LC}(t_f)\frac{d\phi_j}{dt_s} \right] dt_f = 0$$

$$(4.5.6)$$

where Z is a T-periodic solution of the adjoint equation

$$\mathcal{L}^* Z = -\frac{\partial Z}{\partial t_f} - DF(X_{LC}(t_f))^T Z = 0. \qquad (4.5.7)$$

Rearranging equation (4.5.6),

$$\frac{d\phi_j}{dt_s} = \frac{1}{T}\int_0^T Z(t_f) \cdot [I(X_{LC}(t_f), X_{LC}(t_f - (\phi_j(t_s) - \phi_k(t_s))))] dt_f \qquad (4.5.8)$$

where we have normalized $Z(t_f)$ by

$$\frac{1}{T}\int_0^T Z(t_f) \cdot [X'_{LC}(t_f)]dt_f = \frac{1}{T}\int_0^T Z(t_f) \cdot F(X_{LC}(t_f))dt_f = 1. \qquad (4.5.9)$$

This normalization of $Z(t_f)$ is equivalent to setting

$$Z(0) \cdot X'_{LC}(0) = Z(0) \cdot F(X'_{LC}(0)) = 1, \qquad (4.5.10)$$

because $Z(t) \cdot X'_{LC}(t)$ is a constant (see Appendix A).

Finally, recalling that $t_s = \varepsilon t$ and $t_f = t$, we obtain the phase model for the pair of coupled neurons

$$\frac{d\phi_j}{dt} = \varepsilon \frac{1}{T} \int_0^T Z(\tilde{t}) \cdot [I\left(X_{LC}(\tilde{t}), X_{LC}(\tilde{t} - (\phi_j - \phi_k)))\right)]d\tilde{t} = \varepsilon H(\phi_k - \phi_j), \quad (4.5.11)$$

By comparing these phase equations with those derived in the previous sections, it is clear that the appropriately normalized solution to the adjoint equations $Z(t)$ is the iPRC of the neuronal oscillator (see 4.5.2 for further discussion).

4.5.1 Appendix A: A Note on the Normalization of $Z(t)$

$$
\begin{aligned}
\frac{d}{dt}[Z(t) \cdot F(X_{LC}(t))] &= \frac{dZ}{dt} \cdot F(X_{LC}(t)) + Z(t) \cdot \frac{d}{dt}[F(X_{LC}(t))] \\
&= (-DF(X_{LC}(t))^T Z) \cdot F(X_{LC}(t)) \\
&\qquad + Z(t) \cdot (DF(X_{LC}(t))X'_{LC}(t)) \\
&= -Z(t) \cdot (DF(X_{LC}(t))F(X_{LC}(t))) \\
&\qquad + Z(t) \cdot (DF(X_{LC}(t))F(X_{LC}(t))) \\
&= 0.
\end{aligned}
$$

This implies that $Z(t) \cdot F(X_{LC}(t))$ is a constant. The integral form of the normalization of $Z(t)$ (equation (4.5.9)) implies that this constant is 1. Thus,

$$Z(t) \cdot F(X_{LC}(t)) = Z(t) \cdot X'_{LC}(t) = 1, \qquad (4.5.12)$$

for all values of t including $t = 0$.

4.5.2   Appendix B: The Relationship between Adjoints and Gradients

Here, we present Brown et. al's [13] direct proof that $\nabla_X \Phi(X_{LC}(t))$ satisfies the adjoint equation (4.5.7) and the normalization condition (4.5.9) in order to illustrate the relationship between the gradient of the phase map $\nabla_X \Phi(X_{LC}(t))$ to solution of the adjoint equation $Z(t)$.

Consider again the system of differential equations for an isolated neuronal oscillator (4.2.1) that has an asymptotically stable T-periodic limit cycle solution $X_{LC}(t)$. Suppose that $X(t) = X_{LC}(t+\phi)$ is a solution of this system that is on the limit cycle, which starts at point $X(0) = X_{LC}(\phi)$. Further suppose that $Y(t) = X_{LC}(t+\phi)+p(t)$ is a solution that starts at from the initial condition $Y(0) = X_{LC}(\phi) + p(0)$, where $p(0)$ is small in magnitude. Because this initial perturbation $p(0)$ is small and the limit cycle is stable, (i) $p(t)$ remains small and, to $\mathcal{O}(|p|)$, $p(t)$ satisfies the linearized system

$$\frac{dp}{dt} = DF(X_{LC}(t + \phi))p, \qquad (4.5.13)$$

and (ii) the phase difference between the two solutions is

$$\Delta\phi = \Phi(X_{LC}(t+\phi)) - \Phi(X_{LC}(t+\phi) + p(t)) = \nabla_X\Phi(X_{LC}(t+\phi)) \cdot p(t) + \mathcal{O}(|p|^2).$$

(4.5.14)

Furthermore, while the asymptotic phases of the solutions evolve in time, the phase difference between the solutions $\Delta\phi$ remains constant. Therefore, by differentiating equation (4.5.14), we see that to $\mathcal{O}(|p|)$

$$
\begin{aligned}
0 &= \frac{d}{dt}[\nabla_X\Phi(X_{LC}(t+\phi)) \cdot p(t)] \\
&= \frac{d}{dt}[\nabla_X\Phi(X_{LC}(t+\phi))] \cdot p(t) + \nabla_X\Phi(X_{LC}(t+\phi)) \cdot \frac{dp}{dt} \\
&= \frac{d}{dt}[\nabla_X\Phi(X_{LC}(t+\phi))] \cdot p(t) + \nabla_X\Phi(X_{LC}(t+\phi)) \cdot (DF(X_{LC}(t+\phi))p(t)) \\
&= \frac{d}{dt}[\nabla_X\Phi(X_{LC}(t+\phi))] \cdot p(t) + \left(DF(X_{LC}(t+\phi))^T\nabla_X\Phi(X_{LC}(t+\phi))\right) \cdot p(t) \\
&= \left\{\frac{d}{dt}[\nabla_X\Phi(X_{LC}(t+\phi))] + DF(X_{LC}(t+\phi))^T\left(\nabla_X\Phi(X_{LC}(t+\phi))\right)\right\} \cdot p(t).
\end{aligned}
$$

Because p is arbitrary, the above argument implies that $\nabla_X\Phi(X_{LC}(t))$ solves the adjoint equation (4.5.7). The normalization condition simply follows from the definition of the phase map (see (4.4.1)), i.e.

$$\frac{d\theta}{dt} = \nabla_X\Phi(X_{LC}(t)) \cdot X'_{LC}(t) = 1.$$

(4.5.15)

4.5.3   Appendix C: Computing the PRC Numerically Using the Adjoint method

As stated in this beginning of this section, the major practical asset of the singular perturbation approach is that it provides a simple method to compute the iPRC for model neurons. Specifically, the iPRC is a T-period solution to

$$\frac{dZ}{dt} = -DF(X_{LC}(t))^T Z \qquad (4.5.16)$$

subject to the normalization constraint

$$Z(0) \cdot X'_{LC}(0) = 1. \qquad (4.5.17)$$

This equation is the adjoint equation for the isolated model neuron (equation (4.2.1)) linearized around the limit cycle solution $X_{LC}(t)$.

In practice, the solution to equation (4.5.16) is found by integrating the equation backwards in time [112]. The adjoint system has the opposite stability of the original system (equation (4.2.1)), which has an asymptotically stable T-periodic limit cycle solution. Thus, we integrate backwards in time from an arbitrary initial condition so as to dampen out the transients and arrive at the (unstable) periodic solution of equation (4.5.16). To obtain the iPRC, we normalize the periodic solution using (4.5.17). This algorithm is automated in the software package XPPAUT [28], which is available for free on Bard Ermentrout's webpage $www.math.pitt.edu/\sim bard/bardware/$.

4.6 Extensions of Phase Models for Pairs of Coupled Cells

In this section, we show how the phase reduction technique can be extended to incorporate weak heterogeneity and weak noise.

4.6.1 Weak Heterogeneity

Suppose that the following system

$$\frac{dX_j}{dt} = F_j(X_j) + \varepsilon I(X_k, X_j) = F(X_j) + \varepsilon \left[f_j(X_j) + I(X_k, X_j) \right] \tag{4.6.1}$$

describes two weakly coupled neuronal oscillators (note that the vector functions $F_j(X_j)$ are now specific to the neuron). If the two neurons are weakly heterogeneous, then their underlying limit cycles are equivalent up to an $\mathcal{O}(\varepsilon)$ difference. That is, $F_j(X_j) = F(X_j) + \varepsilon f_j(X_j)$, where $f_j(X_j)$ is a vector function that captures the $\mathcal{O}(\varepsilon)$ differences in the dynamics of cell 1 and cell 2 from the function $F(X_j)$. These differences may occur in various places such as the value of the neurons' leakage conductances, the applied currents, or the leakage reversal potentials, to name a few.

As in the previous sections, equation (4.6.1) can be reduced to the phase model

$$\begin{aligned} \frac{d\phi_j}{dt} &= \varepsilon \left(\frac{1}{T} \int_0^T Z(\tilde{t}) \cdot \left[f_j(X_{LC}(\tilde{t})) + I(X_{LC}(\tilde{t}), X_{LC}(\tilde{t} + \phi_k - \phi_j)) \right] d\tilde{t} \right) \\ &= \varepsilon \omega_j + \varepsilon H(\phi_k - \phi_j), \end{aligned} \tag{4.6.2}$$

where $\omega_j = \frac{1}{T} \int_0^T Z(\tilde{t}) \cdot f_j(X_{LC}(\tilde{t})) d\tilde{t}$ represents the difference in the intrinsic frequen-

cies of the two neurons caused by the presence of the weak heterogeneity. If we now let $\phi = \phi_2 - \phi_1$, we obtain

$$
\begin{aligned}
\frac{d\phi}{dt} &= \varepsilon(H(-\phi) - H(\phi) + \Delta\omega) \\
&= \varepsilon(G(\phi) + \Delta\omega),
\end{aligned}
\tag{4.6.3}
$$

where $\Delta\omega = \omega_2 - \omega_1$. The fixed points of (4.6.3) are given by $G(\phi) = -\Delta\omega$.

The addition of the heterogeneity changes the phase-locking properties of the neurons. For example, suppose that in the absence of heterogeneity ($\Delta\omega = 0$) our G function is the same as in Figure 4.2.1, in which the synchronous solution, $\phi_S = 0$, and the anti-phase solution, ϕ_{AP}, are stable. Once heterogeneity is added, the effect will be to move the neurons away from either firing in synchrony or anti-phase to a constant asynchronous phase shift, as in Figure 4.6.1. For example, if neuron 1 is faster than neuron 2, then $\Delta\omega < 0$ and the stable steady-state phase-locked values of ϕ will be shifted to left of synchrony and to the left of anti-phase, as is seen in Figure 4.6.1 when $\Delta\omega = -0.5$. Thus, the neurons will still be phase-locked, but in an asynchronous state that will either be to the left of synchronous state or to the left of the anti-phase state depending on the initial conditions. Furthermore, if $\Delta\omega$ is decreased further, saddle node bifurcations occur in which a stable and unstable fixed point collide and annihilate each other.

4.6.2   Weakly Coupled Neurons with Noise

In this section, we show how two weakly coupled neurons with additive white noise in the voltage component can be analyzed using a probability density approach [54, 75].
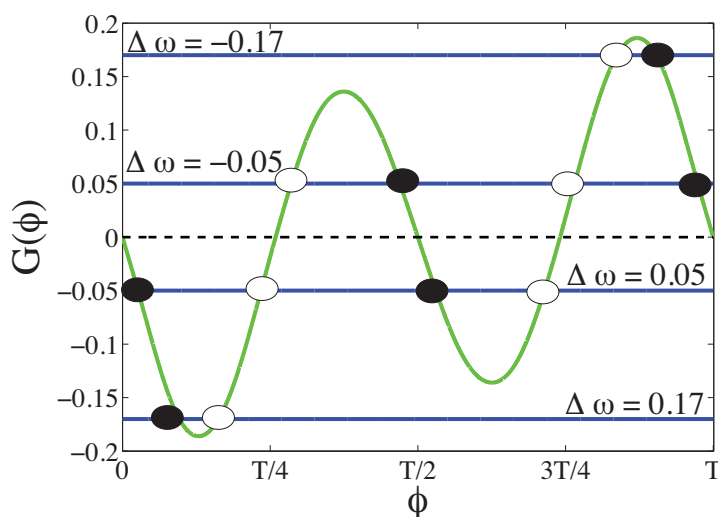
Figure 4.6.1: **Example G Function with Varying Heterogeneity**. Example of varying levels of heterogeneity with the same G function as in Figure 4.2.1. One can see that the addition of any level of heterogeneity will cause the stable steady-state phase-locked states to move to away from the synchronous and anti-phase states to asynchronous phase-locked states. Furthermore, if the heterogeneity is large enough, the stable steady-state phase-locked states will disappear completely through saddle node bifurcations.

The following set of differential equations represent two weakly heterogeneous neurons being perturbed with additive noise

$$\frac{dX_j}{dt} = F_j(X_j) + \varepsilon I(X_k, X_j) + \delta N_j(t), \quad i, j = 1, 2; i \neq j, \tag{4.6.4}$$

where δ scales the noise term to ensure that it is $\mathcal{O}(\varepsilon)$. The term $N_j(t)$ is a vector with Gaussian white noise, $\xi_j(t)$, with zero mean and unit variance (i.e. $\langle \xi_j(t) \rangle = 0$ and $\langle \xi_j(t) \xi_j(t') \rangle = \delta(t - t')$) in the voltage component, and zeros in the other variable components. In this case, the system can be mapped to the phase model

$$\frac{d\phi_j}{dt} = \varepsilon(\omega_j + H(\phi_k - \phi_j)) + \delta\sigma_\phi\xi_j(t), \tag{4.6.5}$$

where the term $\sigma_\phi = \left(\frac{1}{T}\int_0^T [Z(\tilde{t})]^2 d\tilde{t}\right)^{1/2}$ comes from averaging the noisy phase equations [54]. If we now let $\phi = \phi_2 - \phi_1$ we arrive at

$$\frac{d\phi}{dt} = \varepsilon(\Delta\omega + (H(-\phi) - H(\phi))) + \delta\sigma_\phi\eta(t), \tag{4.6.6}$$

where $\Delta\omega = \omega_2 - \omega_1$ and $\eta(t) = \xi_2(t) - \xi_1(t)$ is also Gaussian white noise with zero mean and unit variance.

This non-linear Langevin equation (4.6.6) corresponds to the Fokker-Planck equation [91, 100, 106]

$$\frac{\partial\rho}{\partial t}(\phi, t) = -\frac{\partial}{\partial\phi}[\varepsilon(\Delta\omega + G(\phi))\rho(\phi, t)] + (\delta\sigma_\phi)^2\frac{\partial^2\rho}{\partial\phi^2}(\phi, t), \tag{4.6.7}$$

where $\rho(\phi, t)$ is the probability that the neurons have a phase difference of ϕ at time t. The steady-state $\left(\frac{\partial\rho}{\partial t} = 0\right)$ solution of equation (4.6.7) is

$$\rho(\phi) = \frac{1}{N}e^{M(\phi)}\left[\frac{e^{-\alpha T\Delta\omega} - 1}{\int_0^T e^{-M(\bar{\phi})}d\bar{\phi}}\int_0^\phi e^{-M(\bar{\phi})}d\bar{\phi} + 1\right], \tag{4.6.8}$$

where

$$M(\phi) = \alpha\int_0^\phi (\Delta\omega + G(\bar{\phi}))d\bar{\phi}, \tag{4.6.9}$$

N is a normalization factor so that $\int_0^T \rho(\phi)d\phi = 1$, and $\alpha = \frac{\varepsilon}{\delta^2\sigma_\phi^2}$ represents the ratio of the strength of the coupling to the variance of the noise.

The steady-state distribution $\rho(\phi)$ tells us the probability that the two neurons

will have a phase difference of ϕ as time goes to infinity. Furthermore, Pfeuty et al. [75] showed that spike-train cross-correlogram of the two neurons is equivalent to the steady state distribution (4.6.8) for small ε. Figure 4.6.2 (a) shows the cross-correlogram for two identical neurons ($\Delta\omega = 0$) using the G function from Figure 4.2.1. One can see that there is a large peak in the distribution around the synchronous solution ($\phi_S = 0$), and a smaller peak around the anti-phase solution ($\phi_{AP} = T/2$). Thus, the presence of the noise works to smear out the probability distribution around the stable steady-states of the noiseless system.

(a) **(b)**
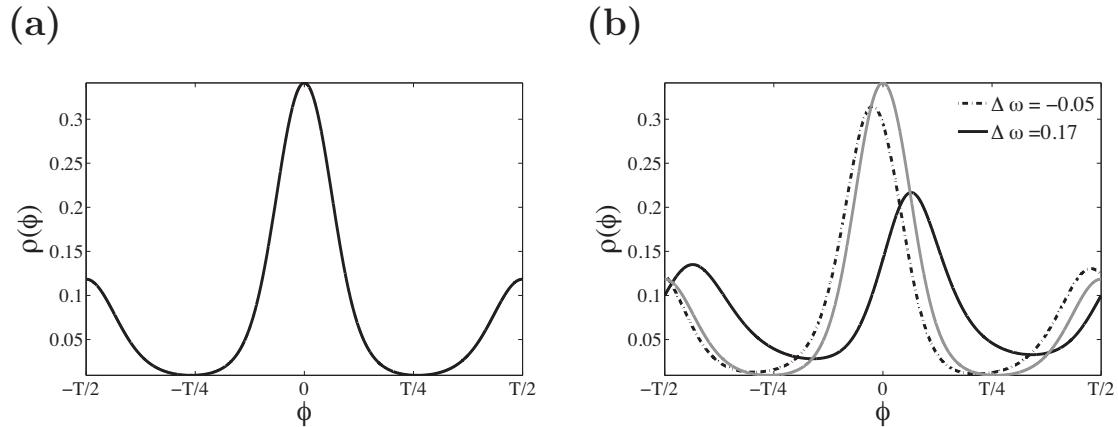
Figure 4.6.2: **The Steady-State Phase Difference Distribution $\rho(\phi)$ is the Cross-Correlogram for the Two Neurons**. (a) Cross-correlogram for the G function given in Figure 4.2.1 with $\alpha = 10$. Note that we have changed the x-axis so that ϕ now ranges from $-T/2$ to $T/2$. The cross-correlogram has two peaks corresponding to the synchronous and anti-phase phase-locked states. This is due to the fact that in the noiseless system, synchrony and anti-phase were the only stable fixed points. (b) Cross-correlograms for two levels of heterogeneity from Figure 4.6.1. The cross-correlogram from (a) is plotted as the light solid line for comparison. The peaks in the cross-correlogram have shifted to correspond with the stable asynchronous steady-states in Figure 4.6.1.

If heterogeneity is added to the G function as in Figure 4.6.1, one would expect that the peaks of the cross-correlogram would shift accordingly so as to correspond to the stable steady-states of the noiseless system. Figure 4.6.2 (b) shows that this is

indeed the case. If $\Delta\omega < 0$ ($\Delta\omega > 0$), the stable steady-states of the noiseless system shift to the left (right) of synchrony and to the left (right) of anti-phase, thus causing the peaks of the cross-correlogram to shift left (right) as well. If we were to increase (decrease) the noise, i.e. decrease (increase) α, then we would see that the variance of the peaks around the stable steady-states becomes larger (smaller), according to equation (4.6.8).

4.7 Networks of Weakly Coupled Neurons

In this section, we extend the phase model description to examine networks of weakly coupled neuronal oscillators.

Suppose we have a one spatial dimension network of M weakly coupled and weakly heterogeneous neurons

$$\frac{dX_i}{dt} = F_i(X_i) + \frac{\varepsilon}{M_0} \sum_{j=1}^{M} I(X_j, X_i), \quad i = 1, ..., M; \tag{4.7.1}$$

where M_0 is the maximum number of cells that any neuron is connected to and the factor of $\frac{1}{M_0}$ ensures that the perturbation from the coupling is $\mathcal{O}(\varepsilon)$. As before, this system can be reduced to the phase model

$$\frac{d\phi_i}{dt} = \omega_i + \frac{\varepsilon}{M_0} \sum_{j=1}^{M} w_{ij} H(\phi_j - \phi_i), \quad i = 1, ..., M. \tag{4.7.2}$$

where $W = \{w_{ij}\}$ is the connectivity matrix of the network. Thus, the pairwise phase models derived in the previous sections are easily extended to model networks of weakly coupled neuronal oscillators.

Because of the non-linear nature of equation (4.7.2), analytic solutions normally

cannot be found. Furthermore, it can be quite difficult to analyze for large numbers of neurons. Fortunately, there exists an approach to simplifying equation (4.7.2) so that mathematical analysis can be utilized, the so-called *continuum* approximation. This is not to say that simulating the system equation (4.7.2) is not useful. Depending upon the type of interaction function that is used, various types of interesting phase-locking behavior can be seen, such as total synchrony, traveling oscillatory waves, or, in two spatial dimensional networks, spiral waves and target patterns, e.g. [54, 33].

4.7.1   Continuum Limit

A powerful approach to analyzing (4.7.2) in the limit that M is very large is to assume that the network of neuronal oscillators forms a spatial continuum [30, 21, 12].

Suppose that we have a one-dimensional array of neurons in which the jth neuron occupies the position $x_j = j\Delta x$ where Δx is the spacing between the neurons. Further suppose that the connectivity matrix is defined by $W = \{w_{ij}\} = W(|x_j - x_i|)$, where $W(|x_j|) \to 0$ as $|x_j| \to \infty$ and $\sum_{j=-\infty}^{\infty} W(x_j)\Delta x = 1$ For example, the spatial connectivity matrix could correspond to a Gaussian function, $W(|x_j - x_i|) = e^{\frac{|x_j - x_i|^2}{2\sigma^2}}$, so that closer neurons have more strongly coupled to each other than to neurons that are further apart. We can now rewrite equation (4.7.2) as

$$\frac{d\phi}{dt}(x_i, t) = \omega(x_i) + \varepsilon \sum_{j=-\infty}^{\infty} \left[w(x_j - x_j) \, \Delta x \, H\left(\phi(x_j, t) - \phi(x_i, t)\right) \right], \, (4.7.3)$$

where $\phi(x_i, t) = \phi_i(t)$, $\omega(x_i) = \omega_i$ and we have taken $1/M = \Delta x$. By taking the limit of $\Delta x \to 0$ ($M \to \infty$) in equation (4.7.3), we arrive at the continuum phase model

$$\frac{\partial \phi}{\partial t}(x,t) = \omega(x) + \varepsilon \int_{-\infty}^{\infty} W(|x - \bar{x}|) \, H(\phi(\bar{x},t) - \phi(x,t)) \, d\bar{x}, \qquad (4.7.4)$$

where $\phi(x,t)$ is the phase of the oscillator at position x and time t.

Various authors have utilized this continuum approach to prove results about the stability of the synchrony and traveling wave solutions of equation (4.7.4) [30, 31, 21, 12]. For example, Crook et al. [21] were able to prove that presence of axonal delay in synaptic transmission between neurons can cause the onset of traveling wave solutions. This is due to the presence of axonal delay which encourages larger phase shifts between neurons that are further apart in space. Similarly, Bressloff and Coombes [12] derived the continuum phase model for a network of integrate-and-fire neurons coupled with excitatory synapses on their passive dendrites. Using this model, they were able to show that long range excitatory coupling can cause the system to undergo a bifurcation from the synchronous state to traveling oscillatory waves. For a rigorous mathematical treatment of the stability results for general continuum and discrete phase model neuronal networks, see [31].

4.8 Summary

In this chapter we have described the main mathematical tool that will be utilized in this dissertation, the theory of weakly coupled oscillators.

Chapter 5

Effects of Dendritic Load on the Firing Frequency of Oscillating Neurons

In this chapter, we study the effects of passive dendritic properties on the dynamics of neuronal oscillators. We find that the addition of a passive dendrite can sometimes have counter-intuitive effects on firing frequency. Specifically, the addition of a hyper-polarized passive dendritic load can either increase, decrease, or have negligible effects on firing frequency. We use the theory of weak coupling to derive phase equations for "ball-and-stick" model neurons and two-compartment model neurons. We then develop a framework for understanding how the addition of passive dendrites modulates the frequency of neuronal oscillators in terms of their phase response curves (PRC). We show that the average value of the neuronal oscillator's PRC measures the sensitivity to the dendritic load, including whether the addition of the dendrite causes an increase or decrease in firing frequency. We link this phenomenon to the

slope of the neuronal oscillator's frequency-applied current (*f-I*) curve. We also show that equivalent results exist for constant and noisy point source input to the dendrite. We note that the results are not specific to neurons but are applicable to any oscillator subject to a passive load.

5.1 Introduction

Neurons can have extensive spatial geometries, but they are often modeled as single-compartment objects that ignore the spatial anatomy of the cell. This simplification is made for mathematical tractability and computational efficiency. However, many neurons are not electrotonically compact, and single-compartment models cannot be expected to fully capture their behavior. Dendritic properties can have substantial effects on the dynamics of single neurons, as well as the activity in neuronal networks. For example, the architecture of a dendritic tree can alter the firing pattern and encoding properties of a neuronal oscillator [52, 56, 61] and dendritic filtering can change the phase-locking behavior in networks of neuronal oscillators [12, 20, 59]. Even the effects of dendrites without active ionic currents are not always straightforward. Intuitively, if the leakage reversal potential of the passive dendrite is lower than the average voltage of the oscillations, then the firing frequency of the neuronal oscillator will decrease with the addition of the dendrite (see Figure 5.4.1 (a)). Surprisingly, however, the passive hyperpolarizing dendritic "load" can sometimes increase a neuron's firing frequency (Figure 5.4.1 (b))[51, 96], or have very little effect on it (Figure 5.4.1 (c)).

In previous modeling and experimental work, Kepler et al. [51] and Sharp et al. [96] examined the influence of electrical coupling between a neuronal oscillator and a passive cell, which is analogous to a two-compartment model of a soma with

a passive dendrite [59]. They demonstrated that when the oscillator has a predominantly hyperpolarized membrane potential wave-form (i.e. a short duty-cycle), the electrical load of the passive cell acted to decrease the frequency of oscillations as the strength of the electrical coupling increased. On the other hand, when the oscillator had a predominantly depolarized membrane potential wave-form (i.e. a long duty-cycle), the electrical load of the passive cell acted to initially increase the frequency of oscillations as the strength of electrical coupling increased until the frequency reached a maximum and then decreased with further increase in coupling strength. In an analogous chemical oscillator system, Dolnik et al. [23] observed similar frequency modulation when properties of the chemical load were altered rather than the waveform of the isolated oscillator.

Here, we extend the results of Kepler et al. by developing a general framework to understand the mechanisms by which dendritic load properties and intrinsic somatic properties affect the firing frequency of the neuronal oscillator. We model a neuron as an isopotential somatic oscillator attached to a thin passive dendritic cable using the "ball-and-stick" model [80], and as an isopotential somatic oscillator compartment electrically coupled to a passive compartment, i.e. a two-compartment model (see Appendix 5.9). We use the theory of weak coupling [29, 54, 71] to derive an equation for the change in the firing frequency of the neuron due to the presence of the dendritic load. We then show how the frequency effects of adding a dendrite to a neuronal oscillator can be understood in terms of dendritic properties and the somatic oscillator's phase response curve. Finally, we link these effects to the shape of the oscillator's frequency-applied current (f-I) curve.

5.2 Ball-and-Stick Model Neuron

We model the electrical activity of a neuron using a "ball-and-stick" model [12, 20] (see also section 3.6) that consists of a spherical active isopotential soma attached to a single thin passive dendrite. The dendrite is modeled as a one-dimensional passive cable of physical length L [78, 84]

$$C_m \frac{\partial v}{\partial t} = \frac{a}{2R_C} \frac{\partial^2 v}{\partial x^2} - g_{LD}(v - E_{LD}), \quad x \in (0, L), \tag{5.2.1}$$

where $v(x, t)$ is the voltage of the dendrite in mV at position x and time t, g_{LD} is the leakage conductance in the dendrite in mS/cm^2, R_C is the cytoplasmic resistivity of the dendrite in $k\Omega \cdot cm$, a is the radius of the dendrite in cm, E_{LD} is the reversal potential of the leakage conductance in the dendrite in mV, and C_m is the membrane capacitance in $\mu F/cm^2$, which is assumed to be constant throughout the neuron.

Hodgkin-Huxley (HH) [44] type equations are used to model the electrical activity of the soma. An application of the conservation of current law at the junction connecting the spherical soma and the thin dendrite ($x = 0$) yields the proximal boundary condition

$$C_m \frac{\partial v}{\partial t}(0, t) = -I_{ion,S}(v(0), \vec{w}) + I + \frac{a^2}{d^2 R_C} \frac{\partial v}{\partial x}(0, t), \tag{5.2.2}$$

where $I_{ion,S}(v, \vec{w})$ represents the sum of the HH-type ionic currents (see appendix), $\vec{w}$ is a vector containing the gating variables of the ionic conductances, and d is the diameter of the soma in cm. The gating variables in the vector $\vec{w}$ are described

by equations of the form $\frac{d\vec{w}}{dt} = \frac{1}{\tau_{\vec{w}}}(\vec{w}_\infty(v) - \vec{w})$. The last term in equation (5.2.2) represents the axial current flowing from the dendrite into the soma. The parameter I is the somatic bias current in $\mu A/cm^2$. Note that changes in I are equivalent to changes in the leakage reversal potential, E_L, and therefore changes in I can be thought of as being due to current input into the soma or due to the effects of a neuromodulator. The values of I and E_L are chosen such that the isolated soma undergoes T-periodic (limit cycle) oscillations. We define $v_{LC}(t)$ to be the membrane potential component of the isolated somatic oscillator's limit cycle.

We assume that no current flows out the distal end of the dendrite, which yields the no flux boundary condition at the end of the dendrite $(x = L)$

$$\frac{\partial v}{\partial x}(L, t) = 0. \tag{5.2.3}$$

The Morris-Lecar model [67, 89] and a neuron model of Traub [47, 104] are used in the simulations presented here. However, similar results were obtained using several other model neurons [1, 27, 35, 44]. Furthermore, the basic analysis that we present here is general and can be applied to any oscillator.

The analysis in this paper relies on a certain combination of model parameters being sufficiently "small". To identify this small compound parameter, we nondimensionalize the model (5.2.1-5.2.3). We set $V = V(\bar{x}, \bar{t}) = \frac{v(\lambda\bar{x}, \tau_S\bar{t}) - E_L}{-E_L}$ (where E_L is the leakage reversal potential in the soma), $\bar{x} = \frac{x}{\lambda}$, $\bar{t} = \frac{t}{\tau_S}$, where $\lambda(a) = \sqrt{\frac{a}{2R_C g_{LD}}}$ is the length constant of the dendrite, and $\tau_S = \frac{C_m}{g_L}$ is the membrane time constant of the soma. The resulting nondimensional equations for the ball-and-stick model neuron are

$$\begin{cases} g\dfrac{\partial V}{\partial \bar{t}} = \dfrac{\partial^2 V}{\partial \bar{x}^2} - (V - \bar{E}_{LD}) \\[2mm] \dfrac{\partial V}{\partial \bar{t}}(0, \bar{t}) = -\bar{I}_{ion,S}(V(0, \bar{t}), \vec{w}) + \bar{I} + \varepsilon(a)\dfrac{\partial V}{\partial \bar{x}}(0, \bar{t}) \\[2mm] \dfrac{\partial V}{\partial \bar{x}}\left(\dfrac{L}{\lambda(a)}, \bar{t}\right) = 0. \end{cases} \quad (5.2.4)$$

where $g = \frac{g_L}{g_{LD}}$, $\bar{E}_{LD} = \frac{E_{LD}-E_L}{-E_L}$, $\bar{I}_{ion,S}(V(0, \bar{t}), \vec{w}) = \frac{1}{-g_L E_L}I_{ion,S}((-E_L)V(0, \bar{t}) +$
$E_L, \vec{w})$, $\bar{I} = \frac{1}{-g_L E_L}I$, and $\varepsilon(a) = \frac{a^2}{d^2 g_L R_C \lambda(a)}$. Also, $\frac{d\vec{w}}{dt} = \frac{1}{\tau_{\vec{w}}}(\vec{w}_\infty(v) - \vec{w})$ becomes
$\frac{d\vec{w}}{d\bar{t}} = \frac{\tau_S}{\tau_{\vec{w}}}(\vec{w}_\infty(-E_L V(0, \bar{t}) + E_L) - \vec{w})$. We define the nondimensionalized period of the
limit cycle to be $\bar{T} = \frac{T}{\tau_S}$, and the nondimensional voltage component of the isolated
soma's limit cycle as $V_{LC}(\bar{t})$.

The term $\varepsilon(a)\frac{\partial V}{\partial \bar{x}}(0, \bar{t})$ in equation (5.2.4) is the nondimensional axial current at the
soma-dendritic junction and is the dendrite's perturbation to the somatic membrane
dynamics. To ensure that this perturbation is weak, we assume that

$$\varepsilon(a) = \frac{a^2}{d^2 g_L R_C \lambda(a)} = \frac{a^2}{d^2}\sqrt{\frac{2g_{LD}}{g_L^2 R_C a}}$$

is small. Essentially, we assume that $a \ll d$, i.e. that the radius of the dendrite is
small relative to the diameter of the soma, and that $\sqrt{\frac{2g_{LD}}{g_L^2 R_C a}}$ is $\mathcal{O}(1)$ so that $\varepsilon(a) \ll 1$.

5.3 Theory of Weak Coupling and Reduction to a Phase Model

The theory of weak coupling [29, 54, 71] (see also Chapter 4), has been widely used to
analyze dynamics in networks of oscillating neurons (e.g. [32, 46, 58, 74]). The theory

can also be used to analyze the dynamics of neurons under the influence of an external forcing. When this perturbing current to an individual neuron is sufficiently weak, the complete state of the neuron can be approximated by its phase on its $\bar{T}$-periodic limit cycle, $\theta(\bar{t}) \in [0, 1)$. Furthermore, the evolution of the neuronal oscillator's phase is governed by its phase-equation

$$\frac{d\theta}{d\bar{t}} = \bar{\omega} + \Delta\bar{\omega} = \bar{\omega} + \frac{1}{\bar{T}} \int_0^{\bar{T}} Z(s)I_{pert}(s)ds, \tag{5.3.1}$$

where $\frac{d\theta}{d\bar{t}}$ is the instantaneous nondimensional frequency of the neuron, and $\bar{\omega} = \frac{1}{\bar{T}}$ is the nondimensional frequency of the isolated (unperturbed) somatic oscillator. $I_{pert}(s)$ is a nondimensional $\bar{T}$-periodic perturbing current that can be thought of as arising from coupling or external input. $Z(s)$ is the nondimensional infinitesimal phase response curve (PRC) of the neuronal oscillator. The PRC quantifies the change in phase due to a δ-function current perturbation at a particular phase on the limit cycle. The PRC can be thought of as a Green's function or impulse response function for a linear oscillator. $\Delta\bar{\omega} = \frac{1}{\bar{T}} \int_0^{\bar{T}} Z(s)I_{pert}(s)ds$ represents the modulation of the isolated oscillator's frequency due to the external current averaged over one period of the oscillations.

The theory of weak coupling can be applied to the ball-and-stick model by considering the dendritic load as the perturbation to the soma, following Crook et al. [20]. During steady oscillations in the ball-and-stick model, a $\bar{T}$-periodic current flows between the soma and dendrite, modulating the intrinsic oscillations of the soma. Therefore, we set $I_{pert}(s) = \varepsilon(a)\frac{\partial V}{\partial \bar{x}}(0, s)$, which is the (nondimensional) current at the soma-dendritic junction. As long as this modulating current is sufficiently weak, the dynamics of the ball-and-stick model can be reduced to the phase model

$$\frac{d\theta}{d\bar{t}} = \bar{\omega} + \frac{1}{\bar{T}} \int_0^{\bar{T}} Z(s)\varepsilon(a)\frac{\partial V}{\partial \bar{x}}(0,s)ds. \tag{5.3.2}$$

In order to close equation (5.3.2), $\frac{\partial V}{\partial \bar{x}}(0,\bar{t})$ needs to be determined. Using our assumption that $\varepsilon(a) \ll 1$, we can find a leading order approximation of $\frac{\partial V}{\partial \bar{x}}(0,\bar{t})$. Because the dendritic perturbation is weak, the soma clings tightly to its limit cycle so that $V(0,\bar{t}) \simeq V_{LC}(\bar{t})$.

This approximation simplifies the boundary condition at the soma ($\bar{x} = 0$) and yields the leading order approximation for the system (5.2.4)

$$\begin{cases} g\dfrac{\partial V}{\partial \bar{t}} = \dfrac{\partial^2 V}{\partial \bar{x}^2} - (V - \bar{E}_{LD}) \\[2mm] V(0,\bar{t}) = V_{LC}(\bar{t}) \\[2mm] \dfrac{\partial V}{\partial \bar{x}}\left(\dfrac{L}{\lambda(a)}, \bar{t}\right) = 0. \end{cases} \tag{5.3.3}$$

System (5.3.3) is a first-order linear partial differential equation with $\bar{T}$-periodic forcing at one end, and the solution can be found using Fourier series. Expanding the somatic potential in a Fourier series, $V_{LC}(\bar{t}) = \frac{1}{\bar{T}}\sum_{n\in\mathbb{Z}} V_n e^{2\pi in\bar{t}/\bar{T}}$, and solving system (5.3.3) yields

$$\begin{aligned} V(\bar{x},\bar{t}) &= \left(\frac{V_0}{\bar{T}} - \bar{E}_{LD}\right)\frac{\cosh\left(\bar{x} - \frac{L}{\lambda(a)}\right)}{\cosh\left(\frac{L}{\lambda(a)}\right)} + \frac{1}{\bar{T}}\sum_{n\neq 0} V_n \frac{\cosh\left(b_n\left(\bar{x} - \frac{L}{\lambda(a)}\right)\right)}{\cosh\left(b_n\left(\frac{L}{\lambda(a)}\right)\right)}e^{2\pi in\bar{t}/\bar{T}} \\ &\quad + \bar{E}_{LD}, \end{aligned} \tag{5.3.4}$$

where $b_n = \sqrt{1 + g2\pi in/\bar{T}}$. Differentiating equation (5.3.4) with respect to $\bar{x}$ and

evaluating at $\bar{x} = 0$ gives

$$\frac{\partial V}{\partial \bar{x}}(0, \bar{t}) = \left(\bar{E}_{LD} - \frac{V_0}{\bar{T}} \right) c_0(a) - \frac{1}{\bar{T}} \sum_{n \neq 0} c_n(a) V_n e^{2\pi i n \bar{t}/\bar{T}}, \tag{5.3.5}$$

where $c_n(a) = b_n \tanh \left(b_n \frac{L}{\lambda(a)} \right)$. Note that $c_n(a)$ are complex numbers that capture the "filtering" effects of the dendrite.

Substituting this expression for $\frac{\partial V}{\partial \bar{x}}(0, \bar{t})$ back into equation (5.3.2) and expanding the PRC in a Fourier series, $Z(\bar{t}) = \frac{1}{\bar{T}} \sum_{m \in \mathbb{Z}} Z_m e^{2\pi i m \bar{t}/\bar{T}}$, yields the phase model for the ball-and-stick model

$$
\begin{aligned}
\frac{d\theta}{d\bar{t}} &= \bar{\omega} + \Delta\bar{\omega} \\
&= \bar{\omega} + \varepsilon(a) \left[\frac{Z_0}{\bar{T}} \left(\bar{E}_{LD} - \frac{V_0}{\bar{T}} \right) c_0(a) - \frac{1}{\bar{T}^2} \sum_{n \neq 0} Z_{-n} V_n c_n(a) \right] \\
&= \bar{\omega} \\
&\quad + \varepsilon(a) \left[\frac{Z_0}{\bar{T}} \left(\bar{E}_{LD} - \frac{V_0}{\bar{T}} \right) c_0(a) - \frac{2}{\bar{T}^2} \sum_{n=1}^{\infty} |Z_n V_n c_n(a)| \cos(\psi_n(a) + \gamma_n - \phi_n) \right],
\end{aligned}
\tag{5.3.6}
$$

where $\psi_n(a)$, γ_n, and ϕ_{-n} are the angles, in radians, corresponding to $c_n(a)$, V_n, and Z_{-n}, respectively.

Below, we will analyze the phase model in order to understand how the addition of the thin passive dendrite alters the frequency of the somatic oscillator. For convenience of physiological interpretation, the values of all quantities are reported in dimensional terms in the results section. The phase model in dimensional terms is

$$
\begin{aligned}
\frac{d\theta}{dt} &= \omega + \Delta\omega \\
&= \omega \\
&\quad + \frac{\varepsilon(a)}{\tau_S}\left[\langle z \rangle (E_{LD} - \langle v_{LC}\rangle)c_0(a) - \frac{2}{T^2}\sum_{n=1}^{\infty}|z_n v_n c_n(a)|\cos(\psi_n(a) + \gamma_n - \phi_n)\right],
\end{aligned}
$$

$$(5.3.7)$$

where v_n and z_n are the Fourier coefficients of the membrane potential oscillations $v_{LC}(t)$ and the dimensional PRC $z(t)$, respectively, and $\langle v_{LC}\rangle = v_0/T$ and $\langle z \rangle = z_0/T$ are the mean values of $v_{LC}(t)$ and $z(t)$, respectively.

In Appendix 5.10 we show how input from point sources on the dendrite can be incorporated into equation (5.3.7) and demonstrate that including point sources with constant input is equivalent to changing E_{LD}. Furthermore, we show that this result holds for noisy input when the correlation time of the noise is sufficiently large.

5.4 Results

In this section, we examine the dependence of firing frequency of the ball-and-stick neuron on the magnitude of the dendritic perturbation $\varepsilon(a)$ and the value of E_{LD}. We emphasize the fact that changes in the bias current, I, can be thought of as either changes in the leakage reversal potential of the soma, E_L or current input to the soma; also changes in the leakage reversal potential of the dendrite, E_{LD}, can be thought of as arising from either global changes in dendritic leakage reversal potential, or point source synaptic inputs to the dendrite (Appendix 5.10). First, we observe the behavior of the simulated model equations (5.2.1-5.2.3), and we show

that this behavior is well approximated by the phase model (5.3.7). We then interpret this behavior in terms of the biophysical quantities in equation (5.3.7): $\langle z \rangle$, $\langle v_{LC} \rangle$, E_{LD}, $\varepsilon(a)$, $c_n(a)$, v_n, and z_n. Lastly, we illustrate a connection between two intrinsic properties of the isolated neuronal oscillator: the frequency-applied current curve and the average value of the PRC.

In all simulations, unless otherwise indicated, somatic dynamics are modeled by the Morris-Lecar equations with parameters given in the Appendix. We also view an increase in $\varepsilon(a)$ as an increase in the dendritic radius a. Note, however, that an increase in a also results in an increase the dendritic space constant, $\lambda(a)$.

5.4.1 Simulations: Passive Dendritic Load Can Either Increase or Decrease Firing Frequency

Figure 5.4.1 plots the somatic voltage traces for two different values of applied current to the soma, $I = 6.4 \ \mu A/cm^2$ (Figure 5.4.1(a)) and $I = 22.4 \ \mu A/cm^2$ (Figure 5.4.1(b)). For both cases, E_{LD} is set to $-60 \ mV$, which is hyperpolarized relative to the somatic membrane potential. Intuitively, we expect that the hyperpolarizing dendritic load should decrease the frequency of the oscillations. This is clearly the case in Figure 5.4.1(a) in which the frequency of the isolated somatic oscillator is greater than the frequency of the oscillator attached to the dendrite. However, in Figure 5.4.1(b), the frequency of the isolated somatic oscillator is lower than the frequency when the somatic oscillator is attached to the dendrite. Furthermore, the frequency of the oscillator can remain unchanged (Figure 5.4.1 (c)) due to the addition of the dendrite. Thus, simply by varying the current applied to the soma, the hyperpolarizing dendritic load can have a decelerating, accelerating, or negligible effect on the frequency of oscillations. As mentioned earlier, this phenomenon is sim-

ilar to what Kepler et al. [51] observed in a model of a neuronal oscillator electrically coupled to a passive cell.

Figure 5.4.2 shows the change in firing frequency of the full ball-and-stick model (dotted line) as a function of $\varepsilon(a)$ with $I = 6.4\ \mu A/cm^2$ and $I = 22.4\ \mu A/cm^2$ for two different values of E_{LD}. For a relatively hyperpolarized value of E_{LD} $(-75\ mV)$, the frequency of oscillations decreases as $\varepsilon(a)$ is increased for $I = 6.4\ \mu A/cm^2$ (Figure 5.4.2 (a)), but the frequency increases as $\varepsilon(a)$ is increased for $I = 22.4\ \mu A/cm^2$ (Figure 5.4.2 (a)). This agrees with the behavior seen in Figure 5.4.1. When the value of E_{LD} is relatively depolarized (i.e. $E_{LD} = 25\ mV$, which is close to the peak of the somatic voltage), the results are reversed. That is, the frequency of oscillations increases as $\varepsilon(a)$ is increased for $I = 6.4\ \mu A/cm^2$ and decreases as $\varepsilon(a)$ is increased for $I = 22.4\ \mu A/cm^2$. Thus, the results in Figure 5.4.2(a) agree with our intuition about the effects of dendritic load: when the leakage reversal potential of the dendrite is hyperpolarized (depolarized) relative to the somatic voltage oscillations, the frequency of oscillations is decreased (increased) as the strength of the dendritic perturbation is increased. However, Figure 5.4.2(b) shows that by changing the intrinsic period of the somatic oscillator, the addition of a passive hyperpolarizing dendrite load can have a counter-intuitive effect and increase the frequency of oscillations.

5.4.2 Mechanisms for Frequency Changes: Insights from the Phase Model

The phase model quantitatively captures the behavior of the full model for sufficiently small values of $\varepsilon(a)$, and Figure 5.4.2 shows that it can also capture the qualitative behavior for moderate values of $\varepsilon(a)$. Therefore, we can use the phase model to explain the effects of dendritic load on firing frequency in terms of cable properties

(a)

(b)

(c)
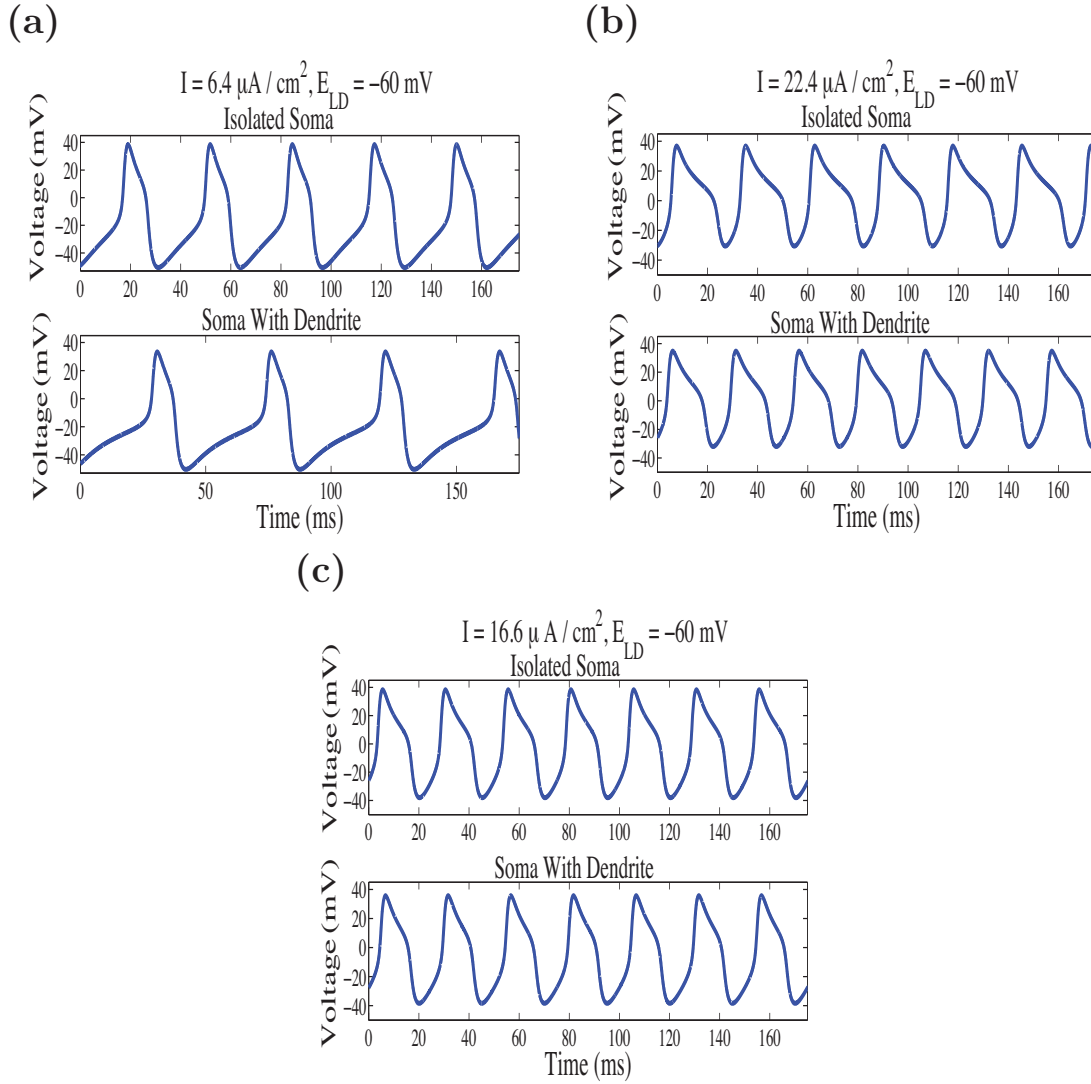
Figure 5.4.1: **The addition of a hyperpolarized dendrite can decrease, increase, or not change firing frequency**. Voltage traces for a Morris-Lecar neuron without a dendritic cable (an isolated soma, $\varepsilon(a) = 0$) and with a passive dendritic cable ($\varepsilon(a) = 0.25$) for three different values of applied current to the soma: (a) $I = 6.4\ \mu A/cm^2$, (b) $I = 22.4\ \mu A/cm^2$, and (c) $I = 16.6\ \mu A/cm^2$. In all cases, the dendritic leakage reversal potential E_{LD} is held at $-60\ mV$, which is hyperpolarized relative to the voltage oscillations. However, the frequency of the somatic oscillator decreases in (a), increases in (b), and changes by a negligible amount in (c).

(a) $I = 6.4 \ \mu A/cm^2$

(b) $I = 22.4 \ \mu A/cm^2$
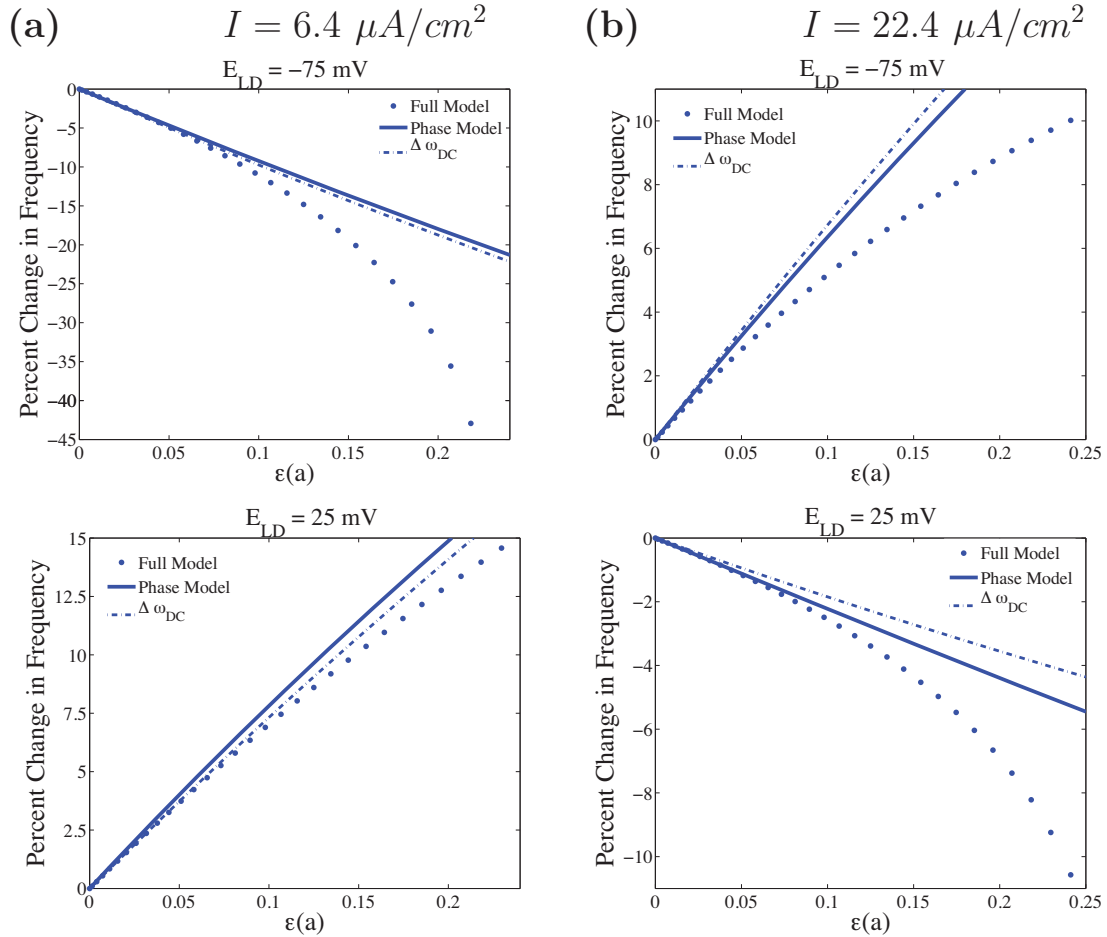
Figure 5.4.2: **Firing frequency can either increase or decrease as a function of increasing magnitude of the dendritic perturbation, $\varepsilon(a)$, depending upon the value of the dendritic leakage reversal potential and the applied current at the soma**. Percent change in firing frequency is plotted as a function of the strength of the dendritic perturbation, $\varepsilon(a)$, for hyperpolarized ($-75 \ mV$) and depolarized ($25 \ mV$) values of E_{LD} when (a) $I = 6.4 \ \mu A/cm^2$ and (b) $I = 22.4 \ \mu A/cm^2$. The dots represent results from simulations of the full ball-and-stick model, equations (5.2.1-5.2.3), the solid line represents results from simulations of the phase model, equation (5.3.7), and the dash-dotted line represents $\Delta\omega_{DC}$, equation (5.4.1). In (a), the addition of the dendrite with a hyperpolarized (depolarized) leakage reversal potential decrease (increases) the frequency of oscillations as $\varepsilon(a)$ is increased. In (b), we see the opposite effect: the addition of the dendrite with a hyperpolarized (depolarized) leakage reversal potential increases (decreases) the frequency of oscillations as $\varepsilon(a)$ is increased. Note that, for all four plots, $\Delta\omega_{DC}$ captures the tendency for the frequency to increase or decrease as a function of $\varepsilon(a)$.

and intrinsic properties of the neuronal oscillator. To do this, it is useful to emphasize the split in the frequency modulation term of the phase model $\Delta\omega$ into the DC ($n = 0$) component $\Delta\omega_{DC}$ and the AC ($n \neq 0$) component $\Delta\omega_{AC}$. That is, $\Delta\omega = \Delta\omega_{DC} + \Delta\omega_{AC}$, where

$$\Delta\omega_{DC} = \frac{\varepsilon(a)}{\tau_S}\langle z\rangle(E_{LD} - \langle v_{LC}\rangle)c_0(a) \tag{5.4.1}$$

$$\Delta\omega_{AC} = -\frac{\varepsilon(a)}{\tau_S}\frac{2}{T^2}\sum_{n=1}^{\infty}|z_n v_n c_n(a)|\cos(\psi_n(a) + \gamma_n - \phi_n). \tag{5.4.2}$$

Note that the DC components $\Delta\omega_{DC}$ corresponding to the examples depicted in Figure 5.4.2 accurately capture the tendency for the frequency to increase or decrease as a function of $\varepsilon(a)$. Given that the DC component plays the dominant role in determining the frequency modulation, equation (5.4.1) reveals the mechanisms underlying the phenomena described in the previous sections. Specifically, the tendency for the frequency of the oscillations to increase or decrease as a function of $\varepsilon(a)$ is determined by the sign of the product of $\langle z\rangle$ and $(E_{LD} - \langle v_{LC}\rangle)$. (Note that $c_0(a)$ is real and positive). In Figure 5.4.3, it can be seen that (a) for $I = 6.4\ \mu A/cm^2$, the average value of the PRC is positive ($\langle z\rangle = 0.0027\ mV^{-1}$) , whereas (b) for $I = 22.4$ $\mu A/cm^2$, the average value of the PRC is negative ($\langle z\rangle = -0.0016\ mV^{-1}$). Therefore, when E_{LD} is less than $\langle v_{LC}\rangle$ (i.e the dendritic load is hyperpolarizing), the frequency of oscillations decreases in case (a) but increases in case (b) as $\varepsilon(a)$ increases. When E_{LD} is greater than $\langle v_{LC}\rangle$, the results are reversed. This simple explanation accounts for all of the behavior in Figure 5.4.2, and it will hold in general whenever $\Delta\omega_{DC}$ is the dominant term in $\Delta\omega$, i.e. whenever $\langle z\rangle$ is not close to zero and/or $\langle v_{LC}\rangle$ is not close to E_{LD}.

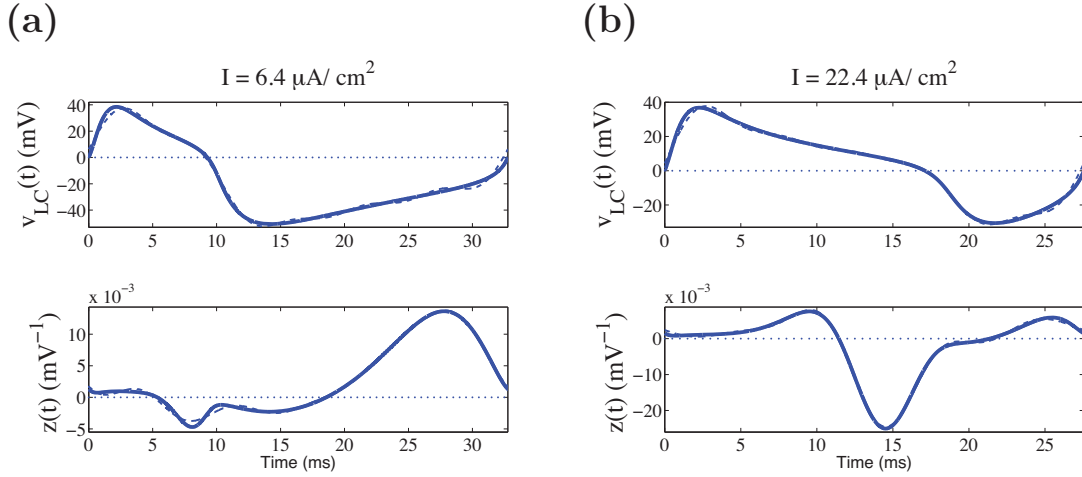**(a)**   **(b)**

Figure 5.4.3: **Voltage component of the limit cycle for the Morris-Lecar neuron and its corresponding phase response curve.** (a) $I = 6.4\ \mu A/cm^2$ and (b) $I = 22.4\ \mu A/cm^2$. The oscillator in (a) has a positive average value of its phase response curve $\langle z \rangle = 0.0027\ mV^{-1}$ and a mean membrane potential of $\langle v_{LC} \rangle = -17.9$ mV, while the oscillator in (b) has $\langle z \rangle = -.0016\ mV^{-1}$ and $\langle v_{LC} \rangle = 3.5\ mV$. The dashed line in all plots is the approximation to the function using the first five Fourier modes in its expansion.

$\Delta\omega_{DC}$ (equation (5.4.1)) predicts that the effect of the dendritic load will switch between decelerating and accelerating as E_{LD} crosses $\langle v_{LC} \rangle$. Figure 5.4.4 plots the change in firing frequency as a function of E_{LD} for the full model (dotted line), the phase model (solid line), and the $\Delta\omega_{DC}$ prediction (dash line) for three different applied currents: (a) $I = 6.4\ \mu A/cm^2$ where $\langle z \rangle > 0$, (b) $I = 22.4\ \mu A/cm^2$ where $\langle z \rangle < 0$, and (c) $I = 16.6\ \mu A/cm^2$ where $\langle z \rangle$ is negative but is two orders of magnitude smaller than that in (b). As expected from the signs of $\langle z \rangle$, the dendritic load changes from having a decelerating effect to an accelerating effect in case (a) and an accelerating effect to a decelerating effect in case (b) as E_{LD} is increased. $\Delta\omega_{DC}$ predicts that the switch occurs at $\langle v_{LC} \rangle = -17.9\ mV$ for (a) and $\langle v_{LC} \rangle = 3.5\ mV$ for (b). These are close to the actual switching points, which are $E_{LD} \sim -22\ mV$ in (a) and $E_{LD} \sim 0\ mV$ in (b). Note that $\langle z \rangle$ does not only predict the increase/decrease

in frequency, but it is also a measure of the sensitivity of the neuronal oscillator to the dendritic load.

In the cases portrayed in Figure 5.4.4(a) and Figure 5.4.4(b), $\Delta\omega_{DC}$ does an excellent job of predicting both the sign and magnitude of the change in frequency over a broad range of E_{LD}. However, as E_{LD} approaches $\langle v_{LC} \rangle$, the magnitude of the DC component becomes smaller than the AC component. As a consequence, $\Delta\omega_{DC}$ incorrectly predicts the sign of frequency change in the interval between the actual and the predicted switching points. The size of this "interval of error" for the DC prediction is

$$|E_{LD} - \langle v_{LC} \rangle| = \frac{\tau_S}{\varepsilon(a)} \frac{\Delta\omega_{AC}}{\langle z \rangle \, c_0(a)} = \frac{\frac{2}{T^2} \sum_{n=1}^{\infty} |z_n v_n c_n(a)| \cos(\psi_n(a) + \gamma_n - \phi_n)}{\langle z \rangle \, c_0(a)}. \quad (5.4.3)$$

The relative magnitude of $\langle z \rangle$ as compared to the AC component in the cases in Figure 5.4.4 (a) and (b) is small and makes the interval of error small (3.5 and 3.8 mV respectively). However, for different parameters, $\langle z \rangle$ can be relatively small and $\Delta\omega_{AC}$ can be the dominant term in $\Delta\omega$. This can cause the interval of error to be large. For example, in Figure 5.4.4(c), where $\langle z \rangle = -4.31 \times 10^{-5} \, mV^{-1}$, the size of the interval of error is 132.6 mV.

Over the range of applied currents tested (4.4-23.6 $\mu A/cm^2$), $\langle z \rangle$ monotonically decreases from 0.0074 to $-0.0036 \, mV^{-1}$, and the magnitude of the normalized AC components $\left| \frac{\Delta\omega_{AC}}{\varepsilon(a)} \right|$ ranges from 0.0059 to 0.027 for $a = 2 \times 10^{-6} \, cm$ ($\epsilon(a) = 0.01118$). Furthermore, $c_0(a) \sim 1$ and the magnitude of the normalized AC components $\frac{\Delta\omega_{AC}}{\varepsilon(a)}$ has a weak dependence on a for the parameters that we considered (i.e. $T \gg \tau_S$ and $L > 1.5\lambda(a)$, see appendix C). As a result, the size of the interval of error for the DC prediction ranges from less than 1 mV near the edges of the applied current range

to infinite when $\langle z \rangle = 0$ near $I = 16 \ \mu A/cm^2$. The range of the applied current over which the size of the interval of error was greater than $20 \ mV$ is 14.4 to 17.6 $\mu A/cm^2$. Within this range, the frequency modulation is primarily due to the AC component and is very weak, i.e. $\Delta \omega$ is on the order of $0.01 \varepsilon(a)$. The dependence of frequency modulation on E_{LD} in this range is also very weak, as is seen in Figures 5.4.4(c) and 5.4.5 and by the fact that $\Delta \omega_{AC}$ is independent of E_{LD}.

5.4.3 Average Value of PRC and Frequency-Applied Current (*f-I*) Curve

The above results describe the mechanisms of frequency modulation due to the dendrite in terms of the average value of the phase response curve $\langle z \rangle$, which is not a commonly considered quantity. Here, we derive the relationship between the familiar frequency-applied current (*f-I*) curve and the average value of the oscillator's phase response curve, and we then link to this relationship back to the frequency effects of the passive dendrite on neuronal oscillations.

Consider an isolated neuronal oscillator subjected to a constant applied current I, and suppose that $\omega(I)$ and $Z(s; I)$ are parameterizations of the frequency and PRC of the oscillator in terms of the applied current. Now suppose that applied current is increased by a small amount ΔI. According to the theory of weak coupling, the new frequency of the oscillator is

$$\omega(I + \Delta I) = \frac{d\theta}{dt} \quad \simeq \quad \omega(I) + \frac{1}{T} \int_0^T Z(s; I) \frac{\Delta I}{C_m} ds \qquad (5.4.4)$$

$$= \quad \omega(I) + \langle z(\cdot; I) \rangle \frac{\Delta I}{C_m}, \qquad (5.4.5)$$
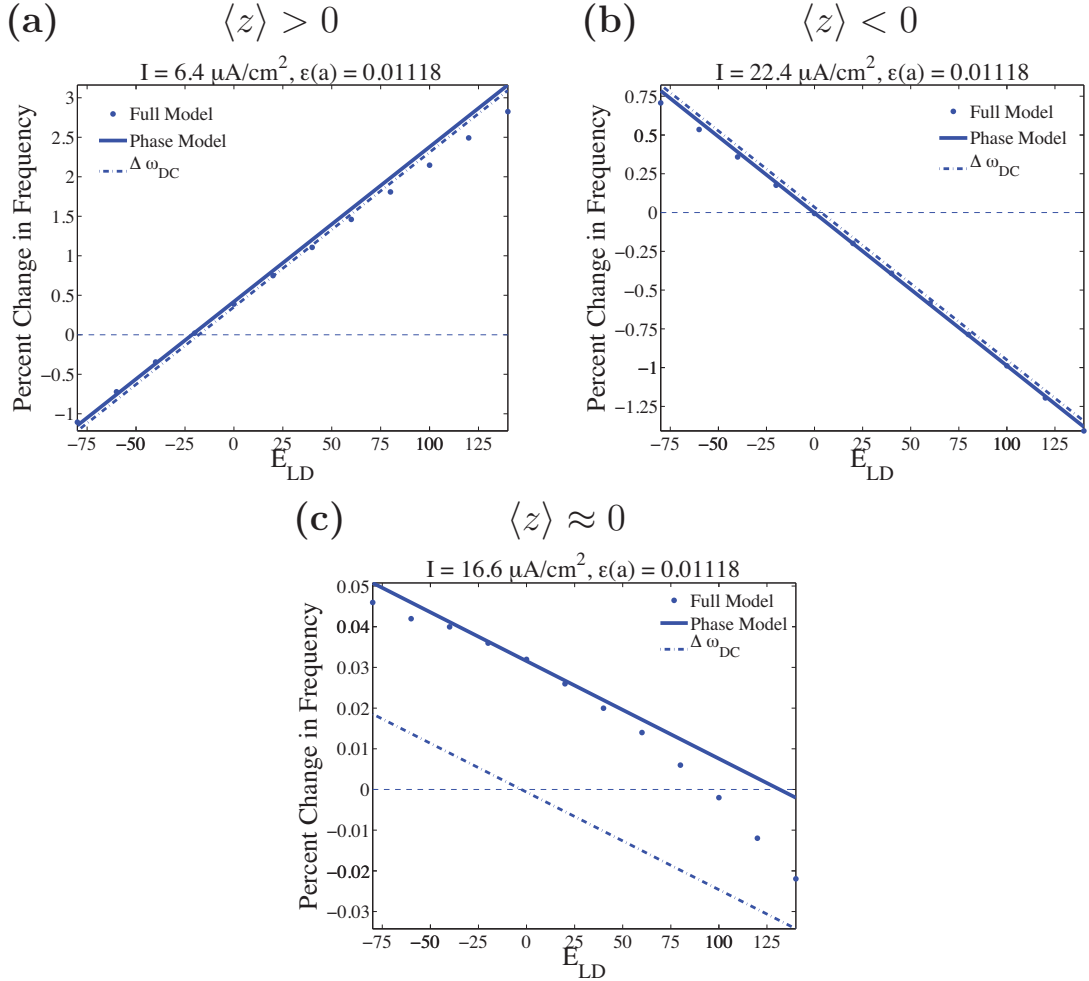
Figure 5.4.4: **Dendritic load switches its effect on frequency as the dendritic leakage reversal potential is increased**. Percent change in firing frequency is plotted as a function of the dendritic leakage reversal potential, E_{LD}, for fixed $\varepsilon(a) = 0.01118$ when (a) $\langle z \rangle > 0$, (b) $\langle z \rangle < 0$, and (c) $\langle z \rangle \approx 0$ ($I = 16.6\ \mu A/cm^2$ and $\langle z \rangle = -4.31 \times 10^{-5}\ mV^{-1}$). The dots represent simulations of full ball-and-stick model (equations (5.2.1-5.2.3)), the solid line represents simulations of the phase equation (5.3.7), and the dash-dotted line represents $\Delta \omega_{DC}$ (equation (5.4.1)). In (a), the dendritic load switches from having a decelerating effect on frequency to an accelerating effect as E_{LD} is increased. While in (b), the dendritic load switches from having an accelerating effect on frequency to a decelerating effect as E_{LD} is increased. In both cases, the 'interval of error' in which $\Delta \omega_{DC}$ incorrectly predicts the sign of frequency change is small, and $\Delta \omega_{DC}$ remains close to the full phase model prediction. When $\langle z \rangle \approx 0$ as in (c), the interval of error is considerably larger. However, the frequency modulation effects are much smaller in (c) than in either (a) or (b).
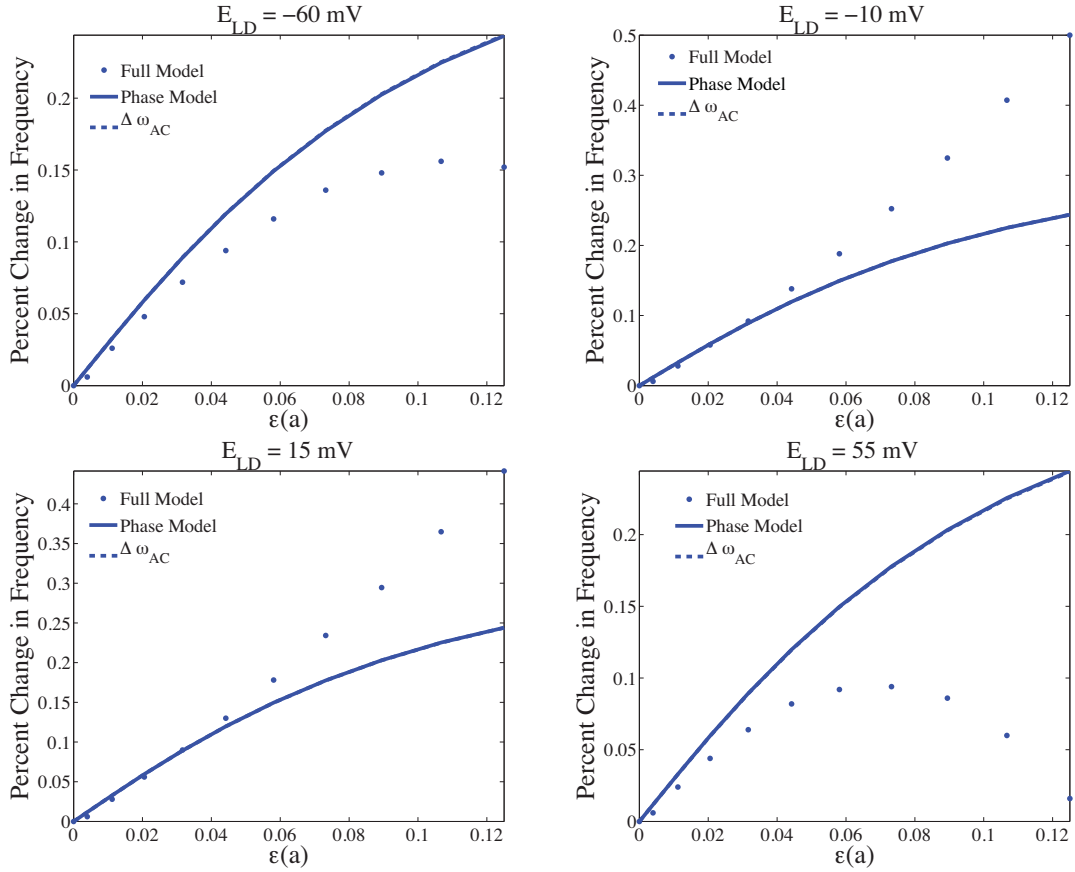
Figure 5.4.5: **When the average value of the PRC $\langle z \rangle \approx 0$, $\Delta\omega_{AC}$ dominates the behavior of the phase model**. Percent change in firing frequency is plotted as a function of $\varepsilon(a)$ when $\langle z \rangle \approx 0$ ($I = 16.32 \, \mu A/cm^2$ and $\langle z \rangle = 1.39 \times 10^{-7} \, mV^{-1}$). The dots represent simulations of full ball-and-stick model (equations (5.2.1-5.2.3)). The simulations of the phase equation (5.3.7) (solid line) and $\Delta\omega_{AC}$ (equations (5.4.1)) (the dashed line) overlap for the four values of the dendritic leakage reversal potential E_{LD}, indictating that $\Delta\omega \simeq \Delta\omega_{AC}$ in this case. This is due to the fact that $\Delta\omega_{DC}$ is close to zero as $\langle z \rangle \approx 0$. Also, because $\Delta\omega_{AC}$ is independent of E_{LD}, the phase model behavior remains virtually unchanged for the four different values of E_{LD}. Note that the frequency modulation effects of the dendrite are smaller than those seen in Figure 5.4.2.

where $\langle z(\cdot; I) \rangle$ denotes the average of the PRC over one period of the oscillations which is parameterized by the bias current I.

Rearranging equation (5.4.5) yields the relationship between the change in the frequency of an oscillator due to the additional applied current and average value of the oscillator's PRC

$$\frac{d\omega}{dI} \simeq \frac{1}{C_m} \frac{\omega(I + \Delta I) - \omega(I)}{\Delta I} = \frac{1}{C_m} \langle z(\cdot; I) \rangle. \qquad (5.4.6)$$

Thus, the average value of an oscillator's phase response curve for a particular value of applied current normalized by the membrane capacitance is equivalent to the instantaneous slope of the oscillator's *f-I* curve at that particular applied current value. That is, $\langle z \rangle$ is a measure of the sensitivity of the neuron to constant input and is proportional to the gain of the neuron. (Note that the right-hand side of equation (5.4.5) is a Taylor series of $\omega(I + \Delta I)$ with $\frac{d\omega}{dI} = \frac{\langle z(\cdot; I) \rangle}{C_m}$).

In the typical case where the DC-component $\Delta\omega_{DC}$ dominates the effect of the dendrite on firing frequency, we can subsitute $C_m \frac{d\omega}{dI}$ for $\langle z(\cdot; I) \rangle$ into equation (5.4.1) to obtain

$$\frac{d\theta}{dt} \simeq \omega + \frac{\varepsilon(a)}{\tau_S} C_m \frac{d\omega}{dI} (E_{LD} - \langle v_{LC} \rangle) c_0(a) \qquad (5.4.7)$$

$$\simeq \omega + \frac{d\omega}{dI} \varepsilon(a) g_L (E_{LD} - \langle v_{LC} \rangle) c_0(a). \qquad (5.4.8)$$

That is, the change in frequency of a neuronal oscillator due to the addition of a passive dendrite is simply given by the product of the average axial current flowing between the dendrite and the soma (i.e. a *constant* current) and the instantaneous

slope of the neuronal oscillator's *f-I* curve.

Figure 5.4.6(a) illustrates the relationship between the *f-I* curve, it's derivative and the average of the PRC $\langle z \rangle$ for the isolated Morris-Lecar neuron (i.e. the soma) as a function of applied current. For this model neuron, the *f-I* curve is non-monotonic: the frequency initially increases with increasing current, but the frequency reaches a maximum and then decreases with increasing current. As a result, the addition of a strictly hyperpolarizing dendritic load will lead to an decrease in firing frequency for relatively low applied currents, but there will be a "counter-intuitive" increase in firing frequency for relatively high applied currents, as shown in Figure 5.4.6(b).

(a)

(b)
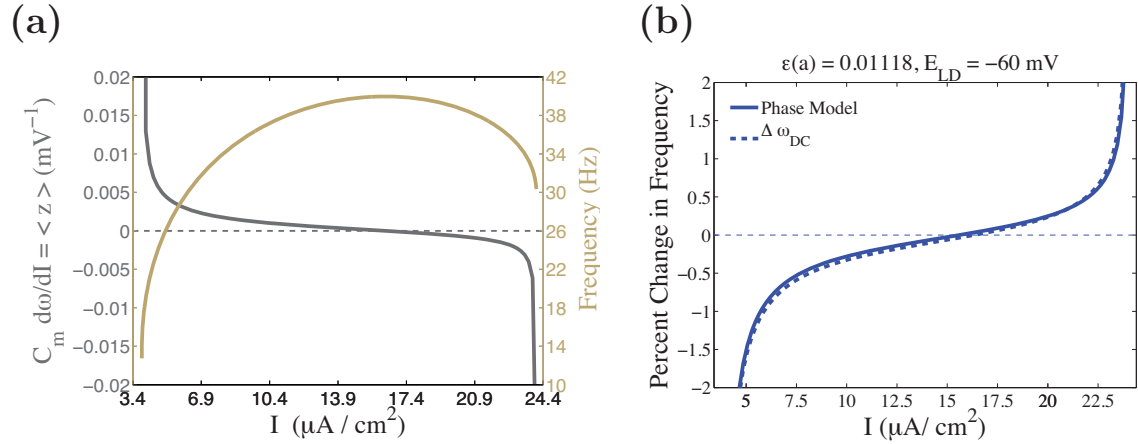
Figure 5.4.6: **(a) Frequency and average value of the somatic oscillator's phase response curve**$\langle z \rangle$ **versus** I**, for an isolated Morris-Lecar neuron**. The plot of the gain of the neuron, $\frac{d\omega}{dI}$, is identical to that of $\langle z \rangle / C_m$. The point at which the frequency of the limit cycle oscillations (light curve) reaches a maximum occurs at the same point that $\langle z \rangle$ (black curve) reaches zero and subsequently becomes negative as I is increased. **(b) Change in frequency due to the presence of the dendrite,** $\Delta\omega$**, as a function of** I. The solid line plots $\Delta\omega$ and the dashed line plots $\Delta\omega_{DC}$. In this case, the dendrite is hyperpolarized relative to the voltage oscillations, i.e. $\Delta I < 0$. Thus, the dendritic load has a decelerating effect on frequency when $\langle z \rangle > 0$ and an accelerating effect when $\langle z \rangle < 0$. Note that for these values of E_{LD} and $\varepsilon(a)$, $\Delta\omega_{DC}$ remains very close to $\Delta\omega$, and both $\Delta\omega$ and $\Delta\omega_{DC}$ retain the shape of the $\langle z \rangle$ versus I curve.

(a)   **(b)**

Figure 5.4.7: $\Delta\omega_{DC}$ **dominates the behavior of the phase model for a more detailed model neuronal oscillator.** (a) Voltage component of the limit cycle for the Traub et al. model neuron [104] when $I = 1.2\ \mu A/cm^2$ and its corresponding phase response curve. The dotted line in both plots is the approximation to the function using the first five Fourier modes. $\langl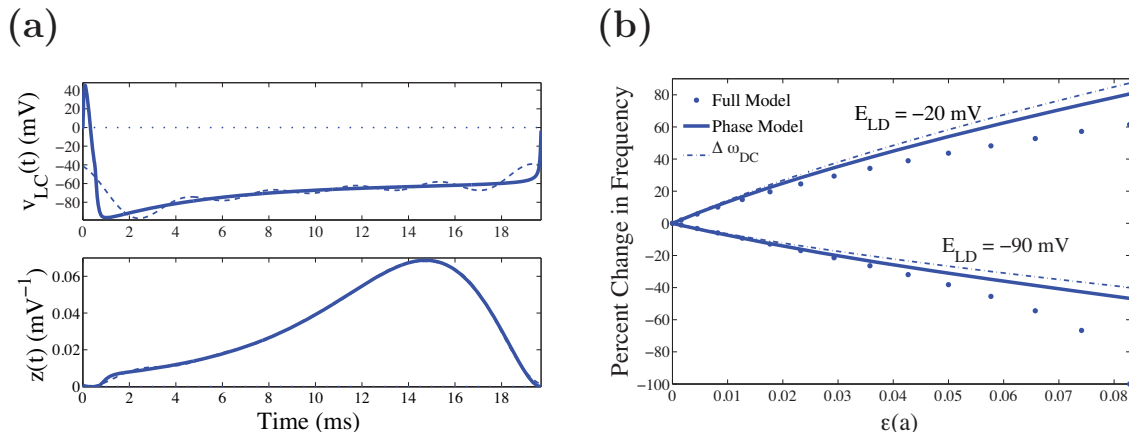e v_{LC} \rangle = -68.02\ mV$ and $\langle z \rangle = 0.032\ mV^{-1}$. (b) Percent change in firing frequency is plotted as a function of the strength of the dendritic perturbation, $\varepsilon(a)$, for a hyperpolarized ($-90\ mV$) and depolarized ($-20\ mV$) value of E_{LD} when $I = 1.2\ \mu A/cm^2$. The dots represent results from simulations of the full ball-and-stick model (equations (5.2.1-5.2.3)) the solid line represents results from simulations of the phase model (equation (5.3.7)) and the dash-dotted line represents $\Delta\omega_{DC}$ (equation (5.4.1)). As in Figure 5.4.2(a), the addition of the dendrite with a hyperpolarized leakage reversal potential decreases the frequency of oscillations as $\varepsilon(a)$ is increased while the addition of the dendrite with a depolarized leakage reversal potential increases the frequency of oscillations as $\varepsilon(a)$ is increased. It is important to note that $\Delta\omega_{DC}$ remains close to the phase model for both values of the dendritic leakage reversal potential.

5.5 Discussion

In this chapter, we examine how a passive dendritic load affects the firing frequency of a ball-and-stick model neuron. Using the theory of weak coupling, we derive an analytical expression that relates the change in frequency to the phase response properties of the model neuron and the properties of the dendrite [20]. We then elucidate the mechanisms that control the sensitivity of the neuron to dendritic load, and, in

doing so, identify the mechanisms underlying the counter-intuitive increases in firing frequency that can occur due to a hyperpolarizing dendritic load. Appendix 5.9 applies similar analysis to the an oscillator electrically coupled to a passive compartment in which case very similar results are obtained.

Three main observations in this article allow the clear identification of the fundamental mechanisms underlying the changes in a neuron's firing frequency due to the addition of a dendritic load: (i) The DC-component of the analytical expression for firing frequency, $\Delta\omega_{DC}$, typically dominates higher modes. This is the case unless the average of the PRC $\langle z \rangle$ is tuned to be close to zero and/or the average of the oscillating membrane potential $\langle v_{LC} \rangle$ is tuned to be close to the reversal potential of the dendrite E_{LD} (in these cases the change in frequency is very small). (ii) The form of $\Delta\omega_{DC}$ indicates that the change in frequency due to the dendritic load is primarily determined by the product $\langle z \rangle (E_{LD} - \langle v_{LC} \rangle)$. Along with the observation (i), this implies that the effect of a passive dendritic load on a neuron's firing frequency is equivalent to that of an additional constant current. (iii) The average value of a PRC $\langle z \rangle$ measures the sensitivity of the neuron to dendritic load and is proportional to the instantaneous slope of the neuron's *f-I* curve. Thus, when $\langle z \rangle > 0$ or equivalently $\frac{df}{dI} > 0$, the addition of a hyperpolarizing dendritic load causes the neuron's frequency to decrease. When $\langle z \rangle < 0$ or equivalently $\frac{df}{dI} < 0$, the addition of a hyperpolarizing dendritic load leads to a "counter-intuitive" increase in the firing frequency of a neuron. When $\langle z \rangle \approx 0$ or equivalently $\frac{df}{dI} \approx 0$, the addition of a hyperpolarizing dendritic load causes a negligible change in firing frequency. Note that the failure of our intuition for this behavior arises from the preconception that frequency always increases with increased applied current.

The mechanisms discussed above provide a general framework for understanding

the influence of passive dendritic properties on the firing frequency of neuronal oscillators. The numerical results presented in 5.4 are for the Morris-Lecar model, but we have obtained similar results for several other neuronal models. For example, Figure 5.4.7 shows that the DC component quantitatively captures the frequency modulation when somatic dynamics are described by the Traub et al. [47, 104] model, which is a more biophysically detailed model (see appendix for equations). In fact, $\langle z \rangle$ is relatively large over the entire oscillatory range for the Traub et al. model, and therefore the DC component correctly predicts the frequency modulation. On the other hand, $\langle z \rangle$ is always positive, and therefore the counter-intuitive increase in response to the addition of a hyperpolarizing dendritic load will not occur. Similar behavior would occur for any stereotypical "type-I" neuron [32].

Counter-Intuitive Behavior and Non-monotonic *f-I* Curves

The counter-intuitive results that we have described occur in model neurons where the *f-I* curve is non-monotonic. These type of curves are seen in real neurons, such as in the auditory cortex of cats [76] and the lobster stomatogastric ganglion [97]. However, it is worth noting that most model and real neurons tend to display a saturated *f-I* curve. Because of our analysis, we know that at the saturation point, the neuron has a zero average value PRC. Thus, the neuron is very insensitive to changes in E_{LD} and thus insensitive to dendritic inputs at this point. Furthermore, our results allow one to quantify the amount of frequency modulation caused by the weak dendritic perturbation by simply observing the slope of the neuron's *f-I* curve.

Relationship to Previous Studies

Skinner et al. [97] found that cultured stomatogastric ganglion (STG) neurons can exhibit either monotonic or non-monotonic *f-I* curves and that neurons are able to switch between these two response properties with pharmacological manipulation. They also demonstrated that modest changes of parameters can switch model neurons between these two behaviors. Furthermore, they showed that, when model neurons with non-monotonic *f-I* curves are coupled by reciprocal inhibition, the frequency of the network can increase beyond the maximum frequency for an isolated cell. The mechanisms responsible for this phenomena is intimately related to those described in this article

As mentioned before, the well-known modeling study by Kepler et al. [51] has previously examined the effects of electrically coupling a neuronal oscillator to a hyperpolarized passive cell in context of central pattern generators in the lobster stomatogastric ganglion. Kepler et al. found that, if the membrane potential of the neuronal oscillator has a short duty-cycle (i.e. a predominantly hyperpolarized wave-form as in Figure 5.4.3(a)), the electrical load of the passive cell acts to decrease the frequency of oscillations as the strength of the electrical coupling is increased. On the other hand, if the membrane potential of the neuron has a long duty-cycle (i.e. a predominantly depolarized wave-form as in Figure 5.4.3(b)), the electrical load of the passive cell can increase the frequency of oscillations. Their explanation for this phenomenon was based on the balance of inward and outward currents in the oscillator compartment. More specifically, they postulated that, during the depolarized phase of the neuronal oscillations, the hyperpolarized passive compartment acts to more rapidly repolarize the neuronal oscillator and therefore acts to decrease period of oscillation. On the other hand, during the subthreshold phase of the neuronal

oscillations, the hyperpolarized passive compartment acts to slow the rate of depolarization towards threshold, and therefore it acts to increase period of oscillation. When the neuronal oscillators has a short duty-cycle, the cycle is dominated by the subthreshold phase and therefore the net effect of the passive load is to decrease the frequency of oscillations. When the neuronal oscillators has long duty-cycle, the cycle is dominated by the depolarized phase and therefore the net effect of the passive load is to increase the frequency of oscillations.

Inherent in the explanation provided by Kepler et al. are the assumptions that the phase response curve of the oscillator will always be negative during the depolarized phase of the cycle and positive during the subthreshold phase of the cycle. Although this is the case for the simple model neuron that they used in their study, phase response properties of neuronal oscillators are typical more complicated than this (see Figure 5.4.3). For instance, neurons often have phase response curves with negative portions during the subthreshold phase [64]. The explanation provided in this article in terms of the oscillator's phase response curve is still conceptually simple and yet is more general in the sense that it can be applied to any oscillator.

Effect of Constant and Noisy Point Source Dendritic Inputs

We also consider the effects of dendritic inputs on firing frequency. In Appendix 5.10 , we show how constant point source synaptic inputs to the thin dendrite are equivalent to shifting the value of the dendritic leakage reversal potential. Furthermore, if one considers white noise input to the dendrite, the current that the soma receives from this input will be a filtered version of the white noise due to the filtering properties of the dendrite. However, the main effect that the noise will have on firing frequency is through its mean value, i.e. because of the linearity of the cable, the mean of the

noisy current would simply shift the value of $\Delta\omega$ in the phase model (5.3.7). Once the mean is taken out, the situation is equivalent to Teramae et al. [101] where they considered filtered zero mean white noise input to a somatic oscillator. In [101], the noisy input was scaled by a factor of σ. They showed that the filtered noise had $\mathcal{O}(\sigma^2)$ effects on the mean frequency of the oscillator. The $\mathcal{O}(\sigma^2)$ term involved the correlation time of the colored noise, the relaxation time back to the limit cycle, and higher order phase response properties of the somatic limit cycle. If the correlation time of the noisy current is comparable to the relaxation time back to the somatic limit cycle, then the effects of the noisy input on firing frequency cannot be ignored. The issue is that this effect is difficult to obtain computationally as it involves higher order phase response properties of the limit cycle [115, 101]. However, in the case of noisy inputs to the ball-and-stick model, the dendrite acts to filter the noisy input, thereby increasing the correlation time of the noise. If the correlation time of the noisy current that flows from the dendrite into the soma is larger than the relaxation time back to the somatic limit cycle, then noisy input will have negligible effects on firing frequency [101].

The Effects of Dendritic Morphology and Active Dendritic Conductances

The analysis presented in this paper relies on the assumptions that (1) the dendrites are thin relative to the diameter of the soma, and therefore only weakly perturb the somatic dynamics, and (2) the dendrites are passive and do not contain active membrane conductances. If the dendritic perturbation to a somatic oscillator is large and/or there are highly active conductances in the dendrites, the dendritic load can fundamentally change firing dynamics, e.g. quenching oscillations altogether or

inducing bursting dynamics [9, 61], in which case our analysis breaks down. On the other hand, our simulations show that the theory qualitatively predicts the firing effects of moderately sized dendritic perturbations despite the fact that the analysis takes the weak perturbation limit. Furthermore, we expect the addition of realistic dendritic morphologies to not change our results substantially, as many dendritic trees can be collapsed into an equivalent cylinder [79]. For these types of neurons, it has been shown that changes in dendritic topology have small effects on firing frequency [24, 107]. In this case, our analysis holds if the portion of the cylinder closest to the soma has a diameter that is thin relative to the diameter to the soma.

Furthermore, our analysis can readily be extended to include weakly nonlinear conductances in the dendrites [40, 10]. We note however that we have found no fundamental changes in the results for this case. These observations suggest that the mechanisms underlying frequency modulation described here are applicable to a range of biologically relevant situations.

5.6   Appendix A: Morris-Lecar Neuron

$$C_m \frac{dv}{dt} = -g_{Ca} m_\infty(v(t))(v(t) - E_{Ca}) - g_K w(v(t) - E_K) - g_L(v(t) - E_L) + I$$
$$\frac{dw}{dt} = \phi \frac{w_\infty(v(t)) - w}{\tau_w(v(t))}$$

where

$$m_\infty(v) = \frac{1}{2}\left[1 + \tanh\left(\frac{v - V_1}{V_2}\right)\right]$$

$$w_\infty(v) = \frac{1}{2}\left[1 + \tanh\left(\frac{v - V_3}{V_4}\right)\right]$$

$$\tau_w(v) = \frac{1}{\cosh\left(\frac{v-V_3}{2V_4}\right)}$$

and the parameters are taken from [89, 97]

$C_m = 1\ \mu F/cm^2$	$g_{Ca} = 0.6\ mS/cm^2$	$g_K = 0.8\ mS/cm^2$
$g_L = 0.2\ mS/cm^2$	$E_{Ca} = 100\ mV$	$E_K = -80\ mV$
$E_L = -50\ mV$	$V_1 = 0\ mV$	$V_2 = 15\ mV$
$V_3 = 0\ mV$	$V_4 = 15\ mV$	$\phi = 0.08\ ms^{-1}$

The cable parameters with the Morris-Lecar neuron are

$$g_{LD} = 0.5\ mS/cm^2 \qquad d = .002\ cm \qquad R_C = 0.1\ k\Omega \cdot cm$$

$$L = .02\ cm$$

5.7 Appendix B: Traub Model Soma

$$C_m\frac{dv}{dt} = -g_{Na}m^3 h(v(t) - E_{Na}) - g_K n^4(v(t) - E_K) - g_L(v(t) - E_L) + I$$

$$\frac{dm}{dt} = \alpha_m(v)(1 - m) - \beta_m(v)m$$

$$\frac{dh}{dt} = \alpha_h(v)(1 - h) - \beta_h(v)h$$

$$\frac{dn}{dt} = \alpha_n(v)(1 - n) - \beta_n(v)n$$

where

$$\alpha_m(v) = 1.28 \frac{(v+54)/4}{1-\exp(-(v+54)/4)} \qquad \beta_m(v) = 1.4 \frac{(v+27)/5}{\exp(-(v+27)/5)-1}$$

$$\alpha_h(v) = 0.128 \exp(-(v+50)/18) \quad \beta_h(v) = 4.0 \frac{1}{1+\exp(-(v+27)/5)}$$

$$\alpha_n(v) = 0.16 \frac{(v+52)/5}{1-\exp(-(v+52)/5)} \qquad \beta_n(v) = 0.5 \exp(-(v+57)/40)$$

and the parameters are taken from [47]

$$C_m = 1 \ \mu F/cm^2 \qquad g_{Na} = 100 \ mS/cm^2 \qquad g_K = 80 \ mS/cm^2$$

$$g_L = 0.2 \ mS/cm^2 \qquad g_{LD} = 0.5 \ mS/cm^2 \qquad E_{Na} = 50 \ mV$$

$$E_K = -100 \ mV \qquad E_L = -67 \ mV$$

The cable parameters with the Traub model soma are

$$g_{LD} = 0.5 \ mS/cm^2 \qquad d = .002 \ cm \qquad R_C = 0.1 \ k\Omega \cdot cm$$

$$L = .01 \ cm$$

5.8 Appendix C: Dendritic Effects in the Ball-and-Stick Phase Model

Recall that the "filtering" effects of the dendrite are captured by $c_n(a)$ in equation (5.3.7). In this section, we show that the $c_n(a)$ terms increase more slowly than the Fourier components v_n and z_n decay and that, for the parameters considered here, $|c_n(a)| \approx 1$ for small n. Therefore, the higher order cable properties of the dendrite (i.e. effects beyond the leakage reversal potential, E_{LD}) do not greatly influence the behavior of the phase model for small n. Moreover, it is most often the case that the Fourier series of the phase response curve is dominated by the first few modes (see Figures 5.4.3 and 5.4.7). Therefore, even if $\varepsilon(a) \frac{\partial V}{\partial x}(0, t)$ contains higher modes in

its Fourier expansion, they will be 'zeroed out' when multiplied by the PRC. Thus, the phase model will not be greatly influenced by the cable properties and will be dominated by the first few modes of the Fourier expansion of the $\Delta\omega$ term.

Recall that $c_n(a) = b_n \tanh(b_n \frac{L}{\lambda(a)})$, with $b_n = \sqrt{1 + \frac{g_L}{g_{LD}} 2\pi i n/\bar{T}}$. For a sufficiently long dendrite $\frac{L}{\lambda(a)} \geq 1.5$, $|\tanh(b_n \frac{L}{\lambda(a)})| \in [0.9, 1.3]$. Thus, $c_n(a) \approx b_n$. Using the fact that the nondimensional period, $\bar{T}$, is equal to the dimensional period, T, divided by the somatic membrane time constant, τ_S, and the fact that $\tau_D = \frac{C_m}{g_{LD}}$, we can rewrite $c_n(a)$ as

$$c_n(a) \approx b_n = \sqrt{1 + \frac{\tau_D}{\tau_S} 2\pi i n \frac{\tau_S}{T}} = \sqrt{1 + \frac{\tau_D}{T} 2\pi i n}. \tag{5.8.1}$$

The magnitude and angle of the $c_n(a)$ terms is then given by

$$|c_n(a)| = \left(1 + n^2 \left(\frac{\tau_D}{T} 2\pi\right)^2\right)^{\frac{1}{4}} \tag{5.8.2}$$

$$\phi_n = \frac{1}{2} \arctan(2\pi n \frac{\tau_D}{T}). \tag{5.8.3}$$

Thus, $|c_n(a)|$ increases like $n^{\frac{1}{2}}$. This implies that the effect of dendrite acts to amplify the higher modes in the Fourier series. However, if $\frac{\tau_D}{T} \ll 1$, then $|c_n(a)| \approx 1$ for small n.

For our simulations, the dendritic membrane time constant, τ_D, is set at $2\ ms$, and the space constant, $\lambda(a)$, ranges from $\mathcal{O}(10^{-3})$ to $\mathcal{O}(10^{-2})\ cm$ for the values of dendritic radii that were used. For the Morris-Lecar and Traub et al. model neurons, $\frac{\tau_D}{T} \sim \mathcal{O}(10^{-1})$. Thus, due to the facts that the Fourier coefficients z_n rapidly decay and that $|c_n(a)| \approx 1$ for small n, the higher order cable properties have a minimal

effect on the phase model.

5.9   Appendix D: Two-Compartment Model

In this section we present the phase model reduction for the two compartment model of a soma electrically coupled to a dendritic compartment. In this case, the phase model can be obtained using two different limits: the limit of weak electrical coupling and the limit of a large oscillator compartment attached to a smaller dendritic compartment. However, in both limits, the behavior of the phase model qualitatively matches that of the phase model derived from the ball-and-stick model. Thus, our explanation for the non-intuitive frequency effects seen in the cable model can be directly applied to the two-compartment model studied in Kepler et al. [51].

The soma is modeled as an isopotential compartment with Hodgkin-Huxley currents and the dendrite is modeled as a passive compartment electrically coupled to the soma [59]

$$C_m \frac{dv_S}{dt} = -I_{ion,S}(v_S(t), \vec{w}) + I + g_C \left(\frac{a_D}{a_S} \right)^2 (v_D - v_S) \qquad (5.9.1)$$

$$C_m \frac{dv_D}{dt} = -g_{LD}(v_D - E_{LD}) + g_C(v_S - v_D), \qquad (5.9.2)$$

where $v_S(t)$ and $v_D(t)$ represent the voltage, in mV, of the somatic and dendritic compartment, respectively, at time t, g_C is the gap junctional conductance in mS/cm^2, a_S and a_D represent the radii of the somatic and dendritic compartments, respectively, in cm, and $I_{ion,S}(v, \vec{w})$, $\bar{I}$, g_{LD}, C_m, and E_{LD} are the same as in the ball-and-stick model. In addition, I is assumed to be large enough so that the soma undergoes periodic firing, i.e. limit cycle oscillations.

Let $V_{S,D} = V_{S,D}(t) = \frac{v_{S,D}(\tau_D \bar{t}) - E_L}{-E_L}$ (where E_L is the leakage reversal potential in the soma), $\bar{t} = \frac{t}{\tau_D}$, and $\tau_D = C_m / g_{LD}$ is the membrane time constant of the dendritic compartment. Then, our equations become

$$\frac{dV_S}{d\bar{t}} = -\bar{I}_{ion,S}(V(\bar{t}), \vec{w}) + \bar{I} + \varepsilon\gamma(V_D - V_S) \tag{5.9.3}$$

$$\frac{dV_D}{d\bar{t}} = -(V_D - \bar{E}_{LD}) + \varepsilon(V_S - V_D), \tag{5.9.4}$$

where $\gamma = \left(\frac{a_D}{a_S}\right)^2$, $\varepsilon = \frac{g_C}{g_{LD}}$, and $\bar{E}_{LD}$, $\bar{I}_{ion,S}(V(\bar{t}), \vec{w})$, and I are the same as for the ball-and-stick model.

There are two possible approaches to the phase reduction at this point: (1) assume that ε is the small parameter, or (2) assume that γ is the small parameter. Let us first examine the case where ε is small and γ is $\mathcal{O}(1)$.

As with the ball-and-stick model, we can reduce the dynamics of our two compartment model to a single phase equation by assuming that $g_C \ll g_{LD}$ and that γ is $\mathcal{O}(1)$. Note, in this case, our assumption is that the coupling between the two compartments is what we are assuming is small while the ratio of the radii is assumed to be $\mathcal{O}(1)$. Since ε appears in both equations (5.9.3) and (5.9.4), both compartments will be behaving very similarly to their unperturbed ($\varepsilon = 0$) counterparts. Thus, the dendritic compartment will go to its steady state, $\bar{E}_{LD}$, and the membrane potential of the somatic compartment will go to its limit cycle, $V_{LC}(\bar{t})$. Our phase equation is then

$$\frac{d\theta}{d\bar{t}} = \bar{\omega} + \Delta\bar{\omega} = \bar{\omega} + \frac{\varepsilon\gamma}{\bar{T}} \int_0^{\bar{T}} Z(s)(\bar{E}_{LD} - V_{LC}(s))ds, \tag{5.9.5}$$

where $\varepsilon\gamma(\bar{E}_{LD} - V_{LC})$ is the nondimensional coupling current under the assumption that both V_S and V_D cling tightly to their steady states. Expanding $Z(\bar{t})$ and $V_{LC}(\bar{t})$ in Fourier series yields

$$\frac{d\theta}{d\bar{t}} = \bar{\omega} + \varepsilon\gamma\langle Z\rangle(\bar{E}_{LD} - \langle V_{LC}\rangle) - \frac{\varepsilon\gamma}{\bar{T}^2}\sum_{n\neq 0} Z_{-n}V_n. \tag{5.9.6}$$

where V_n are the coefficients of V_{LC}, Z_n are the coefficients of Z, and we have replaced $V_0/\bar{T}$ and $Z_0/\bar{T}$ with $\langle V_{LC}\rangle$, and $\langle Z\rangle$ as in equation (5.3.7). Note that this is the same as the phase equation for the ball-and-stick model without the terms describing the influence of the cable, i.e. $c_n(a)$.

Next, let us assume that γ is small and that ε is $\mathcal{O}(1)$. In this case, we are assuming that the somatic compartment is much larger than the dendritic compartment. Thus, the dendrite will have a minimal effect on the dynamics of the soma, implying that the membrane potential of the somatic compartment will cling to its limit cycle, $V_{LC}(\bar{t})$, while the somatic compartment will have an $\mathcal{O}(1)$ effect on the dynamics of the dendritic compartment. Our phase equation is then

$$\frac{d\theta}{d\bar{t}} = \bar{\omega} + \Delta\bar{\omega} = \bar{\omega} + \frac{\varepsilon\gamma}{\bar{T}}\int_0^{\bar{T}} Z(s)(V_D(s) - V_{LC}(s))ds, \tag{5.9.7}$$

where the first order approximation to $V_D(\bar{t})$ is found by solving

$$\frac{dV_D}{d\bar{t}} = -(V_D - \bar{E}_{LD}) + \varepsilon(V_{LC}(\bar{t}) - V_D). \tag{5.9.8}$$

Solving the above equation using Fourier series and plugging the result into equation (5.9.7) yields

$$\frac{d\theta}{d\bar{t}} = \bar{\omega} + \gamma \langle Z \rangle (\bar{E}_{LD} - \langle V_{LC} \rangle) \left[\frac{\varepsilon}{1 + \varepsilon} \right] - \frac{\gamma}{\bar{T}^2} \sum_{n \neq 0} Z_{-n} V_n c_n, \qquad (5.9.9)$$

where $c_n = \frac{\varepsilon(1 + 2\pi in/\bar{T})}{2\pi in/\bar{T} + (1+\varepsilon)}$. Thus, in this limit, there are filtering effects due to the addition of the dendritic compartment. Recall that time was nondimensionalized using τ_D. This implies that $\bar{T} = T/\tau_D$, where T is the dimensional period of oscillations. Therefore, the magnitude of the c_n terms can be written as

$$|c_n| = \varepsilon \left(\frac{1 + (2\pi n \frac{\tau_D}{T})^2}{(2\pi n \frac{\tau_D}{T})^2 + (1+\varepsilon)^2} \right)^{\frac{1}{2}}. \qquad (5.9.10)$$

Equation (5.9.10) limits to 1 as $n \to \infty$. When $\frac{\tau_D}{T} \ll 1$, $|c_n| \approx \frac{\varepsilon}{1+\varepsilon}$ for small n, which implies that the filtering effects are minimal.

In both scenarios presented above, the phase models qualitatively match the dynamics of the phase model derived from the ball-and-stick model.

5.10 Appendix E: The Effects of Dendritic Inputs at Point Sources

In this section, we discuss how inputs to a thin dendrite affect the frequency of the somatic oscillator. We show that point source inputs to the thin dendrite have the same effect on the frequency as shifting the leakage reversal potential of the dendrite,

E_{LD}, by a constant value.

In the limit of $\varepsilon \ll 1$, a dendrite receiving K point source inputs and being driven by an oscillatory soma is described by the following system of equations

$$g\frac{\partial V}{\partial \bar{t}} = \frac{\partial^2 V}{\partial \bar{x}^2} - (V - \bar{E}_{LD}) + \sum_{n=1}^{K} \bar{A}_n \delta(\bar{x} - \bar{x}_n) \tag{5.10.1}$$

$$V(0, \bar{t}) = V_{LC}(\bar{t}) \tag{5.10.2}$$

$$\frac{\partial V}{\partial \bar{x}}\left(\frac{L}{\lambda(a)}, \bar{t}\right) = 0. \tag{5.10.3}$$

Due to the principle superposition, we can separate out the dendritic inputs and the oscillatory boundary condition and solve

$$g\frac{\partial V}{\partial \bar{t}} = \frac{\partial^2 V}{\partial \bar{x}^2} - V + \sum_{n=1}^{K} \bar{A}_n \delta(\bar{x} - \bar{x}_n) \tag{5.10.4}$$

$$V(0, \bar{t}) = 0 \tag{5.10.5}$$

$$\frac{\partial V}{\partial \bar{x}}\left(\frac{L}{\lambda(a)}, \bar{t}\right) = 0, \tag{5.10.6}$$

and

$$g\frac{\partial V}{\partial \bar{t}} = \frac{\partial^2 V}{\partial \bar{x}^2} - (V - \bar{E}_{LD}) \tag{5.10.7}$$

$$V(0, \bar{t}) = V_{LC}(\bar{t}) \tag{5.10.8}$$

$$\frac{\partial V}{\partial \bar{x}}\left(\frac{L}{\lambda(a)}, \bar{t}\right) = 0, \tag{5.10.9}$$

separately. Note that we solve equations (5.10.7-5.10.9) in section 5.3. Since we are

concerned with the steady-state current that the dendritic inputs cause to be injected into the soma, we can set the time derivative equal to zero in (5.10.4) and solve

$$-\frac{d^2V}{d\bar{x}^2} + V = \sum_{n=1}^{K} \bar{A}_n \delta(\bar{x} - \bar{x}_n) \qquad (5.10.10)$$

$$V(0) = 0 \qquad (5.10.11)$$

$$\frac{dV}{d\bar{x}}\left(\frac{L}{\lambda(a)}\right) = 0. \qquad (5.10.12)$$

The solution of the above system is given by the following Green's function

$$g(\bar{x}, \bar{x}_n) = \begin{cases} \bar{A}_n \sinh(\bar{x}) \cosh\left(\bar{x}_n - \frac{L}{\lambda(a)}\right) / \cosh\left(\frac{L}{\lambda(a)}\right) & \text{if } 0 \leq \bar{x} \leq \bar{x}_n \leq \frac{L}{\lambda(a)} \\ \bar{A}_n \sinh(\bar{x}_n) \cosh\left(\bar{x} - \frac{L}{\lambda(a)}\right) / \cosh\left(\frac{L}{\lambda(a)}\right) & \text{if } 0 \leq \bar{x}_n \leq \bar{x} \leq \frac{L}{\lambda(a)} \end{cases}$$

$$(5.10.13)$$

Therefore, the current that the soma receives from these K dendritic inputs is given by the following constant term

$$\bar{I}_{input} = \sum_{n=1}^{K} g_{\bar{x}}(0, \bar{x}_n) = \sum_{n=1}^{K} \bar{A}_n \frac{\cosh\left(\bar{x}_n - \frac{L}{\lambda(a)}\right)}{\cosh\left(\frac{L}{\lambda(a)}\right)}. \qquad (5.10.14)$$

Adding the above term to equation (5.3.5) yields

$$\frac{\partial V}{\partial \bar{x}}(0, \bar{t}) = \left(\bar{E}_{LD} - \frac{V_0}{\bar{T}}\right) c_0(a) - \frac{1}{\bar{T}} \sum_{n \neq 0} c_n(a) V_n e^{2\pi i n \bar{t}/\bar{T}} + \bar{I}_{input}. \qquad (5.10.15)$$

This changes the phase equation (5.3.7) to

$$
\begin{aligned}
\frac{d\theta}{dt} \;=\;\; & \omega + \frac{\varepsilon(a)}{\tau_S}\left[\langle z\rangle\left((E_{LD} - \langle v_{LC}\rangle)c_0(a) + \frac{1}{g_{LD}}I_{input}\right)\right. \\
& \left. -\frac{2}{T^2}\sum_{n=1}^{\infty}|z_n v_n c_n(a)|\cos(\psi_n(a) + \gamma_n - \phi_n)\right],
\end{aligned}
\qquad (5.10.16)
$$

where $I_{input} = -g_{LD}E_L\bar{I}_{input}$. Thus, the addition of point source inputs to the dendrite can be completely incorporated into E_{LD}, as $c_0(a) \sim 1$ for the parameter range we considered.

If the point source input to the dendrite was noisy rather than constant, then the current that the soma receives from this input will be a filtered version of the noise due to the filtering properties of the dendrite. The main effect that this noisy input will have on firing frequency is through its mean value, i.e. because of the linearity of the cable, the mean of the noisy current would simply shift the value of $\Delta\omega$ in the phase model (5.3.7). This is due to the fact that the filtering effects of the dendrite act to increase the correlation time of the noise. If the correlation time of the noisy current that flows from the dendrite into the soma is larger than the relaxation time back to the somatic limit cycle, then noisy input will have negligible effects on firing frequency (see discussion) [101]. In this case, the noisy point source input will affect firing frequency in the same way as a constant point source input which was discussed above.

5.11   Summary and Closing Remarks

We have used the theory of weakly coupled oscillators to show that when the dendritic influence is weak, its effect on the firing frequency of a nonlinear somatic oscillator

is the same as an additional constant current injection to the soma. As such, the dendrites' affect on firing frequency can be understood in terms of the instantaneous slope of the isolated neuronal oscillators frequency-applied current (*f-I*) curve (with the caveat being that the cell is away from any saturation points).

The assumption that the dendritic influence on the somatic oscillator is weak might be accurate for some neurons in certain areas of the brain. However, it could certainly be the case that the dendrites of some neurons have a significant impact on their electrical activity. Therefore, in the next chapter, we extend the results presented in this chapter to examine how non-weak dendritic influences affect the dynamics of neurons. We accomplish this by restricting the somatic dynamics to be a variant of the leaky-integrate-fire neuron [1] that was discussed in Chapter 2. This simplifies the ball-and-stick model since the integrate-and-fire model is linear until it reaches a threshold nonlinearity.

Chapter 6

Bistability in a Leaky Integrate-and-Fire Neuron with a Passive Dendrite

In this chapter, we examine the influence of dendritic load on the firing dynamics of a spatially extended leaky-integrate-and-fire neuron that explicitly includes spiking dynamics. We obtain an exact analytical solution for this model using a non-orthogonal basis expansion technique. We use this solution to derive a return map for the voltage of the dendrite. The map reveals that the addition of the dendrite can cause the system to display bistable behavior between periodic firing and quiescence. The periodic behavior arises from a "ping-pong" effect between the somatic and proximal dendritic membrane potentials. This ping-pong effect was previously only described in models that contain active dendritic conductances. We then show that the same qualitative behavior is captured in a two-compartment model with a leaky-integrate-and-fire compartment electrically coupled to a passive compartment.

6.1 Introduction

Neurons are spatially extensive, heterogeneous objects. They typically consist of a dendritic tree where the majority of inputs to the cell are received; a soma, or cell body, where these inputs are integrated, an axon hillock where the integrated inputs can cause the initiation of an action potential; and an axon where the action potential propagates along until it reaches the synaptic terminal and causes the release of neurotransmitter onto a postsynaptic cell. The type of model one uses to represent a neuron depends upon a balance between mathematical tractability and biological realism and on the issue that is being addressed. A common technique in neuronal modeling is to represent the neuron as a single-compartment object that ignores the spatial anatomy of the cell. Although this simplification allows for greater mathematical tractability and computational efficiency, many neurons are not electrotonically compact. Thus, single-compartment models cannot be expected to fully capture the electrical behavior of neurons.

There are two main approaches utilized in examining the spatial properties of neurons [11]. The first is using a system of ordinary differential equations connected by electronic coupling (resistors) to model the neuron as a multi-compartmental object [102]. Using this approach, various authors have shown that dendritic properties can substantially change the firing pattern (e.g. induce bursting), encoding properties, and phase-locking behavior of neuronal oscillators [9, 22, 56, 59, 61, 77, 109]. Although this technique allows for greater flexibility in reproducing biological data, the resulting models can be quite difficult to analyze when there is a large number of compartments. The second technique involves using partial differential equations to continuously model the spatial dynamics of the neuron [78, 79]. This approach allows one to model the spatial voltage dynamics of the neuron continuously, and is

somewhat more amenable to mathematical analysis. This is the approach we utilize in this article.

In the previous work [94] (see also Chapter 5), we identified the mechanisms by which weak dendritic influences modulate the firing frequency of a somatic oscillator. We modeled the neuron as an isopotential somatic oscillator attached to a thin passive dendritic cable, i.e. a "ball-and-stick" model [80], and as an isopotential somatic oscillator compartment electrically coupled to a passive compartment, i.e. a two-compartment model. We made no assumption about the dynamics of the somatic oscillator, but we assumed that the dendrite was sufficiently thin so that the dynamics of the soma were only weakly perturbed. Here, we extend our previous results to examine the effects of non-weak dendritic influences. We make no assumptions about the strength of the dendritic perturbation. Instead, we idealize our somatic dynamics as a leaky-integrate-and-fire model that explicitly includes spike effects [17, 50, 58]. In this case, we obtain an exact analytical solution of the ball-and-stick model using a non-orthogonal basis expansion technique [25, 18]. By examining the bifurcation structure of the system under various parameter variations, we show that the influence of the passive dendrite can cause the neuron to display bistability between periodic firing and quiescence for certain somatic spike parameters. In this bistable regime, the periodic behavior arises from a "ping-pong" effect [9, 109] between the somatic and proximal dendritic membrane potentials. We then demonstrate that the same qualitative behavior is captured in the two-compartment model.

6.2 Leaky-Integrate-and-Fire Ball-and-Stick Model

We model a neuron as an isopotential spherical soma attached to a passive dendrite, i.e. a ball-and-stick model [20]. The dendrite is modeled as a one-dimensional passive

cable of electrotonic length ℓ using the cable equation [78, 79, 80]

$$C_m \frac{\partial \bar{V}}{\partial \bar{t}} = \frac{a}{2R_c} \frac{\partial^2 \bar{V}}{\partial \bar{x}^2} - g_{LD}(\bar{V} - E_{LD}), \tag{6.2.1}$$

where $\bar{V}(\bar{x}, \bar{t})$ is the voltage of the cable at position $\bar{x}$ and time $\bar{t}$, C_m is the membrane capacitance, g_{LD} is the leakage conductance, E_{LD} is the leakage reversal potential, R_c is the cytoplasmic resistivity, and a is the radius of the dendrite. Note that the cable can be thought of as a single dendrite or as the equivalent cylinder of a branched dendritic structure [79, 81].

No current is assumed to pass through the the distal end, $\bar{x} = \ell$, of the dendrite, resulting in the boundary condition

$$\frac{\partial \bar{V}}{\partial \bar{x}}(\ell, \bar{t}) = 0. \tag{6.2.2}$$

The boundary condition at $\bar{x} = 0$ is provided by the somatic dynamics and an application of Kirchhoff's law of current conservation. We use a leaky integrate-and-fire neuron that includes a spike to model our isopotential soma [17, 50, 58]. Thus, the non-spiking portion of the model is described by

$$C_m \frac{\partial \bar{V}}{\partial \bar{t}}(0, \bar{t}) = -g_L(\bar{V}(0, \bar{t}) - E_L) + \bar{I} + \frac{a^2}{d^2 R_c} \frac{\partial \bar{V}}{\partial \bar{x}}(0, \bar{t}), \tag{6.2.3}$$

where g_L is the somatic leakage conductances, E_L is the somatic leakage reversal potential, d is the diameter of the soma, and $\bar{I}$ is the current applied to the soma.

Note that equations (6.2.1)-(6.2.3) describe the Rall lumped soma model (see section 3.5).

To incorporate spiking dynamics into the model, we require that when the somatic membrane potential reaches a threshold potential of V_{th} at time $\bar{t}_s$, i.e. $\bar{V}(0, \bar{t}_s) = V_{th}$, the proximal boundary condition ($\bar{x} = 0$) is changed to

$$\bar{V}(0, \bar{t}) = \bar{h}(\bar{t} - \bar{t}_s); \ \ \bar{t} \in (\bar{t}_s, \bar{t}_s + \bar{T}_a], \tag{6.2.4}$$

where $\bar{h}(\bar{t} - \bar{t}_s)$ is some function to approximate the shape of the spike, and $\bar{T}_a$ is the duration of the spike.

In order to have the dynamics of the system uniquely determined, we also assume that at time $\bar{t} = 0$, the initial voltage profile is described by some function $\bar{V}^0(\bar{x})$

$$\bar{V}(\bar{x}, 0) = \bar{V}^0(\bar{x}), \ \ \bar{x} \in [0, \ell], \tag{6.2.5}$$

where the superscript in $\bar{V}^0(\bar{x})$ is used to denote it as being the initial condition. Thus, in non-dimensional form, the full leaky-integrate-and-fire ball-and-stick model that incorporates spiking dynamics is given by

$$\frac{\partial V}{\partial t} = \frac{\partial^2 V}{\partial x^2} - V, \tag{6.2.6}$$

$$\begin{cases} \dfrac{\partial V}{\partial t}(0,t) = -G_L V(0,t) + I + \gamma \dfrac{\partial V}{\partial x}(0,t) & \text{if } V(0,t) \leq 1 \text{ and } t \notin (t_s, t_s + T_a] \\ V(0,t) = h(t - t_s) & \text{if } V(0,t) > 1 \text{ or } t \in (t_s, t_s + T_a] \end{cases} \tag{6.2.7}$$

$$\frac{\partial V}{\partial x}(L,t) = 0 \tag{6.2.8}$$

$$V(x,0) = V^0(x), \tag{6.2.9}$$

where $V = V(x,t) = \frac{\bar{V}(\bar{x}/\lambda, \bar{t}/\tau_D) - E_{LD}}{V_{th} - E_{LD}}$, $\lambda = \sqrt{\frac{a}{2R_c g_{LD}}}$ is the space constant of the dendrite, $\tau_D = C_m/g_{LD}$ is the time constant of the dendrite, $t_s = \bar{t}_s/\tau_D$, $T_a = \bar{T}_a/\tau_D$, $h(t) = \frac{\bar{h}(\bar{t}/\tau_D) - E_{LD}}{V_{th} - E_{LD}}$, $L = \frac{\ell}{\lambda}$ is the electrotonic length of the dendrite, $G_L = g_L/g_{LD}$, $I = \frac{\bar{I} + g_L(E_L - E_{LD})}{g_{LD}(V_{th} - E_{LD})}$, and $\gamma = \frac{a^2}{d^2 R_c g_{LD} \lambda}$. Note that γ represents the strength of the perturbation to the soma. The above model displays two types of characteristic behavior depending on the value of I: (i) spatially constant steady-state behavior, or (ii) repetitive firing.

6.3 Derivation of Return Map for the Cable Model

In this section, we outline the steps involved in obtaining the analytical solution to the system described by equations (6.2.6)-(6.2.9). We construct a piecewise solution to the entire system by piecing together the solution from time $t = 0$ to $t = t_s$ and the solution from time $t = t_s$ to $t = t_s + T_a$. More precisely, we first solve (6.2.6) with the non-spiking proximal boundary condition in (6.2.7). If the somatic membrane potential reaches 1, we call the time that is does so t_s and then switch to the spike proximal boundary condition and solve (6.2.6) in the time interval $(t_s, t_s + T_a]$. If the

somatic membrane potential never reaches 1, then the full solution is given solving the non-spiking portion of the model.

6.3.1 Non-Spiking Solution

In order to solve the non-spiking portion of the model, we first make the change of variables $W(x,t) = V(x,t) - V(x,\infty)$, where

$$V(x,\infty) = \rho \cosh(L - x), \tag{6.3.1}$$

is the steady state solution of the pre-spike system and $\rho = \frac{I}{\gamma \sinh(L) + G_L \cosh(L)}$. Using separation of variables, $W(x,t)$ can be written as

$$W(x,t) = [C_1 \sin(\alpha(L - x)) + C_2 \cos(\alpha(L - x))]e^{-(1+\alpha^2)t}, \tag{6.3.2}$$

where α is the separation constant.

Applying the non-spiking proximal boundary condition and the no-flux distal boundary condition, one finds that $C_1 = 0$ and that the eigenvalues α are the solutions of the transcendental equation

$$1 = \frac{G_L - (1 + \alpha^2)}{\alpha\gamma} \cot(\alpha L), \tag{6.3.3}$$

which has an infinite number of solutions (see Figure 6.3.1). $W(x,t)$ can now be written as an infinite series expansion in terms of eigenfunctions

$$W(x,t) = \sum_{n=0}^{\infty} B_n \cos(\alpha_n(L - x))e^{-(1+\alpha_n^2)t}. \tag{6.3.4}$$
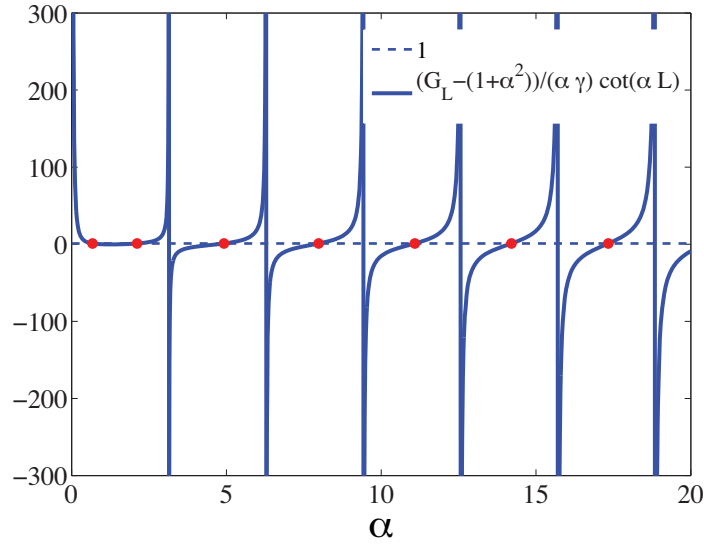
Applying the initial condition $(t = 0)$

Figure 6.3.1: **Graphical representation of the eigenvalues (6.3.3).** There are an infinite number of solutions α_n given by the intersection of the solid and dashed lines. Since the eigenfunctions $X_n = \cos(\alpha_n(L - x))$ are even, we need only consider positive α_n.

$$W(0, t) = \sum_{n=0}^{\infty} B_n \cos(\alpha_n(L - x)) = V^0(x) - V(x, \infty). \qquad (6.3.5)$$

In order to find the coefficients B_n, the far right hand side of equation (6.3.5) must be expanded in terms of the eigenfunctions $X_n(x) = \cos(\alpha_n(L - x))$. The coefficients of this expansion are easily determined if the set $X_n(x)$ is orthogonal. In the limit as $\gamma \to 0$ and $\gamma \to \infty$, the set of eigenfunctions $X_n(x)$ are orthogonal. However, for moderate values of γ, $X_n(x)$ do not form an orthonormal set. This issue was encountered in Durand [25] in their derivation of the somatic shunt cable model and we follow their use of the modified orthogonality relation of Churchill [18] in order to obtain the values for the expansion coefficients B_n. Specifically, Churchill [18] showed that the set $X_n(x)$ are orthogonal given the modified inner product

$$B(f,g) = \int_0^L fg\,dx + b_0 f(0)g(0) + b_1 f(L)g(L), \qquad (6.3.6)$$

i.e. $B(X_n(x), X_m(x)) = 0$. Since the boundary conditions are what make the set $X_n(x)$ non-orthogonal under the usual L_1 inner product, equation (6.3.6) allows $X_n(x)$ to form an orthogonal set by modifying the usual L_1 inner product to take into account the boundary effects. Thus, the expansion coefficients are given by

$$B_n = \frac{B(V^0(x) - V(x,\infty), X_n(x))}{B(X_n(x), X_n(x))}. \qquad (6.3.7)$$

The coefficients b_0 and b_1 in equation (6.3.6) are found to be $\frac{1}{\gamma}$ and 0, respectively, by converting the boundary conditions to the form

$$a_0\, V|_{x=0} + \left.\frac{dV}{dx}\right|_{x=0} - b_0 \left.\frac{d^2V}{dx^2}\right|_{x=0} = 0 \qquad (6.3.8)$$

$$a_1\, V|_{x=L} + \left.\frac{dV}{dx}\right|_{x=L} + b_1 \left.\frac{d^2V}{dx^2}\right|_{x=L} = 0. \qquad (6.3.9)$$

Expanding $V^0(x)$, and $V(x,\infty)$ in terms of the nonorthogonal basis elements $X_n(x)$, we can write the solution of the non-spiking portion of the model as

$$
\begin{aligned}
V(x,t) &= W(x,t) + V(\infty,t) & (6.3.10)\\
&= \sum_{n=0}^{\infty} B_n e^{-(1+\alpha_n^2)t} \cos(\alpha_n(L-x)) + \rho \sum_{n=0}^{\infty} g_n \cos(\alpha_n(L-x)), & (6.3.11)
\end{aligned}
$$

where

$$B_n = V_n^0 - \rho g_n \tag{6.3.12}$$

$$V^0(x) = \sum_{n=0}^{\infty} V_n^0 \cos(\alpha_n(L - x)) \tag{6.3.13}$$

$$g_n = \begin{cases} \dfrac{2\cosh(L)}{\cos(\alpha_n L)} \dfrac{1}{1 + \alpha_n^2} \dfrac{\gamma \tanh(L) + G_L}{\beta_n + L\gamma/\cos^2(\alpha_n L) + 2} & \text{if } \alpha_n \neq 0 \\[2em] \dfrac{\sinh(L) + \frac{1}{\gamma}\cosh(L)}{L + 1/\gamma} & \text{if } \alpha_n = 0 \end{cases} \tag{6.3.14}$$

$$\beta_n = \frac{G_L - (1 + \alpha_n^2)}{\alpha_n^2} \tag{6.3.15}$$

Equation (6.3.11) describes the non-spiking voltage of the dendrite. To obtain the firing time, t_s, of the soma, one must solve the following transcendental equation

$$V(0, t_s) = \sum_{n=0}^{\infty} (B_n e^{-(1+\alpha_n^2)t_s} + \rho g_n) \cos(\alpha_n L) = 1. \tag{6.3.16}$$

6.3.2 Dynamics During the Spike

Once the spike time t_s is obtained, (6.2.6) is then solved with the spike boundary condition from time t_s to $t_s + T_a$. To solve this system, we introduce the new variable $U(x, t) = V(x, t) - Y(x, t)$, where

$$Y(x, t) = h(t - t_s)\frac{\cosh(x - L)}{\cosh(L)}. \tag{6.3.17}$$

This leads to the system

$$\frac{\partial U}{\partial t} = \frac{\partial^2 U}{\partial x^2} - U - F(x, t) \tag{6.3.18}$$

$$U(0, t) = 0 \tag{6.3.19}$$

$$\frac{\partial U}{\partial x}(L, t) = 0 \tag{6.3.20}$$

$$U(x, t_s) = \sum_{n=0}^{\infty} (B_n e^{-(1+\alpha_n^2)t_s} + \rho g_n) \cos(\alpha_n(L - x)) - Y(x, t_s), \tag{6.3.21}$$

where $F(x, t) = h'(t - t_s)\frac{\cosh(x-L)}{\cosh(L)}$. The solution of (6.3.18)-(6.3.21) is then found using separation of variables, which yields the following solution for spiking portion of the model

$$V(x, t) = \sum_{m=0}^{\infty} T_m(t) \cos(\lambda_m(x - L)) + h(t - t_s)\frac{\cosh(x - L)}{\cosh(L)}; \quad t \in (t_s, t_s + T_a], \tag{6.3.22}$$

where

$$\lambda_m = \frac{(2m + 1)^2 \pi^2}{4L^2} + 1 \tag{6.3.23}$$

$$T_m(t) = -e^{-\lambda_m t} \int_{t_s}^{t} F_m(s)e^{\lambda_m s} ds + e^{-\lambda_m(t-t_s)} T_m(t_s) \tag{6.3.24}$$

$$F_m(t) = \frac{2h'(t - t_s)}{L \cosh(L)} \frac{2L(2m + 1)\pi(-1)^m \cosh(L)}{4L^2 + (2m + 1)^2 \pi^2} \tag{6.3.25}$$

$$F(x, t) = \sum_{m=0}^{\infty} F_m(t) \cos(\lambda_m(x - L)) \tag{6.3.26}$$

$$T_m(t_s) = \frac{2}{L} \left[\sum_{n=0}^{\infty} \left(B_n e^{-(1+\alpha_n^2)t_s} + \rho g_n - \frac{h(0)}{\cosh(L)} g_n \right) \right.$$
$$\left. \times \frac{2(2m + 1)\frac{\pi}{L}(-1)^m \cos(\alpha_n L)}{[(2m + 1)\frac{\pi}{L}]^2 - 4\alpha_n^2} \right]. \tag{6.3.27}$$

6.3.3 Full Solution and Return Map

The full solution of system (6.2.6)-(6.2.9) from time $t = 0$ to $t = t_s + T_a$ is given by

$$V(x,t) = \begin{cases} \sum_{n=0}^{\infty} (B_n e^{-(1+\alpha_n^2)t} + \rho g_n) \cos(\alpha_n(L-x)) & \text{if } 0 < t \le t_s \\ \sum_{n=0}^{\infty} (A_n(t) + H(t)g_n) \cos(\alpha_n(L-x)) & \text{if } t_s < t \le t_s + T_a, \end{cases}$$

$$(6.3.28)$$

where

$$A_n(t) = \frac{\sum_{m=0}^{\infty} T_m(t) \left[\frac{4\gamma(2n+1)\pi/L(-1)^n}{((2n+1)\pi/L)^2 - 4\alpha_n^2} + 2\cos(\frac{(2m+1)\pi}{2}) \right]}{\cos(\alpha_n L)(\beta_n + L\gamma/\cos^2(\alpha_n L) + 2)} \tag{6.3.29}$$

$$H(t) = \frac{h(t-t_s)}{\cosh(L)}. \tag{6.3.30}$$

We have expanded the eigenfunctions of (6.3.18)-(6.3.21) in terms of the nonorthogonal eigenfunctions of the non-spiking solution for simplicity of notation. If we now let t_s^j be the time of the jth somatic spike, the general solution can be written as

$$V(x,t) = \begin{cases} \sum_{n=0}^{\infty} (B_n^j e^{-(1+\alpha_n^2)(t-(t_s^{j-1}+T_a))} + \rho g_n) \cos(\alpha_n(L-x)) & \text{if } t_s^{j-1} + T_a < t \le t_s^j \\ \sum_{n=0}^{\infty} (A_n^j(t) + H(t)g_n) \cos(\alpha_n(L-x)) & \text{if } t_s^j < t \le t_s^j + T_a. \end{cases}$$

$$(6.3.31)$$

Let V_n^j be the coefficients of the nonorthogonal basis expansion of the voltage trace right after the jth spike. We can then define a return map for the coefficients of our expansions

$$\phi_1 : V_n^j \rightarrow B_n^{j+1} e^{-(1+\alpha_n^2)(t_s^{j+1} - (t_s^j + T_a))} + \rho g_n$$

$$\phi_2 : B_n^{j+1} e^{-(1+\alpha_n^2)(t_s^{j+1} - (t_s^j + T_a))} + \rho g_n \rightarrow A_n^{j+1}(t_s^{j+1} + T_a) + H(t_s^{j+1} + T_a)g_n = V_n^{j+1}$$

$$\Phi = \phi_2 \circ \phi_1 : V_n^j \rightarrow V_n^{j+1}, \tag{6.3.32}$$

again where t_s^{j+1} is found by solving

$$\sum_{n=0}^{\infty} (B_n^{j+1} e^{-(1+\alpha_n^2)(t_s^{j+1} - (t_s^j + T_a))} + \rho g_n) \cos(\alpha_n L) = 1, \tag{6.3.33}$$

and $B_n^{j+1} = V_n^j - \rho g_n$. Figure 6.3.2 plots an example of the return map (6.3.32). Fixed points of this map correspond to either oscillatory or constant somatic dynamics.

In the next section, we use the analytic solution to probe the model's behavior. Although the solution is in the form of an infinite series, the coefficients decay fairly rapidly as n is increased. Therefore, we truncate the series to include the first 10 terms. We checked the accuracy of the truncated series against the solution found from numerically simulating the model (6.2.6)-(6.2.9) using the Crank-Nicolson method. We found that the two solutions were in very good agreement and that the analytic solution was obtained in far less time than the numerically simulated one.

6.4   Model Behavior

In this section, we describe the results obtained by numerically iterating the map found in the previous section using two different spike approximation functions, $h(t)$: a "sigmoidal" spike, and a "linear" spike. We analytically determine the param-
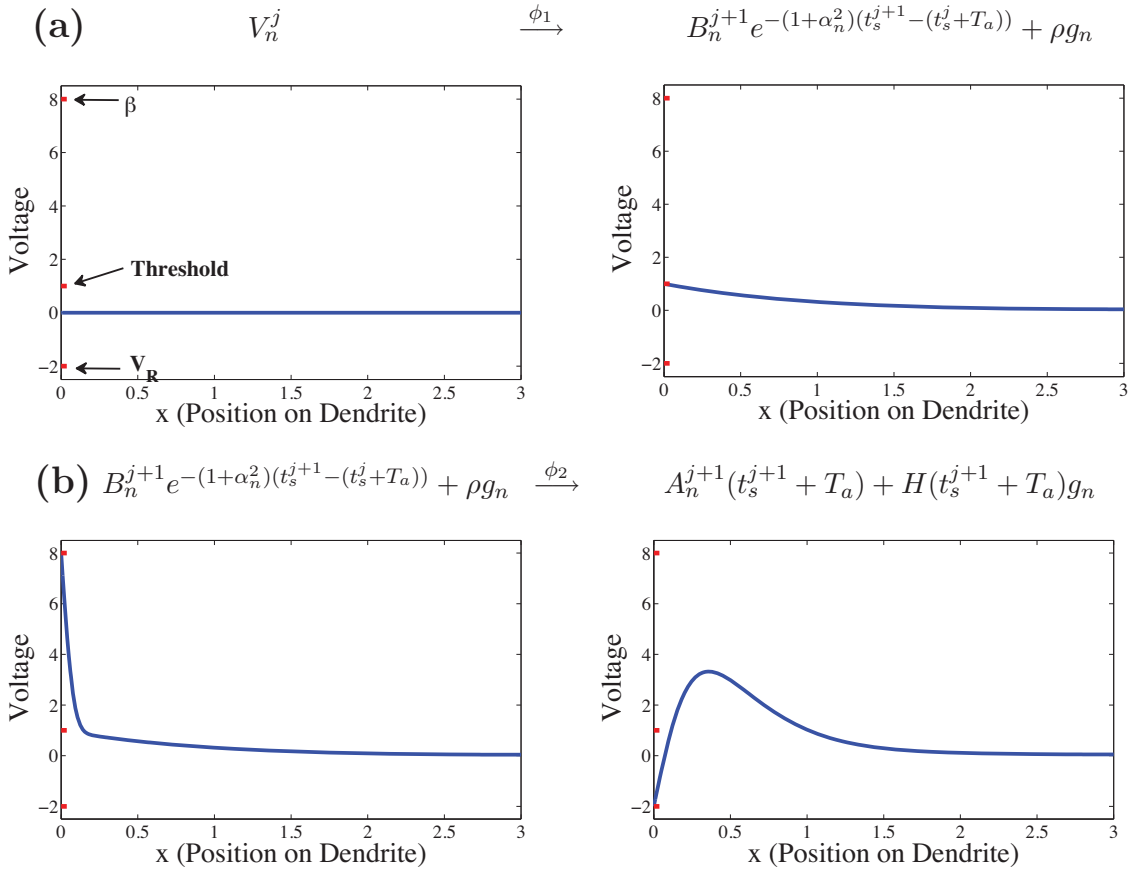
(a) V_n^j $\xrightarrow{\phi_1}$ $B_n^{j+1}e^{-(1+\alpha_n^2)(t_s^{j+1}-(t_s^j+T_a))} + \rho g_n$

(b) $B_n^{j+1}e^{-(1+\alpha_n^2)(t_s^{j+1}-(t_s^j+T_a))} + \rho g_n$ $\xrightarrow{\phi_2}$ $A_n^{j+1}(t_s^{j+1}+T_a) + H(t_s^{j+1}+T_a)g_n$

Figure 6.3.2: **Return Map for the Leaky-Integrate-and-Fire Ball-and-Stick Model**. (a) ϕ_1 maps the voltage profile of the dendrite immediately after the jth somatic spike $t = t_s^j + T_a$ to the voltage profile when the the somatic $(x = 0)$ voltage has reached 1, i.e. $V(0, t_s^{j+1}) = 1$. (b) ϕ_2 jumps the voltage at the soma up to a value β at time t_s^{j+1} then maps the corresponding voltage profile to the voltage profile at the end of the $j+1^{st}$ spike where the somatic voltage is reset to V_R. The composition of the two maps $\Phi = \phi_2 \circ \phi_1$ maps the voltage profile from immediately after the jth somatic spike to the profile at the end of the $j + 1^{st}$ spike.

eter values where the quiescent state disappears and leads to periodic oscillations. Furthermore, by using the map, we find regions in parameter where the system can display bistability between periodic firing and quiescence. We then examine the effects of altering the various parameters on the size of the bistable region.

6.4.1   "Sigmoidal" Spike

When the voltage at the soma reaches threshold, the sigmoidal spike jumps the voltage up to a value β, holds it there for a time T_a, and then quickly, but smoothly, resets the somatic voltage to a value of V_R (see Figure 6.4.1). In equation form, the sigmoidal spike is

$$h(t - t_s) = \beta(1 - e^{p(t-t_s-T_a)})^4 + V_R(1 - (1 - e^{p(t-t_s-T_a)})^4); \quad t \in (t_s, t_s + T_a], \quad (6.4.1)$$

where β represents the maximal somatic potential that is reached during the spike, T_a is the duration of the spike, V_R is the value of the somatic potential after the spike has completed, and we set $p = 80$ in all of the figures shown. Note that the function $h(t)$ converges to the heaviside function (6.7.1) as $p \to \infty$. Thus, the sigmoidal spike can be thought of a continuous approximation to the box function.

Somato-Dendritic "Ping-Pong"

Recall that the steady state voltage of equation (6.2.6) with the non-spiking proximal boundary condition is described by equation (6.3.1). Using this equation, one can determine that the amount of current needed to bring the steady state voltage of the soma $(x = 0)$ above threshold is

$$\bar{I}_s = \gamma \tanh(L) + G_L. \quad (6.4.2)$$

If a current greater than $\bar{I}_s$ is applied to the soma, i.e. $I > \bar{I}_s$, then the steady-state voltage of the soma is guaranteed to be above the threshold voltage of 1. This implies
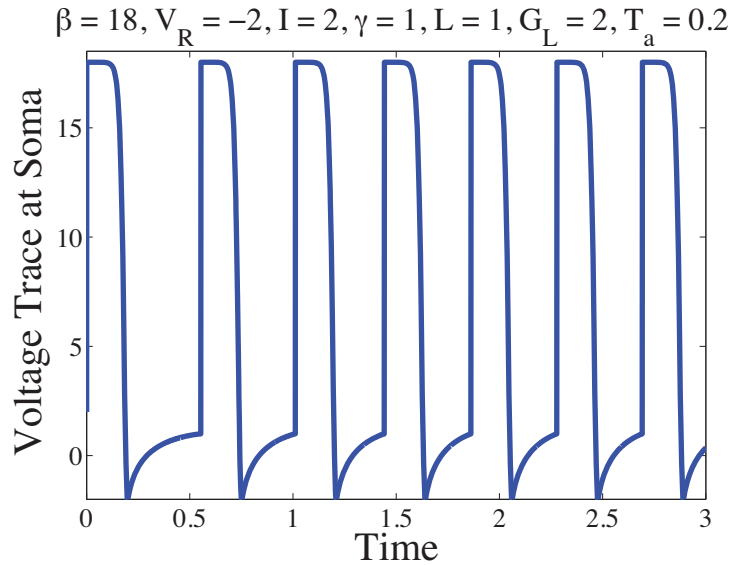
Figure 6.4.1: **Voltage Trace at the Soma $(x = 0)$ with the "Sigmoidal" Spike Function (6.4.1)**. The sigmoidal spike jumps the voltage up to a value β, holds it there for a time T_a, and then quickly, but smoothly, resets the somatic voltage to a value of V_R. In all of the subsequent figures, $p = 80$.

the steady-state voltage profile given by (6.3.1) has disappeared, and the soma will fire periodically. On the other hand, if $I < \bar{I}_s$, then the system will go to the steady-state voltage profile given by equation (6.3.1). Notice that equation (6.4.2) separates the influences of the dendrite from the intrinsic properties of the leaky-integrate-and-fire soma. That is, the first term on the righthand side accounts for the effects of the dendritic load on the firing dynamics of the soma. Since this term limits to γ as $L \to \infty$, an applied current greater than $\gamma + G_L$ guarantees that the soma will fire periodically. Thus, the length of the dendrite has a limited effect on the firing dynamics of the soma, while increasing the strength of the dendritic perturbation, γ, will always increase the applied current necessary to guarantee periodic firing of the soma. The second term on the righthand side of equation (6.4.2) is what one would obtain for the standard leaky-integrate-and-fire model and it tells us that, as

the soma gets leakier, more applied current is needed to guarantee periodic firing.

The frequency-applied current curve for the standard leaky-integrate-and-fire neuron, which corresponds to $\gamma = 0$ in our model, is plotted in Figure 6.4.2 (a). As expected from equation (6.4.2), an applied current greater than G_L causes the stable steady-state to disappear, and the system to fire periodically. If $\gamma \neq 0$ as in Figure 6.4.2 (b), one can see that the system does indeed fire periodically when $I > \bar{I}_s \approx 3$. However, the oscillatory regime also extends backwards beyond $\bar{I}_s$. That is, the addition of the dendrite causes there to be a region of bistability between periodic firing and a stable steady-state, i.e. quiescence.
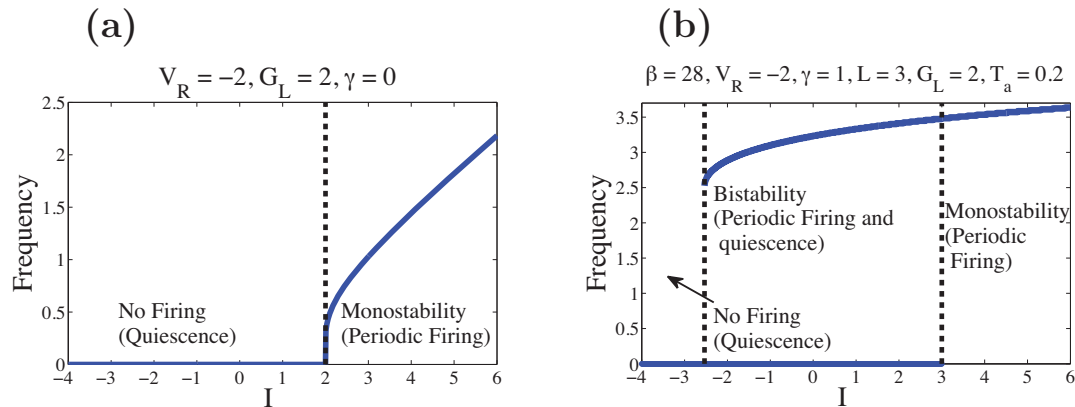

Figure 6.4.2: **Addition of the Dendrite Causes Bistability in the Leaky-Integrate-and-Fire Neuron.** (a) Frequency-applied current curve for the standard leaky-integrate-and-fire neuron, $\gamma = 0$ in our model, when $G_L = 2$ and $V_R = -2$. As predicted from equation (6.4.2), an applied current greater than 2 causes the stable steady-state corresponding to quiescence to disappear. As such, the system only has a stable oscillatory solution and fires periodically. (b) Frequency-applied current curve for the leaky-integrate-and-fire ball-and-stick model. For these parameters, the current needed to bring the steady state voltage of the soma above threshold is $\bar{I}_s \approx 3$. However, it is clearly seen that the periodic solution stably coexists with the quiescent solution before the applied current reaches $\bar{I}_s$.

The periodic firing of the soma when $I < \bar{I}_s$ seen in Figure 6.4.2 (b) can be explained by examining the spatial voltage profiles at different times during the cycle
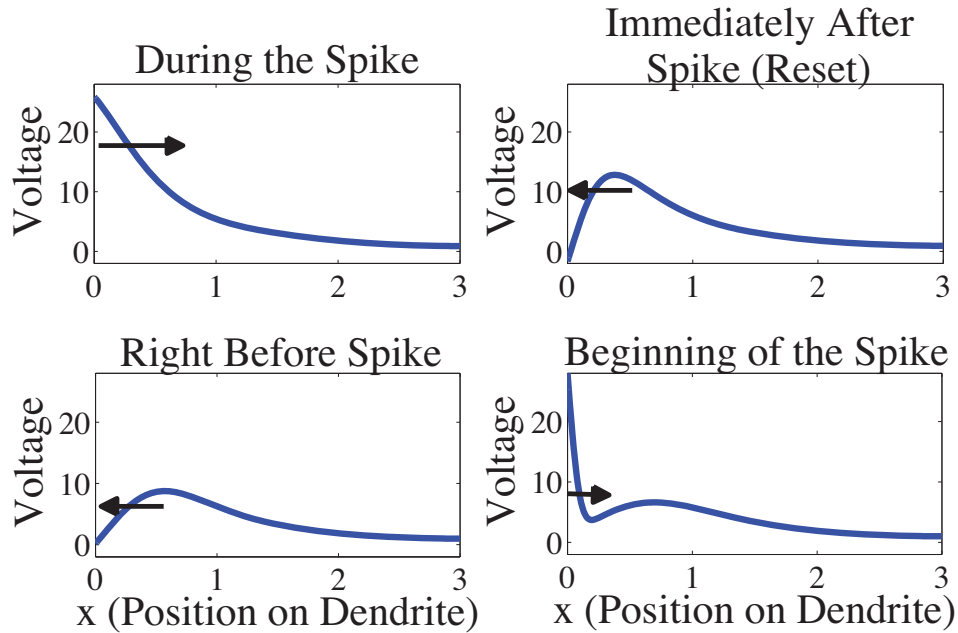
Figure 6.4.3: **Voltage Traces of the Dendrite at Different Times During the Cycle Illustrating Somato-Dendritic "Ping-Pong" for the "Sigmoidal" Spike.** As the soma spikes, the dendrite is depolarized to a large enough potential so that, when the somatic potential is reset, the the potential difference between the soma and proximal dendrite causes a depolarizing current to flow into the soma. This current brings the soma back above threshold even though the applied current is below $\bar{I}_s$. The parameters used in this simulation are $L = 3$, $G_L = 2$, $\gamma = 1$, $I = 1.5$, $\beta = 28$, $V_R = -2$, $T_a = .2$. Note that for these parameter values, $\bar{I}_s = 3$. The arrows indicate the direction of depolarizing current flow between the soma and dendrite.

as in Figure 6.4.3. The portion of the dendrite proximal to the soma becomes so depolarized during a spike that, once the soma has been reset, the potential gradient between the soma and proximal dendrite causes a depolarizing current to flow into the soma. This current brings the membrane potential of the soma back above threshold even when the applied current to the soma is insufficient to bring the steady-state somatic potential above threshold. Thus, the cell is held in the oscillatory regime by a constant "ping-ponging" of the somatic and dendritic potentials. Note that this behavior can only occur when the area of the spike is sufficiently large and when the

dendrite has a non-weak effect on the soma, i.e. γ is not small. That is, the height of the somatic spike β has to be sufficiently large and has to occur for a long enough period of time so as to allow the proximal dendrite time to depolarize. When the soma is reset, the current that flows into the soma due to potential gradient between the soma and proximal dendrite is represented by the term $\gamma \frac{\partial V}{\partial t}(0, t)$ in the non-spiking boundary condition. Thus, if γ is very small, the current that flows into the soma after the spike will not be sufficient to drive its voltage back above threshold.

In the next section, we examine the effects that changing the different system parameters have on the size of the bistable region.

Effects of Parameters on the Region of Bistability

Figure 6.4.4 shows how the spike parameters β and T_a affect the region of bistability. The figure shows two parameter bifurcation diagrams for the applied current to the soma, I, versus the maximum somatic depolarization during the spike, β, and I versus the duration of the spike, T_a. Note that, for all values of β and T_a, the neuron is in the monostable firing regime when the applied current is above $\bar{I}_s$ (solid black line in both plots). This is due to the fact that the spike parameters β and T_a do not affect $\bar{I}_s$. Figure 6.4.4 (a) shows that a sufficiently large amplitude of the spike is needed in order for bistability to occur, and that, as β is increased, the size of the bistable region increases as well, i.e. the dash-dotted line decreases as β is increased. This is due to the fact that larger somatic spike heights cause a larger depolarizations of the proximal dendrite. Figure 6.4.4 (b) shows that, as the duration of the spike is increased, the size of the bistable region initially increases, but eventually reaches a constant value with further increases in T_a. This can be explained as follows. When T_a is large, the somatic potential is held at the depolarized value of β for a long

time. This allows the potential of the dendrite time to equilibrate to the somatic potential. This gives rise to a large amount of current that flows back into the soma after the somatic reset, thus producing the ping-pong effect, i.e. the dash-dotted line branching off from the solid line in the figure. However, further increases in T_a will result in only minimal increases in the proximal dendritic potential, i.e. the maximum amount of current that the dendrite can drive back into the soma after reset saturates as T_a is increased. Thus, further increases in T_a do not decrease the amount of applied current necessary to sustain the ping-pong effect.

(a) $V_R = -2, \gamma = 1, L = 1, G_L = 2, T_a = 0.2$

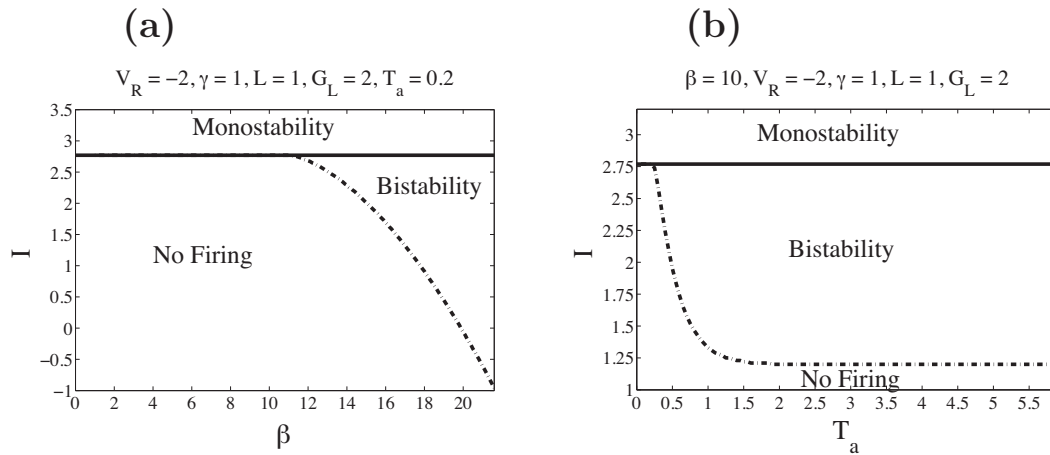**(b)** $\beta = 10, V_R = -2, \gamma = 1, L = 1, G_L = 2$

Figure 6.4.4: **Effects of Altering Spike Parameters on the Size of the Bistable Region Using the Sigmoidal Spike.** In this figure and all subsequent figures, the solid line represents $\bar{I}_s$ while the dash-dotted line represents the minimum amount of applied current needed to sustain the ping-pong effect, i.e. the curve in parameter space where the oscillatory solution first stably coexists with the quiescent solution. (a) Two parameter bifurcation diagram for the applied current to the soma, I, versus β reveals that a sufficiently large amplitude of the somatic spike is necessary for the ping-pong effect to occur. (b) The I versus T_a bifurcation diagram shows that increasing T_a initially decreases the applied current needed to sustain the ping-pong effect (dash-dotted line), but a point is eventually reached where further increases in T_a no longer affect the size of the bistable region.

Figure 6.4.5 illustrates how changes in the dendritic parameters affect the region of bistability. Figure 6.4.5 (a) shows the two parameter bifurcation diagram of the

applied current versus the parameter γ, which scales the dendritic current that flows into the soma. The figure reveals that the amount of applied current needed to drive the neuron into the monostable firing regime increases linearly as γ is increased. Note that this relationship follows directly from equation (6.4.2). However, by non-dimensionalizing the system, we have lost any dependence of $\bar{I}_s$ on the leakage reversal potential of the dendrite E_{LD}. Intuitively, if the dendrite acts as a "load" on the soma, i.e. $E_{LD} < V_{th}$, then the amount of applied current needed to sustain monostable firing should increase as the dendritic influence on the soma, γ, is increased. On the other hand, if $E_{LD} > V_{th}$, the dendrite should drive depolarizing current into the soma (when the somatic potential is subthreshold) and the amount of applied current needed to sustain monostable firing should decrease with increasing γ. Therefore, for further insight into system behavior, we present the dimensional form of $\bar{I}_s$, $\bar{i}_s$

$$\bar{i}_s = \gamma g_{LD}(V_{th} - E_{LD})\tanh(L) + g_L(V_{th} - E_L). \qquad (6.4.3)$$

When $E_{LD} < V_{th}$ ($E_{LD} > V_{th}$), $\bar{i}_s$ increases (decreases) with increasing γ. Thus, $\bar{i}_s$ agrees with our physical intuition about the load properties of the dendrite. Figure 6.4.5 (a) also shows that γ has to be sufficiently large in order for the ping-pong effect to occur, and that further increases in γ decrease the amount of applied current needed to sustain the ping-pong effect. This can be explained by considering the non-spiking somatic boundary condition. That is, the dendritic current ($\gamma\frac{\partial V}{\partial x}(0, t)$) can be quite large after the spike due to the potential gradient. Increasing γ increases the depolarizing current that flows from the dendrite into the soma after the spike. Thus, the soma requires less applied current to sustain the ping-pong effect as γ is increased.

Figure 6.4.5 (b) plots the two parameter bifurcation diagram of the applied current
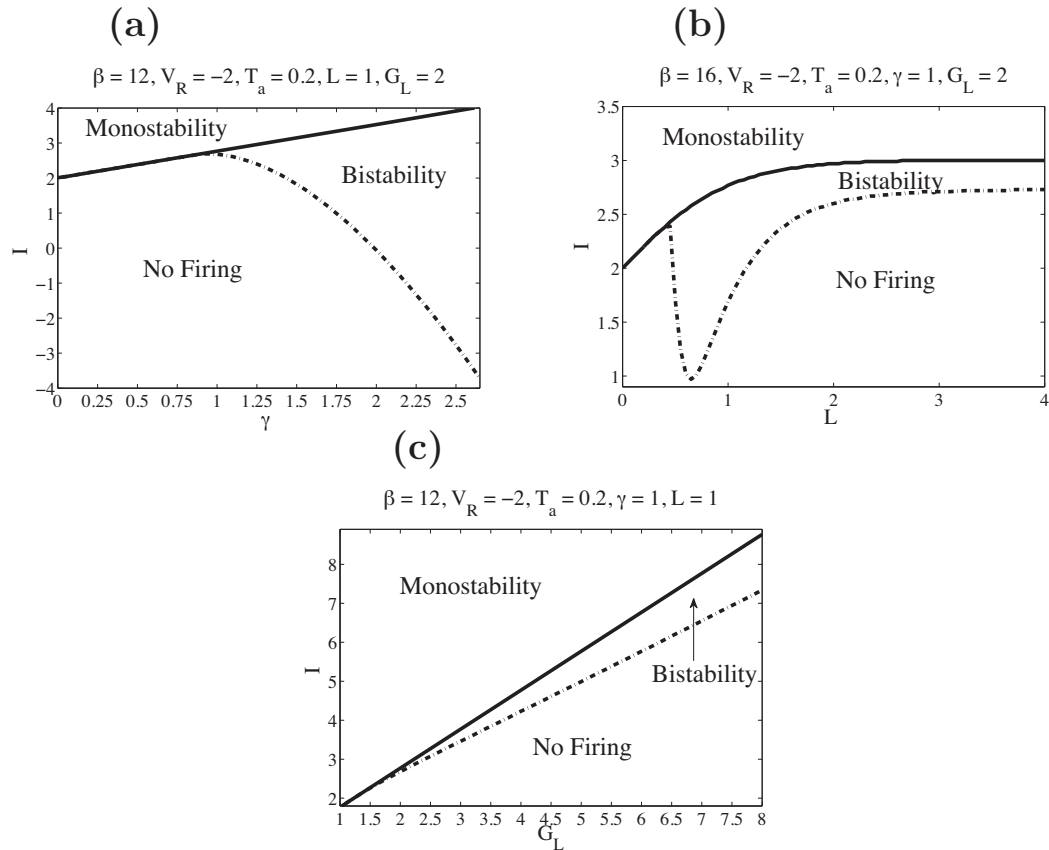
(a)

(b)

(c)

Figure 6.4.5: **Effects of Altering Intrinsic Parameters on the Size of the Bistable Region Using the Sigmoidal Spike.** (a) Two parameter bifurcation diagram of the applied current versus the parameter γ which represents the strength of the dendritic perturbation. The amount of current needed to drive the neuron into the monostable firing regime increases linearly as γ is increased as illustrated by equation (6.4.2). However, the amount of applied current needed to sustain the ping-pong effect decreases and even becomes negative as γ is increased. (b) Two parameter bifurcation diagram of the applied current versus the electrotonic length of the dendrite, L. The diagram reveals that there is an optimal length of the dendrite for which there is the largest range of applied current that sustains the ping-pong effect. Also, the figure shows that it is possible for the system to transition from monostable firing to quiescence to bistable firing and back to quiescence as L is increased. (c) Two parameter bifurcation diagram of the applied current versus the ratio of the somatic and dendritic leakage conductance, G_L. As with increasing γ, the amount of current needed to push the cell into the monostable firing regime increases linearly as G_L is increased (see equation (6.4.2)). The diagram reveals that, for the spike parameters listed, the soma has to be "leakier" than the dendrite in order for the ping-pong effect to occur. However, if the soma becomes too leaky, then the oscillations can be killed off altogether.

versus the electrotonic length of the dendrite, L. For small values of I, i.e. below about .8, there are no values of L for which the cell fires periodically. For values of I from around .8 to 2, the neuron does not fire periodically for small values of L. This occurs because, when the length of dendrite is small, the dynamics of the dendritic potential are dominated by the dynamics of the the somatic potential. Therefore, if $I < \bar{I}_s$, then the neuron goes to the stable steady-state (quiescence). Eventually, as L is increased, the cable becomes long enough so that the dynamics of the dendritic potential can differ from that of the somatic potential, i.e. the dendritic potential can remain depolarized even after somatic reset. This causes the ping-pong effect to occur, and the neuron can fire periodically. However, as L is increased further, the neuron no longer fires periodically and goes back to quiescence. This is due to the fact that when the length of the dendrite is large, the dendrite acts as a current sink for the soma, and more applied current is needed to sustain the ping-pong effect. For intermediate values of I, from 2 to about 2.48, the current is enough to bring the potential soma above threshold for small L. However, as L is increased, the applied current becomes insufficient to drive the somatic potential above threshold and the neuron enters a small region of quiescence. This is due to the fact that $\bar{I}_s$ is an increasing function of L. Therefore, as soon as $\bar{I}_s$ becomes greater than I, the neuron goes back to quiescence because the dendrite is still short enough so that its voltage dynamics are dominated by the somatic potential. As with the values of I between .8 and 2, the neuron then goes to bistability followed by quiescence as L is increased further. There is also a region of applied current, around 2.7 to 2.8, where the neuron starts off in the monostable firing regime, and then enters and remains in the bistable firing regime as L is increased. This occurs because I stays above $\bar{I}_s$ even when L becomes large enough for the ping-pong effect to occur. Therefore,

as soon as $\bar{I}_s$ becomes greater than I, the neuron goes into the bistable region, and never goes into a state of only quiescence. The figure also reveals that there is an optimal length of the cable for which there is the largest range of applied current that sustains the ping-pong effect. This occurs at the point where the dendrite drives the maximum amount of depolarizing current into the soma after somatic reset.

Figure 6.4.5 (c) plots the two parameter bifurcation diagram of the applied current versus the ratio of the somatic and dendritic leakage conductance, G_L. The figure shows that if the dendrite is more leaky than the soma, i.e. $G_L < 1$, the ping-pong effect can not occur for the spike parameters given. Triggering the ping-pong effect to when $G_L < 1$ would require and even larger somatic spike height. When the soma is more leaky, i.e. $G_L > 1$, a greater amount of current is needed to drive it above threshold. However, if the soma is started off spiking, the spike causes a large depolarization in the dendrite, as it is less leaky than the soma, and the dendrite drives a greater amount of depolarizing current into the soma after somatic reset. Thus, less applied current is needed to sustain the ping-pong affect. However, since the soma becomes more leaky as G_L is increased, the amount of applied current needed to sustain the ping-pong effect also increases.

6.4.2 "Linear" Spike

When the voltage at the soma reaches threshold, the linear spike jumps the voltage up to a value β and then linearly decreases the voltage with slope $\frac{V_R - \beta}{T_a}$ until it reaches V_R (see Figure 6.4.6). In equation form, the linear spike is

$$h(t - t_s) = \left(\frac{V_R - \beta}{T_a} \right) (t - t_s) + \beta. \tag{6.4.4}$$

Once again, β represents the maximum somatic potential that is reached during the
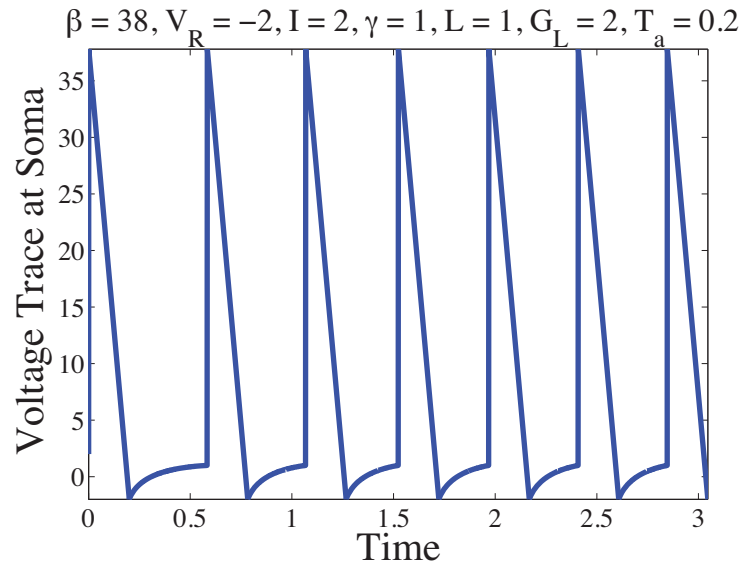
Figure 6.4.6: **Voltage Trace at the Soma ($x = 0$) with the "Linear" Spike Function (6.4.4).** After reaching threshold, the somatic potential is jumped up to a value β. The potential then linearly decreases to V_R.

spike, T_a is the duration of the spike, and V_R is the value of the somatic potential after the spike has completed.

As in the case of the sigmoidal spike, bistability between periodic firing and quiescence can also be seen with the linear spike. The bistability again occurs as a result of a somato-dendritic ping-pong effect. The bifurcation diagrams for the linear spike are all qualitatively similar to those for the sigmoidal spike except for the two diagrams shown in Figure 6.4.7. Compare the diagram for I versus T_a in Figure 6.4.7 (a) to that of Figure 6.4.4 (b). Although the bifurcation to bistability occurs similarly for both spike types, bistability eventually ceases as the duration of the linear spike becomes too large. This is due to the fact that as the duration of the spike becomes larger, the slope of the linear spike gets smaller, allowing the dendrite more time to equilibrate to the somatic potential. Eventually, the duration of the spike

is long enough so that the proximal dendritic potential is able to exactly track the somatic potential as it decreases to the reset potential. Thus, there is no longer a large potential gradient between the proximal dendrite and the soma after the spike, and the ping-pong effect ceases to occur.
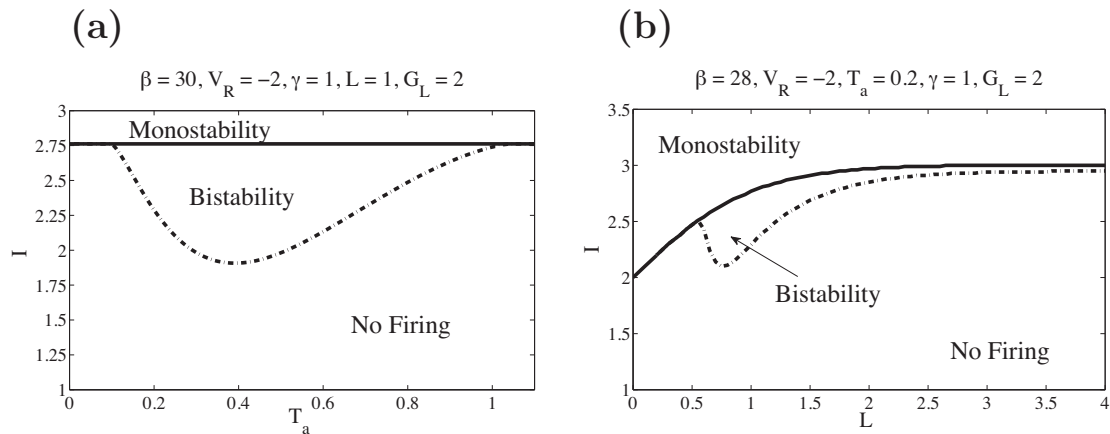

Figure 6.4.7: **Altering Spike Duration and Electrotonic Length of the Dendrite Using the Linear Spike Reveal Differences in the Qualitative Behavior of the System with the Different Spike Shapes.** (a) Applied current versus spike duration bifurcation diagram shows that there is an optimal length of the spike for which there is the largest range of applied current that sustains the ping-pong effect. This is due to the fact that the linear spike has a slower reset as T_a is increased. (b) Applied current versus eletrotonic length bifurcation diagram for the linear spike shows that there is a region of applied current for which the neuron can go from the monostable firing regime to quiescence and never pass into the bistable region as L is increased.

Figure 6.4.7 (b) reveals that the bifurcation diagram for applied current versus electrotonic length for the linear spike is similar to the sigmoidal spike (see Figure 6.4.5 (b)) except that the linear spike causes there to be a region of applied current, around 2 to 2.1, such that the cell can go from the monostable firing regime to quiescence and never pass into the bistable region as L is increased. This is due to the fact that the sigmoidal spike allows the dendrite more time to equilibrate to the

maximum somatic potential during the spike. This causes more current to be driven into the soma after reset, which means that less applied current is needed to sustain the ping-pong effect. Thus, the size of the bistable region for the sigmoidal spike will be larger than that of the linear spike.

6.5 Two Compartment Leaky-Integrate-and-Fire Model

Although we are able to derive the analytical solution to the leaky-integrate-and-fire ball-and-stick model, the form of the solution is difficult to analyze mathematically. In order to obtain a more tractable solution, we reduce the complexity of the leaky-integrate-and-fire ball-and-stick model by lumping the dendritic cable into a single passive compartment that is electrically coupled to a leaky-integrate-and-fire neuron that explicitly includes spike effects, i.e. a two-compartment model [9, 22, 59, 77]. In this case, we obtain a one-dimensional map that completely captures the dynamics of the system.

The dendrite is now modeled a single passive compartment that is electrically coupled to the soma

$$C_m\frac{d\bar{V}_D}{d\bar{t}} = -g_{LD}(\bar{V}_D - E_{LD}) + \frac{g_c}{A_D}(\bar{V}_S - \bar{V}_D) \qquad (6.5.1)$$

where $\bar{V}_D$ is the voltage of the dendritic compartment, C_m is the membrane capacitance, g_{LD} is the dendritic leakage conductance, E_{LD} is the dendritic leakage reversal potential, g_c is the gap junctional conductance, and A_D is the area of the dendritic compartment.

The soma is modeled as a leaky-integrate-and-fire compartment. The non-spiking

voltage of the soma is governed by

$$C_m \frac{d\bar{V}_S}{d\bar{t}} = -g_{LS}(\bar{V}_S - E_{LS}) + \frac{g_c}{A_S}(\bar{V}_D - \bar{V}_S) + \bar{I}, \tag{6.5.2}$$

where $\bar{V}_S$, is the voltage of the somatic compartment, E_{LS} is the leakage reversal potential of the somatic compartments, g_{LS} is the somatic leakage conductance, $\bar{I}$ is the applied current to the soma, and A_S is the area of the somatic compartment. As in the previous section, when V_S reaches a threshold voltage at time $\bar{t}_s$, $\bar{V}_S(\bar{t}_s) = V_{th}$, the voltage of the soma is then given by

$$\bar{V}_S(\bar{t}) = \bar{h}(\bar{t} - \bar{t}_s), \tag{6.5.3}$$

where $\bar{h}(\bar{t})$ is some function to approximate the shape of the spike for $\bar{t} \in (\bar{t}_s, \bar{t}_s + \bar{T}_a]$.

In non-dimensional form, the leaky-integrate -and-fire two-compartment model is given by

$$\frac{dV_D}{d\bar{t}} = -V_D + \alpha g(V_S - V_D) \tag{6.5.4}$$

$$\begin{cases} \dfrac{dV_S}{dt} = -g_{lk}V_S + g(V_D - V_S) + I & \text{if } V_S(t) \le 1 \text{ and } t \notin (t_s, t_s + T_a] \\ V_S(t) = h(t - t_s) & \text{if } V_S(t) > 1 \text{ or } t \in (t_s, t_s + T_a], \end{cases} \tag{6.5.5}$$

where $V_j(t) = \frac{\bar{V}_j(\bar{t}/\tau_D) - E_{LD}}{V_{th} - E_{LD}}$ and $j = S, D$, $\tau_D = C_m/g_{LD}$, $\alpha = \frac{A_S}{A_D}$, $g = \frac{g_c}{A_S g_{LD}}$, $g_{lk} = g_{LS}/g_{LD}$, $I = \frac{\bar{I} + g_{LS}(E_{LS} - E_{LD})}{g_{LD}(V_{th} - E_{LD})}$, and $h(t) = \frac{\bar{h}(\bar{t}/\tau_D) - E_{LD}}{V_{th} - E_{LD}}$.

6.6   One Dimensional Map for the Two Compartment Model

We reduce the dynamics of the full two-compartment model to a one-dimensional return map. The idea behind this is as follows. When the steady-state of the non-spiking somatic dynamics is above the threshold of 1, the soma fires periodically and the system is in the monostable oscillatory regime. However, if the steady-state is below 1, then there are three scenarios that can take place depending upon initial value of the dendritic potential (see Figure 6.6.1). The first scenario is that the system goes to its steady-state corresponding to quiescence (far left trajectory in Figure 6.6.1). The second scenario is that the trajectory of the system crosses threshold (far right trajectory in Figure 6.6.1), and the somatic dynamics are switched to the spiking dynamics for a time T_a after which the potential is returned to a value V_R and everything starts all over again. The last scenario is that the trajectory touches the threshold, but does not cross it and the system goes to the steady-state (middle trajectory in Figure 6.6.1). This last scenario separates the system trajectories into values of the initial dendritic voltage that will lead to steady-state behavior, $V_D(0) < V^*$, and values of the initial dendritic voltage that will lead to spiking, $V_D(0) > V^*$. The ping-pong effect has a chance of occurring only when $V_D(0) > V^*$. Therefore, to derive the return map for the system we must first derive the analytical solution for the non-spiking portion of the model, find the value for V^* that separates initial dendritic voltages that lead to steady-state behavior from those that lead to spiking, and then derive the analytical solution for the spiking portion of the model.
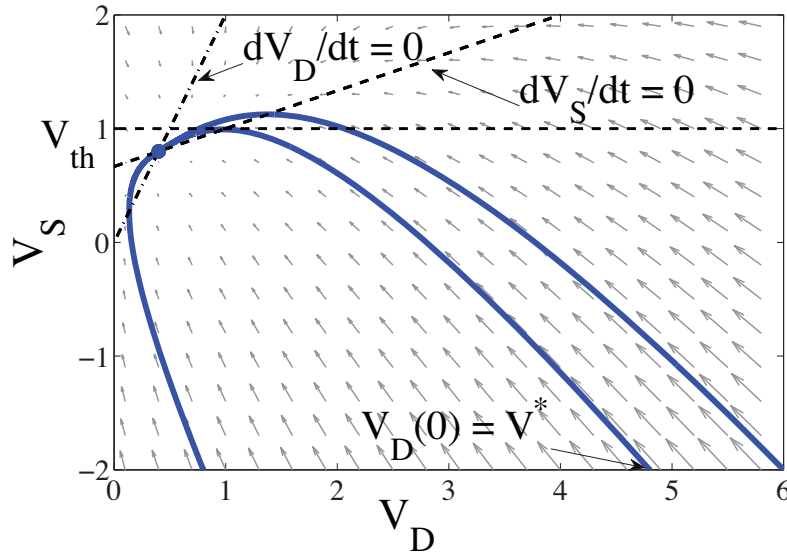
Figure 6.6.1: **Phase Plane for the Non-Spiking Portion of the Two-Compartment Model.** The trajectory that begins at (V^*, V_R) touches the somatic threshold value of 1, but does not cross it. Therefore, V^* is the value of $V_D(0)$ (given that $V_S(0) = V_R$) that separates trajectories between those that cross threshold and those that converge to the steady state. Note that, once the trajectory crosses threshold, the dynamics are then governed by the spiking portion of the model after which the somatic potential is brought back to $V_R = -2$.

6.6.1 Non-Spiking Solution

The solution to the non-spiking portion of the two-compartment model is given by

$$V_S(t) = c_1 v_{11} e^{\lambda_1 t} + c_2 v_{21} e^{\lambda_2 t} + V_S^{ss} \qquad (6.6.1)$$

$$V_D(t) = c_1 v_{12} e^{\lambda_1 t} + c_2 v_{22} e^{\lambda_2 t} + V_D^{ss}, \qquad (6.6.2)$$

where

$$V_S^{ss} = \frac{I(1 + \alpha g)}{g + g_{lk} + g\alpha g_{lk}} \tag{6.6.3}$$

$$V_D^{ss} = \frac{I\alpha g}{g + g_{lk} + g\alpha g_{lk}} \tag{6.6.4}$$

$$\lambda_1 = \frac{1}{2}\left(-1 - g - g_{lk} - g\alpha - \sqrt{(1 + g + g_{lk} + g\alpha)^2 - 4(g + g_{lk} + g\alpha g_{lk})}\right) \tag{6.6.5}$$

$$\lambda_2 = \frac{1}{2}\left(-1 - g - g_{lk} - g\alpha + \sqrt{(1 + g + g_{lk} + g\alpha)^2 - 4(g + g_{lk} + g\alpha g_{lk})}\right) \tag{6.6.6}$$

$$v_{11} = \frac{1 + g\alpha + \lambda_1}{g\alpha} \tag{6.6.7}$$

$$v_{12} = 1 \tag{6.6.8}$$

$$v_{21} = \frac{1 + g\alpha + \lambda_2}{g\alpha} \tag{6.6.9}$$

$$v_{22} = 1 \tag{6.6.10}$$

$$c_1 = \frac{v_{11}v_{21}(V_D^{ss} - V_D(0)) + (v_{11} + v_{22})(V_S(0) - V_S^{ss})}{v_{11}(v_{11} - v_{12}v_{21} + v_{22})} \tag{6.6.11}$$

$$c_2 = \frac{v_{12}(V_S(0) - V_S^{ss}) - v_{11}(V_D(0) - V_D^{ss})}{v_{12}v_{21} - v_{11}v_{22}}. \tag{6.6.12}$$

An examination of the phase portrait in Figure 6.6.1 reveals that the system has one stable fixed point given by (V_D^{ss}, V_S^{ss}). Using equation (6.6.3) one can determine the amount of current needed to raise V_S^{ss} above threshold

$$\bar{I}_s = \frac{g}{1 + \alpha g} + g_{lk}. \tag{6.6.13}$$

If $I > \bar{I}_s$ then $V_S^{ss} > 1$ and the soma will be in the oscillatory regime. As with the ball-and-stick model, equation (6.6.13) separates out the influences of the dendrite from the intrinsic properties of the leaky-integrate-and-fire soma. That is, the first term on the righthand side is the dendritic influence on the firing dynamics of the soma. If $g = 0$, meaning the two compartments are uncoupled, this term disappears and

$\bar{I}_s$ simplifies to what one would obtain from the usual leaky-integrate-and-fire model. The first term on the righthand side also disappears if $\alpha \gg 1$. This implies that the soma is much larger than the dendrite, and its dynamics dominate the dynamics of the two-compartment model. On the other hand, if the dendrite is much larger than the soma, then $\alpha \approx 0$ and $\bar{I}_s = g + g_{lk}$. Thus, it would appear that the dendrite always acts as load on the soma, and increasing g would cause the amount of current needed to drive the cell into the oscillatory regime, $\bar{I}_s$, to also increase. However, as with the ball-and-stick model, let us examine the dimensional version of $\bar{I}_s$, $\bar{i}_s$

$$\bar{i}_s = \frac{g_c(V_{th} - E_{LD})}{1 + \alpha g} + g_{LS}(V_{th} - E_{LS}). \tag{6.6.14}$$

Now, when the dendrite is much larger than the soma, i.e. $\alpha \approx 0$, $\bar{i}_s = g_c(V_{th} - E_{LD}) + g_{LS}(V_{th} - E_{LS})$. Therefore, when $E_{LD} < Vth$ the dendrite acts as a load on the soma, while when $E_{LD} > V_{th}$ the dendrite acts as a current source, and increasing g_c causes $\bar{i}_s$ to decrease. Note that this is exactly what was found before with the ball-and-stick model. However, for moderate values of α, $\bar{I}_s$ limits to $\frac{1}{\alpha} + g_{lk}$. Thus, increasing g will have a limited effect on the behavior of the system for moderate values of α. This is similar to increasing L in equation (6.4.2)

6.6.2   Derivation of V^*

As stated earlier, even if the steady state somatic potential is below threshold, there may still be initial values of the dendritic potential that will cause the trajectory in phase space to cross the threshold. Given that the initial somatic voltage is V_R, the value of the initial dendritic potential that separates trajectories from those that cross threshold and those that go to the steady state is given by V^*. The trajectory that starts at this value (V^*, V_R) touches the threshold, but does not cross it. Thus,

we know that this trajectory passes through the point where $\frac{dV_S}{dt} = 0$ and $V_S = 1$.
Using the nullcline for V_S, we find that the solution curve must pass through the
point $(V_D, V_S) = \left(\frac{g_{lk}+g-I}{g}, 1\right)$. The trajectory that passes through this point is given
by

$$V_S^*(t) = c_1^* v_{11} e^{\lambda_1 t} + c_2^* v_{21} e^{\lambda_2 t} + V_S^{ss} \tag{6.6.15}$$

$$V_D^*(t) = c_1^* v_{12} e^{\lambda_1 t} + c_2^* v_{22} e^{\lambda_2 t} + V_D^{ss} \tag{6.6.16}$$

$$c_1^* = \frac{v_{11} v_{21}(V_D^{ss} - \left(\frac{g_{lk}+g-I}{g}\right)) + (v_{11} + v_{22})(1 - V_S^{ss})}{v_{11}(v_{11} - v_{12}v_{21} + v_{22})} \tag{6.6.17}$$

$$c_2^* = \frac{v_{12}(1 - V_S^{ss}) - v_{11}(\left(\frac{g_{lk}+g-I}{g}\right) - V_D^{ss})}{v_{12}v_{21} - v_{11}v_{22}}. \tag{6.6.18}$$

The following equation is then solved to find the time t^* when $V_S^*(t^*) = V_R$

$$V_S^*(t^*) = c_1^* v_{11} e^{\lambda_1 t^*} + c_2^* v_{21} e^{\lambda_2 t^*} + V_S^{ss} = V_R. \tag{6.6.19}$$

The value of the initial dendritic potential that separates trajectories from those that
cross threshold and those that go to the steady state is then given by $V^* = V_D^*(t^*)$.

6.6.3   Spiking Solution and Return Map

The map that takes an initial value of V_D when $V_S = V_R$ to its value when $V_S = 1$
can now be written as

$$\phi_1(V_D^k) = \begin{cases} c_1(V_D^k)v_{12}e^{\lambda_1 t_s^k} + c_2(V_D^k)v_{22}e^{\lambda_2 t_s^k} + V_D^{ss} & \text{if } V_D^k > V^* \\ V_D^{ss} & \text{if } V_D^k \leq V^*, \end{cases} \qquad (6.6.20)$$

where V_D^k is the potential of the dendritic compartment immediately after the kth somatic spike and

$$c_1(V_D^k) = \frac{v_{11}v_{21}(V_D^{ss} - V_D^k) + (v_{11} + v_{22})(V_R - V_S^{ss})}{v_{11}(v_{11} - v_{12}v_{21} + v_{22})} \qquad (6.6.21)$$

$$c_2(V_D^k) = \frac{v_{12}(V_R - V_S^{ss}) - v_{11}(V_D^k - V_D^{ss})}{v_{12}v_{21} - v_{11}v_{22}}. \qquad (6.6.22)$$

The time of the kth somatic spike, t_s^k, is obtained from solving

$$c_1(V_D^k)v_{11}e^{\lambda_1 t_s^k} + c_2(V_D^k)v_{21}e^{\lambda_2 t_s^k} + V_S^{ss} = 1. \qquad (6.6.23)$$

Lastly, the value of V_D after the cell has spiked is obtained by solving equation (6.5.4) from time $t = t_s^k$ to $t = t_s^k + T_a$ using $\phi_1(V_D^k)$ as the initial condition

$$V_D^{k+1} = \phi_2 \circ \phi_1(V_D^k) = \begin{cases} e^{-(1+\alpha g)T_a} \left(\phi_1(V_D^k) + \alpha g \int_0^{T_a} h(s)e^{(1+\alpha g)s}ds \right) & \text{if } V_D^k > V^* \\ V_D^{ss} & \text{if } V_D^k \leq V^*. \end{cases}$$
$$(6.6.24)$$

Note that, when $V_D^k > V^*$, ϕ_2 is a linear map and, in the limit as $h(t) \to \beta\delta(t)$ and $T_a \to 0$, ϕ_2 simply increases the value of ϕ_1 by $\beta\alpha g$. Fixed points of the above map

when $V_D^k > V^*$ correspond to parameter values where the system exhibits periodic firing.

6.7 Two-Compartment Model Behavior

We now examine the behavior of the two-compartment model with two different spike functions a square spike and a linear spike, and we compare the results to those obtained with the ball-and-stick model. As with the ball-and-stick model, we find that the two compartment model exhibits bistable behavior caused by the ping-pong effect between the somatic and dendritic potentials.

6.7.1 Square Spike

We describe the spike by a square pulse

$$h(t - t_s) = \begin{cases} \beta & \text{if } t_s < t < T_a \\ V_R & \text{if } t = t_s + T_a. \end{cases} \qquad (6.7.1)$$

As with the other spike functions, β represents the maximal somatic potential that is reached during the spike, T_a is the duration of the spike, and V_R is the value of the somatic potential after the spike has completed. Figure 6.7.1 (a) plots an example of the somatic and dendritic voltage traces found using the above spike function. Note that the heaviside function described by equation (6.7.1) is the limit of the sigmoidal spike function as $p \to \infty$.

Recall that if $I > \bar{I}_s$, the system is guaranteed to be in the oscillatory regime because V_S^{ss} will be greater than 1. However, as with the ball-and-stick model, the

(a)

$\beta = 13, T_a = 0.2, V_R = -2, g = 1.5, g_{lk} = 2,$
$\alpha = 1, I = 2.5$

(b)

$\beta = 13, T_a = 0.2, V_R = -2, g = 1.5, g_{lk} = 2,$
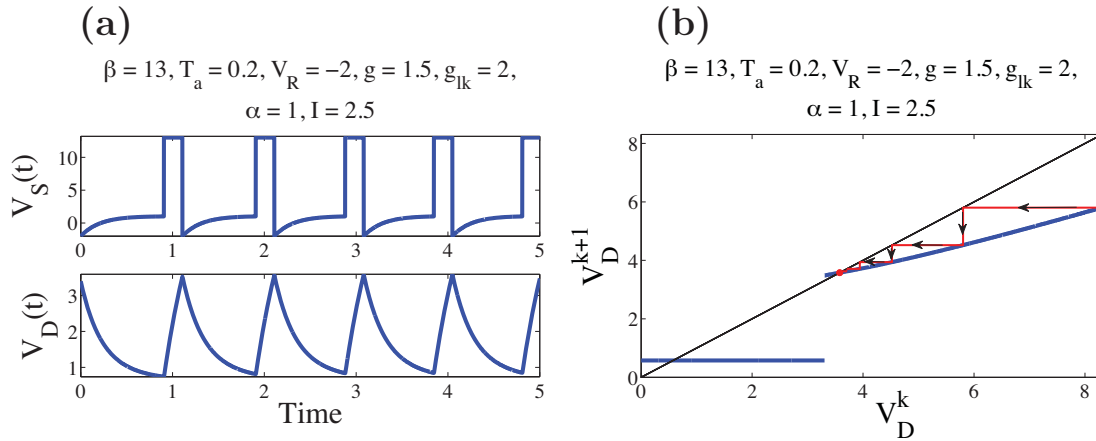$\alpha = 1, I = 2.5$

Figure 6.7.1:   **The Ping-Pong Effect and Bistability in the Two-Compartment Model with the Square Spike Function.** (a) Voltage traces of the somatic and dendritic compartments with the square spike as in equation (6.7.1). For these parameter values, $\bar{I}_s = 2.6$. Thus, the ping-pong effect between the somatic and dendritic compartment potentials holds the system in the oscillatory regime. (b) Return map (6.6.24) derived from the two compartment model with the square spike. The black line is $V_D^{k+1} = V_D^k$. The map has two stable fixed points revealing that the full system displays bistability between periodic firing and quiescence. The lower fixed point represents the stable fixed point (V_D^{ss}, V_S^{ss}) in the full system, and the upper fixed point corresponds to periodic firing in the full system.

two compartment model can still exhibit periodic firing when $I < \bar{I}_s$ as seen in Figure 6.7.1 (a). The plot of the return map (6.6.24) in Figure 6.7.1 (b) reveals that the map has two stable fixed points corresponding to bistability in the full system. All subsequent bifurcation diagrams are generated by finding $\bar{I}_s$ and the location of the upper stable fixed point of the return map.

Effects of Parameters on the Region of Bistability

Altering the spike amplitude β and spike duration duration T_a in the two compartment model with the square spike yields very similar dynamics to the ball-and-stick model with the sigmoidal spike as seen in Figure 6.7.2. A sufficient amplitude of

the spike is needed in order for bistability to occur, and the size of the bistable region increases as β is increased. Also, as the duration of the spike is increased, the amount of applied current needed to sustain the ping-pong effect initially decreases, but eventually approaches a minimum value with further increases in T_a.
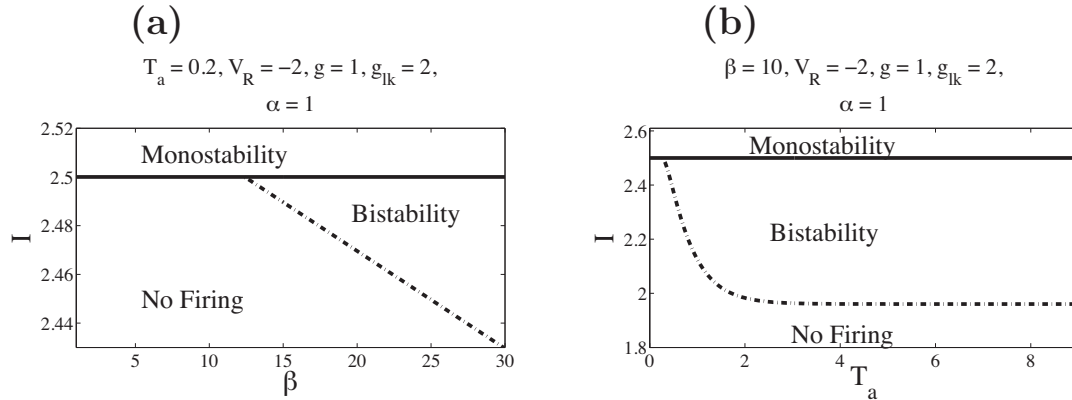

Figure 6.7.2: **Changing Spike Parameters in the Two-Compartment Model with the Square Spike Yields Similar Dynamics to the Ball-and-Stick Model with the Sigmoidal Spike.** (a) Two parameter bifurcation diagram of applied current versus the maximum somatic depolarization during the spike, β. (b) Two parameter bifurcation diagram of applied current versus the duration of the spike, T_a. Both diagrams reveal that the dynamics of the two compartment model with the square spike are qualitatively similar to the ball-and-stick model with the sigmoidal spike (Figure 6.4.4).

Figure 6.7.3 examines how changing other parameters in the two compartment model affect the size of the region of bistability. Figure 6.7.3 (a) depicts the two parameter bifurcation diagram of applied current versus the coupling conductance, g. The diagram reveals that more applied current is required to drive the system into the monostable firing regime as g is increased. This agrees with our interpretation of equation (6.6.13) for moderate values of α. That is, $\bar{I}_s$ limits to $\frac{1}{\alpha} + g_{lk}$ as $g \to \infty$ which is 3 in the figure. However, increasing g also increases the size of the bistable region. This can be explained by considering the non-spiking portion of the model.

The coupling current that the soma receives ($g(V_D - V_S)$) can be quite large after the spike due to the fact that the potential of the dendritic compartment is larger than the potential of the somatic compartment. Increasing g increases this depolarizing coupling current that flows into the soma after the spike. Thus, the soma requires less applied current to sustain the ping-pong effect as g is increased. This is very similar to increasing γ in the ball-and-stick model (see Figure 6.4.5 (a)).

Figure 6.7.3 (b) shows that less applied current is needed to sustain monostable firing as α is increased. This again agrees with our interpretation of equation (6.6.13). That is, increasing α causes the somatic compartment to become larger than the dendritic compartment. Thus, when α is large, the somatic dynamics dominate the behavior of the system. This is evidenced by the fact that $\bar{I}_s$ limits to g_{lk} as $\alpha \to \infty$ which is 2 in the figure. Note since $\bar{I}_s$ limits to a constant value as α is increased, this implies that I should really be interpreted as a non-dimensional current density. The figure also shows that the amount of applied current needed to sustain the ping-pong effect initially decreases with increasing α, but then reaches a minimum and subsequently increases and closes off the bistable region as α is increased. This is due to the fact that when α is small, the dendritic compartment is much larger than the somatic compartment. In this case, the dendrite acts as a current sink for the soma, and the ping-pong effect cannot occur. As α is increased the dendritic compartment becomes less of a current sink allowing the ping-pong effect to occur. Increasing α further causes the soma to become much larger than the dendrite. In this case, the somatic dynamics dominate the dynamics of the dendritic compartment and the ping-pong effect cannot occur. Thus, increasing α is similar to decreasing L in the ball-and-stick model (see Figure 6.4.5 (b)).

Figure 6.7.3 (c) shows that altering the ratio of the leakage conductances in the

two compartment model yields very similar results to the ball-and-stick model. That is, for the spike parameters listed, the soma has to be sufficiently more leaky than the dendrite in order for the ping-pong effect to occur.
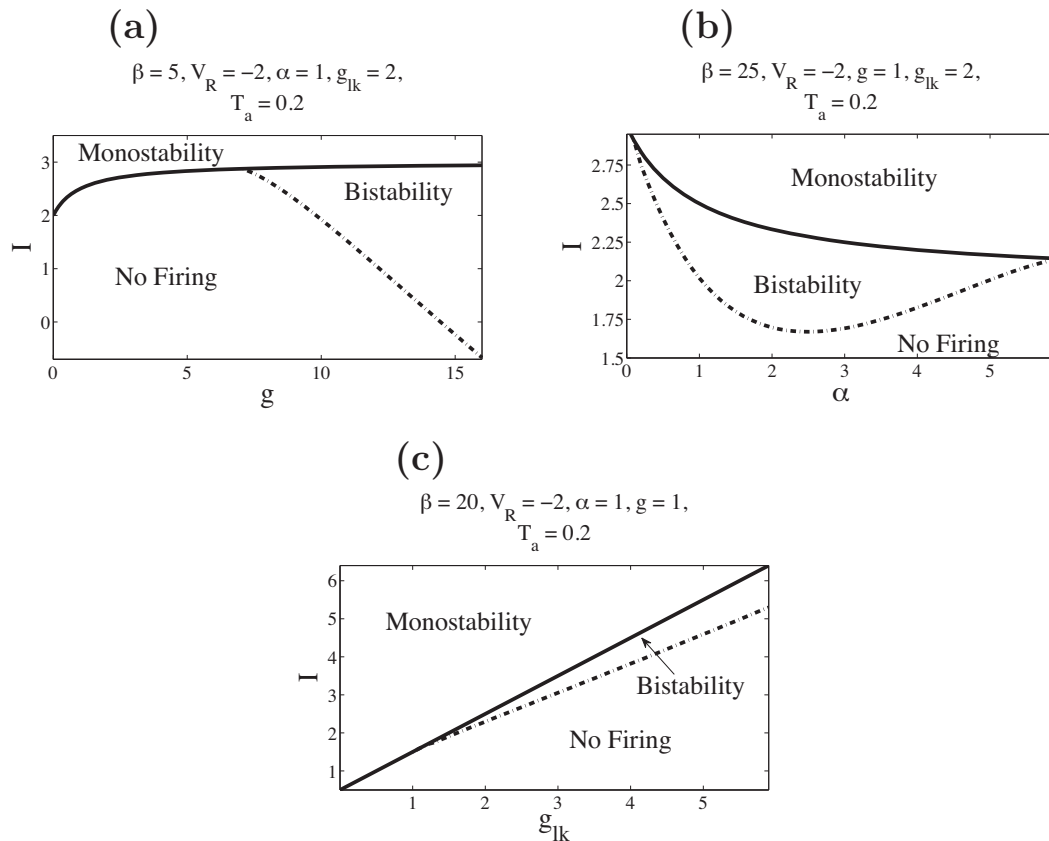

Figure 6.7.3: **Effects of Altering Intrinsic Parameters on the Size of the Bistable Region in the Two-Compartment Model with the Square Spike.** (a) Applied current versus coupling conductance, g, two parameter bifurcation diagram. Once the bistable region appears, it increases in size as g is increased. This is similar to changing the γ parameter in the ball-and-stick model. (b) Applied current versus relative compartment size, α, two parameter bifurcation diagram. As α is increased, the somatic compartment becomes large relative to the dendritic compartment. The diagram reveals that , similar to changing L in the ball-and-stick model, there is an optimal value of α for which you have the largest range of applied current that sustains the ping-pong effect. (b) Applied current versus relative leakage conductance, g_{lk}, two parameter bifurcation diagram. The dynamics are qualitatively similar to changing G_L in the ball-and-stick model.

$$\beta = 15, \, T_a = 0.2, \, V_R = -2, \, g = 1, \, g_{lk} = 2,$$
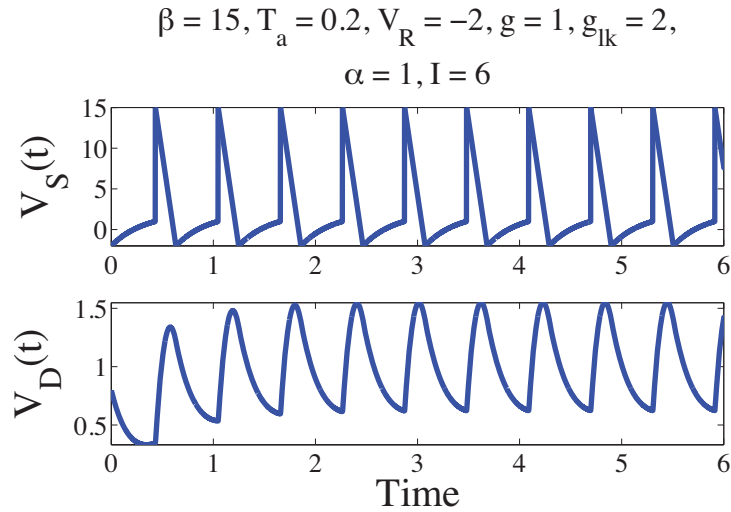$$\alpha = 1, \, I = 6$$

Figure 6.7.4: **Voltage Traces of the Somatic and Dendritic Compartments with the Linear Spike Function.**

6.7.2   Linear Spike

The linear spike is described in section 6.4.2. Figure 6.7.4 plots an example of the somatic and dendritic voltage traces found using the linear spike function. Somato-dendritic ping-pong causes the system to display oscillatory behavior even when the applied current to the soma is below $\bar{I}_s$.

Figure 6.7.5 shows that altering the spike parameters with the linear spike yield qualitatively similar dynamics to the ball-and-stick model with the linear spike (see Figure 6.4.7 (a)). Thus, the two compartment model captures the qualitative behavior of the cable model when considering alterations in the spike parameters. Changing other parameters in the model with the linear spike also yield similar results to those seen with the square spike.

(a)

$T_a = 0.2, V_R = -2, g = 1, g_{lk} = 2,$
$\alpha = 1$

(b)

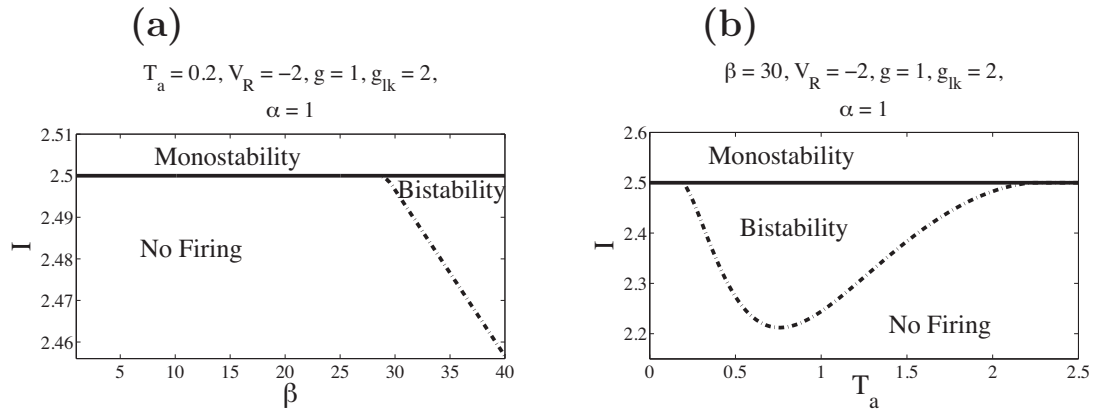$\beta = 30, V_R = -2, g = 1, g_{lk} = 2,$
$\alpha = 1$

Figure 6.7.5: **Altering Spike Parameters in the Two-Compartment Model with the Linear Spike Yields Similar Dynamics to the Ball-and-Stick Model with the Sigmoidal Spike..** (a) Two parameter bifurcation diagram of applied current versus β. (b) Two parameter bifurcation diagram of applied current versus T_a. Both diagrams reveal that the dynamics of the two compartment model with the linear spike are qualitatively similar to the ball-and-stick model with the linear spike function.

6.8   Discussion

In this chapter, we examine the effects of a passive dendrite on the firing dynamics of a leaky-integrate-and-fire neuron that includes spike effects. We model the dendrite as both a passive cable using the cable equation and as a passive compartment. In each case, we analytically derive the amount of applied current necessary to guarantee periodic firing of the soma. We also show that each of the model dynamics can be reduced to a return map. Using the analytical form for the applied current necessary to guarantee periodic firing of the soma and the return map, we show that the addition of the dendrite can cause the system to display bistable behavior between periodic firing and a quiescent state. We identify the mechanism that causes the periodic behavior in the bistable regime as somato-dendritic ping-pong. We then examine the effects of altering system parameters on the size of the bistable region. Lastly, we

show that both models, the ball-and-stick model and the two-compartment model, display qualitatively similar dynamics with regards to the aforementioned bistable behavior.

In previous work, the interaction between the somatic and dendritic membrane potentials has been shown to be important in generating neuronal bursting, in which a cell periodically switches between a quiescent state and a rapidly spiking state [9, 22, 55, 77, 109]. Somato-dendritic ping-pong has been identified in other two-compartmental systems as a mechanism to sustain the repetitive firing seen during neuronal bursts [9, 77, 109]. In the aforementioned systems, the dendritic compartment contained nonlinear active currents. These active currents play a role in initiating the somato-dendritic ping-pong, and in shutting down the ping-pong effect in order to bring the system back to quiescence in between bursts [9]. Active dendritic conductances have also been shown to play a role in different types of bursting such as "ghostbursting" [22, 55]. Here, we show that somato-dendritic ping-pong can occur in a completely passive dendritic compartment. However, adding active currents in our system would make it easier for the ping-pong effect to occur. For example, adding a persistent sodium channel to the dendrite could cause a larger and faster depolarization of the dendritic potential after the somatic spike. Furthermore, one could also induce bursting in our system by adding a slowly activating outward current in the soma [9].

In a related study, Peercy and Keener [73] examined the effects of coupling an ischemic cell to a normal excitatory cell using a two-compartment approach. They found that when the excitatory cell is coupled to a cell with elevated extracellular potassium (caused by ischemia), the two cells begin to oscillate even though each of the isolated cells are non-oscillatory. The mechanisms responsible for this behavior

are intimately tied to the results we found for the two-compartment model. That is, raising the extracellular potassium levels raises the reversal potential of the potassium channel, thus bringing the resting membrane potential closer to $0\ mV$ for the ischemic cell. Our results with the two-compartment model show that, if $E_{LD} > V_{th}$, the dendritic compartment acts as a current source for the soma, and less applied current is needed to sustain the periodic firing caused by somato-dendritic ping-pong. Thus, the induced oscillatory behavior observed by Peercy and Keener when coupling an ischemic cell to a normal excitatory cell could be a result of the ischemic cell acting as a current source for the normal cell which would make it easier for the ping-pong effect to occur.

Lánský and Rodriguez [56] showed how the addition of a passive compartment can affect the firing dynamics of the leaky-integrate-and-fire neuron. Specifically, they were interested in how the addition of the dendrite affects the encoding properties of the leaky-integrate-and-fire neuron. They defined the encoding range of the neuron as the portion of the $f - I$ curve prior to saturation. They found that the addition of passive dendritic compartment to the leaky-integrate-and-fire neuron increases the encoding range of neuron. Here, we show that the addition of the dendrite not only affects the encoding properties of the neuron by effectively flattening out its $f - I$ curve (see Figure 6.4.2), but it can also induce bistability between periodic firing and quiescence. The fact that Lánský and Rodriguez did not include the effects of the somatic spike on the dendritic compartment prevented them from observing the bistable behavior that we describe here. Thus, we are able to extend their results to show that, the inclusion of spatial properties not only alters the encoding properties of the leaky-integrate-and-fire neuron, but it also affects the onset of oscillatory behavior in the neuron.

One can view the onset of oscillations in the leaky-integrate-and-fire neuron as arising from a discontinuous infinite period bifurcation (e.g. a discontinuous saddle-node-on-an-invariant-cycle bifurcation, see Figure 6.4.2 (a)). When the effects of the dendrite are sufficiently large and a somatic spike is explicitly included, we find that the addition of the dendrite causes the onset of oscillations in the leaky-integrate-and-fire neuron to arise from a discontinuous subcritical Hopf bifurcation (Figure 6.4.2 (b)). Thus, the addition of the dendrite affects the neurons excitability classification [45]. That is, the standard leaky-integrate-and-fire neuron can fire action potentials at arbitrarily low frequencies, and is classified as Type I neural excitability. Neurons where the onset of oscillations occur at a non-zero frequency, and whose frequency is relatively insensitive to changes in applied current are in the Type II class of neural excitability. We find that increasing the effects of the dendrite can cause the leaky-integrate-and-fire neuron to transition from Type I to Type II neural excitability. This is not the first time that cable properties have been shown to alter the bifurcation structure of a system. Rinzel and Keener [90] found that, for an active cable modeled with FitzHugh-Nagumo dynamics [35, 69], the onset of periodic oscillations can arise out of either a supercritical or subcritical Hopf bifurcation depending upon the level of excitability of the cable and the speed of the recovery dynamics.

6.9   Summary

We have examined how the influence of dendritic properties affect the dynamics of a leaky-integrate-and-fire model neuron that explicitly includes spiking dynamics. We found that addition of the dendrite can cause the leaky-integrate-and-fire neuron to display bistable behavior between periodic firing and quiescence. The mechanism of the periodic firing in the bistable regime was identified to be somato-dendritic ping-

pong. We then showed that the same qualitative behavior is captured in a reduced two-compartment model.

Chapter 7

Effects of Dendritic Properties on the Phase-Locking Dynamics of Electrically Coupled Neuronal Oscillators

7.1 Introduction

Synchronization of oscillatory activity in neuronal networks arises in many areas of neuroscience and has been linked to various behavioral functions. There is little doubt that the oscillatory behavior of these networks plays a major role in generating motor patterns of repetitive activity such as locomotion, feeding, and breathing [86, 92, 105]. In the mammalian cortex, oscillatory behavior arises as a result of the synchronized electrical activity of large populations of cortical neurons. This oscillatory behavior is apparent in electroencephalogram (EEG) recordings and can occur in different

frequency bands and in different areas of the cortex [14]. Oscillations within these different frequency bands have been hypothesized to correspond with different behavioral functions. For example, synchronized gamma-frequency (30-80Hz) oscillations in the mammalian sensory cortex have been hypothesized to be important in sensory information processing, e.g. in the olfactory system [57] and the visual system [42], in motor programming [68], and associative learning [66]. However, directly linking these cortical oscillations to precise functional roles is a difficult task and more work has to be done before this can occur. Therefore, rather than directly addressing the issue of the functional role of these oscillations, one can first address the question of what are the biophysical mechanisms that underly the observed synchronous electrical activity? A deep understanding of these mechanisms can allow one to extract the functional role of the aforementioned synchronous oscillatory behavior.

The majority of neurons in the brain transmit electrical activity to one another via either chemical synapses or electrical synapses. In neurons coupled with chemical synapses, an action potential initiated in the presynaptic cell causes the release of a neurotransmitter at the site of the synapse onto the postsynaptic cell. If the neurotransmitter causes the membrane potential of the postsynaptic cell to increase (decrease), then the synapse is referred to as excitatory (inhibitory). In general, one usually refers to a neuron as being excitatory (inhibitory) if it forms excitatory (inhibitory) synapses onto other neurons. On the other hand, electrical coupling between neurons is usually mediated by gap junctions, which are clusters of intercellular channels formed from connexin proteins. They were first observed among interneurons in invertebrates where they are now known to play an important role in networks generating rhythmic motor outputs [72, 87]. These gap junctions are basically non-specific ion channels that allow ions to flow down their electrical gradient.

As such, they are usually modeled as linear Ohmic resistors.

Networks of inhibitory neurons are thought to play a fundamental role in generating the oscillatory electrical behavior seen in the mammalian neocortex [4, 15, 93, 98]. As a result, synchronization in inhibitory networks is a topic of much theoretical and experimental research [64, 65]. Many of these studies have revealed that inhibitory interneurons of the same type[1] are highly interconnected by electrical synapses and that this electrical coupling aides in the synchronization of their electrical behavior [85, 19, 37, 38, 39, 58, 64, 103]. This activity is not limited to inhibitory neurons in the neocortex. For example, experimental evidence has been found to suggest that gap junctions can enhance the synchrony of oscillations at gamma frequencies in spatially extended networks of hippocampal interneurons [103]. Studies have also shown that small clusters of electrically coupled neurons can drive synchronous activity in the thalamic reticular nucleus [60].

In studying the synchronization properties of these inhibitory networks, many theoretical studies model neurons as single-compartment objects ignoring the spatial anatomy of the cell. This simplification is made for mathematical tractability and computational efficiency. However, many neurons are not electrotonically compact, and single-compartment models cannot be expected to fully capture their behavior. Furthermore, experimental studies have revealed that cortical inhibitory neurons are highly interconnected by electrical synapses on their dendrites [2, 36], and that the dendrites of these inhibitory neurons appear to display effectively passive electrical behavior [48]. Theoretical studies have shown that passive dendritic filtering can change the phase-locking behavior in networks of neuronal oscillators [12, 20, 59]. Therefore, dendritic properties can be important in the flow of electrical activity

---

[1]Gibson et al [38] classified two types inhibitory interneurons in the neocortex according to physiological properties; so-called fast-spiking (FS) cells and low-threshold-spiking (LTS) cells.

between inhibitory neurons in the cortex, and, consequently, in the generation of the synchronous electrical activity seen there.

Here, we investigate the effects of passive dendritic properties on the phase-locking dynamics of electrically coupled neuronal oscillators. We model a neuron as an isopotential somatic oscillator attached to a thin passive dendritic cable using the "ball-and-stick" model [80]. Each neuron in the network is coupled to other neurons in the network by a gap junction on the distal end of their dendrites. We use the theory of weakly coupled oscillaors [29, 54, 71] to derive the corresponding phase model of each neuron in the network. This reduces the dynamics of each neuron in the network down to the consideration of a single phase variable which governs how quickly the neuron moves around its underlying limit cycle. We then use the phase model to examine how the different properties of the passive dendritic filtering can alter the phase-locking dynamics of networks of electrically coupled neuronal oscillators.

7.2   Electrically Coupled Ball-and-Stick Model

We model the electrical activity of a single neuron using the "ball-and-stick" model [12, 20] (see 3.6) that consists of a spherical active isopotential soma attached to a single thin passive dendrite. We then make the assumption that the electrical synapse between the two neurons is located on the dendrite at the end furthest away from the cell body (see Figure 7.2.1). This assumption is made for ease of mathematical computation and can easily be relaxed to place the synapse at any point along the dendrite (e.g. [12]). However, by examining the case where the electrical synapse is furthest away from the cell bodies, we can see how the maximum amount of dendritic filtering of the electrical signal between the two cells affects phase-locking.

The dendrite of each neuron is modeled as a one-dimensional passive cable of

physical length L [78, 84]

$$C_m \frac{\partial v_j}{\partial t} = \frac{a}{2R_c} \frac{\partial^2 v_j}{\partial x^2} - g_{LD}(v_j - E_{LD}^j), \quad x \in (0, L), \quad (7.2.1)$$

where $v_j(x,t)$ is the voltage (in units of mV) in the dendrite of the jth neuron at position x and time t, g_{LD} is the leakage conductance in the dendrite in units of mS/cm^2, R_c is the cytoplasmic resistivity of the dendrite in units of $k\Omega \cdot cm$, a is the radius of the dendrite in units of cm, E_{LD}^j is the reversal potential of the leakage conductance in the dendrite of the jth neuron in units of mV, and C_m is the specific membrane capacitance in units of $\mu F/cm^2$, which is assumed to be constant throughout each neuron. Note that we have assumed that all cable parameters are the same for the two neurons except we allow for the possibility for their leakage reversal potentials to be different.

Hodgkin-Huxley (HH) type equations are used to model the electrical activity of each soma. An application of the conservation of current law at the junction connecting the spherical soma and the thin dendrite ($x = 0$) yields the equation for the proximal boundary condition

$$C_m \frac{\partial v_j}{\partial t}(0, t) = -I_{ion,S}(v_j(0), \vec{w}) + I + \frac{a^2}{d^2 R_c} \frac{\partial v_j}{\partial x}(0, t), \quad (7.2.2)$$

where $I_{ion,S}(v_j, \vec{w})$ represents the sum of the HH-type ionic currents in the jth soma, $\vec{w}$ is a vector containing the gating variables of the ionic conductances, and d is the diameter of the soma in cm. The gating variables in the vector $\vec{w}$ are described by equations of the form

$$\frac{d\vec{w}}{dt} = \frac{1}{\tau_{\vec{w}}}(\vec{w}_\infty(v) - \vec{w}). \tag{7.2.3}$$

The last term in equation (7.2.2) represents the axial current flowing between the dendrite and the soma. The parameter I is the somatic bias current in $\mu A/cm^2$. Note that changes in I are equivalent to changes in the leakage reversal potential, E_L, and therefore changes in I can be thought of as being due to current input into the soma or due to the effects of a neuromodulator. The values of I and E_L are chosen such that the isolated soma undergoes T-periodic (limit cycle) oscillations. Since the two isolated somata are assumed to be the same, we define $v_{LC}(t)$ to be the membrane potential component of the isolated somatic oscillator's limit cycle.

The two neurons are electrically coupled at the distal end $(x = L)$ of their respective dendrites (see Figure 7.2.1). Invoking conservation of current once again yields the distal boundary condition

$$\frac{\pi a^2}{R_c} \frac{\partial v_j}{\partial x}(L, t) = g_c(v_k(L, t) - v_j(L, t)), \tag{7.2.4}$$

where the electrical synapse is modeled as a linear ohmic resistor with conductance g_c in units of mS. It is important to note that, since the two neurons are electrically coupled on their dendrites, the term $\frac{a^2}{d^2 R_c} \frac{\partial v_j}{\partial x}(0, t)$ in equation (7.2.2) also incorporates the effects of the electrical coupling on the dynamics of the somatic oscillator.

This model is similar to the one studied by Crook et al. [20] except for the fact that they studied two ball-and-stick neurons coupled with chemical synapses. The Fast-spiking interneuron model of Erisir et al. [27] is used in the simulations presented here. However, the basic analysis that we use is general and can be applied to any
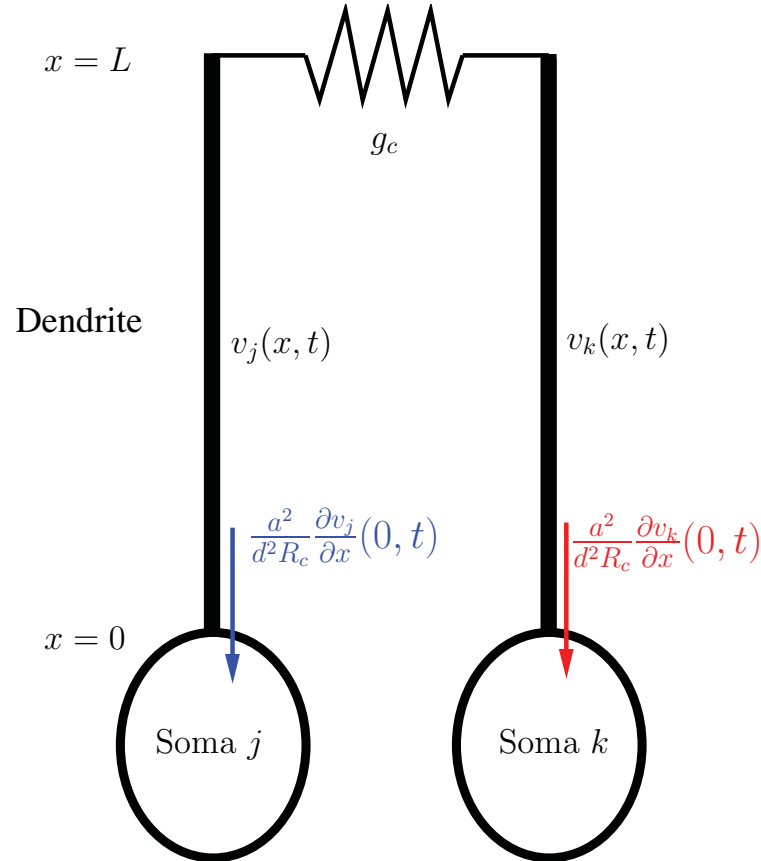
neuronal oscillator.

Figure 7.2.1: **Two Electrically Coupled Ball-and-Stick Neurons**. Each neuron is modeled as a ball-and-stick neuron which consists of an active soma attached to a thin passive dendritic cable. The two neurons are then electrically coupled by a linear ohmic resistor with conductance g_c at the distal ($x = L$) end of the dendrite. The terms next to the arrows represent axial currents flowing between the dendrites and the somata.

The subsequent analysis relies on a certain combination of model parameters being sufficiently "small". To identify this small compound parameter, we nondimensional-ize the model (7.2.1-7.2.4). We set $V_j = V_j(\bar{x}, \bar{t}) = \frac{v_j(\lambda \bar{x}, \tau_D \bar{t})}{-E_L}$ (where E_L is the leakage reversal potential in the soma), $\bar{x} = \frac{x}{\lambda}$, $\bar{t} = \frac{t}{\tau_D}$, $\lambda = \sqrt{\frac{a}{2R_c g_{LD}}}$ is the length constant of the dendrite, and $\tau_D = \frac{C_m}{g_{LD}}$ is the membrane time constant of the dendrite. The

resulting nondimensional equations for the coupled ball-and-stick model neurons are

$$
\begin{cases}
\dfrac{\partial V_j}{\partial \bar{t}} = \dfrac{\partial^2 V_j}{\partial \bar{x}^2} - (V_j - \bar{E}^j_{LD}) \\[2mm]
\dfrac{\partial V_j}{\partial \bar{t}}(0,\bar{t}) = -\bar{I}_{ion,S}(V_j(0,\bar{t}),\vec{w}) + \bar{I} + \varepsilon \dfrac{\partial V_j}{\partial \bar{x}}(0,\bar{t}) \\[2mm]
\dfrac{\partial V_j}{\partial \bar{x}}\left(\dfrac{L}{\lambda},\bar{t}\right) = g\left(V_k\left(\dfrac{L}{\lambda},\bar{t}\right) - V_j\left(\dfrac{L}{\lambda},\bar{t}\right)\right).
\end{cases}
\tag{7.2.5}
$$

where $j,k = 1,2$ with $j \neq k$, $\frac{L}{\lambda}$ is the electrotonic length of the dendrite, $g = \frac{g_c R_c \lambda}{\pi a^2}$, $\bar{E}_{LD} = \frac{E_{LD}}{-E_L}$, $\bar{I}_{ion,S}(V(0,\bar{t}),\vec{w}) = \frac{1}{-g_{LD}E_L}I_{ion,S}((-E_L)V(0,\bar{t}),\vec{w})$, $\bar{I} = \frac{1}{-g_{LD}E_L}I$, and $\varepsilon = \frac{a^2}{d^2 g_{LD} R_c \lambda}$. Also, equation (7.2.3) becomes $\frac{d\vec{w}}{dt} = \frac{\tau_D}{\tau_{\vec{w}}}(\vec{w}_\infty(-E_L V(0,\bar{t})) - \vec{w})$. We also define the nondimensionalized period of the limit cycle to be $T_{nd} = \frac{T}{\tau_D}$ and the nondimensional voltage component of the isolated soma's limit cycle as $V_{LC}(\bar{t})$.

The term $\varepsilon \frac{\partial V_j}{\partial \bar{x}}(0,\bar{t})$ in equation (7.2.5) is the axial current at the soma-dendritic junction and is the jth dendrites perturbation to the jth somas membrane dynamics and incorporates the effects of the electrical coupling. To ensure that this perturbation is weak, we assume that

$$
\varepsilon = \frac{a^2}{d^2 g_{LD} R_c \lambda} = \frac{a^2}{d^2}\sqrt{\frac{2}{g_{LD} R_c a}}
$$

is small. This can be interpreted as $a \ll d$, i.e. that the radius of each dendrite is small relative to the diameter of each of the somata, and that $\sqrt{\frac{2}{g_{LD} R_c a}}$ is $O(1)$ so that $\varepsilon \ll 1$. It is important to note that under this assumption, it does not matter if the conductance of the electrical synapse is small or large because the dendritic influence on each of the somata is what is assumed to be weak.

7.3   Theory of Weak Coupling and Reduction to a Phase Model

The theory of weak coupling [29, 54, 71] (see also Chapter 4), has been widely used to analyze dynamics in networks of oscillating neurons (e.g. [32, 46, 58, 74]). The theory can also be used to analyze the phase-locking dynamics of neurons with dendritic coupling under the assumption that the current flowing from each of the dendrites into the respective somata only weakly affect the somatic dynamics [12, 20, 88]. In this case, the complete state of each neuron can be approximated by its relative phase on its T_{nd}-periodic limit cycle, $\phi_j(\bar{t}) \in [0, T_{nd})$. Thus, using this theory enables one to reduce the number equations that describe a neuronal network. For example suppose the network contained N model neurons each described by M equations. The total number of equations for the network would be MN. The theory of weak coupling reduces this number down to only N phase equations. For the sake of illustration, we present the phase reduction technique on a pair of coupled neurons. The relative phase of each cell is given by

$$
\begin{aligned}
\frac{d\phi_j}{d\bar{t}} &= \frac{1}{T_{nd}} \int_0^{T_{nd}} Z(s + \phi_j) I_{coupl}(s, \phi_j, \phi_k) ds \\
&= \frac{1}{T_{nd}} \int_0^{T_{nd}} Z(s) I_{coupl}(s, 0, \phi_k - \phi_j) ds \\
&= \varepsilon H(\phi_k - \phi_j), \quad j, k = 1, 2; j \neq k,
\end{aligned}
\tag{7.3.1}
$$

where $\frac{d\phi_j}{d\bar{t}}$ is the small modulation of the jth oscillators instantaneous nondimensional frequency due to the coupling. $I_{coupl}(s, 0, \phi_k - \phi_j)$ is a nondimensional T_{nd}-periodic coupling current, i.e. input stemming from coupling between the two neurons. Note

that, $I_{coupl}(s, 0, \phi_k - \phi_j)$ is a function of the relative phases of neuron j and neuron k. $Z(\cdot)$ is the infinitesimal phase response curve (PRC) of the neuronal oscillator. The PRC quantifies the change in phase due to a δ-function current perturbation at a particular phase on the limit cycle. The PRC can be thought of as a Green's function or impulse response function for a linear oscillator. The term $H(\phi_k - \phi_j)$ is known as the interaction function and represents the modulation of the isolated oscillator's frequency due to the coupling averaged over one period of the oscillations.

As stated earlier, the theory of weak coupling can be applied to the ball-and-stick model by considering the "dendritic current" as the weak perturbation to the soma, following [12, 20, 88]. During steady oscillations in the coupled ball-and-stick model, a current flows between the electrical synapse connecting the two cells, and, subsequently, between the soma and the dendrite of each of the two neurons. This current then acts to modulate the intrinsic oscillations of each of the somata. In system (7.2.5)-(7.2.5), the current that modulates the frequency of the jth somata is given by $\varepsilon \frac{\partial V_j}{\partial \bar{x}}(0, \bar{t})$. However, as written, this term does not have an explicit dependence on the phase of the two neurons. The way to obtain the explicit dependence on phase is to solve the leading order approximation of system (7.2.5)-(7.2.5). That is, because the dendritic perturbation is weak, the soma of each neuron clings tightly to its underlying limit cycle so that $V_j(0, \bar{t}) \simeq V_{LC}(\bar{t} + \phi_j)$. This approximation simplifies the boundary condition at the soma ($\bar{x} = 0$) and yields the leading order approximation for the system

$$\begin{cases} \dfrac{\partial V_j}{\partial \bar{t}} = \dfrac{\partial^2 V_j}{\partial \bar{x}^2} - (V_j - \bar{E}^j_{LD}) \\[2mm] V_j(0,\bar{t}) = V_{LC}(\bar{t} + \phi_j) \\[2mm] \dfrac{\partial V_j}{\partial \bar{x}}\left(\dfrac{L}{\lambda}, \bar{t}\right) = g\left(V_k\left(\dfrac{L}{\lambda}, \bar{t}\right) - V_j\left(\dfrac{L}{\lambda}, \bar{t}\right)\right). \end{cases} \quad (7.3.2)$$

Although system (7.3.2) may look complicated, it is a first-order linear partial differential equation with T_{nd}-periodic forcing at one end, and a time-dependent Neumann boundary condition at the other end. As such, the solution can be found using Fourier series. Expanding the somatic potential in a Fourier series, $V_{LC}(\bar{t} + \phi_j) = \frac{1}{T_{nd}} \sum_{n \in \mathbb{Z}} V_n e^{2\pi i n(\bar{t}+\phi_j)/T_{nd}}$, and solving system (7.3.2) yields

$$\begin{aligned} V_j(\bar{x}, \bar{t}, \phi_j, \phi_k) &= \left[\left(\frac{v_0}{T_{nd}} - \bar{E}^k_{LD}\right) c_0 + \left(\frac{v_0}{T_{nd}} - \bar{E}^j_{LD}\right) d_0\right] \sinh(\bar{x}) \\ &\quad + \left(\frac{v_0}{T_{nd}} - \bar{E}^j_{LD}\right) \cosh(\bar{x}) + \frac{1}{T_{nd}} \sum_{n \neq 0} \left[v_n \left(\frac{1}{b_n} c_n e^{2\pi i n \phi_k/T_{nd}}\right.\right. \\ &\quad \left.\left. + \frac{1}{b_n} d_n e^{2\pi i n \phi_j/T_{nd}}\right) \sinh(b_n \bar{x}) + v_n e^{2\pi i n \phi_j/T_{nd}} \cosh(b_n \bar{x})\right] e^{2\pi i n \bar{t}/T_{nd}} \\ &\quad + \bar{E}^j_{LD} \end{aligned} \quad (7.3.3)$$

where $b_n = \sqrt{1 + 2\pi i n/T_{nd}}$ and

$$c_n = \frac{g}{\cosh^2\left(b_n\frac{L}{\lambda}\right) + \frac{g}{b_n}\sinh\left(2b_n\frac{L}{\lambda}\right)} \tag{7.3.4}$$

$$d_n = \frac{g^2}{b_n}\frac{1}{\cosh^2\left(b_n\frac{L}{\lambda}\right)}\frac{1}{2\left(g/b_n\right)^2\tanh\left(b_n\frac{L}{\lambda}\right) + 3(g/b_n) + \coth\left(b_n\frac{L}{\lambda}\right)} \tag{7.3.5}$$
$$-b_n\frac{\sinh\left(b_n\frac{L}{\lambda}\right) + \frac{g}{b_n}\cosh\left(b_n\frac{L}{\lambda}\right)}{\cosh\left(b_n\frac{L}{\lambda}\right) + \frac{g}{b_n}\sinh\left(b_n\frac{L}{\lambda}\right)}.$$

Note that equation (7.3.3) reduces to equation (5.3.4)

$$V(\bar{x},\bar{t}) = \left(\frac{V_0}{\bar{T}} - \bar{E}_{LD}\right)\frac{\cosh\left(\bar{x} - \frac{L}{\lambda}\right)}{\cosh\left(\frac{L}{\lambda}\right)} + \frac{1}{\bar{T}}\sum_{n\neq 0}V_n\frac{\cosh\left(b_n\left(\bar{x} - \frac{L}{\lambda}\right)\right)}{\cosh\left(b_n\left(\frac{L}{\lambda}\right)\right)}e^{2\pi in\bar{t}/\bar{T}}$$
$$+\bar{E}_{LD}, \tag{7.3.6}$$

as $g \to 0$. Furthermore, (7.3.5) reduces to the filtering coefficients $c_n = b_n\tanh\left(b_n\frac{L}{\lambda}\right)$ that were examined in Chapter 5.

Differentiating equation (7.3.3) with respect to $\bar{x}$ and evaluating at $\bar{x} = 0$ gives

$$\frac{\partial V_j}{\partial \bar{x}}(0,\bar{t},0,\phi_k - \phi_j) = \left[\left(\frac{V_0}{T_{nd}} - \bar{E}_{LD}^k\right)c_0 + \left(\frac{V_0}{T_{nd}} - \bar{E}_{LD}^j\right)d_0\right] \tag{7.3.7}$$
$$+\frac{1}{T_{nd}}\sum_{n\neq 0}\left[V_n c_n e^{2\pi in(\phi_k - \phi_j)/T_{nd}} + V_n d_n\right]e^{2\pi in\bar{t}/T_{nd}}.$$

Therefore, we now have an explicit dependence on phase in the dendritic current term and we can set $I_{coupl}(s,0,\phi_k - \phi_j) = \varepsilon\frac{\partial V_j}{\partial \bar{x}}(0,s,0,\phi_k - \phi_j)$ in equation (7.3.1). This yields the phase model for the system

$$\frac{d\phi_j}{d\bar{t}} = \frac{1}{T_{nd}} \int_0^{T_{nd}} Z(s)\varepsilon \frac{\partial V_j}{\partial \bar{x}}(0,s,0,\phi_k-\phi_j)ds, \quad j,k=1,2; j \neq k. \tag{7.3.8}$$

Substituting (7.3.7) into equation (7.3.8) and expanding the PRC in a Fourier series, $Z(\bar{t}) = \frac{1}{T_{nd}}\sum_{m\in\mathbb{Z}} Z_m e^{2\pi i m \bar{t}/T_{nd}}$, yields

$$
\begin{aligned}
\frac{d\phi_j}{d\bar{t}} &= \varepsilon \Bigg(\frac{Z_0}{T_{nd}} \left[\left(\frac{V_0}{T_{nd}} - \bar{E}_{LD}^k \right) c_0 + \left(\frac{V_0}{T_{nd}} - \bar{E}_{LD}^j \right) d_0 \right] \\
&\qquad + \frac{1}{T_{nd}^2} \sum_{n\neq 0} \left[Z_{-n} V_n c_n e^{2\pi i n(\phi_k-\phi_j)/T_{nd}} + Z_{-n} V_n d_n \right] \Bigg) \\
&= \varepsilon \Bigg(\langle Z \rangle \left(\langle V_{LC} \rangle - \tilde{E}_{LD} \right) (c_0 + d_0) \\
&\qquad + \frac{1}{T_{nd}^2} \sum_{n\neq 0} \left[Z_{-n} V_n c_n e^{2\pi i n(\phi_k-\phi_j)/T_{nd}} + Z_{-n} V_n d_n \right] - \omega_{jk} \Bigg) \tag{7.3.9}
\end{aligned}
$$

where $\langle V_{LC} \rangle = V_0/T_{nd}$ and $\langle Z \rangle = Z_0/T_{nd}$ are the mean values of $V_{LC}(t)$ and $Z(t)$, respectively, $\omega_{jk} = \langle Z \rangle \left[C^j c_0 + C^k d_0 \right]$ is the heterogeneity between the two neurons caused by the small difference in the leakage reversal potential of the dendrite, and $C^{j,k} = \bar{E}_{LD}^{j,k} - \tilde{E}_{LD}$ is the difference between the leakage reversal potential of the dendrite with and some common potential $\tilde{E}_{LD}$. Using equation (7.3.9), we will examine how the filtering properties of the passive dendrite, along with dendritic heterogeneity affect the phase-locking dynamics of a pair of electrically coupled neurons.

7.4 Phase-Locking Dynamics in a Pair of Electrically Coupled Ball-and-Stick Neurons

If we set $\phi = \phi_k - \phi_j$ and subtract the the respective differential equations, we obtain the equation for the evolution of the phase difference of the two oscillators

$$\frac{d\phi}{d\bar{t}} = \varepsilon\left(\gamma + G(\phi)\right), \tag{7.4.1}$$

where

$$\gamma = \langle Z \rangle \alpha [\bar{E}^j_{LD} - \bar{E}^k_{LD}] \tag{7.4.2}$$

$$\alpha = c_0 - d_0 = \frac{\tanh\left(\frac{L}{\lambda}\right) + 2g}{1 + 2g\tanh\left(\frac{L}{\lambda}\right)} \tag{7.4.3}$$

$$G(\phi) = \frac{1}{T^2_{nd}}\sum_{n\neq 0} Z_{-n}V_n c_n[e^{-2\pi in\phi/T_{nd}} - e^{2\pi in\phi/T_{nd}}] \tag{7.4.4}$$

In the next section, we will consider the homogeneous case where $\bar{E}^j_{LD} = \bar{E}^k_{LD}$, i.e. the neurons are identical, and examine how dendritic properties affect the phase-locking dynamics of two identical ball-and-stick neurons.

7.4.1 Identical Neurons

If $\bar{E}^j_{LD} = \bar{E}^k_{LD}$, then $\gamma = 0$ in equation (7.4.1). Therefore, the zeros of the function $G(\phi)$ will correspond to the steady-state phase difference ϕ_{ss} between the two neurons. A steady-state ϕ_{ss} will be stable if $G'(\phi_{ss}) < 0$. We will now illustrate how dendritic properties affect the steady-state phase difference of a pair of identical electrically coupled ball-and-stick neurons using the fast-spiking neuron of Erisir et al. [27] to

model our somatic dynamics.

Figure 7.4.1 plots the bifurcation diagrams showing the stability of the steady-state phase difference of the two neurons as a function of the electrotonic length of the dendrite. First off, when $\frac{L}{\lambda} = 0$, one can see that for low firing frequencies[2] (Figure 7.4.1 (a)) there is bistability between synchrony ($\phi/T_{nd} = 0, 1$) and anti-phase ($\phi/T_{nd} = .5$). As the firing frequency is increased, this bistability is lost leaving only synchrony to be stable when $\frac{L}{\lambda} = 0$ (Figure 7.4.1 (b) and (c)). This agrees with previous results for two single-compartment oscillatory neurons coupled by a gap junction. More specifically, it has been shown that electrical coupling promotes bistability between synchrony and anti-phase at low firing frequencies in single-compartment neurons, and this bistability is lost as the firing frequency is increased [58, 64].

When the electrical coupling is away from the soma on the dendrite, for example $\frac{L}{\lambda} = 2$, one can see that at low firing frequencies there is again bistability between synchrony and anti-phase. At intermediate frequencies, only synchrony is stable, while at high firing frequencies, anti-phase becomes the only stable state. This also agrees with previous results that found that placing the electrical coupling away from the soma in a two compartment model can substantially affect synchronization patterns, i.e. see Figure 2 in [59]. However, since this study utilized two-compartment model neurons. they were unable to examine how further increasing the distance between the soma and the electrical coupling affected the stability of the phase-locked states.

For low firing frequencies, as the electrotonic length of the dendrite is increased,

---

[2]Note that dimensional frequency is related to nondimensional frequency by $\frac{1}{T} = \frac{1}{T_{nd}\tau_D}$, where T is the dimensional period of the oscillations and τ_D is the dendritic membrane time constant which we take to be 5 $msec$ in the figures presented here. We present the frequency in terms of dimensional units from now on for ease of physical interpretation.

the anti-phase solution loses stability leaving synchrony as the only stable state. When the firing frequency is in the intermediate range (Figure 7.4.1 (b)), the synchronous solution loses stability as the electrotonic length of the dendrite is increased leading to stable anti-phase. Although the figure only shows electrotonic lengths up to 5, if $\frac{L}{\lambda}$ were increased further, there would be continual alternation between the anti-phase and synchronous solutions being stable. Lastly, when the firing frequency is high, there are sudden switches in the stability of the synchronous and anti-phase states as $\frac{L}{\lambda}$ is increased. Note that this alternation of stability between synchrony and anti-phase as the electrical synapse is mover further away from the soma was also found by Crook et al [20] and Bressloff and Coombes [12]. We also find that increasing the conductance of the electrical synapse g causes the bifurcation diagrams to be shifted to the right (bottom of Figure 7.4.1). This implies that increasing the conductance of the electrical synapse decreases the effect of the dendritic filtering, so that the two coupled ball-and-stick cells display somewhat similar phase-locking dynamics to two coupled single-compartment neurons.

By examining the filtering properties of the dendrite, we can explain the alternation in stability of synchrony and anti-phase that is seen at higher firing frequencies. First, note that the effects of the dendritic filtering are completely captured by the c_n terms in equation (7.4.4). More specifically, since the c_n are complex numbers, they can be rewritten in terms of angles in the complex plane

$$c_n = |c_n|e^{i\psi_n}. \tag{7.4.5}$$

Equation (7.3.4) reveals that the attenuation and phase shift from c_n terms are a function of the nondimensional gap junctional conductance, g, the electrotonic length
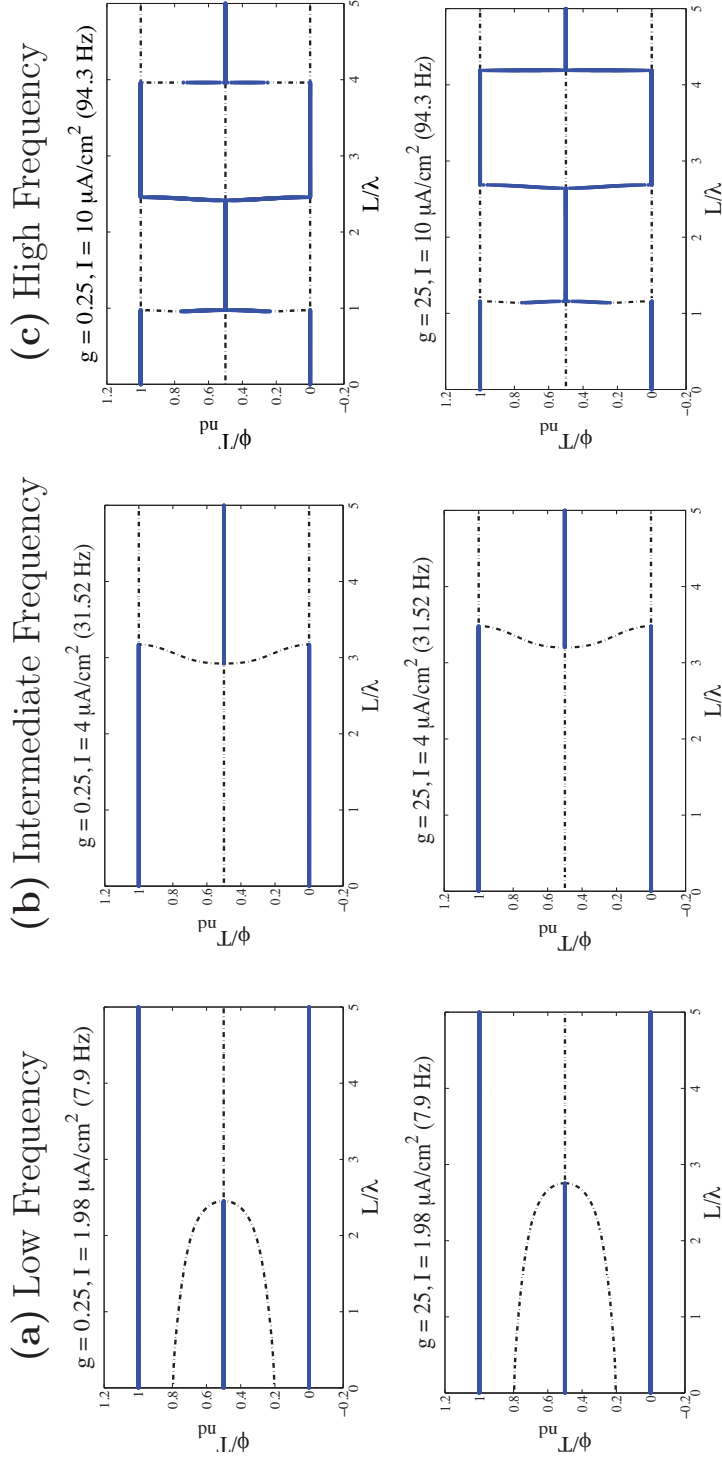
Figure 7.4.1: **Stability of the Steady-States of (7.4.1) with** $\gamma = 0$ **as a Function of the Electrotonic Length of the Dendrite**. In all simulations, $\tau_D = 5$ $msec$. The solid (dash-dotted) line corresponds to stable (unstable) fixed states. $\phi/T_{nd} = 0, 1$ corresponds to synchrony, $\phi/T_{nd} = .5$ corresponds to anti-phase, and any other fixed points are asynchronous states. The plots are shown for $g = 0.25$ (top) and $g = 25$ (bottom) with neurons firing at (a) 7.9 Hz, (b) 31.52 Hz, (c) 94.3 Hz. Notice that there is bistability between anti-phase and synchrony for low frequency oscillations (a). This bistability disappears as the frequency is increased (b) leading to alternating regimes of synchrony and anti-phase being stable as $\frac{L}{\lambda}$ is increased (c). Note also that an increase in g causes all bifurcation diagrams to be shifted to the right.

of the dendrite, $\frac{L}{\lambda}$, and the frequency of the oscillations[3], $\frac{1}{T_{nd}}$. Figure 7.4.2 plots $|c_n|/g$ and ψ_n as a function of $\frac{L}{\lambda}$ (left-hand side) and n (right-hand side) for $g = 0.25$ and firing frequency (a) $20\ Hz$ and (b) $100\ Hz$. Because the dendrites are passive, it is no surprise that c_n acts like a low pass filter, with $|c_n|$ the attenuation factor and ψ_n the phase shift. We can then rewrite $G(\phi)$ as

$$G(\phi) = \frac{1}{T_{nd}^2} \sum_{n \neq 0} |Z_{-n} V_n c_n| e^{i(\xi_n + \psi_n)} [e^{-2\pi i n \phi / T_{nd}} - e^{2\pi i n \phi / T_{nd}}], \qquad (7.4.6)$$

where ξ_n is the angle in the complex plane corresponding to $Z_{-n} V_n$.

From the top panels in Figure 7.4.2 (a) and (b), it is clear that increasing the firing frequency increases the relative dendritic attenuation of the higher modes in the Fourier expansion of $G(\phi)$. Thus, at high frequencies, the $n = 1$ mode will dominate the sum in equation (7.4.4) and

$$
\begin{aligned}
G(\phi) &\approx 2\frac{1}{T_{nd}^2}|Z_1 V_1 c_1| \left[\cos(\xi_1 + \psi_1 - 2\pi\phi/T_{nd}) - \cos(\xi_1 + \psi_1 + 2\pi\phi/T_{nd})\right] \\
&= \left[2\frac{1}{T_{nd}^2}|Z_1 V_1 c_1| \sin(\xi_1 + \psi_1)\right] \sin(2\pi\phi/T_{nd}), \qquad (7.4.7)
\end{aligned}
$$

where the term in brackets determines the amplitude of $G(\phi)$ while the other term determines the shape. Recall that, $G(\phi_{ss}) = 0$. This implies that, at high frequencies,

$$G'(\phi_{ss}) = \left[\frac{4\pi}{T_{nd}^3}|Z_1 V_1 c_1|\right] \sin(\xi_1 + \psi_1). \qquad (7.4.8)$$

Thus, the stability of the synchronous or anti-phase state will be determined by the sign of $\sin(\xi_1 + \psi_1)$, while the term in brackets in (7.4.8) affects the robustness of the

---

[3]c_n depends on $\frac{1}{T_{nd}}$ through $b_n = \sqrt{1 + 2\pi i n / T_{nd}}$
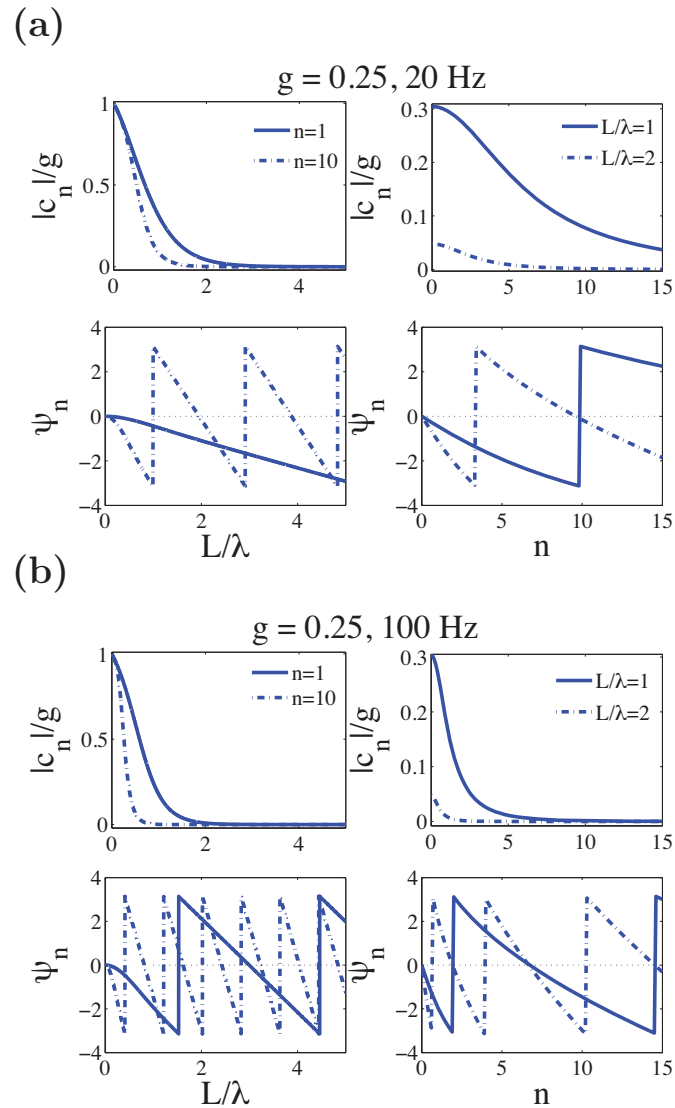
(a)

(b)

Figure 7.4.2: **Dendritic Filtering Properties** (a) The attenuation factor $|c_n|/g$ and the phase shift ψ_n as a function of $\frac{L}{\lambda}$ (left) and n (right) when $g = 0.25$ and the neuron is firing at a frequency of 20 Hz. On the left (right) hand side, the solid line corresponds to $n = 1$ ($\frac{L}{\lambda} = 1$) while the dash-dotted line corresponds to $n = 10$ ($\frac{L}{\lambda} = 2$). (b) Same as in (a) except that the neuron is firing at 100 Hz. Notice that increasing the frequency increases the attenuation of the higher modes, top half of (a) and (b), and also increases the frequency of the phase shift oscillations, lower half of (a) and (b).
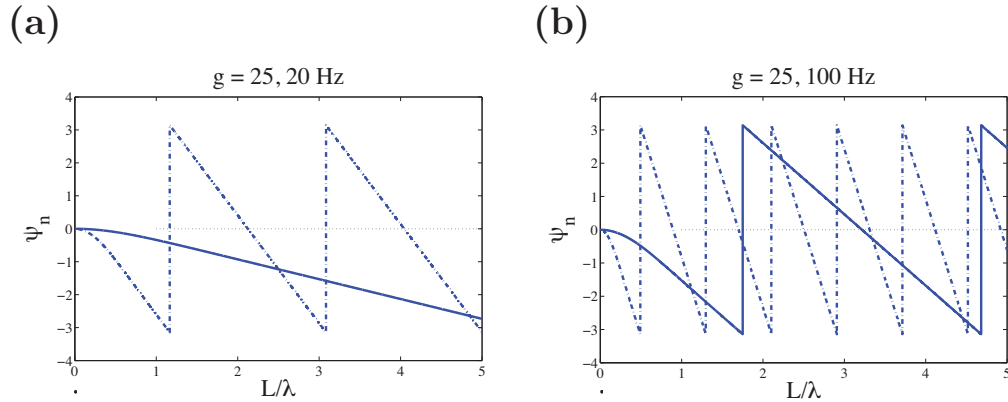
(a) **(b)**

Figure 7.4.3: **Increasing the Nondimensional Gap Junctional Conductance g Causes the Dendritic Phase Shift Factor ψ_n to be Shifted to the Right as Function of the Electrotonic Dendritic Length**. The phase shift ψ_n as a function of $\frac{L}{\lambda}$ when $g = 25$ and the neuron is firing at a frequency of (a) $20\ Hz$ and (b) $100\ Hz$. As in Figure 7.4.2, the solid line corresponds to $n = 1$ while the dash-dotted line corresponds to $n = 10$. Notice that, in comparison to the lower left plots in Figure 7.4.2 (a) and (b), ψ_n is shifted rightward.

stable states. Since $\sin(\xi_1 + \psi_1)$ alternates between being positive and negative as ψ_1 changes with increasing $\frac{L}{\lambda}$ (see lower left of Figure 7.4.2 (a) and (b)), the stability of the synchronous and anti-phase states will also alternate. Also, increasing g causes the phase shift factor ψ_1 to shift rightwards as a function of $\frac{L}{\lambda}$ (Figure 7.4.3). Thus, increasing g acts to decrease the effects of the dendritic phase shift which, in turn, causes the rightwards shift in the bifurcation diagrams of Figure 7.4.1.

7.4.2 Weakly Heterogeneous Neurons

We examine how weak heterogeneity can affect the phase-locking dynamics we have observed for identical neurons. When $\bar{E}_{LD}^j \neq \bar{E}_{LD}^k$, we can rewrite equation (7.4.1) as

$$\frac{d\phi}{d\bar{t}} = \varepsilon \left(\gamma + G(\phi) \right), \tag{7.4.9}$$

where $\gamma = \langle Z \rangle \alpha [\bar{E}_{LD}^j - \bar{E}_{LD}^k]$ and

$$\alpha = c_0 - d_0 = \frac{\tanh\left(\frac{L}{\lambda}\right) + 2g}{1 + 2g \tanh\left(\frac{L}{\lambda}\right)}. \tag{7.4.10}$$

Therefore, steady-state phase differences now correspond to the zeros of $G(\phi) + \gamma$. Figure 7.4.4 plots the bifurcation diagrams of the heterogeneous system when $\bar{E}_{LD}^j - \bar{E}_{LD}^k = -7.143 \times 10^{-4}$ and all other parameters are the same as in Figure 7.4.1. One can see that this small amount of heterogeneity alters the bifurcation structure of the system in a significant way. The most striking difference is perhaps the disappearance of any steady-states as the electrotonic length of the dendrite becomes large. This is primarily due to the contribution of the term α in γ. α is a function of $\frac{L}{\lambda}$ and starts off at $2g$ and asymptotes to 1 as $\frac{L}{\lambda}$ increases from 0 (see Figure 7.4.5). Since the c_n terms in $G(\phi)$ decrease to 0 as $\frac{L}{\lambda}$ increases, this means that $-\gamma$ will eventually be larger than the maximum of $G(\phi)$ causing the disappearance of the fixed points that is seen in Figure 7.4.4.

7.5 Phase-Locking Dynamics in a One-Dimensional Network of Electrically Coupled Ball-and-Stick Neurons

Equation (7.4.1) can be generalized to model a network of N electrically coupled ball-and-stick neurons by summing up the effects of the pairwise interactions between the neurons in the network (see Chapter 4 also [46]):
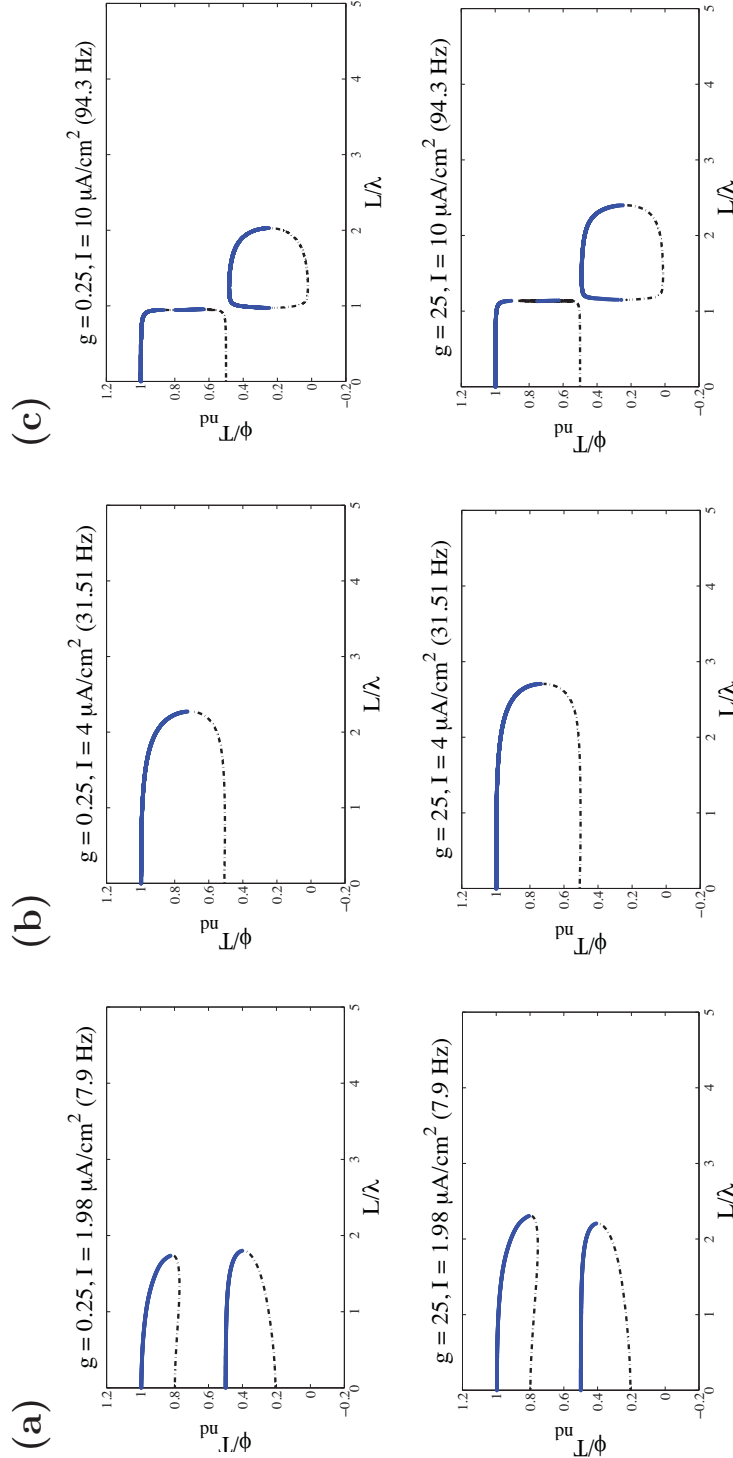
Figure 7.4.4: **Weak Heterogeneity Can Significantly Alter the Phase-Locking Behavior of the Two Neurons.** Bifurcation diagrams showing the stability of the steady-state phase difference of the two neurons as the electrotonic length of the dendrite is varied and $\bar{E}_{LD}^j - \bar{E}_{LD}^k = -7.143 \times 10^{-4}$. All other parameters are the same as in Figure 7.4.1. The presence of the heterogeneity in the leakage reversal potentials changes the bifurcation structure in a significant way, This is primarily due to the presence of the term α in γ.
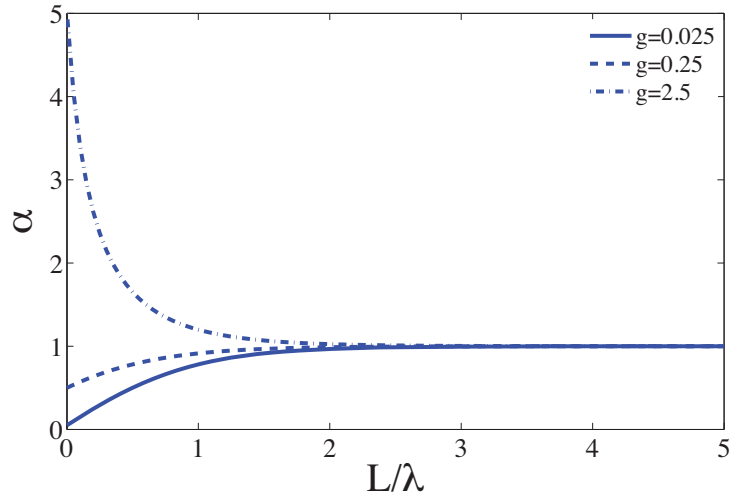
Figure 7.4.5: **Dependence of the Heterogeneity on the Electrotonic Length of the Dendrite**. Plot of the function α as $\frac{L}{\lambda}$ is increased for different values of g. One can see that α starts off at $2g$ when $\frac{L}{\lambda} = 0$ and asymptotes to 1 as $\frac{L}{\lambda}$ increases. The fact that α asymptotes to 1 causes the disappearance of the fixed points seen in Figure 7.4.4 since The c_n terms in $G(\phi)$ limit to 0 as $\frac{L}{\lambda}$ increases.

$$\frac{d\phi_j}{d\bar{t}} = \frac{\varepsilon}{N-1}\sum_{k=1}^{N}\left\{ \langle Z \rangle \left(\langle V \rangle - \tilde{E}_{LD}\right)\left(c_0\left(\frac{L_{jk}}{\lambda}\right) + d_0\left(\frac{L_{jk}}{\lambda}\right)\right)\right.$$

$$\left. + \frac{1}{T_{nd}^2}\sum_{n\neq 0}\left[Z_{-n}V_n c_n\left(\frac{L_{jk}}{\lambda}\right)e^{2\pi i n(\phi_k - \phi_j)/T_{nd}} + Z_{-n}V_n d_n\left(\frac{L_{jk}}{\lambda}\right)\right] - \omega_{jk}\right\}, \qquad (7.5.1)$$

where the factor of $\frac{1}{N-1}$ is included to ensure that the sum in the above equation is $\mathcal{O}(1)$ and we have now explicitly included the dependence of c_n and d_n on the length of the dendrite. L_{jk} is the length of the dendrite connecting the jth soma to the electrical synapse with the kth neuron, and $j = 1, ..., N$. Note that it is assumed that $L_{jk} = L_{kj}$.

System (7.5.1) can be quite difficult to analyze when $N \gg 1$. However, the system

can be simplified if we assume that the network of neuronal oscillators forms a spatial continuum [12, 21, 30, 41].

7.5.1   Continuum Limit

Suppose that we are examining a one-dimensional array of neurons in a domain Ω. If the length of the domain is D and there are N neurons, then the cell body of each neuron is located at a position $x_j = j\Delta x$, where $\Delta x = \frac{D}{N-1}$. Furthermore, the electrotonic length of each dendrite is now given by $\frac{L_{jk}}{\lambda} = \frac{1}{2}\frac{D}{N-1}|j - k|$ (see Figure 7.5.1). Next, if we multiply equation (7.5.1) by a factor of $\frac{D(N-1)}{D(N-1)}$ and assume that $\frac{D}{N-1} \ll 1$, then we can use the continuum approximation
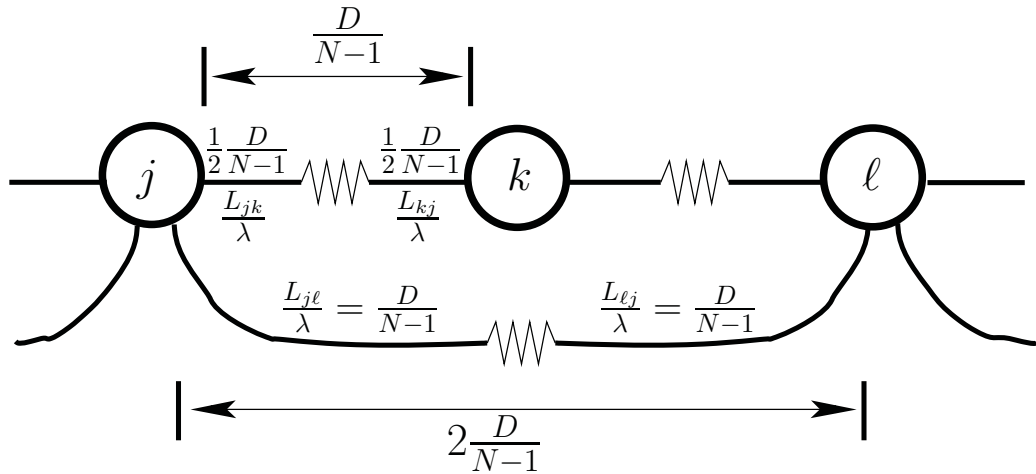

Figure 7.5.1: **Schematic Diagram of the Continuum Ball-and-Stick Network**. The soma (cell body) of each neuron is located at a position $x_j = j\Delta x$, where $\Delta x = \frac{D}{N-1}$ and D is the length of the domain. Since the neurons are coupled by gap junctions at the distal end of their dendrites, the dendrite of each neuron now has an electrotonic length equal to half the distance between the cell bodies, i.e. $\frac{L_{jk}}{\lambda} = \frac{1}{2}\frac{D}{N-1}|j - k|$.

$$\frac{\partial \phi}{\partial \bar{t}}(x, \bar{t}) = \frac{\varepsilon}{D} \int_{\Omega} \left\{ \langle Z \rangle \left(\langle V \rangle - \tilde{E}_{LD} \right) \left(c_0 \left(\frac{|x - \hat{x}|}{2} \right) + d_0 \left(\frac{|x - \hat{x}|}{2} \right) \right) \right. \tag{7.5.2}$$

$$+ \frac{1}{T_{nd}^2} \sum_{n \neq 0} \left[Z_{-n} V_n c_n \left(\frac{|x - \hat{x}|}{2} \right) e^{2\pi i n (\phi(\hat{x},t) - \phi(x,t))/T_{nd}} + Z_{-n} V_n d_n \left(\frac{|x - \hat{x}|}{2} \right) \right]$$

$$\left. - \omega(x, \hat{x}) \right\} d\hat{x},$$

If we let $y = x - \hat{x}$, we can rewrite the above equation as

$$\frac{\partial \phi}{\partial \bar{t}}(x, \bar{t}) = \frac{1}{D} \frac{\varepsilon}{T_{nd}^2} \sum_{n \neq 0} Z_{-n} V_n \int_{-\infty}^{\infty} \left\{ c_n \left(\frac{|y|}{2} \right) e^{2\pi i n (\phi(x-y,t) - \phi(x,t))/T_{nd}} - \omega(x, x - y) \right\} dy$$

$$+ K_{DC} + K, \tag{7.5.3}$$

where

$$K_{DC} = \frac{1}{D} \varepsilon \int_{-\infty}^{\infty} \left\{ \langle Z \rangle \left(\langle V \rangle - \tilde{E}_{LD} \right) \left(c_0 \left(\frac{|y|}{2} \right) + d_0 \left(|y| \right) \right) \right\} \tag{7.5.4}$$

$$K = \frac{1}{D} \frac{\varepsilon}{T_{nd}^2} \sum_{n \neq 0} Z_{-n} V_n \int_{-\infty}^{\infty} d_n \left(\frac{|y|}{2} \right) dy, \tag{7.5.5}$$

and the domain is taken to be the real line. Note that the magnitude of the function $c_n(\frac{|y|}{2})$, which describes the filtering effects of the dendrites, also acts as the weight function for the network in that it controls how large of an effect neurons have on each other as a function of the nondimensional distance y.

7.5.2   Solutions and Stability for a Homogeneous Network

Using the continuum approximation, we will now analyze the network behavior by seeking the conditions under various solutions are stable. For the sake of simplicity, we first find the the stability conditions for spatially periodic waves and the spatially homogenous synchronous solution on a domain of length D. We assume that all the neurons in the network are identical. Thus, $\omega(\cdot, \cdot) = 0$ and we can rewrite equation (7.5.3) as

$$\frac{\partial \phi}{\partial \bar{t}}(x, \bar{t}) = \frac{1}{D} \frac{2\varepsilon}{T_{nd}^2} \sum_{n=1}^{\infty} |Z_{-n} V_n|$$
$$\times \left[\int_{-\infty}^{\infty} \left| c_n \left(\frac{|y|}{2} \right) \right| \cos(\xi_n + \psi_n(|y|/2) + 2\pi n(\phi(x - y, t) - \phi(x, t))/T_{nd}) dy \right]$$
$$+ K_{DC} + K, \tag{7.5.6}$$

where ξ_n and $\psi_n(|y|/2)$ are the angles in the complex plane corresponding to $Z_{-n} V_n$ and $c_n \left(\frac{|y|}{2} \right)$, respectively. By plugging the ansatz $\phi_S^\alpha(x, \bar{t}) = \alpha x + \Omega_\alpha \bar{t}$ into equation (7.5.6), one finds that there is a one parameter family of spatially periodic traveling wave solutions with

$$\Omega_\alpha = \frac{1}{D} \frac{2\varepsilon}{T_{nd}^2} \sum_{n=1}^{\infty} |Z_{-n} V_n| \int_{-\infty}^{\infty} \left| c_n \left(\frac{|y|}{2} \right) \right| \cos(\xi_n + \psi_n(|y|/2) - 2\pi n \alpha y/T_{nd}) dy + K_{DC} + K, \tag{7.5.7}$$

and $\alpha = h \frac{T_{nd}}{D}$ is the wave number with $h \in \mathbb{Z}^+$ (the nonnegative integers). Note that $\alpha = 0$ corresponds to the spatially homogeneous synchronous solution $\phi_S^0(x, \bar{t}) = \Omega_0 \bar{t}$, while $\alpha > 0$ corresponds to spatially periodic traveling wave solutions.

We can now linearize around ϕ_S^α to find the conditions under which the different

solutions are stable. Setting $\phi = \phi_S^\alpha + p(x, \bar{t})$ and linearizing equation (7.5.6) around ϕ_S yields the variational equation

$$
\begin{aligned}
\frac{\partial p}{\partial \bar{t}}(x, \bar{t}) = & -\frac{1}{D} \frac{2\pi\varepsilon}{T_{nd}^3} \sum_{n=1}^{\infty} n |Z_{-n} V_n| \\
& \times \int_{-\infty}^{\infty} \left| c_n \left(\frac{|y|}{2} \right) \right| \sin(\xi_n + \psi_n(|y|/2) - 2\pi n\alpha y/T_{nd}) \left[p(x - y, \bar{t}) - p(x, \bar{t}) \right] dy.
\end{aligned}
$$

$$(7.5.8)$$

Equation (7.5.8) has solutions of the form $p(x, \bar{t}) = e^{\lambda_k \bar{t}} e^{ikx}$, where

$$
\begin{aligned}
\lambda_k = & -\frac{1}{D} \frac{4\pi\varepsilon}{T_{nd}^3} \sum_{n=1}^{\infty} n |Z_{-n} V_n| \\
& \times \int_{-\infty}^{\infty} \left| c_n \left(\frac{|y|}{2} \right) \right| \sin(\xi_n + \psi_n(|y|/2) - 2\pi n\alpha y/T_{nd}) \left[e^{-iky} - 1 \right] dy. \quad (7.5.9)
\end{aligned}
$$

Thus, a solution ϕ_S^α will be stable if

$$
\begin{aligned}
Re(\lambda_k) = & -\frac{1}{D} \frac{4\pi\varepsilon}{T_{nd}^3} \sum_{n=1}^{\infty} n |Z_{-n} V_n| \\
& \times \int_{-\infty}^{\infty} \left| c_n \left(\frac{|y|}{2} \right) \right| \sin(\xi_n + \psi_n(|y|/2) - 2\pi n\alpha y/T_{nd}) \left[\cos(ky) - 1 \right] dy,
\end{aligned}
$$

$$(7.5.10)$$

is less than zero for all $k \in \mathbb{Z}$. Note that the $k = 0$ eigenvalue is always zero, which corresponds to the arbitrary phase shift of the synchronous solution. Therefore, we really need $Re(\lambda_k) < 0$ for all $k \neq 0$.
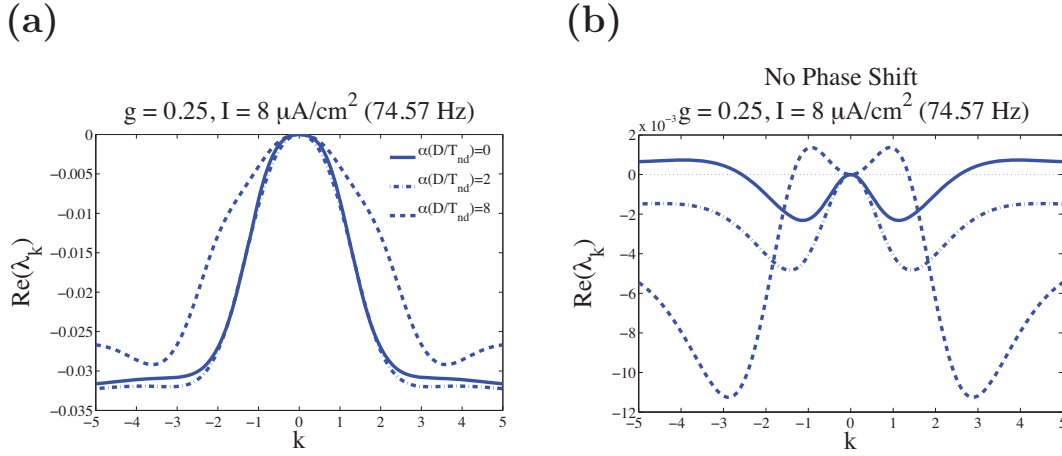
(a)

(b)

Figure 7.5.2: **Inclusion of the Dendritic Phase Shift Can Alter the Stability of Solutions of (7.5.6)**. $Re(\lambda_k)$ as a function of k for wave numbers $\alpha\frac{D}{T_{ind}} = 0$ (solid), $\alpha\frac{D}{T_{ind}} = 2$ (dash-dotted), and $\alpha\frac{D}{T_{ind}} = 8$ (dashed) for a neuron firing at 74.57 Hz and $g = 0.25$ and $D = 40$ when the dendritic phase shift ψ_n is (a) included and (b) excluded. Notice that inclusion of ψ_n causes the synchronous, $\alpha\frac{D}{T_{ind}} = 0$, and 8th traveling wave solution to be stable.

Recall that the function $|c_n(|y|/2)|$ describes the attenuation of the signal due to dendritic filtering as a function of the distance between the neurons. Thus, $|c_n(|y|/2)|$ acts as the weight function for the network (see 4.7) since closer neurons are more strongly coupled to each other than to neurons that are further apart. The function $\psi_n(|y|/2)$ describes the phase shift that occurs as a result of the dendritic filtering. Therefore, we can use equation (7.5.10) to examine how the different properties of dendritic filtering, i.e. attenuation and phase shift, affect the stability of the various solutions of equation (7.5.6). Figure 7.5.2 plots the real part of λ_k as a function of k for a neuron firing at 74.57 Hz when the dendritic phase shift ψ_n is included (a), and when it is excluded (b). Notice that in (a), the wave numbers 0, 2, and 8 are all stable, while in (b) only wave number 2 is stable.

We confirm the results found in Figure 7.5.2 by discretizing and numerically simulating equation (7.5.6). Figure 7.5.3 plots the numerical solution of (7.5.6) starting

near the traveling wave initial condition with wave number $\alpha \frac{D}{T_{ind}} = 8$ when ψ_n is included (a) and excluded (b). Notice that the network converges to the traveling wave solution with wavenumber $\alpha \frac{D}{T_{ind}} = 8$ in (a), and diverges in (b).

Figure 7.5.4 plots the stability of the various traveling wave solutions as a function of the firing frequency of the neurons with the dendritic phase shift (top) and without the dendritic phase shift (bottom). One can see that, in the top plots, increasing g encourages the stability of the lower wave numbers at higher frequencies. While increasing g without the dendritic phase shift (bottom) decreases the number stable waves in the middle of the firing frequency range shown. More interestingly, there is a significant difference between the plots with the dendritic phase shift and without the dendritic phase shift. That is, the inclusion of the dendritic phase shift causes a wider range of traveling wave solutions to be stable at all firing frequencies.

7.6 Dynamics in a Two-Dimensional Network of Electrically Coupled Ball-and-Stick Neurons

Equation (7.5.1) can be extended to model a two-dimensional $N \times N$ network of electrically coupled ball-and-stick neurons [46]:

$$
\begin{aligned}
\frac{d\phi_{j\ell}}{d\bar{t}} = {} & \frac{\varepsilon}{(N-1)^2} \sum_{k=1}^{N} \sum_{m=1}^{N} \left\{ \langle Z \rangle \left(\langle V \rangle - \tilde{E}_{LD} \right) \left(c_0 \left(\frac{L_{j\ell km}}{\lambda} \right) + d_0 \left(\frac{L_{j\ell km}}{\lambda} \right) \right) \right. (7.6.1) \\
& \left. + \frac{1}{T_{nd}^2} \sum_{n \neq 0} \left[Z_{-n} V_n c_n \left(\frac{L_{j\ell km}}{\lambda} \right) e^{2\pi i n (\phi_{km} - \phi_{j\ell})/T_{nd}} + Z_{-n} V_n d_n \left(\frac{L_{j\ell km}}{\lambda} \right) \right] \right\},
\end{aligned}
$$

where $\phi_{j\ell}$ is the phase of the neuron at position (j, ℓ) and $L_{j\ell km}$ is the length of the dendrite connecting the soma of the neuron at (j, ℓ) to the electrical synapse with the
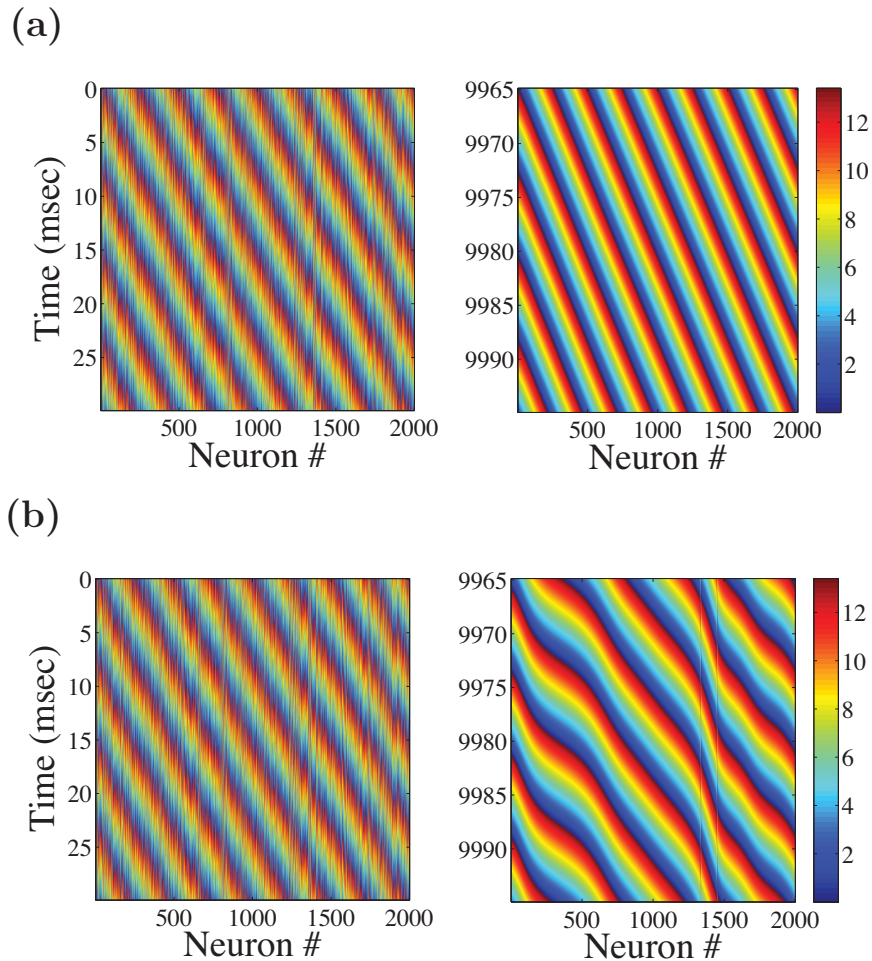
Figure 7.5.3: **Traveling Wave Solutions of (7.5.6)**. Numerical simulation of equation (7.5.6) with $N = 2001$, $D = 40$, and $\varepsilon = .1$ when the dendritic phase shift is included (a), and excluded (b). All other parameters are the same as in Figure 7.5.2. The network is given initial conditions close to the traveling wave solution with wave number $\alpha \frac{D}{T_{ind}} = 8$. The $y-axis$ is time in $msec$, while the $x-axis$ is the neuron number, which ranges from 1 to 2001. The colorscale represents the phase of the neurons which goes from 0 to $T = 13.4$ $msec$. The leftmost panels show the activity of the network from time 0 to 30 $msec$, while the rightmost panels show the activity from time 9965 to 9995 $msec$. As predicted in Figure 7.5.2, the network with the dendritic phase shift, (a), converges to traveling wave solution, while the network without the phase shift, (b), diverges away from the traveling wave solution with wavenumber $\alpha \frac{D}{T_{ind}} = 8$.
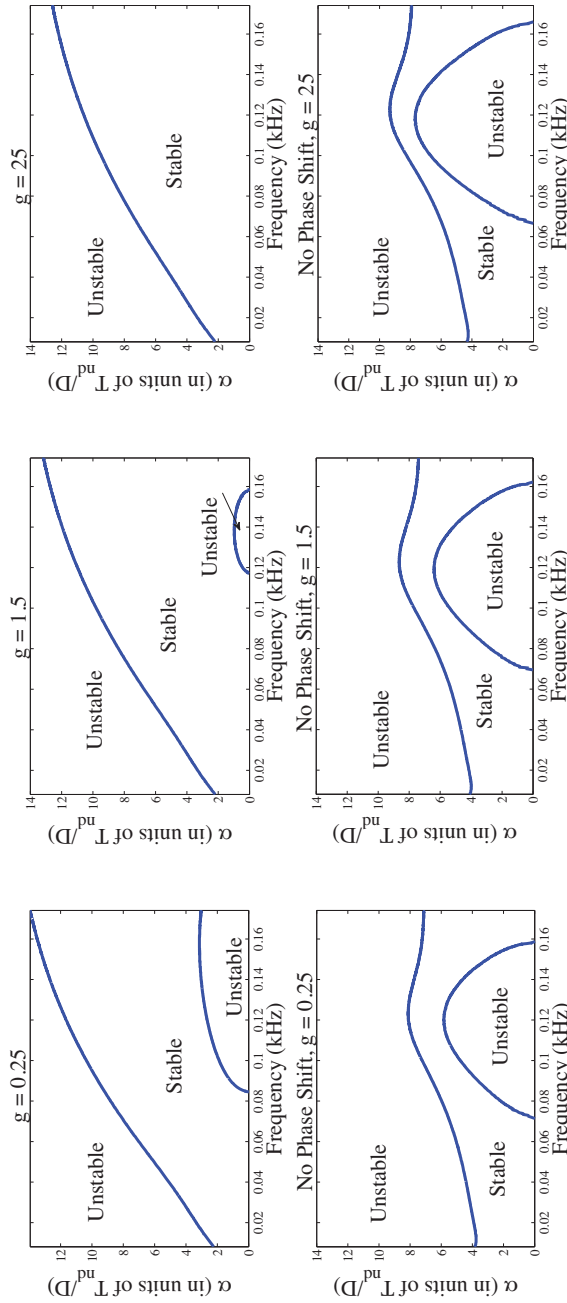
Figure 7.5.4: **Stability of Traveling Wave Solutions as Function of Neuronal Firing Frequency**. The top plots show the two parameter bifurcation diagrams of wave number versus firing frequency when the dendritic phase shift is included and when g increasing from 0.25 (left) to 25 (right). Increasing g appears to encourage the stability of the lower wave numbers at higher frequencies while at the same time causing the higher wave number to become unstable. The lower plots are the same as in the upper plots except that the dendritic phase shift is excluded. Increasing g in these plots decreases the number of stable waves in the frequency range of roughly 0.9 kHz to 0.14 kHz. Furthermore, the inclusion of the dendritic phase shift appears to allow a wider range of traveling wave solutions to be stable.

neuron whose soma is at position (k, m). This network can display many different types of behavior such as traveling waves and spiral waves (see Figure 7.6.1).
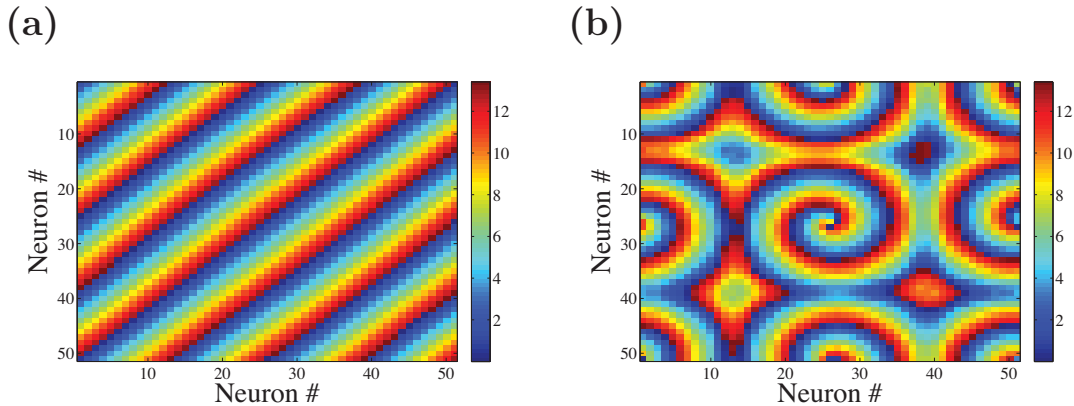
(a) **(b)**

Figure 7.6.1: **Examples of Two-Dimensional Network Behavior.** Numerical simulation of (7.6.1) with a network of 51×51 neurons. The plots show the network behavior at a single point in time. The colorscale represents the phase of the neurons which goes from 0 to $T = 13.4$ *msec*. The two-dimensional electrically coupled ball-and-stick network can display different types of interesting behavior such as (a) traveling waves and (b) spiral waves of activity.

7.7 Future Directions

In the future, we plan to further examine the behavior of networks of electrically coupled ball-and-stick neurons. For example, in the two-cell case, we can examine the effects of different length dendrites on the phase-locking behavior of the two cells. We will also see how adding noise to the system can affect the phase-locking behavior using the recent extensions in the theory of weakly coupled oscillators to include the effects of noise, e.g. [101, 115]. In the one-dimensional network case, we will examine how heterogeneity and different network topologies will affect the phase-locking dynamics we have observed here. Lastly, we would like to first quantify the different types of phase-locking behavior we have seen in the two-dimensional

network, and then see how heterogeneity and different network topologies alter these

results.

References

[1] L.F. Abbott. Lapicques introduction of the integrate-and-fire model neuron (1907). *Brain Res. Bull.*, 50(5-6):303–304, 1999.

[2] Y. Amitai, J.R. Gibson, M. Beierlein, P.L. Patrick, A.M. Ho, B.W. Connors, and D. Golomb. The spatial dimensions of electrically coupled networks of interneurons in the neocortex. *J. Neurosci.*, 22(10):4142–4152, 2004.

[3] R. Azouz and C. M. Gray. Cellular mechanisms contributing to response variability of cortical neurons in vivo. *J. Neurosci.*, 19:2209–2223, 1999.

[4] M. Beierlein, J.R. Gibson, and B.W. Connors. A network of electronically coupled interneurons drives synchronized activity in neocortex. *Nature Neurosci.*, 3:904–910, 2000.

[5] B.D. Bennett, J.C. Callaway, and C.J. Wilson. Intrinsic membrane properties underlying spontaneous tonic firing in neostriatal cholinergic interneurons. *J. Neurosci.*, 20(22):8493–8503, 2000.

[6] B.D. Bennett and C.J. Wilson. Spontaneous activity of neostriatal cholinergic interneurons *in vitro*. *J. Neurosci.*, 19(13):5586–5596, 1999.

[7] M.D. Bevan and C.J. Wilson. Mechanisms underlying spontaneous oscillation and rhythmic firing in rat subthalamic neurons. *J. Neurosci.*, 19(17):7617–7628, 1999.

[8] C. Börgers, S. Epstein, and N. Kopell. Background gamma rhythmicity and attention in cortical local circuits: A computational study. *Proc. Nat. Acad. Sci.*, 102(19):7002–7007, 2005.

[9] A. Bose and V. Booth. Bursting in 2-compartment neurons: A case study of the Pinsky-Rinzel model. In S. Coombes and P. Bressloff, editors, *Bursting: The genesis of rhythm in the nervous system*, pages 123–144. World Scientific, 2005.

[10] P.C. Bressloff. Resonantlike synchronization and bursting in a model of pulse-coupled neurons with active dendrites. *J. Comput. Neurosci.*, 6:237–249, 1999.

[11] P.C. Bressloff and S. Coombes. Physics of the extended neuron. *J. Mod. Phys. B*, 11:2343–2392, 1997.

[12] P.C. Bressloff and S. Coombes. Synchrony in an array of integrate-and-fire neurons with dendritic structure. *Physical Review Letters*, 78:4665–4668, 1997.

[13] E. Brown, J. Moehlis, and P. Holmes. On the phase reduction and response dynamics of neural oscillator populations. *Neural Comp.*, 16:673–715, 2004.

[14] G. Buzsáki and A. Draguhn. Neuronal oscillations in cortical networks. *Science*, 304(5679):1926–1929, 2004.

[15] J.A. Cardin, M. Carlén, K. Meletis, U. Knoblich, F. Zhang, K. Deisseroth, L. Tsai, and C.I. Moore. Driving fast-spiking cells induces gamma rhythm and controls sensory responses. *Nature*, 459:663–667, 2009.

[16] M.J. Chacron, K. Pakdaman, and A. Longtin. Interspike interval correlations, memory, adaptation, and refractoriness in a leaky integrate-and-fire model with threshold fatigue. *Neural Comp.*, 15:253–278, 2003.

[17] C. C. Chow and N. Kopell. Dynamics of spiking neurons with electrical coupling. *Neural Computation*, 12:1643–1678, 2000.

[18] R.V. Churchill. Expansions in series of non-orthogonal functions. *Am. Math Soc. Bull.*, 48:143–149, 1981.

[19] B.W. Connors and M.A. Long. Electrical synapses in the mammalian brain. *Annu. Rev. Neurosci.*, 27:393–418, 2004.

[20] S.M. Crook, G.B. Ermentrout, and J.M. Bower. Dendritic and synaptic effects in systems of coupled cortical oscillators. *J. Comp. Neurosci.*, 5:315–329, 1998.

[21] S.M. Crook, G.B. Ermentrout, M.C. Vanier, and J.M. Bower. The role of axonal delay in the synchronization of networks of coupled cortical oscillators. *J. Comp. Neurosci.*, 4:161–172, 1997.

[22] B. Doiron, C. Laing, and A. Longtin. Ghostbursting: A novel neuronal burst mechanism. *J. Comp. Neurosci.*, 12:5–25, 2002.

[23] M. Dolnik, T.S. Gardner, I. R. Epstein, and J. J. Collins. Frequency control of an oscillatory reaction by reversible binding of an autocatalyst. *Phys. Rev. Lett.*, 82(7):1582–1585, 1999.

[24] J. Duijnhouwer, M.W.H. Remme, A. van Ooyen, and J. van Pelt. Influence of dendritic topology on firing patterns in model neurons. *Neurocomputing*, 38–40:183–189, 2001.

[25] D. Durand. The somatic shunt cable model for neurons. *Biophys J*, 46:645–653, 1984.

[26] J.C. Eccles. *The Physiology of Nerve Cells*. Johns Hopkins University Press, Baltimore, 1980.

[27] A. Erisir, D. Lau, B. Rudy, and C.S. Leonard. Function of specific k+ channels in sustained high-frequency firing of fast-spiking neocortical interneurons. *J. Neurophysiol.*, 82:2476–2489, 1999.

[28] B. Ermentrout. *Simulating, Analyzing, and Animating Dynamical Systems: A Guide to XPPAUT for Researchers and Students*. SIAM, 2002.

[29] G.B. Ermentrout. n:m phase-locking of weakly coupled oscillators. *J. Math. Bio.*, 12:327–342, 1981.

[30] G.B. Ermentrout. The behavior of rings of coupled oscillators. *J. Math. Biology*, 23:55–74, 1985.

[31] G.B. Ermentrout. Stable periodic solutions to discrete and continuum arrays of weakly coupled nonlinear oscillators. *SIAM J. Appl. Math.*, 52(6):1665–1687, 1992.

[32] G.B. Ermentrout. Type 1 membranes, phase resetting curves, and synchrony. *Neural Computation*, 8:1979–1001, 1996.

[33] G.B. Ermentrout and D. Kleinfeld. Traveling electrical waves in cortex: Insights from phase dynamics and speculation on a computational role. *Neuron*, 29:33–44, 2001.

[34] G.B. Ermentrout and N. Kopell. Multiple pulse interactions and averaging in systems of coupled neural oscillators. *J. Math. Bio.*, 29:33–44, 1991.

[35] R. FitzHugh. Impulses and physiological states in theoretical models of nerve membrane. *Biophys. J.*, 1(6):445–466, 1961.

[36] T. Fukuda, T. Kosaka, W. Singer, and R.A.W. Galuske. Gap junctions among dendrites of cortical gabaergic neurons establish a dense and widespread inter-columnar network. *J. Neurosci.*, 26:3434–3443, 2006.

[37] M. Galaretta and S. Hestrin. A network of fast spiking cells in the neocortex connected by electrical synapses. *Nature*, 402:72–75, 1999.

[38] J.R. Gibson, M. Beierlein, and B.W. Connors. Two networks of electrically coupled inhibitory neurons in neocortex. *Nature*, 402:75–79, 1999.

[39] J.R. Gibson, M. Beierlein, and B.W. Connors. Functional properties of electrical synapses between inhibitory interneurons of neocortical layer 4. *J. Neurosci.*, 93:467–480, 2005.

[40] J. A. Goldberg, C. A. Deister, and C. J. Wilson. Response properties and synchronization of rhythmically firing dendritic neurons. *J. Neurophysiol.*, 97(1):208–219, 2007.

[41] D. Golomb and Y. Amitai. Propagating neuronal discharges in neocortical slices: Computational and experimental study. *J. Neurophysiol.*, 78:1199–1211, 1997.

[42] C.M. Gray, P. Konig, A.K. Engel, and W. Singer. Oscillatory responses in cat visual cortex exhibit inter-columnar synchronization which reflects global stimulus properties. *Nature*, 338:334–337, 1989.

[43] J. Guckenheimer and P. Holmes. *Nonlinear Oscillations, Dynamical Systems, and Bifurcations of Vector Fields.* Springer-Verlag, NY, 1983.

[44] A. Hodgkin and A. Huxley. A quantitative description of membrane current and its application to conduction and excitation in nerve. *J. Physiol.*, 117:500–544, 1952.

[45] A.L. Hodgkin. The local electric changes associated with repetitive action in a non-medulated axon. *J. Physiol.*, 107:165–181, 1948.

[46] F. C. Hoppensteadt and E. M. Izikevich. *Weakly Connected Neural Networks.* Springer-Verlag, New York, 1997.

[47] F. C. Hoppensteadt and C. Peskin. *Modeling and simulation in medicine and the life sciences. Second Edition.* Springer-Verlag, New York, 2001.

[48] H. Hu, M. Martina, and P. Jonas. Dendritic mechanisms underlying rapid synaptic activation of fast-spiking hippocampal interneurons. *Science*, 327:52–58, 2010.

[49] E. M. Izhikevich. *Dynamical Systems in Neuroscience: the Geometry of Excitability and Bursting.* MIT Press, Cambridge, MA, 2007.

[50] R. Jolivet, T.J. Lewis, and W. Gerstner. Generalized integrate-and-fire models of neuronal activity approximate spike trains of a detailed model to a high degree of accuracy. *J. Neurophysiol.*, 92:959–976, 2004.

[51] T.B. Kepler, E. Marder, and L.F. Abbott. The effect of electrical coupling on the frequency of model neuronal oscillators. *Science*, 248:83–85, 1990.

[52] C. Koch and I. Segev. The role of single neurons in information processing. *Nature*, 3:1171–1177, 2000.

[53] N. Kopell and G.B. Ermentrout. Chemical and electrical synapses perform complementary roles in the synchronization of interneuronal networks. *Proc. Nat. Acad. Sci.*, 101:15482–15487, 2003.

[54] Y. Kuramoto. *Chemical Oscillations, Waves, and Turbulence.* Springer-Verlag, Berlin, 1984.

[55] C. Laing and A. Longtin. A two-variable model of somatic-dendritic interactions in a bursting neuron. *Bull. Math. Bio.*, 64(5):829–860, 2002.

[56] P. Lánský and R. Rodriguez. The spatial properties of a model neuron increases its coding range. *Biol. Cybern.*, 81:161–167, 1999.

[57] G. Laurent and H. Davidowitz. Encoding of olfactory information with oscillating neural assemblies. *Science*, 265:1872–1875, 1994.

[58] T.J. Lewis and J. Rinzel. Dynamics of spiking neurons connected by both inhibitory and electrical coupling. *J. Comp. Neurosci.*, 14:283–309, 2003.

[59] T.J. Lewis and J. Rinzel. Dendritic effects in networks of electrically coupled fast-spiking interneurons. *Neurocomputing*, 58-60:145–150, 2004.

[60] M.A. Long, C.E. Landisman, and B.W. Connors. Small clusters of electrically coupled neurons generate synchronous rhythms in the thalamic reticular nucleus. *J. Neurosci.*, 24(2):341–349, 2004.

[61] Z.F. Mainen and T.J. Sejnowski. Influence of dendritic structure on firing pattern in model neocortical neurons. *Nature*, 382:363–366, 1996.

[62] I.G. Malkin. *Methods of Poincare and Liapunov in Theory of Non-Linear Oscillations.* Gostexizdat, Moscow, 1949.

[63] I.G. Malkin. *Some Problems in Nonlinear Oscillation Theory.* Gostexizdat, Moscow, 1956.

[64] J.G. Mancilla, T.J. Lewis, D.J. Pinto, J. Rinzel, and B.W. Connors. Synchronization of electrically coupled pairs of inhibitory interneurons in neocortex. *J. Neurosci.*, 27(8):2058–2073, 2007.

[65] C.J. McBain and A. Fisahn. Interneurons unbound. *Nature Reviews*, 2:11–23, 2001.

[66] W.H.R. Miltner, C. Braun, M. Arnold, H. Witte, and E. Taub. Coherence of gamma-band eeg activity as a basis for associative learning. *Nature*, 397:434–436, 1999.

[67] C. Morris and H. Lecar. Voltage oscillations in the barnacle giant muscle fiber. *Biophys J*, 35:193–213, 1981.

[68] V.N. Murthy and E.E. Fetz. Oscillatory activity in sensorimotor cortex of awake monkeys: Synchronization of local field potentials and relation to behavior. *J.Neurophysiol.*, 76:3949–3967, 1996.

[69] J. Nagumo, S. Arimoto, and S. Yoshizawa. An active pulse transmission line simulating nerve axon. *Proc. IRE.*, 50(10):2061–2070, 1962.

[70] T.I. Netoff, C.D. Acker, J.C. Bettencourt, and J.A. White. Beyond two-cell networks: experimental measurement of neuronal responses to multiple synaptic inputs. *J. Comput. Neurosci.*, 18:287–295, 2005.

[71] J.C. Neu. Coupled chemical oscillators. *SIAM J. Appl. Math.*, 37(2):307–315, 1979.

[72] Kiehn O. and M.C. Tresch. Gap junctions and motor behavior. *TRENDS in Neurosci,*, 25(2):108–115, 2001.

[73] B.E. Peercy and J.P. Keener. Coupled cell model of border zone arrhythmias. *SIAM J. Appl. Dyn. Sys.*, 4(3):679–710, 2005.

[74] B. Pfeuty, G. Mato, D. Golomb, and D. Hansel. Electrical synapses and synchrony: The role of intrinsic currents. *J. Neurosci.*, 23(15):6280–6294, 2003.

[75] B. Pfeuty, G. Mato, D. Golomb, and D. Hansel. The combined effects of inhibitory and electrical synapses in synchrony. *Neural Computation*, 17:633–670, 2005.

[76] D.P. Phillips and D.R.F. Irvine. Responses of single neurons in physiologically defined primary auditory cortex (a1) of the cat: Frequency tuning and responses to intensity. *J. Neurophysiol.*, 45(1):48–58, 1981.

[77] P.F. Pinsky and J. Rinzel. Intrinsic and network rhythmogenesis in a reduced traub model for ca3 neurons. *J. Comp. Neurosci..*, 1:39–60, 1994.

[78] W. Rall. Membrane time constants of motoneurons. *Science*, 126:454, 1957.

[79] W. Rall. Branching dendritic trees and motoneuron membrane resistivity. *Expt. Neurology*, 2:491–527, 1959.

[80] W. Rall. Membrane potential transients and membrane time constant of motoneurons. *Expt. Neurology*, 2:503–532, 1960.

[81] W. Rall. Theory of physiological properties of dendrites. *Ann. N.Y. Acad. Sci.*, 96:1071–1092, 1962.

[82] W. Rall. Distribution of potential in cylindrical coordinates and time constants for a membrane cylinder. *Biophys. J.*, 9:1509–1541, 1969.

[83] W. Rall. Time constants and electrotonic length of membrane cylinders and neurons. *Biophysical Journal*, 9:1483–1508, 1969.

[84] W. Rall. *Time constants and electrotonic length of membrane cylinders and neurons. In: Handbook of Physiology. The Nervous System I, Ed: J.M. Brookhart and V.B. Mountcastle.* American Physiological Society, Bethesda, MD, 1977.

[85] J.C. Rekling and J.L. Feldman. Electrical coupling and neuronal synchronization in the mammalian brain. *Neuron*, 41(4):495–511, 1998.

[86] J.C. Rekling and J.L. Feldman. Pre-bötzinger complex and pacemaker neurons: Hypothesized site and kernel for respiratory rhythm generation. *Ann. Rev. of Physiol.*, 60:385–405, 1998.

[87] L. Rela and L. Szczupak. Gap junctions: Their importance for the dynamics of neural circuits. *Molecul. Neurobio.*, 30(3):341–357, 2004.

[88] M. Remme, M. Lengyel, and B.S. Gutkin. Democracy-independence trade-off in oscillating dendrites and its implications for grid cells. *Neuron*, 66(3):429–437, 2010.

[89] J. Rinzel and G.B. Ermentrout. *Analysis of Neural Excitability and Oscillations. In: Koch C, Segev I (eds) Methods in Neuronal Modelling: from Synapses to Networks.* MIT Press, Cambridge, Mass. pp 135-171, 1989.

[90] J. Rinzel and J.P. Keener. Hopf bifurcation to repetitive activity in nerve. *SIAM J. Appl. Math.*, 43(4):907–922, 1983.

[91] H. Risken. *The Fokker-Planck Equation: Methods of Solution and Applications.* Springer-Verlag, NY, 1989.

[92] P.R. Roelfsema, A.K. Engel, P. König, and W. Singer. Visuomotor integration is associated with zero time-lag synchronization among cortical areas. *Nature*, 385(9):157–161, 1997.

[93] E. Salinas and T.J. Sejnowski. Correlated neuronal activity and the flow of neural information. *Nat. Rev. Neurosci.*, 2:539–550, 2001.

[94] M.A. Schwemmer and T.J. Lewis. Effects of dendritic load on the firing frequency of oscillating neurons. *Phys. Rev. E (submitted)*, 2010.

[95] I. Segev, J. Rinzel, and G.M. Shepherd, editors. *The Theoretical Foundations of Dendritic Function: The Selected Papers of Wilfrid Rall with Commentaries.* MIT Press, 1994.

[96] A. A. Sharp, L. F. Abbott, and E. Marder. Artificial electrical synapses in oscillatory networks. *J. Neurophysiol.*, 67(6):1691–1694, 1992.

[97] F.K. Skinner, G.G. Turrigiano, and E. Marder. Frequency and burst duration in oscillating neurons and two-cell networks. *Biol. Cybern.*, 69:375–383, 1993.

[98] V.S. Sohal, F. Zhang, O. Yizhar, and K. Deisseroth. Parvalbumin neurons and gamma rhythms enhance cortical circuit performance. *Nature*, 459:698–702, 2009.

[99] R.B. Stein. Some models of neuronal variability. *Biophys. J.*, 7:37–68, 1967.

[100] R.L. Stratonovich. *Topics in the Theory of Random Noise.* Gordon and Breach, NY, 1967.

[101] J. Teramae, H. Nakao, and G.B. Ermentrout. Stochastic phase reduction for a general class of noisy limit cycle oscillators. *Phys. Rev. Lett.*, 102:194102, 2009.

[102] R. Traub, R. Wong, R. Miles, and H. Michelson. A model of a ca3 hippocampal pyramidal neuron incorporating voltage-clamp data on intrinsic conductances. *J. Neurophysiol.*, 66:635–649, 1991.

[103] R.D. Traub, N. Kopell, A. Bibbig, E. Buhl, F.E.N. LeBeau, and M.A. Whittington. Gap junctions between interneuron dendrites can enhance synchrony of gamma oscillations in distributed networks. *J. Neurosci.*, 21(23):9478–9486, 2001.

[104] R.D. Traub and R. Miles. Pyramidal cell-to-inhibitory cell spike transduction explicable by active dendritic conductances in inhibitory cell. *J. Comp. Neurosci.*, 2(4):291–298, 1995.

[105] M.C. Tresch and O. Kiehn. Synchronization of motor neurons during locomotion in the neonatal rat: Predictors and mechanisms. *J. Neurosci*, 22(22):9997–10008, 2002.

[106] N.G. van Kampen. *Stochastic Processes in Physics and Chemistry*. Amsterdam: Elsevier Science, 1981.

[107] A. van Ooyen, J. Duijnhouwer, M.W.H. Remme, and J. van Pelt. The effect of dendritic topology on firing patterns in model neurons. *Network: Comput. Neural Syst.*, 13:311–325, 2002.

[108] C. Van Vreeswijk, L.F. Abbott, and G.B. Ermentrout. When inhibition not excitation synchronizes neural firing. *J. Comp. Neurosci.*, 1(4):313–321, 1994.

[109] X.J. Wang. Fast firing and short-term synaptic plasticity: A model of neocortical chattering neurons. *Neuroscience*, 89(2):347–362, 1999.

[110] X.J. Wang and G. Buzsáki. Gamma oscillation by synaptic inhibition in a hippocampal interneuronal network model. *J. Neurosci.*, 16(20):6401–6413, 1996.

[111] X.J. Wang and J. Rinzel. Alternating and synchronous rhythms in reciprocally inhibitory model neurons. *Neural Comp.*, 4(1):84–97, 1992.

[112] T.L. Williams and G. Bowtell. The calculation of frequency-shift functions for chains of coupled oscillators, with application to a network model of the lamprey locomotor pattern generator. *J. Comput. Neurosci.*, 4:47–55, 1997.

[113] C.J. Wilson and P.M. Groves. Spontaneous firing patterns of identified spiny neurons in the rat neostriatum. *Brain Res.*, 220:67–80, 1981.

[114] A. T. Winfree. *The Geometry of Biological Time.* Springer, NY, 1980.

[115] K. Yoshimura and K. Arai. Phase reduction of stochastic limit cycle oscillators. *Phys. Rev. Lett.*, 101:154101, 2008.

[116] T. Zahid and F.K. Skinner. Predicting synchronous and asynchronous network groupings of hippocampal interneurons coupled with dendritic gap junctions. *Brain Research*, 1262:115 – 129, 2009.